Development of Nanopore Based Label-Free Optical Sensors

A thesis submitted in fulfilment of the requirement for the degree of

Doctor of Philosophy

Engineering (Nanotechnology)

By Tushar Kumeria

April 2015

School of Chemical Engineering

Faculty of Engineering, Computer, and Mathematical Sciences

The University of Adelaide

CONTENT

ABSTRACT **iv**

PREFACE **vii**

LIST OF PUBLICATIONS **viii**

Journal Articles Published **viii**

Journal Articles in Preparation **xi**

Book Chapters **xi**

Conference Articles (peer reviewed) **xii**

Conference Presentations **xii**

DECLARATION **xv**

ACKNOWLEDGEMENTS **xvi**

CHAPTER 1: Introduction **1**

1.1. Sensors Introduction 2

1.2. Nanoporous Anodic Alumina (NAA) 5

1.2.1. History of NAA 5

1.2.2. Fabrication of NAA 7

1.2.3. Structural Engineering and Optical Optimization of NAA 13

1.2.4. Surface Chemistry and Functionalization of NAA 19

1.2.4.1. *Self-Assembled Monolayers (SAMs)* 22

1.2.4.2. *Sputter Coating* 27

1.2.5. Properties of NAA for Optical Sensing 28

1.2.5.1. *NAA based Optical Sensors* 28

1.3. Reflectometric Interference Spectroscopy (RIfS) 31

1.3.1. Principle 31

1.3.2. RIfS for Sensing and Biosensing 33

1.3.3. Challenges for NAA based Optical Sensing 40

1.4. Objectives 41

1.5. Thesis Structure 43

1.6. References 45

CHAPTER 2 **66**

2.1. Introduction and Objectives 67

2.2. Electrochemical Anodization for Fabrication of NAA 67

2.3. Functionalization of NAA with silanes using CVD process 71

2.4. Design and fabrication of bulk and microfluidic flow cells 72

2.5. RIfS setup for optical sensing measurements 75

2.6. References 76

CHAPTER 3: Ultrasensitive nanoporous interferometric sensors for label-free detection of gold (III) ions **78**

CHAPTER 4: Structural and optical nanoengineering of nanoporous anodic alumina rugate filters for real-time and label-free biosensing applications **96**

CHAPTER 5: Nanoporous anodic alumina rugate filters for sensing of ionic mercury: Toward environmental point-of-analysis systems **112**

CHAPTER 6: Advanced structural design of nanoporous photonic structures: Modulating nanopore architecture to enhance sensing properties **131**

CHAPTER 7: Optically optimized photoluminescent and interferometric biosensors based on nanoporous anodic alumina: a comparison **146**

CHAPTER 8: Real-time and in situ drug release monitoring from nanoporous implants under dynamic flow conditions by reflectometric interference spectroscopy **167**

CHAPTER 9 **182**

9.1. Conclusions 183

9.1.1. Ultrasensitive Nanoporous Interferometric Sensors for Label-Free Detection of Gold (III) Ions 184

9.1.2. Structural and Optical Nanoengineering of Nanoporous Anodic Alumina Rugate Filters for Real-Time and Label-Free Biosensing Applications 185

9.1.3. Nanoporous Anodic Alumina Rugate Filters for Sensing of Ionic Mercury: Toward Environmental Point-of-Analysis Systems 186

9.1.4. Advanced Structural Design of Nanoporous Photonic Structures: Modulating Nanopore Architecture to Enhance Sensing Properties 187

9.1.5. Optically Optimized Photoluminescent and Interferometric Biosensors Based on Nanoporous Anodic Alumina: A Comparison 188

9.1.6. Real-Time and In Situ Drug Release Monitoring From Nanoporous Implants under Dynamic Flow Conditions by Reflectometric Interference Spectroscopy 189

9.2. Recommendations for Future Work 190

APPENDIX A: Photo-Switchable Membranes based on Peptide-Modified Nanoporous Anodic Alumina: Toward Smart Membranes for On-Demand Molecular Transport **192**

APPENDIX B: Nanoporous anodic alumina platforms: Engineered surface chemistry and structure for optical sensing applications **199**

ABSTRACT

Optical sensors play an important role and are employed for more application in today's lives than ever before. As an example, optical sensing systems have established strong footprints in quality assurance (i.e. ensuring safe levels of controlled substances in drinks and food products) and self-diagnostics (e.g. detection and quantification of glucose in blood or pregnancy assessment test). Conventional optical sensor read-out is based on colour change or signal variation (i.e. absorbance or fluorescence intensity) of the label/tag molecule (i.e. dyes) conjugated to the capture probes. However, requirement of expensive and sophisticated labels/tags and instruments, skilled personnel, and other inherent issues with the dye labels (i.e. short lift-time, concentration dependent quenching etc.) limit their broader application. Therefore, label-free sensors present a great advantage over their label based counterparts. Label-free optical sensors rely on changes in physical properties (e.g. refractive index: n) of the sensing substrate occurring during a binding event. Nanoporous substrates (i.e. porous silicon, nanoporous anodic alumina, and titania nanotubes arrays) prepared by simple and scalable electrochemical anodization process in combination with spectroscopy techniques that can be realized with miniature spectrometer (e.g. reflectometric interference spectroscopy, localized surface plasmon resonance spectroscopy etc.) can potentially overcome the limitations of label-based sensing systems. However, comprehensive and extensive fundamental research must be carried out in this field to make this technology feasible, efficient, reliable, sensitive, selective and inexpensive.

In this scenario, this thesis puts forward a novel combination of nanoporous anodic alumina (NAA) and reflectometric interference spectroscopy (RIfS) for developing a highly sensitive detection system for environmental and biomedical sensing application. High surface area, modifiable surface chemistry, and optical activity make NAA a perfect substrate for highly sensitive label-free detection using RIfS platform. Moreover, the geometric features of NAA can

be controlled during the fabrication process to generate more complex optical photonic structures. The simplicity and versatility of this combination (i.e. NAA and RIfS) also allows for real-time monitoring of the release of drug for the NAA pores. The most relevant features of this thesis are:

1. *NAA Substrate and its Surface Chemistry*: Optimization and fabrication of NAA substrate with straight pores using two step electrochemical anodization process. Optimization and modification of NAA surface chemistry with different silanes (e.g. amine terminated or thiol terminated) to impart it selectivity and specificity towards analyte molecules.

2. *NAA Photonic Structures*: Designing, fabrication, and optimization of NAA pore geometry (i.e. effective medium) to obtain photonic structures (i.e. Rugate filters) that display highly sensitive and selective detection capabilities in combination with RIfS. Comparison of sensing capabilities of NAA straight pores with NAA photonic structures.

3. *Flow Cells for Sensing*: Designing and fabrication of different types of flow cells including bulk and micro-fluidic flow cell that can accommodate NAA substrates.

4. *Sensing of Heavy Metal Ions*: Modification of NAA substrate with silane which specifically bind to heavy metal ions such as gold (III) and mercury (II) ions in model solvent (i.e. mili-Q water) and real-life samples (i.e. tap water and water from river Torrens in Adelaide, South Australia).

5. *RIfS vs Photoluminescence using NAA Substrate*: Sensing properties of NAA studied using RIfS and photoluminescence as the detection techniques, when analytes were introduced into NAA pores under non-specific and specific binding conditions.

6. *Real-time Drug Release Monitoring from NAA Pores*: NAA pores can act as nanocontainers which can hold substantial amounts of drug molecules that can be released over an extended

period of time. NAA loaded with model drug acts as a way of measuring the drug release from its pores in real-time and under dynamic flow conditions using RIfS.

The results presented in this thesis are expected to open doors for the development of more innovative and complex NAA photonic structures and surface chemistries aimed to produce highly sensitive and selective miniature, portable, and point-of-care analysis system for various industrial, environmental, and biomedical applications.

PREFACE

The research during the three years of this PhD resulted in successful publication or submission of 22 peer-reviewed articles in reputed journals in the respective fields and 4 book chapters. Additionally, 3 other journal articles are under final preparation and will be submitted in 2015. Also, the research carried out during this PhD study was presented at 15 national and international conferences. This thesis is submitted as a thesis by publications according to the "Specifications for Thesis 2013" of The University of Adelaide. The six chapters (i.e. articles) presented in the thesis were published in the most highly ranked journal in the field (i.e. impact factor higher than 5). A complete list of publications is provided in following pages.

LIST OF PUBLICATIONS

Peer-reviewed Journal Articles Published:

1. **T. Kumeria**, J. Yu, M. Alsawat, M. D. Kurkuri, A. Santos, A. D. Abell, Dusan Losic "Photo-Switchable Membranes based on Peptide-Modified Nanoporous Anodic Alumina: Toward Smart Membranes for On-Demand Molecular Transport**"** *Advanced Materials*, 2015, **DOI:** 10.1002/adma.201500473 (Featured as Journal Cover, IF=15.41).
2. **T. Kumeria**, H. Mon, M. S. Aw, K. Gulati, A. Santos, H. J. Griesser, D. Losic "Advanced biopolymer-coated drug-releasing titania nanotubes (TNTs) implants with simultaneously enhanced osteogenic and antibacterial properties" *Colloids and Surfaces B: Biointerfaces*, 2015, **DOI:** 10.1016/j.colsurfb.2015.04.021 (IF=4.42) (Accepted).
3. M. Alsawat, T. Altalhi, **T. Kumeria**, A. Santos, D. Losic, "Carbon nanotube membranes with controllable inner diameters and surface chemistry: Influence on molecular transport and chemical selectivity" Carbon, 2015 (IF=6.16, Under review).
4. V. S. Saji, **T. Kumeria**, M. Shafi, K. Gulati, G. J. Atkins, D. Losic "Selenium loaded nanoporous anodized aluminium oxide for potential localized cancer therapy" *Journal of Materials Chemistry B,* 2015 (IF=6.63) (Under review).
5. S. Maher, M. Alsawat, **T. Kumeria**, D. Fathalla, F. Gihan, A. Santos, H. Fawzia, D. Losic, "Luminescent silicon diatom replicas: Self-reporting and degradable drug carriers with biologically derived shape for sustained delivery of therapeutics" Advanced Functional Materials, 2015 (IF=10.4, Under review).
6. Y. Chen, A. Santos, Y. Wang, **T. Kumeria**, D. Ho, J. Li, C. Wang, D. Losic, "Rational design of photonic dust from nanoporous anodic alumina films: A versatile photonic nanotool for visual sensing" Scientific Reports, 2015 (IF=5.1, Under review).

7. Y. Chen, A. Santos, Y. Wang, **T. Kumeria**, C. Wang, J. Li, D. Losic "Interferometric nanoporous anodic alumina photonic coatings for optical sensing" *Nanoscale*, 2015, **DOI:** 10.1039/C5NR00369E (IF=6.74).
8. C. S. Law, A. Santos, **T. Kumeria**, D. Losic "Engineered Therapeutic-Releasing Nanoporous Anodic Alumina-Aluminum Wires with Extended Release of Therapeutics" *ACS Applied Materials and Interfaces*, 2015, **7**, 3846 (IF=5.9).
9. **T. Kumeria**, A. Santos, M. M. Rahman, J. Ferre-Borrull, L. F. Marsal, D. Losic "Advanced structural design of nanoporous photonic structures: Modulating nanopore architecture to enhance sensing properties" *ACS Photonics,* 2014, **1**, 1298.
10. **T. Kumeria**, M. M. Rahman, A. Santos, J. Ferre-Borrull, L. F. Marsal, D. Losic "Nanoporous anodic alumina rugate filters for sensing of ionic mercury: Toward environmental point-of-analysis systems" *ACS Applied Materials & Interfaces*, 2014, **6**, 12971 (IF=5.90).
11. A. Santos, M. Sinn Aw, M. Bariana, **T. Kumeria**, Y. Wang, D. Losic "Drug-releasing implants: Current progress, challenges and perspectives" *Journal of Materials Chemistry B*, 2014, **2**, 6157 (IF=6.63).
12. **T. Kumeria**, A. Santos, D. Losic "Nanoporous anodic alumina platforms: Engineered surface chemistry and structure for optical sensing applications" *Sensors*, 2014, **14**, 11878 (IF=2.05).
13. A. Santos, **T. Kumeria**, D. Losic "Nanoporous anodic alumina: A versatile platform for optical biosensors" *Materials*, 2014, **7**, 4297 (IF=1.88).
14. A. Santos, **T. Kumeria**, Y. Wang, D. Losic "In situ monitored engineering of inverted nanoporous anodic alumina funnels: On the precise generation of 3D optical nanostructures" *Nanoscale*, 2014, **6**, 9991 (Featured as Journal Cover, IF=6.74).

15. S. Kabiri, M. D. Kurkuri, **T. Kumeria**, D. Losic "Frit free PDMS Microfluidic Devices for Chromatographic Separation and On-Chip Detection' *RSC Advances,* 2014, **4**, 15276 (IF=3.74).
16. **T. Kumeria**, M. M. Rahman, A. Santos, J.Ferre-Borrull, L. F. Marsal, D. Losic "Structural and Optical Nanoengineering of Nanoporous Anodic Alumina Rugate Filters for Real-Time and Label-Free Biosensing Applications" *Analytical Chemistry*, 2014, **86**, 1837 (IF=5.83).
17. **T. Kumeria**, A. Santos, D. Losic "Ultrasensitive nanoporous interferometric sensors for label-free detection of gold (III) ions", *ACS Applied materials & interfaces*, 2013, **5**, 11783 (IF=5.90).
18. **T. Kumeria**, M. Bariana, T. Altalhi, M. Kurkuri, C. T. Gibson, W. Yang, and D. Losic "Graphene oxide decorated diatom silica particles as a new nano-hybrid: towards smart natural drug microcarriers", *Journal of Materials Chemistry B*, 2013, **1**, 6302 (IF=6.63).
19. A. Santos, **T. Kumeria**, D. Losic "Optically optimized photoluminescent and interferometric biosensors based on nanoporous anodic alumina: a comparison" *Analytical Chemistry*, 2013, **85**, 7904 (IF=5.83).
20. T. Altalhi, **T. Kumeria**, A. Santos, D. Losic "Synthesis of well organised carbon nanotubes from non-degradable plastic bags with tuneable molecular transport: Towards smart nanotechnological recycling" *Carbon*, 2013, **63**, 423 (IF=6.16).
21. **T. Kumeria**, K. Gulati, A. Santos, D. Losic "Real-time and in situ drug release monitoring from nanoporous implants under dynamic flow conditions by reflectometric interference spectroscopy" *ACS Applied materials & interfaces*, 2013, **5**, 5436 (IF=5.9).
22. A. Santos, **T. Kumeria**, D. Losic "Nanoporous anodic aluminium oxide for chemical sensing and biosensors" *Trends in analytical chemistry*, 2013, **44**, 25 (Review paper) (IF=6.61).

Journal Articles in Preparation:

23. **T. Kumeria**, J. Wang, A. Santos, D. Losic, M. J. Sailor "Size exclusion based porous silicon microparticle and polymer composite for artificial pigments" 2015 (Under preparation).
24. **T. Kumeria**, J. S. Gofus, A. Santos, D. Losic, M. J. Sailor "Carbonized porous silicon photonic crystals for organic vapour sensing" 2015 (Under preparation).
25. J. Wang, **T. Kumeria**, A. Santos, D. Losic, M. J. Sailor "Calcium and magnesium based core/shell porous silicon microparticles with highly efficient drug loading and release capacities" 2015 (Under preparation).

Book Chapters:

1. **T. Kumeria** and A. Santos "Sensing and biosensing applications of nanoporous anodic alumina" in book *Electrochemically engineered nanoporous materials - Methods, properties and applications* 2015, ed. By D. Losic and A. Santos (Springer International Publishing AG - Germany) (Accepted).
2. **T. Kumeria** and A. Santos "Nanoporous Alumina Membranes for Chromatography and Molecular Transporting" in book *Nanoporous alumina - Fabrication, structure, properties and applications* 2015, Edited by D. Losic and A. Santos (Springer International Publishing AG - Germany) (Accepted).
3. A. Santos and **T. Kumeria** "Electrochemical etching methods for producing porous silicon" in *Electrochemically engineered nanoporous materials - Methods, properties and applications* 2015, (Springer International Publishing AG - Germany) (Accepted).
4. A. Santos and **T. Kumeria** "Nanoporous anodic alumina for optical biosensing" in *Nanoporous alumina - Fabrication, structure, properties and applications* 2015, (Springer International Publishing AG - Germany) (Accepted).

Conference Articles (peer reviewed):

1. **T. Kumeria**, T. Altalhi, D. Losic "Reflective interference study of binding nickel ions on nitrilotriacetic (NTA) nanoporous alumina chips for detections of his-tagged proteins" CHEMECA 2012, Wellington, New Zealand, Sept 2012.

Conference Presentations:

1. **T. Kumeria,** A. Santos, D. Losic "Structural engineering of nanoporous anodic alumina for environmental and biomedical sensing applications" Nanomaterials and Electrochemistry Symposium 2014, Sydney, Australia, Dec 2014. **(Invited talk).**
2. J. Wang, **T. Kumeria**, A. Santos, D. Losic, M. J. Sailor "Encapsulation of Layered Porous Silicon Photonic Crystals in Polymers by Size Exclusion" Silicon containing polymers and composites 2014, San Diego, California, USA Dec 2014. **(Best poster award).**
3. **T. Kumeria**, A. Santos, M. M. Rahman, J. Ferré-Borrull, L. F. Marsal, D. Losic "Nanoporous Anodic Alumina Rugate Filters for Sensing of Ionic Mercury" Biosensors 2014, Melbourne, Australia, May 2014. **(Poster presentation).**
4. A. Santos, **T. Kumeria**, M. M. Rahman, J. Ferré-Borrull, L. F. Marsal, D. Losic "Structural engineering of nanoporous anodic alumina rugate filter for detection of glucose: Perspective and limitations" Biosensors 2014, Melbourne, Australia, May 2014. **(Poster presentation).**
5. **T. Kumeria**, A. Santos, D. Losic "Nanoporous interferometric sensor for detection of Nickel (II) and Gold (III) ions: A comparative study" International Conference on Nanoscience and Nanotechnology 2014, Adelaide, Australia, Feb 2014. **(Oral presentation).**
6. M. Bariana, **T. Kumeria**, A. Santos, S. Ranjitkar, J. Kaidonis, D. Losic, P. Anderson, "Nanoporous anodic alumina as protein-delivery system for localised therapy: controlling drug-releasing characteristics by structural modifications" International Conference on Nanoscience and Nanotechnology 2014, Adelaide, Feb 2014 **(poster presentation).**

7. **T. Kumeria**, M. Bariana, T. Altalhi, M. Kurkuri, S. Kabiri, D. Losic "Graphene oxide diatomaceous earth hybrid as a drug microcarrier for poorly water soluble drugs" 4th International Nanomedicine Conference, University of New South Wales, Sydney, Australia, July 2013 **(Poster presentation).**
8. S. Foong, A. Santos, **T. Kumeria**, D. Losic "Structural Optimisation Interferometric Enzymatic Nanoreactors Based on Nanoporous Anodic Alumina Funnels" 4th International Nanomedicine Conference, University of New South Wales, Sydney, Australia, July 2013 **(Poster presentation).**
9. A. Santos, **T. Kumeria**, D. Losic "Optimisation and Comparison between Interferometric and Photoluminescent Optical Biosensors Based on Nanoporous Anodic Alumina" 4th International Nanomedicine Conference, University of New South Wales, Sydney, Australia, July 2013 **(Oral presentation).**
10. **T. Kumeria**, A. Santos, K. Gulati, D. Losic "Drug release kinetics from nanoporous anodic aluminium oxide under dynamic flow conditions" 4th ANZ micro/nanofluidics symposium and workshop, University of South Australia and Flinders University, Adelaide, Australia, April 2013 **(Poster presentation).**
11. **T. Kumeria**, M. Bariana, T. Altalhi, H. Y. Chen, M. D. Kurkuri, W. Cheng, D. Losic "Diatomite Silica – Graphene oxide based Nanohybrid Structures" OzCarbon 2012, University of Adelaide, Adelaide, Australia, July 2012 **(Poster presentation).**
12. **T. Kumeria**, A. Santos, D. Losic "Label-free reflectometric interference microchip biosensing using nanopore structures" Gordon Research Conference, Microfluidics, Physics and Chemistry of Challenges, Advances and New Technologies for Diagnostics, Luca, Italy June 2013, **(poster presentation).**
13. **T. Kumeria**, A. Santos, Q. Li, D. Losic "Enhanced Photoluminescence of Carbon Nanodots decorated on Nanotextures of Anodic Aluminium Oxide Substrate" International conference on Emerging Advanced Nanomaterials, Brisbane, Australia, Oct 2012 **(poster presentation).**

14. **T. Kumeria** and Dusan Losic "Study of Nickel Ions Binding Kinetics on Chelate modified Nanopores using Reflective Interference Spectroscopy" International conference on Emerging Advanced Nanomaterials, Brisbane, Australia, Oct 2012 **(poster presentation).**
15. D. Losic, M. Sinn Aw, K. Gulati, **T. Kumeria** "Self-organized nanopore and nanotube arrays for biomedical applications" International Nanomedicine conference, Sydney, Australia, July 2012 **(invited key lecture).**

DECLARATION

I certify that this work contains no material which has been accepted for the award of any other degree or diploma in any university or other tertiary institution and, to the best of my knowledge and belief, contains no material previously published or written by another person, except where due reference has been made in the text. In addition, I certify that no part of this work will, in the future, be used in a submission for any other degree or diploma in any university or other tertiary institution without the prior approval of the University of Adelaide and where applicable, any partner institution responsible for the joint-award of this degree.

I give consent to this copy of my thesis when deposited in the University Library, being made available for loan and photocopying, subject to the provisions of the Copyright Act 1968. The author acknowledges that copyright of published works contained within this thesis resides with the copyright holder(s) of those works. I also give permission for the digital version of my thesis to be made available on the web, via the University's digital research repository, the Library catalogue and also through web search engines, unless permission has been granted by the University to restrict access for a period of time.

10/04/2015

TUSHAR KUMERIA

ACKNOWLEDGEMENTS

Optics and photonics was one of my least favourite subjects during my bachelors and masters but this has changed in three years of PhD. I am really thankful to Prof. Dusan Losic and Dr. Abel Santos for introducing me to the coolness of Photonics and optics (in particular sensing using porous substrates). As my PhD supervisors Prof. Losic and Dr. Santos have done everything possible to make sure I didn't lose my interest in this subject. Above all, Prof. Losic and Dr. Santos have been a constant source of support and inspiration throughout this amazing three years long journey (PhD degree). I particularly appreciate Prof. Losic, who along with all the knowledge and support, gave me his priceless trust and total freedom to explore the exciting possibilities optical sensing with nanoporous alumina.

I cannot express my gratitude towards Dr. Abel Santos and his contribution in my Phd study in words. He is a brilliant scientist (one of the best I know) and has taught me a lot about science (how to design, carry out experiments and manage work) and life (in general, over coffee every morning). He has not only mentored me during this degree but has treated me like a friend and a younger brother.

I am highly grateful to have Dr. Tariq Altalhi, Manpreet Bariana, and Charu Rohatgi as my family away from home. The crazy talks over coffee and lunch, and the playstation games with Tariq have been the best stress buster. Without his support and friendship I will never ever be able to succeed.

Manpreet has been the strongest pillar of support during my PhD, who has always supported me in my goals and cheered me up when I am feeling low. Her patience for me is amazing, despite my endless tantrums… She just seems to have a knack of setting me straight, and telling me not to sway when in doubt. We have supported each other in lab as well in life (at home). I hope she will overcome all the hurdles soon and obtain her PhD (from Adelaide dental school).

I want to extend my thanks to Charu Rohatgi (Charu di), who has treated me like a family since the first day I arrived in Australia. She is an amazing cook, which is why I never missed home cooked food here in Adelaide. I hope she will finish her PhD soon as well.

I would like to thank my colleague Mohammed Alswat, who is a great man with a very generous and kind heart and has always supported me during the hard times of this PhD study. I have always received great support from the entire Losic group's member including Dr. Mahaveer Kurkuri, Dr. Lucas Johnson, Shervin Kabiri, Karan Gulati, and Krishna Kant in particular.

For this PhD work, I would like to extend my gratitude to workshop staff from the School of Chemical Engineering, particularly Jason Peak, Michael Jung, and Jeffrey Hiorns, for assistance with the fabrication of the flow cell for RIfS. Also, I want to thank Ken Neubauer from Adelaide Microscopy for always coating my SEM samples at very short notice and reserving the booking when needed.

I am grateful to have to worked with Prof. Michael J Sailor (UCSD, California) and thankful to him for providing me this opportunity. I made some great friends during my stay at UCSD who made my stay pleasant and fun. In particular, I would like to thank Joanna Wang (JoJo), Byungji Kim (BJ), Rhiannon Kennard (crazy cat lady), Maite Bezem (+ her husband and 1 yr old son), Tiago Paes (Aladeen), Jonathan Rasson (Brüno), and Jon Zuedema (Lütz) for their company and support during my stay. I also want to thank Kadiatou Aicha Sylla (Kaicha) for all the fun and food we shared in California. I want to thank Pearl Tangri, the most special and amazing person I met during my stay in USA, for sticking with me during hardest of times, always giving me the best suggestions in the world, and teaching me so many things about life.

I want to thank my friends outside of work including Albert Anthony (for his non-sense talks), Alwyn Madyiwa (for his great music), and Surojit Pradhan (for his great food).

And last but not least, I thank my father and my sister for all the support, thank you for believing in me, and my dreams. Your sheer love is unparalleled.

I dedicate this thesis to these very special people in my life:

My Grandmother

My Father

My Sister

And my Mother, who has been & still is, most sorely missed.

CHAPTER 1

INTRODUCTION

Tushar Kumeria

School of Chemical Engineering, The University of Adelaide, South Australia 5005, Australia

This chapter is based on the following published Review articles and Book chapter:

1. **T. Kumeria**, A. Santos, D. Losic "Nanoporous anodic alumina platforms: Engineered surface chemistry and structure for optical sensing applications" *Sensors*, 2014, **14**, 11878.
2. A. Santos, **T. Kumeria**, D. Losic "Nanoporous anodic alumina: A versatile platform for optical biosensors" *Materials*, 2014, **7**, 4297.
3. A. Santos, **T. Kumeria**, D. Losic "Nanoporous anodic aluminium oxide for chemical sensing and biosensors" *Trends in analytical chemistry*, 2013, **44**, 25.
4. **T. Kumeria** and A. Santos "Sensing and biosensing applications of nanoporous anodic alumina" in *Electrochemically engineered nanoporous materials - Methods, properties and applications* 2015, (Springer International Publishing AG - Germany) (Accepted).

CHAPTER 1: INTRODUCTION

1.1. Sensors Introduction

A sensor can be defined as an analytical device that measure any change in a physical or chemical quantity and present it as a readable output, which is easily understood by an observer [1]. A simple chemical or bio-sensor consist of three fundamental components (**Figure 1**); a) Sensing layer; that captures or binds to the target analyte (i.e. a chemical or biological molecule) to be detected, b) transducer; which converts the capturing or binding event into a readable signal (i.e. colorimetric, optical, electric, etc.), and c) display; which shows the final output reading obtained corresponding to the capturing event [1-3]. Over the last few decades, the research for new and more effective sensing tools for biomedical research, healthcare, pharmaceuticals, environmental monitoring, homeland security, and the battlefield has led to the development of a new generation of more powerful and smart sensors. Sensors and biosensors used in various application fields have a huge market of over several billion US$ every year. According to a recent study by www.persistencemarketresearch.com the global sensors market was USD 12.9 billion in 2014 and is expected to reach USD 22.5 billion by 2020, growing at a CAGR of 9.7% from 2014 to 2020. The report suggested Asia-pacific to witness the highest growths in this field by 2018 (i.e. more than 18%) according to a previous study [4-5]. Most conventional sensors developed over the past few decades rely on a labelling strategy, in which a label or a tag molecule (fluorescent or radioactive) is attached to the sensing element or the analyte to confirm the critical sensing reaction. Although label-based sensing methods are really sensitive and can provide detection limit up-to single molecule scale, preparation of the suitable label/tag and attaching it to the sensing entity is a labour intensive and expensive task [6]. This makes label-based sensing systems un-attractive for several

applications. Recently, a new breed of sensing devices has evolved which does not require labelling or tagging, thus omitting the inherent problem of labelled sensors. These sensors are called label-free sensors. Furthermore, the enormous amount of development in the mobile phone technology has given rise to a completely new plethora of compact, smart, low-cost, and simple sensing systems. Label-free sensing systems rely on changes in physical properties such as refractive index, mass, electrical parameters (potential, current, resistance and so on) and others in response to binding of receptor with the target analyte. Label-free sensing devices can be classified into optical, piezoelectric, and electrochemical devices on the basis of their transduction mechanism [7-9].

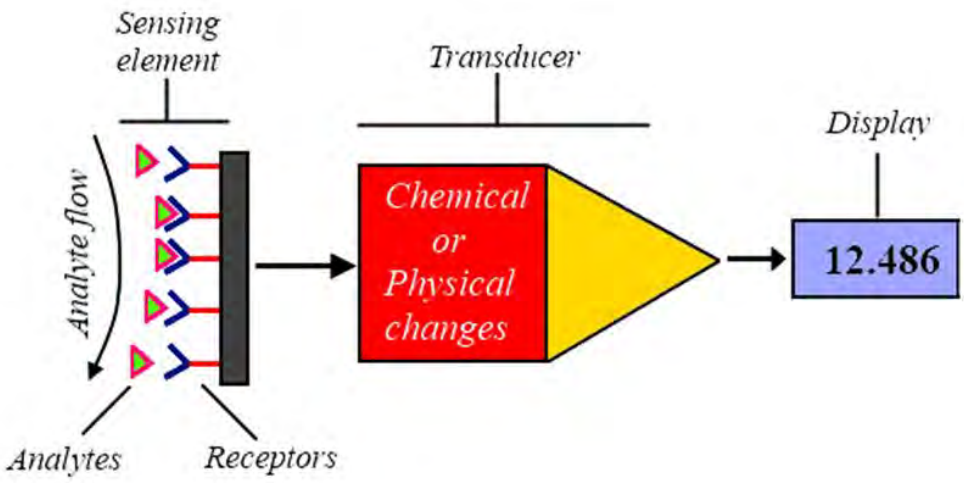

Figure 1.1. Schematic showing a typical Label-free sensor and its three components.

Optical sensing methods are one of the most powerful analytical tool of all the sensing techniques for detection and analysis of analytes of chemical and biological origin. Therefore, optical sensing devices are widely employed for analysis and quality assurance in a vast number of fields especially in biotechnology research, pharmaceuticals, biomedical detection including in-vivo monitoring of vital body conditions, environmental monitoring, and so on [7]. Optical sensing devices offer numerous advantages over devices based on other transduction systems as

they are immune to electromagnetic fields, can provide multiple detection on single chip, are useful in both label based and label-free detection, and are capable of being used for remote sensing. Surface plasmon resonance (SPR), surface enhanced Raman spectroscopy, optical waveguide spectroscopy, photonic crystals and optical fibres, and reflectometric interference spectroscopy (RIfS) are the most common optical detection techniques used for sensing purposes [10-13]. In this regard, SPR has been the most popular optical sensing technique for almost all the application fields (i.e. biomedical, environmental, industrial and others), however, it suffers from some inherent problems such as expensive sample substrate requiring noble metal coatings (mostly gold), large sample volumes, bulkiness of the system, inability to integrate with other detection techniques and so on [14-16].

In the recent times, sensors research has focused efforts on developing portable, miniature, point-of-care like label-free sensing devices for on-site sample analysis and self-diagnosis applications. This has resulted in an intense research activity on new optically active materials and their integration with simple, yet highly sensitive optical detection techniques. Integration of new porous substrates (i.e. porous silicon, nanoporous anodic alumina, and titania nanotube arrays) with reflectometric interference spectroscopy (RIfS) is a clear example of this trend [11-12]. In this combination, porous substrates provide high surface area for increased receptor density (i.e. higher number of receptor-analyte binding events) and are optically active, whereas RIfS provides a simple and highly sensitive sensing method. RIfS is a simple and sensitive technique based on interference of white light from top and bottom layer of a thin film giving rise to constructive interference of light at certain wavelengths which fulfil the mathematical requirements. The detection of analyte molecules is based on changes in effective refractive index of the film. Furthermore, it also allows for real-time monitoring of the receptor-analyte binding event to provide exclusive details about the mechanism and kinetics of the process [17].

The prime focus of this PhD thesis has been on combining a nanostructured substrate, nanoporous anodic alumina (NAA), with RIfS for development of a low-cost, simple, portable, and point-of-care type sensing system for environmental and biomedical applications. NAA's structural features (i.e. controlled pore size, shape, and geometry) and optical activity make it a highly versatile substrate for such applications. This PhD thesis focuses on three aspects for developing in a NAA-based RIfS sensing device; a) fabrication, optimization, and structural engineering the NAA pore geometry for enhanced optical activity, b) modification of the pore surface chemistry (i.e. silanes and drug loading) for providing selectivity and specificity to the detection process, and c) real-time monitoring of the receptor-analyte binding even inside the pores of optimized NAA sensing substrate (i.e. in terms of structure and surface chemistry) using RIfS detection method. The following sections will provide a through literature review about the efforts on developing NAA and its structural engineering, surface chemistry modification of NAA, and RIfS based sensing systems in combination with non-porous and porous sensing substrates.

1.2. Nanoporous Anodic Alumina (NAA)

1.2.1. History of NAA

This thesis is focused on self-ordered nanostructured materials, which boast of periodically arranged nanopores due to their extraordinary properties and interesting opportunities regarding their application in sensing. A dense array of hexagonally organized nanopores can be easily obtained by electrochemical anodization process on valve metals [18]. So far, self-organized nanopore structure formation using electrochemical anodization process have been reported for aluminium (Al), titanium (Ti), and a few others [18-21]. Due to its widespread commercial and scientific applications (i.e. corrosion protection, drug delivery, sensing, etc.) nanoporous anodic

alumina (NAA) is one of the most significant and popular nanoporous material with hexagonally organized pores [11, 17, 22].

Electrochemical anodization has been around for over a century now and is well known and vastly studied technique. In late 19th century and early 20th century it was mainly employed for colouring of Al for infrastructure and artistic purposes, and protection of metal from corrosion. Electrochemical anodization of Al is still heavily utilized for surface finishing, automobile engineering, machinery and corrosion protection. The first scientific patent for growing alumina through electrochemical anodization on Al for protecting aluminium and its alloys from corrosion was awarded in 1923 to Bengough and Stuart [23-24]. A new decorative process was discovered by Carboni (1936) to provide Al with decorative colour. The process consisted of two steps, first; anodization of Al in sulphuric acid electrolyte and two; followed by the application of an alternating current in a metal salt solution [25]. Therefore, a huge number of scientific research groups have studied anodization of aluminium in a large array of acidic electrolyte including sulphuric acid, phosphoric acid, citric acid, oxalic acid and many others using both A.C. and D.C. power supply [11-13, 26].

The pore formation mechanism in NAA is not yet completely understood but considerable efforts have been made in this direction since 1940. These efforts take into account all the possible environmental and structural aspects including defects on surface of Al, applied current density or potential, temperature, stress and so on [27-29]. The theory proposed by Keller et al. in 1953 is the most accepted theoretical explanation about mechanism for nanopores formation in NAA. This model suggests that the anodization process begins by formation of a homogeneous barrier type oxide film formation initially, which subsequently dissolves at site of defect due to higher current density (i.e. Joule's heating effect). This dissolution of the oxide in the barrier film at these spots is followed by the current, which repairs the damage to the oxide layer [30]. This

theory also suggests that hexagonal organization of pores is due to the natural existing tendency of spherical distribution of potential and current around the pore (defect). In general it cites that the hexagonal arrangement of pores in NAA is derived from pores due to stress between the adjacent nanopores, which feature a hemispherical cap at their tip. Note that the closed-packing of hexagonal arrangement of pores in NAA is a result of steric factors.

Due to its unique physical, mechanical and chemical properties NAA has been vastly explored for preparation of other nanostructured materials by a range of methods (including simple evaporation deposition, electrochemical deposition, electroless deposition, thermal decomposition or physical vapour deposition). Now-a-days NAA is one of the most prominently and popular template material for synthesis of 1D and 2D nanostructures (i.e. nanowires, nanorods, nanotubes, and their arrays) [31].

1.2.2. Fabrication of NAA

NAA is produced by self-ordering electrochemical anodization of aluminium in aqueous acid electrolytes (e.g. oxalic, sulphuric, phosphoric, etc.). This electrochemical anodization process has been used for over a century for a broad range of applications, including surface coating, automobile engineering, and corrosion protection and so on [32]. However, it was only after the widespread usage of electron microscopy in 1950s that revealed the nanoporous structure of the alumina layer fabricated by this electrochemical anodization process. The discovery of nanopores in the alumina film generated a huge interest in this material and as a result a large number of efforts were put in to study its physical and chemical properties [30, 33-35]. In particular, many studies aimed to fabricate anodic alumina under different electrolytes, temperatures, during the latter half of the 20th century but the most important milestone in the fabrication process of NAA was reported by Masuda and Fukuda in 1995, who introduced the two-step anodization

process and two years later in 1997, they used nanoimprint technology to synthesize mono-domain nanoporous anodic alumina structure for the first time [18, 36-37]. In the two-step electrochemical anodization approach, the nanoporous oxide layer grown during the first step of anodization is chemically removed in a selective manner to pattern the surface of the aluminium substrate with dimple like pits. During the second anodization step these patterns (dimple like pits) act as nucleation and propagation site for self-organised growth of cylindrical nanopores from top to bottom. This two-step anodization process provides a simple, low-cost, and commercially viable method to produce NAA with highly ordered nanopores whereas competing techniques (e.g. lithography) are either too expensive or complicated. The porous structure of NAA displays self-organized arrays of hexagonally arranged cells with a cylindrical nanopores at its center, grown perpendicular to the underlying Al substrate surface from top to bottom (**Figures 1.2a and b**). A schematic of the electrochemical setup used to produce NAA is presented in **Figure 1.2c**. The setup consists of an Al foil packed in a specially designed holder (**Figure 2.1, Chapter 2**) connected to the positive terminal of the power supply (Anode) whereas a platinum wire acts as cathode to complete the circuit (**Figure 1.2d**). The anodization of aluminium is generally carried out in aqueous acid electrolytes solutions. On application of a specific voltage between the two electrodes (i.e. anode and cathode), pores start to nucleate and grow perpendicularly to Al substrate surface. In the case of nanoimprint based mono-domain NAA pore structure, a silicon carbide stamp is first lithographically fabricated with desired shape (i.e. semi-spheres or pyramids) and dimensions and the stamp structure is imprinted onto electropolished Al chips [32, 36-38]. These pre-patterned Al chips are then anodized under specific anodization voltage that satisfies the interpore distance conditions.

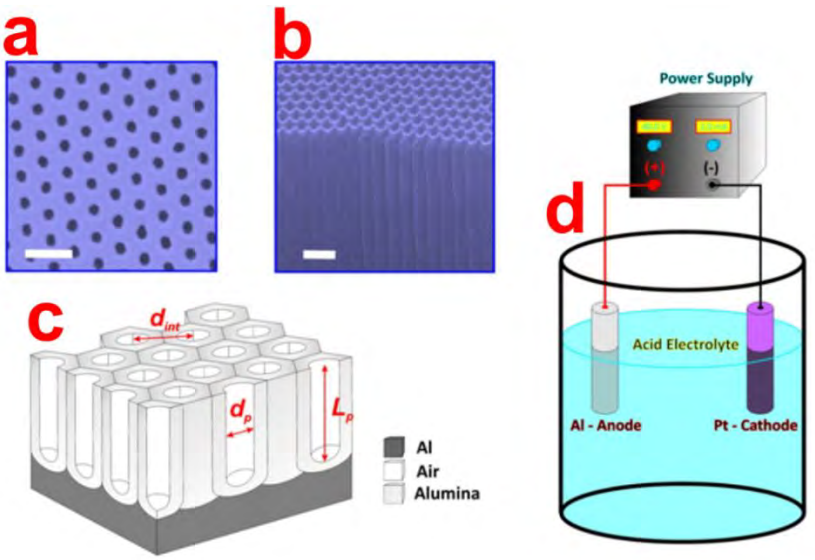

Figure 1.2. Scanning electron microscopy (SEM) images of NAA with (a) Top view (scales bar = 400 nm). (b) Cross-sectional view (scales bar = 250 nm). (c) An illustrative schematic describing the geometric features of NAA (i.e. pore diameter, pore length and interpore distance). (d) Schematic illustration of the basic electrochemical anodization setup used to produce NAA (Source [13]).

An SEM images of perfectly ordered NAA structure obtained by stamp based nanoimprinting is presented are **Figure 1.3.**

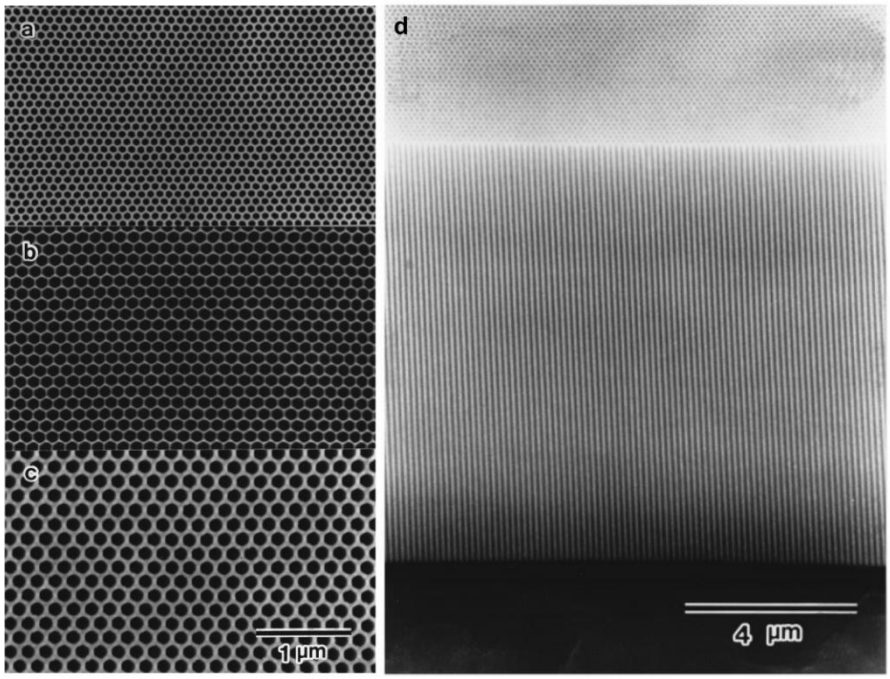

Figure 1.3. SEM images of cell configuration of perfectly ordered NAA fabricated using nanoimprinting method with different interpore distance (a) 100 nm. (b) 150 nm. (c) 200 nm. (d) Cross-sectional view of NAA prepared by nanoimprinting showing perfect organization of pores (i.e. negative of the stamp) running straight from top to bottom (Source [37]).

The mechanism of pore growth is based on steady state regime of two competing processes; first, formation of aluminium oxide (Al_2O_3) and second, dissolution of this oxide layer at specific pore nucleation sites [38]. First, a barrier type aluminium oxide grows at the aluminium-alumina interface because of the counter-migration of ionic charge carriers (i.e. Al^{3+} and O^{2-}). Second, Al_2O_3 is dissolved at the alumina-electrolyte interface due to uneven distribution of electric field on the oxide layer resulting in localized heating and dissolution. This electrochemical process can be described by the following redox equations:

i) Formation of alumina (aluminium-alumina interface – anode)

$$2Al(s) + 3H_2O(l) \leftrightarrow Al_2O_3(s) + 6H^+(aq) + 6e^- \quad (1.1)$$

ii) Dissolution of alumina (alumina-electrolyte interface – anode)

$$Al_2O_3(s) + 6H^+(aq) \rightarrow 2Al^{3+}(aq) + 3H_2O(l) \quad (1.2)$$

iii) Diffusion of aluminium cations (within oxide barrier layer – anode)

$$2Al(s) \rightarrow 2Al^{3+}(aq) + 6e^- \quad (1.3)$$

iv) Hydrogen evolution (electrolyte-cathode interface – cathode)

$$6H^+(aq) + 6e^- \rightarrow 3H_2(g) \quad (1.4)$$

Note that, other side reactions such as evolution of oxygen at the anode also take place during the anodization process. Therefore, the anodic current efficiency during anodization of Al is always lower than 100 % [38].

The structural parameters of NAA pores (i.e. pore diameter; d_p, pore length; L_p, interpore distance; d_{int}, and oxide barrier layer thickness; S_{obl}) are described in **Figure 1.2c**. These structural parameters of NAA can be precisely tuned by the anodization conditions with pore diameter in the range 10–400 nm, pore length from several nm to hundreds of μm, interpore

distance in the range 50–600 nm, and barrier layer thickness between 30–250 nm for S_{obl}. In addition, the pore density and porosity can be controlled between 109–1011/cm^2 and 5–50%, respectively [11-13, 26]. This ability to specifically tune the pore geometry of NAA depending on the application is a result of several decades of intensive research in this field studying the influence of the anodization parameters on NAA pore geometry [38]. Mainly, anodization voltage or current density, and electrolyte type, concentration and temperature have been the most critical parameters studied to control the self-organizing process and the geometry of the NAA. Generally, aqueous solutions of sulphuric acid (H_2SO_4), oxalic acid ($H_2C_2O_4$), and phosphoric acid (H_3PO_4) used to prepare NAA with self-organized pores at 25, 40, and 195 V, respectively [39-44]. This conventional anodization process is called ‘‘mild’’ anodization (MA) as the process occurs under low or mild electric field conditions. The growth mechanism of NAA under MA regime is rate-limited by the ionic transport of ionic species (i.e. Al^{3+} and O^2) across the aluminium-alumina interface [26, 41]. Besides the three aforementioned acid electrolytes, several other acidic electrolytes have also been reported to generate NAA with self-organized pores including aqueous solutions of citric, maleic, malonic, tartaric and sulfamic acids [45-50]. However, the organization of pores is poor for these acidic electrolytes. Although MA process provides highly organized porous NAA structure, it is industrially inviable due to inherently slow pore growth rate (i.e. 2–7 μm/h). This problem was addressed by Gösele’s group in 2006 by introducing a new high electric field based anodization process ‘‘hard’’ anodization (HA). The pore growth rate under HA conditions could range between 50–100 μm/h, which is tens of times higher than MA conditions [32]. HA process also extended the range of interpore distance into regimes not attainable by MA conditions. The growth mechanism under HA process is controlled by transport of oxygen-containing anionic species (i.e. HO^- and O^{2-}) from the bulk electrolyte to the reaction interface (i.e. alumina-aluminium interface) [32]. The difference in the mechanism can be clearly observed in the MA and HA anodization profiles (**Figure 1.4a**).

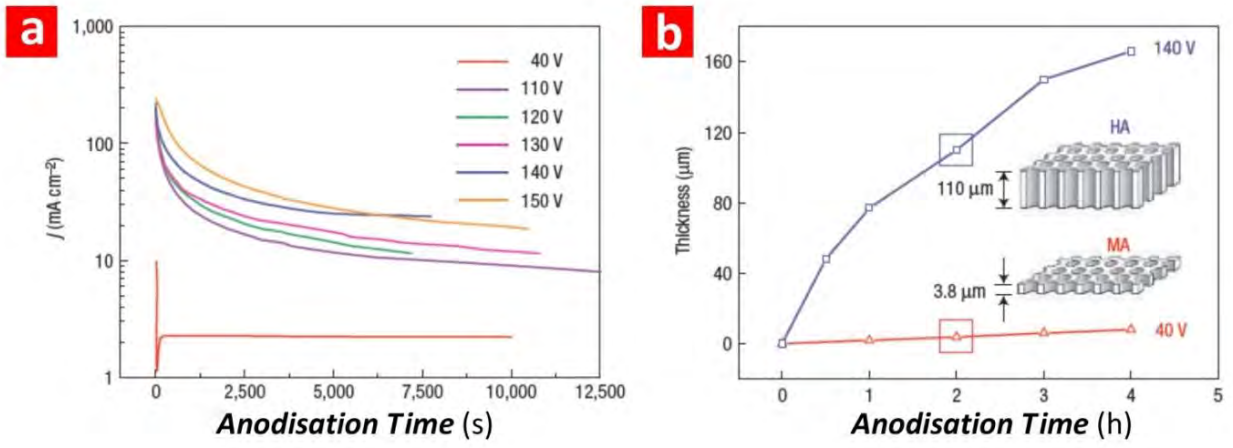

Figure 1.4. (a) Comparison of current density profiles under MA and HA conditions for NAA produced in oxalic acid. (b) Growth rate under MA and HA conditions for NAA produced in oxalic acid (Source [32]).

Therefore, the pore growth rate is almost constant under MA conditions, while it becomes exponentially decreasing under HA (i.e. the longer the pore length the slower the transport of oxygen-containing anionic species from the bulk electrolyte to the reaction interface) (**Figure 1.4b**). Notice that, the pore geometries of NAA can be tuned specifically in a broad range by selectively choosing the anodization conditions such as anodization regime (i.e. HA or MA) and electrolyte type and concentrations. The pore geometry of NAA can further be engineered by post processing steps as wet chemical etching to provide desired pore dimensions and shapes. A number of complex pore geometries in NAA have been successfully fabricated by periodic change of anodization conditions (voltage or current) along time with or without replacement of the acid electrolyte [51-57]. A wide variety of pore morphologies including funnel-type, branched pores, periodically-shaped pore structures, and hierarchical and multi-structured pores have been produced so far [52-61]. **Table 1** summarises the most representative MA and HA anodization conditions as well as the geometric features of the resulting NAA.

Table 1. Summary of the most representative fabrication conditions for NAA produced in MA and HA regimes and geometric characteristics of the resulting nanostructures.

Acid Electrolyte	Anodisation Regime	V (V)	T (^{0}C)	d_p (nm)	d_{int} (nm)	Growth Rate (μm h^{-1})	References
H_2SO_4 0.3 M	MA	25	5-8	25	63	7.5	[44]
H_2SO_4 0.3 M	HA	40	0-1	30	78	85	[42]
$H_2C_2O_4$ 0.3 M	MA	40	5-8	30	100	3.5	[18]
$H_2C_2O_4$ 0.3 M	HA	140	0-1	50	280	50	[51]
H_3PO_4 0.1 M	MA	195	0-1	160	500	2	[43]

1.2.3. Structural Engineering and Optical Optimization of NAA

The pore geometry of NAA can be specifically designed and engineered by applying a range of different electrochemical anodization approaches. A broad library of NAA pore geometries including modulated, hierarchical, serrated, three-dimensional, funnel-like, and multilayered type have been engineered and fabricated using innovative anodization techniques [51-61]. **Figure 1.5** shows SEM images and schematics of some of the most representative NAA structures generated by different electrochemical approaches. Pore geometry variations are mostly produced by switching between "Hard" and "Mild" anodization regimes repeatedly resulting in pores with different pore diameters (i.e. porosity, MA results in 10% porosity while HA only produces NAA with 3% porosity). In this regard, a periodic pore diameter modulation in NAA along the pore length was first reported by Lee *et al.* (**Figure 1.5a**) [32, 51]. In this report, perfectly ordered NAA was fabricated first using a master stamp imprinting method (*vide infra*) on an

electropolished Al chip using phosphoric acid electrolyte (H_3PO_4: 0.4 M, 110 V and 10 °C). Phosphoric acid electrolyte was replaced with 0.015 M oxalic acid ($H_2C_2O_4$) after 15 min of anodization and anodization was continued at 137 V at 0.5 °C for 2 min. This whole process was repeated several times to obtain NAA with uniform periodic pore diameter modulations with constant interpore distance. It is worth noticing that the anodization voltages for both the acidic electrolytes were selected carefully to yield the same interpore distance in MA and HA conditions and prevent pore branching. The pore diameter and the interpore distance were found to be a function of anodization voltage (corresponding to specific electrolyte), while the pore length was controlled by the anodization time. This report was the starting point, which inspired other researchers across the globe to investigate on different electrochemical approaches to generate pore diameter modulations in NAA. A similar approach was adopted by Pitzschel *et al.* fabricated pore diameter modulations in NAA, where the period of nanoimprint master stamp was 235nm and the corresponding NAA substrate was used as a template to prepare magnetic nanotubes by depositing Fe_3O_4 using ferrocene and ozone as precursors through atomic layer deposition (ALD) [62]. A new, cyclic anodization approach was introduced by Losic *et al.* in 2009, where anodization current is periodically oscillated to obtain pore modulations along the length **(Figure 1.5b)** [52].

A hierarchical type pore morphology with multiple small pores within single concave cavity of the pre-patterned Al chip was generated by Santos *et al*. changing one or more than one anodization parameter during second anodization step than first one [63]. Zhu *et al.* generated a new type of pore geometry in NAA described as serrated pores because the pores display secondary pores growing at an angle to the primary pore [64]. This angular orientation of provide the pore a serrated type structure. They proposed a new growth model for serrated type of pores in NAA emphasizing on the close relationship between pore generation and oxygen evolution.

This was confirmed by Li *et al.* on the basis of the results obtained from their experiments and simulations regarded the initiation and formation of serrated-like NAA pores to the evolution of oxygen gas bubbles during the anodization [65]. All the previous NAA pore modulation were along the length of pores (i.e. 2D), a new 3D type NAA pore modulation was generated by Losic *et al.*, where cyclic anodization was combined with wet chemical etching in phosphoric acid [58]. Similar 3D type NAA pore modulations were generated by Santos *et al.* by combining discontinuous anodization and wet chemical etching steps with phosphoric acid [66]. Very recently, Martin *et al.* fabricated 3D ordered NAA structure using pulsed anodization process and wet chemical etching in phosphoric acid. The resulting multilayered 3D NAA structure was utilized as a template to fabricate polymer imprints with specific optical properties (i.e. polymer photonic crystals) [67]. Another pore geometry of NAA, known as funnel like NAA, has been reported in several studies [53-55, 61]. This structure is called funnel like NAA because, similar to a funnel, pore diameter on the top layer of the sample is larger than the bottom layer (i.e. decreasing pore diameter from top to bottom). Funnel like NAA pores are prepared by combining multiple anodization and pore widening steps **(Figure 1.5c)** [53]. Similar to the NAA with modulated pores, the pore length is a function of anodization time whereas the pore diameter is established by the pore widening time in phosphoric acid. Low aspect ratio funnel-like NAA were fabricated by Nagaura *et al.* and structure was manipulated by varying the number of anodization and pore widening cycles [54]. These low-aspect ratio funnel like NAA structures were utilized as template to fabricate nickel films with nanoconical surface morphology [55]. Polymer photo-imprinting process was also used for fabricating and replicating similar low-aspect ratio funnel like NAA structure into polymer films [57]. These polymer replicas of funnel like NAA pores were investigated for their antireflection properties under transmission mode. On the other hand, Santos *et al.* prepared high aspect ratio funnel like NAA structure using similar anodization and wet chemical etching process. The length of each layer was precisely controlled by total charge passed through the

system during anodization of each segment. They were able to fabricate funnel like NAA structure with multiple layers (i.e. two, three, and four layers of decreasing pore diameter from top to bottom) [53].

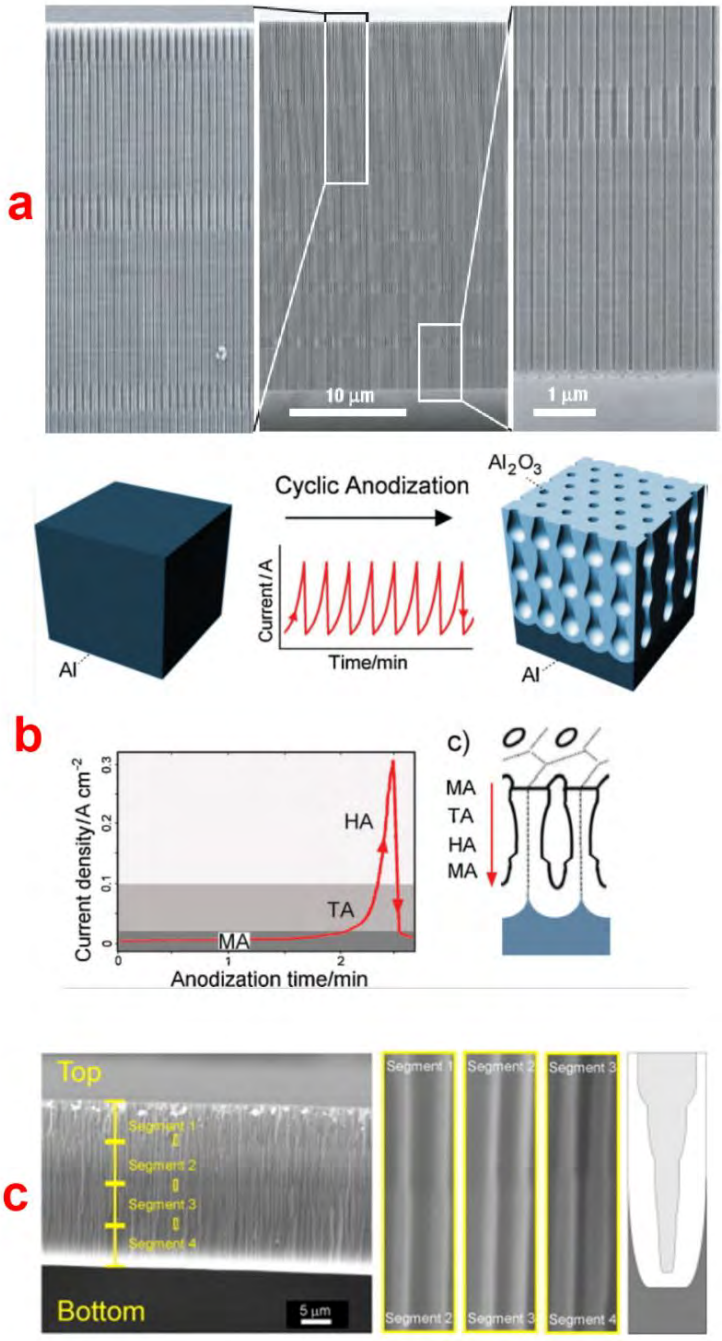

Figure 1.5. (a) Cross-sectional SEM images of pore diameter modulations in NAA produced by switching the anodization between MA and HA regimes. (b) Schematic illustration of cyclic anodization process. (c) Cross-sectional SEM images of high aspect ratio funnel-like NAA (sources [32], [52], and [53]).

Li *et al.* reported an innovative method to tailor the pore geometry of funnel like NAA pore structures to obtain linear cones, whorl-embedded cones, funnels, pencils, parabolas and trumpets-like nanopore structures by electrochemical approach [56]. These fascinating funnel like NAA pores were fabricated by specifically controlling the anodization parameters like anodization time, etching time and cycle times. Recently, Santos *et al*. reported on fabrication of inverted type nano-funnel like NAA porous substrates, which has increasing pore diameter along the pore length from top to bottom [61]. The inverted type nano-funnels were fabricated by taking advantage of the fact that chemical dissolution rate of NAA lowers as a function on annealing temperature (i.e. higher the anneal temperature, lower is the wet chemical etching rate in phosphoric acid). They successfully fabricated inverted NAA nano-funnel like porous structures with two and three layer by repeated annealing and anodization steps. For example, the two layered inverted nano-funnel like structure was prepared by combining two anodization steps with one annealing and wet chemical etching step. For this, first anodized NAA layer (i.e. after electropolishing and removal of sacrificial first anodization layer) was annealed at temperature in excess of 300ºC and subjected to another anodization step. Next, this bi-layered NAA structure was subjected to wet chemical etching under phosphoric acid for a specific time. Interestingly, the fabrication process of inverted NAA nano-funnels was recorded in real-time using reflective interference spectroscopy method.

The ability to exclusively engineer the nanoporous structure of NAA has been implemented for generation of optically active structures such as distributed Bragg reflectors (DBRs), microcavities, rugate filters (RFs), omnidirectional mirrors and waveguides [13]. The fabrication of such optical nanostructures is possible due to the ability of electrochemical anodization process to produce variations in porosity (i.e. refractive index) of the NAA structure depending upon the type and regime of anodization. Periodic variation in porosity of NAA layers in a multilayered

NAA structures can be modulated to generate optical nanostructures such as DBRs, optical microcavities, rugate filters and other optical and photonic structures. Multilayered NAA structures with periodic variations in porosity can be prepared by periodically alternating the voltage or current during the anodization process. Anodization profiles such as stepwise, sinusoidal, pseudo-sinusoidal, saw-like and so on have been applied to engineer the porosity (*i.e.*, refractive index) of NAA layers along the thickness [13]. The ability to specifically design and engineer the porosity of NAA according to anodization profile allows for specifically tuning light-matter interaction in NAA, which is critical to develop platforms with optimized properties for chemical and biosensing applications. Multilayered NAA structure was first fabricated by Lee *et al.* using pulse anodization process, in which potential or current during aodization process is pulsed between low and high values (i.e. MA and HA regime) [51]. The prepared multilayered NAA structure under potentiostatic pulsed anodization in sulfuric acid and oxalic acid displayed periodic neck-like constrictions along the length of the tubes whereas nanoporous structure with periodic variation in pore diameter was observed for oxalic acid electrolyte. This type of multilayered NAA structure was employed as a templet by Sulka *et al.* to fabricate modulated metal nanowires. Distributed Bragg reflector (DBR) optical structure was prepared in NAA using this anodization approach by the same group [68]. The NAA-DBR structure with periodically modulated porosity (i.e. low and high refractive index) were observed to effectively reflect light in two different ranges of wavelength, which was in good agreement with the mathematical calculated reflection spectrum.

NAA based DBR mirrors were fabricated by Zheng *et al.* using a pseudo-sinusoidal voltage profile in oxalic acid electrolyte [69]. The anodization temperature was varied in order to tune the transmission peak of the prepared NAA-DBRs in the desired spectral range. The authors could practically tune the transmission band in the whole visible spectral range by

adjusting the anodization temperature between 7 to 14 °C. Another approach was recently published by Rahman *et al.* to produce NAA-DBRs using an innovative cyclic anodization approach [70-71]. They tuned the stop band (i.e. transmission peak) of the prepared NAA-DBRs as a function of number of anodization cycles, anodization time, and pore widening time (i.e. modulating the refractive index contrast between the layers). Recently, Macias *et al.* fabricated NAA rugate filters (NAA-RFs) using a galvanostatic anodization process with sinusoidal profile. The reflection and transmission band of the resulting NAA-RFs were observed to be directly dependent on the period of the sinusoidal waveform and pore widening time [72].

Fabrication of nanoporous anodic alumina rugate filters (NAA-RFs) by anodizing Al under pseudo-sinusoidal potentiostatic conditions in oxalic acid electrolyte is presented **Chapter 4**, **Chapter 5**, and **Chapter 6** of this thesis.

1.2.4. Surface Chemistry and Functionalization of NAA

The inherent surface chemistry of NAA is depicted to be embedded with electrolytic impurities (e.g. sulfate, oxalate, and phosphate) distributed in an onion-like layered manner. There exists a gradient of electrolytic impurities in NAA from the center of pore (i.e. outer layer) to away from the center of pore (i.e. inner layers) in a cell. It was experimentally proven that layer close to the center of the pore has higher electrolytic impurities and the inner layers mainly composed of pure Al_2O_3 [39]. Although the onion like surface chemistry profile (i.e. layered gradient of acid impurities) is generally accepted but there is a large variation in the number of layers reported by different studies. Some reports argue that there are two onion-like layers in NAA while others claim up to four such layers exist. In this regard, Thompson *et al.* claim, there exist only two layer of onion-like structure with the more contaminated outer layer and inner layer is dense pure alumina [60]. In another study, Yamamoto *et al.* argue that NAA structure has three onion-like

surface chemistry layers. The number of layers was indicated by recording photoluminescence spectrum of NAA after specific chemical etching steps [73]. A recent study by, Santos *et al.* suggest that there are four onion-like layers exist in the chemical structure of NAA with decreasing electrolytic impurities from the outer to the inner layer [61]. The existence of four layers was indicated by real-time monitoring of reflection signal during wet chemical etching. A schematic illustration of onion-like chemical structure of NAA is provided in **Figure 1.6**. The presence of acid electrolyte impurities in alumina as onion-like layers is important as it provides NAA with specific optical properties (e.g. PL) that depend fundamentally on the acid electrolyte used during the anodization process.

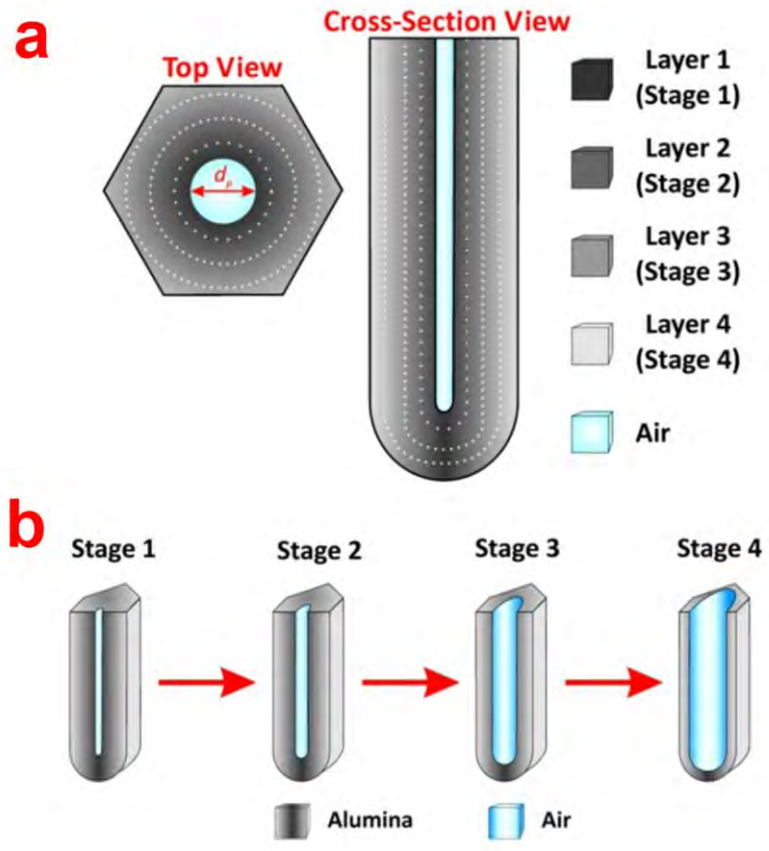

Figure 1.6. (a) Schematic of top and cross-sectional view showing the distribution of impurities in a NAA pore cell. (b) Four different stages of dissolution of NAA alumina layer under acidic conditions (5 *v* % H_3PO_4 at 35 °C) (Source [61]).

The presence of acidic impurities in the outer layer of NAA makes it possible to easily generate reactive hydroxyl groups on its pore surface. Surface hydroxyl groups can be easily modified further using a number of well-established chemical functionalization techniques. The main reason for modifying NAA surface is either to protect it from acid attack or imparting selective surface chemistry for a specific application. The surface functionalization techniques are majorly divided into two categories as physical/gas-phase techniques which include thermal vapor deposition, chemical vapor deposition (CVD), plasma polymerization and atomic layer deposition (ALD) and chemical methods including self-assembly processes of silanes, organic and phosphonic acids, layer-by-layer deposition, polymer grafting, sol-gel processing, electrochemical and electroless deposition (**Figure 1.7**) [12, 59]. The functionalized NAA can be subsequently modified target molecule for specific applications (i.e. sensing, chromatography and others) or utilized for fabrication a wide variety of functional nanomaterials (e.g., nanorods, nanoparticles, nanotubes). A combination of aforementioned functionalization techniques can also be employed for complex and innovative surface chemistries and applications. This section will briefly describe the surface functionalization utilized for this thesis and summarize the previous efforts towards innovative and functional surface modification of NAA substrates.

Two surface modification techniques primarily utilized in this thesis are self-assembled monolayer formation and sputter coating. In this, self-assembly provides selectivity to the surface of NAA for binding to target analyte molecules whereas sputter coating with metal (Gold in this thesis) is used for enhancing the reflection intensity of the NAA based sensing substrates.

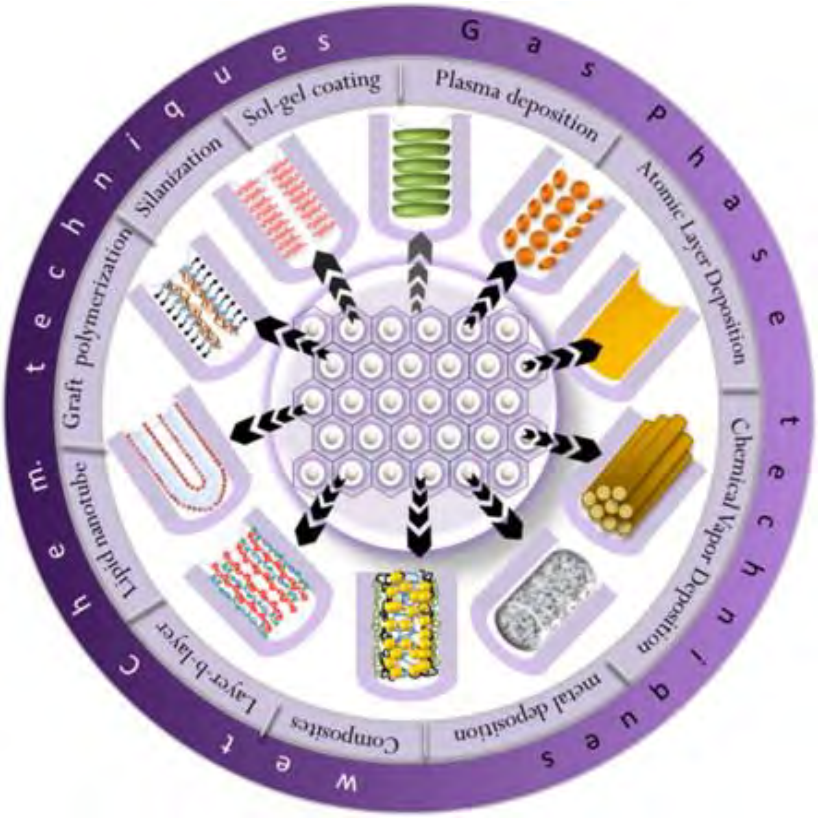

Figure 1.7. A summary of typical wet chemical and gas phase techniques used to modify the surface of NAA (Source [59]).

1.2.4.1. Self-Assembled Monolayers (SAMs). Self-assembled monolayers (SAMs) are formed by spontaneous attachment and arrangement of molecules from liquid phase to solid substrate. SAMs of a variety of molecules including organic acids, organosilanes, phosphonates and others have been successfully prepared on NAA surface for specific applications. The major advantage of SAMs based NAA functionalization are the ease of functionalization process and availability of SAM precursors with a huge variety of terminal groups such as amine, carboxyl, epoxy and so on [59]. Furthermore, SAM precursors such as organosilanes can be exclusively designed and tailor-made suiting the need of a particular application. SAMs formation on NAA surface was initially presented for assembly of alkanethiols on gold-coated NAA substrates [74]. Although a large number of SAMs precursors are available (as mentioned above), organosilanes are used in this thesis due to their versatility and stability during sensing process. A schematic of

organosilanes attachment to hydroxylated NAA surface is presented in **Figure 1.8.** Organosilane SAMs formed onto hydroxylated NAA surfaces have been employed to tune the surface wettability and adsorption properties of NAA [75]. A summary of the variety of organosilanes successfully attached to NAA surface and their applications have been listed in **Table 1.2**.

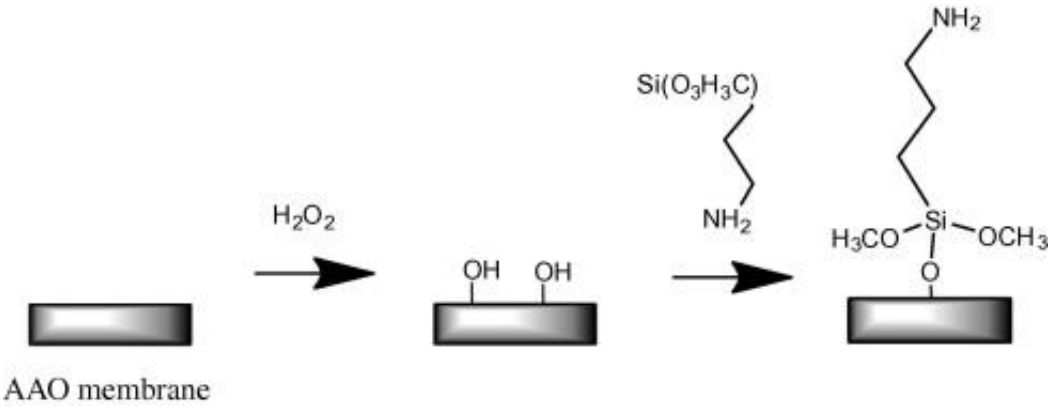

Figure 1.8. Schematic of silanization process used for modifying NAA (Source [75]).

NAA surface wettability has been previously selectively tuned to provide it different hydrophobicity using alkyl-trichloro-silanes or perfluoroalkyl-silanes [76-78]. Alkyl-trichlorosilanes with carbon chain length varying between 1 and 8 were successfully used to render the surface of NAA hydrophobic. The samples were completely hydrophobized in a way that the pores remain filled with air even after complete immersion into an aqueous medium (buffer in this case) [79]. On the other hand, NAA surface has been completely hydrophilized using silane with functional groups as PEG-silanes, amine-terminated silanes, epoxy-silanes and others. Besides tuning the surface wettability of NAA PEG-silane is proven to efficiently control biofouling under both *in vitro* and *in vivo* conditions, improve biocompatibility, and reduce the pore diameter of NAA for molecular separation [80-83].

Table 1.2. Summary of the variety of silanes used to functionalize NAA and their applications.

Types	Silane Name	Modification Method	Application(s)	Ref.(s)
Amino-silane	Aminopropyl-triethoxy silane	Solution based	Immobilization	[60]
PEG-silane	mPEG-silane	Solution based	Hydrophylization	[80-81]
Fluorinated-silane	perfluoroalkyl-silanes	Solution based	Transporting and separation	[78]
Mercapto-silane	Mercaptopropyl-triethoxy silane	CVD based	Sensing	[12]

Silanes are mainly used for immobilization of active biomolecules, polymers, nanoparticles, DNA, cells, quantum dots, and lipid bilayers onto the surface of NAA for sensing and biosensing applications [83-86]. Amine terminated silane, amino-propyltryethoxy silane (APTES) is the most commonly used silane for this purpose. APTES modified NAA has been demonstrated for grafting polymers as N-hydroxy-succinimidyl carbonate-polyethylene–glycol (NHS-PEG) and poly(γ-benzyl-l-glutamate) (PBLG). The former polymer modification was utilized for fusing vesicles to NAA pore wall while the later was used for tailoring the filtration and separation properties of NAA based [87-88]. Also, APTES-modified NAA have been grafted with poly-N-isopropylacrylamide (PNIPAM) through atom-transfer radical polymerization (ATRP) [89].

In a new paradigm, APTES modified NAA substrates have been used to assemble and fabricate metal nanoparticles or nanotubes by electroless deposition. For example, Pd nanotubes

inside APTES-modified NAA templates were synthesized by Wang *et al.* using electroless deposition techniques. The electroless deposition process involved sequential immersion of NAA in aqueous solution of $SnCl_2$ and HCl followed by a solution of $PdCl_2$ and HCl to generate Pd nanotubes [90]. Nanoparticles have been also immobilized inside NAA modified with APTES to make the structure conductive [91]. Similar approach was taken up by Lahav *et al.* to simultaneously immobilize Au and Pd nanoparticles, which were then transformed into bimetallic nanotubes of Au-Pd upon drying, due to solidification of nanoparticles and leading in formation of multiwalled metallic nanotubes [92].

Losic and co-workers devises an innovative approach to make layered surface chemistry on NAA by attaching multiple silanes in a single NAA substrate. The layered surface chemistry was achieved by a combination of anodization and silanization cycles [96-97]. They demonstrated modification of NAA surface with up to three layers of different silanes (pentafluorophenyl-dimethylpropylchloro-silane (PFPTES), APTES and N-triethoxysilylpropyl-(O-polyethyleneoxide) urethane (PEG-silane)), providing a spectrum of surface functionalities and wettabilities as shown in **Figure 1.9** [93-94]. This approach makes it possible to control the thickness of each functional silane layer by controlling the thickness of NAA grown during each anodization and silanization cycle.

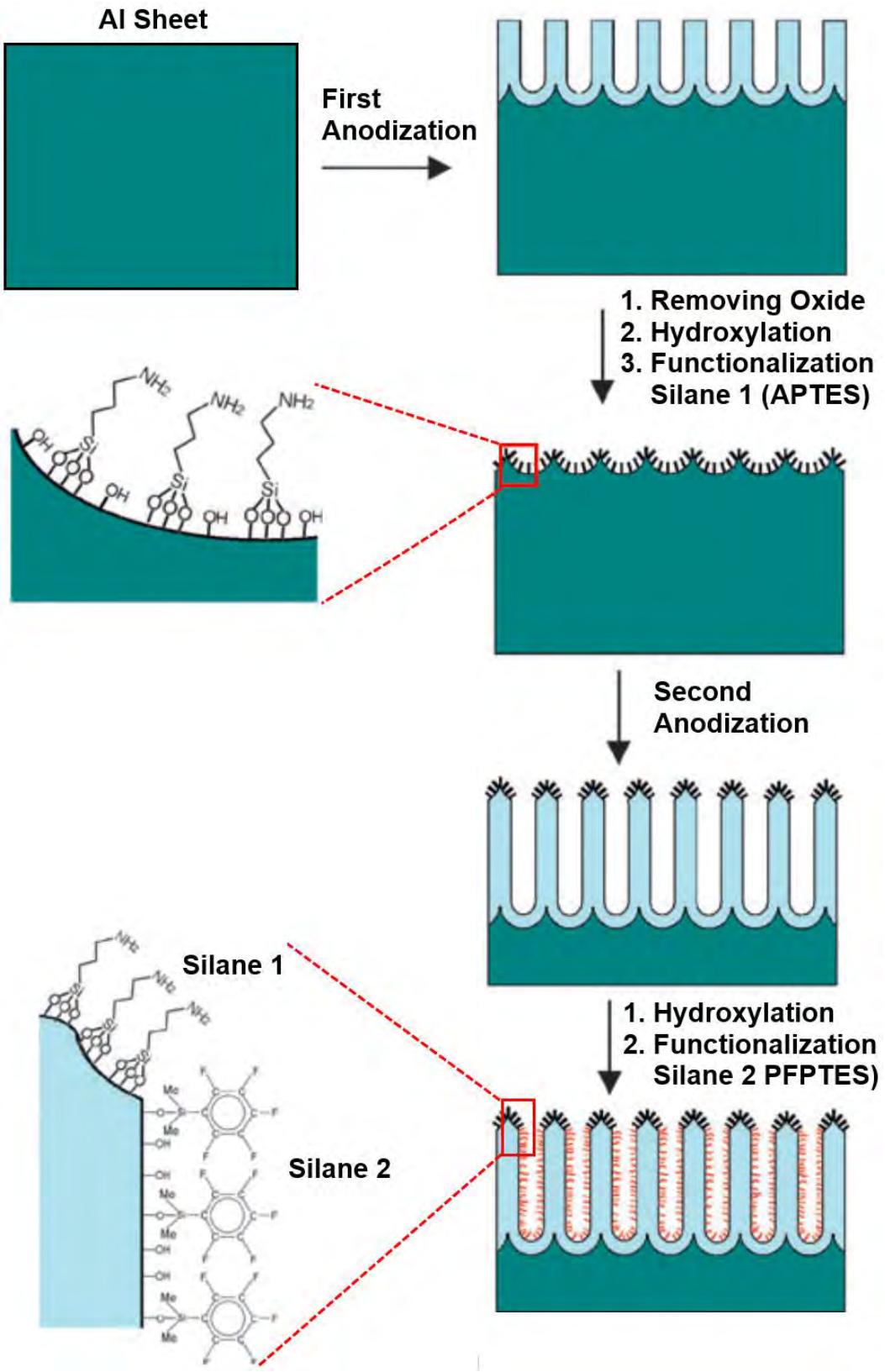

Figure 1.9. Schematic illustrating the process of obtaining layered silane chemistries inside NAA pores for imparting multi-functionalities to NAA surface (Source [94]).

1.2.4.2. Sputter Coating. Metal deposition on NAA substrate is generally used to fabricate hexagonally packed array of metallic nanocaps, which are highly attractive for surface enhanced Raman or localized surface plasmon resonance based sensing applications [12, 59]. In this regards, sputter coating provides a powerful and convenient tool for quick and controlled deposition of metal thin films. A broad variety of sputter coating techniques are available and have been used for deposition of thin films of various metals and properties. Few studies have reported the use of sputter coating method to exploit hexagonal arrangements of NAA pores for preparing active substrates for SERS by depositing noble metal thin films [95-98]. Direct-current magnetron sputtering was used by Qui *et al.* to deposit Ag layers on the top surface of NAA templates [95]. The resulting metal nanocap like structure was used for SERS application as a regular arrangement of noble metal nanostructures act as Raman hot spots **(Figure 1.10)**. Alloy based nanostructures have also been prepared using sputter coating on NAA surface. Fe-Pd permalloy nanostructure were prepared by Béron *et al.* using ion beam sputtering on top of an NAA template [96, 99].

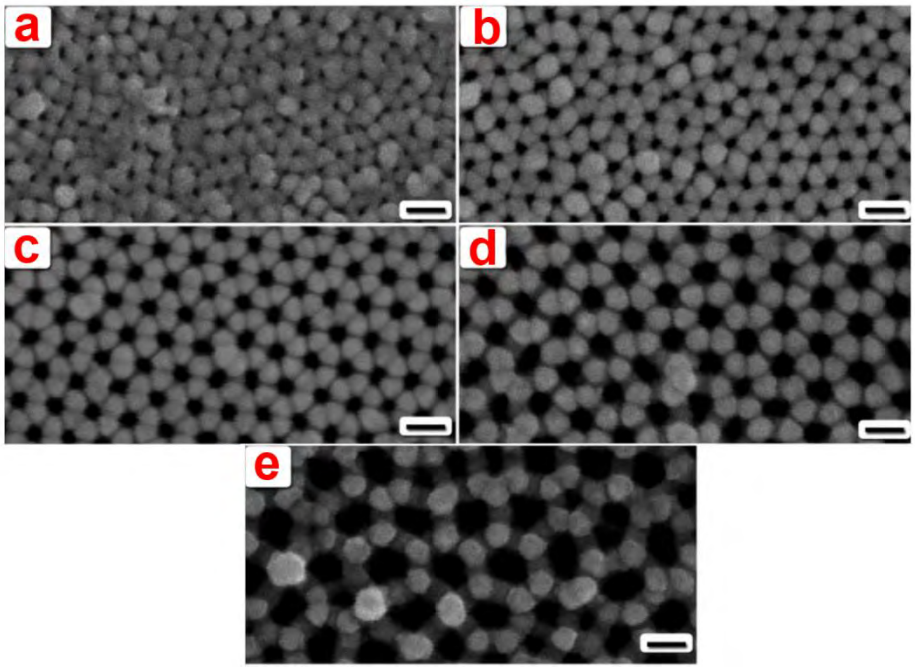

Figure 1.10. SEM images of DC-magnetron Ag sputter-coated NAA membranes fabricated at different voltages and sputtering time set to 10 min (scale bar = 100 nm): (a) 20 V. (b) 30 V. (c) 40 V. (d) 50 V. (e) 60 V (Source [95]).

1.2.5. Properties of NAA for optical sensing

This part of the thesis is devoted to the various properties of NAA which make this nanoporous material so attractive for optical sensing applications. NAA displays a unique set of physical and chemical properties that make it an excellent platform for developing sensing devices. In particular, the optical properties of NAA allow it to interact with light in a unique way to generate photoluminescence (PL) and display extraordinary transmittance, reflectivity, and absorbance. These unique optical interactions with light allow for fabrication of highly sensitive, selective chemical and biological sensors. In addition, the ability to integrate NAA into microchip and microfluidics based platforms is highly attractive for developing miniature and portable sensing devices [11-13, 59]. The pores of NAA can act as container and its high surface area allows for accommodation of large number of analyte-receptor binding events inside the pores. Along with these properties, the ability to tailor the pore structure and surface chemistry of NAA make it highly relevant for sensing applications. These modifications not only improve the properties of NAA but also can endow this material with multifunctional properties for development of advanced and much sophisticated sensing platforms. On the other hand, materials as porous silicon have also been intensively investigated as a suitable substrate for developing optical sensing devices due to its outstanding optical and electronic properties. However, porous silicon degrades under biological and environmental conditions and needs to be passivated through a laborious process in order to achieve stable optical signals. In contrast, NAA is chemically and mechanically as-produced and provides stable optical signals without further passivation.

1.2.5.1. NAA based Optical sensors. Previous sections of this chapter provide evidence of why NAA has become an attractive material to develop optical detection systems. In this context, a new generation of optical sensing devices based on NAA has recently emerged and their sensing

performance has successfully been explored for many analytical applications. It is worth noticing that the interaction of light with NAA is highly dependent on its structural and chemical properties. NAA displays extraordinary reflection, transmission, photoluminescence, and wave-guiding properties and can be tailored according to NAA structure and chemical nature [11-13, 100]. These optical properties can be used to design and develop a new generation of nanoporous substrate, for optical sensing and biosensing devices. NAA based optical sensing tools have been explored for a range of applications as environmental and clinical analysis, industrial and food control, and defence and homeland security. Detailed review about optical sensing applications of NAA are provided in references [11-13].

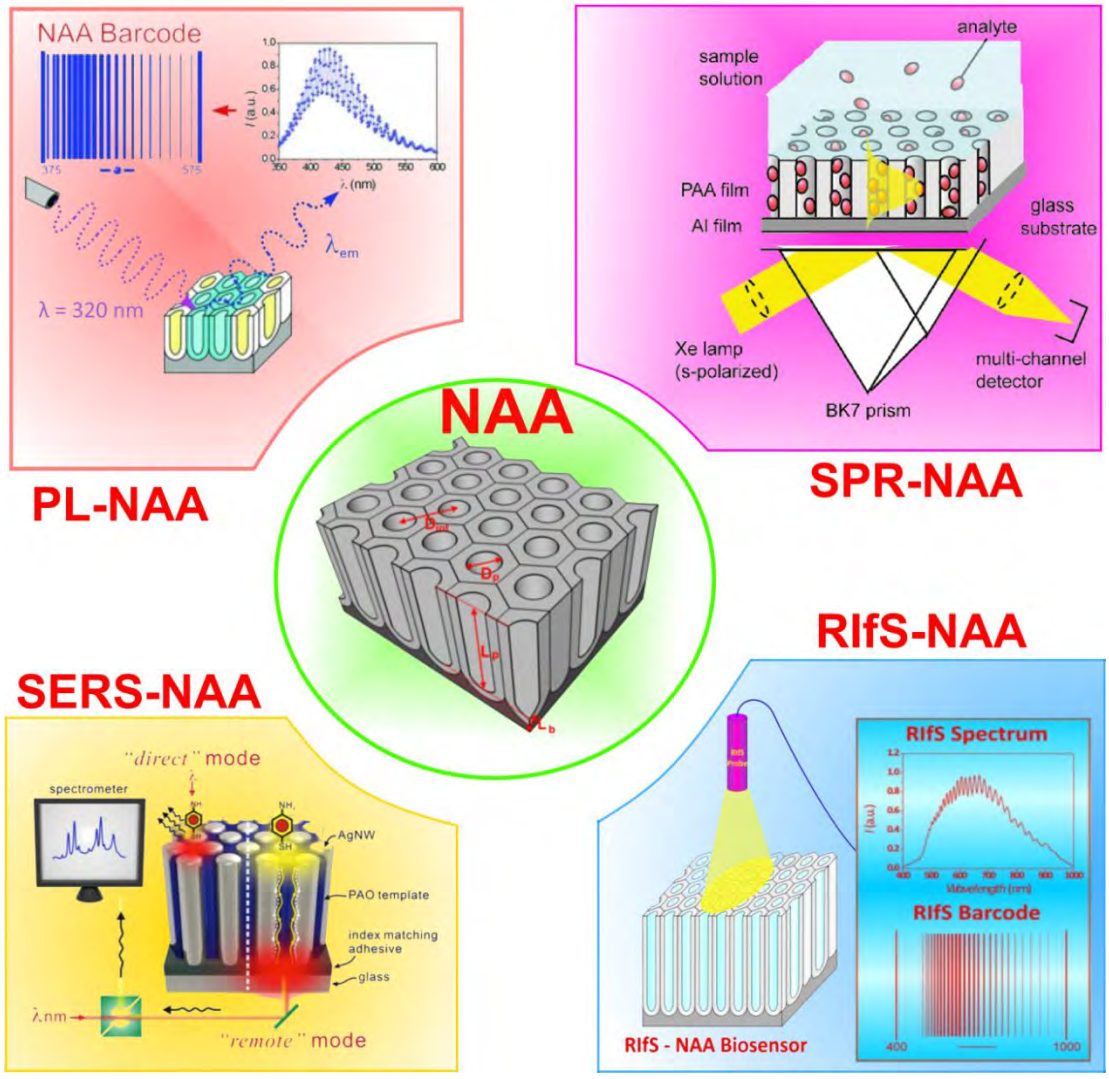

Figure1.11. A schematic showing all four optical sensing techniques coupled with NAA for developing highly sensitive optical sensors (Source [103]).

Efforts on developing NAA based optical sensing systems are mainly focused on integrating NAA with PL, SPR, SERS, and RIfS detection techniques (**Figure 1.11**). The most representative advances in development and applications of optical NAA biosensors are summarized in **Table 1.3**. Although PL, SPR, and SERS have been used for development of NAA based optical sensors, this thesis focuses on integration of NAA with RIfS for development of a new generation of highly sensitive and portable point-of-care sensors.

Table 1.3 Summary of optical sensing systems based on nanoporous anodic alumina, their detection principle, application and performance (Source [11])

Optical Technique	Analyte	Detection Limit/Concentration
PL	Morin	$5 \cdot 10^{-6}$ M
	Trypsin	40 µg·mL^{-1}
		0.1 mg·mL^{-1}
	DNA	100 mM
	Oxazine 170	$6.5 \cdot 10^{-3}$ M
	Glucose	0.1 M
SPR-LSPR	Avidin	10 µg·mL^{-1}
	Anti-5-Fluorouracil	100 mg·mL^{-1}
	$Ru[BPhen_3]^{2+}$	2 µM
	$Fe[Phen_3]^{2+}$	1 µM
	BSA	60 nM
	Invertase	10 nM
	Melittin	100 ng·mL^{-1}
SERS	p-aminothiophenol	0.5 M
	4-mercaptopyridine	$1 \cdot 10^{-6}$ M
	3-mercaptobenzoic	3 mM
RIfS	H_2S	0.5% v
	DNA	2 nmol·cm^{-2}
	Circul. Tumor Cells	1000 cells·mL^{-1}
	Immunoglobulin	0.1 mg·mL^{-1}

1.3. Reflectometric Interference Spectroscopy (RIfS)

1.3.1. Principle

Reflectometric Interference Spectroscopy (RIfS) is a simple and highly sensitive label-free detection technique that is inspired by nature. In this, the light reflection of white light from a thin film due to the unique micro and nano structures of the film gives rise to interference phenomenon [101-102]. Naturally occurring pearls, abalone-shells, and living creatures like butterfly and Drosophila wings, beetles, peacock feathers, humming birds, blue jays, and pheasants successfully use this phenomenon to their advantage for displaying vivid colours [103]. For example, the wings of a blue *Morpho* butterfly consists of a colourless translucent membrane covered by a thin layer of scales made up of lamellae. Light reflects from upper and lower part of these scales (upper and lower lamellae) which results in the interference of the two reflected beams that provides the beautiful blue colour to its wings [104]. Similarly, on shining white light on an artificial thin film (of thickness comparable to wavelength of reflected light) gets reflected form two interfaces air-thin film interface (top of the thin film) and thin film-base substrate interface (bottom of the thin film) (**Figure 1.12a**). The light reflected at two interfaces interferes due to the difference in their optical path length and phase giving rise to alternate maxima and minima in the reflection pattern. This enhancement of the optical field is at wavelengths which satisfy the mathematical requirements. This phenomenon is known as Fabry-Pérot interference and is governed by the Fabry-Pérot interference equation, given below.

$$OT_{eff} = 2n_{eff}LCos\theta = m\lambda \tag{1.5}$$

where, n_{eff} is the effective refractive index of NAA, L is the thickness of the film and m is the order of the fringe located at the wavelength λ [105-107]. According to **Eq. (1.5)**, any variation in the thickness or in effective refractive index of the thin film is directly reflected in the optical

spectrum as a shift peak wavelength of the interference maxima. This shift in interference peaks is the base for label-free detection, and real-time and in situ monitoring of analyte-receptor binding events of biomolecules using RIfS. A typical RIfS based sensor consists of a sensing substrate functionalized with a receptor entity (such as antibodies, oligonucleotides, chelates, or aptamers) either through simple adsorption or covalent attachment, and binding of analyte molecules to the receptor (immobilized on sensing substrate) is detected in terms of shift in interference pattern as a result of a change in the effective refractive index of the thin film [105]. RIfS not only provides qualitative information about the binding of analyte to receptor but also can be used for quantitative analysis as the shift in the reflection fringes is directly proportional to the amount of analyte bound to receptor on sensor surface. Furthermore, integration of RIfS substrate in a flow cell allows for real-time monitoring of the analyte-receptor binding reaction taking place on thin film surface (i.e. kinetics).

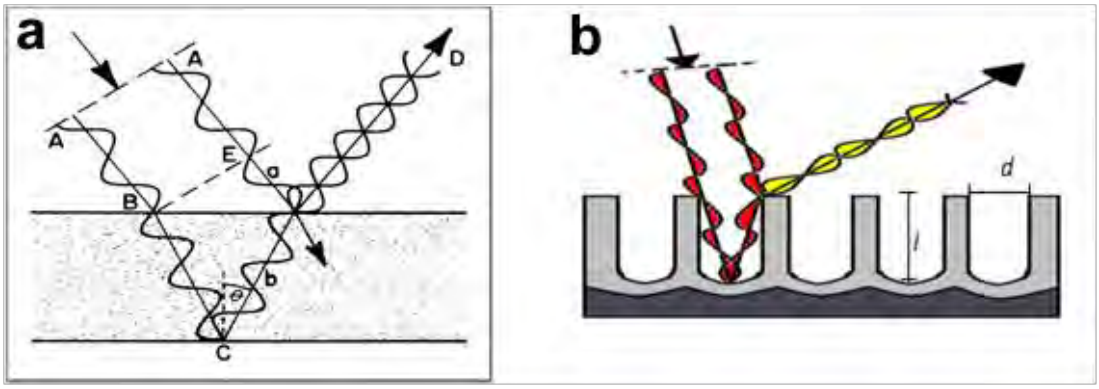

Figure 4: (a) A schematic showing Fabry-Perot interference of light rays reflected from top and bottom layer of a thin film. (b) Fabry-Perot interference from a nanoporous material layer.

Likewise, inorganic nanoporous films such as porous silicon, nanoporous alumina, and titania nanotube arrays also generate well-resolved Fabry-Perot interference fringes with alternate minima and the maxima of the interference spectra, which is also governed by **Eq. (1.5)** (**Figure 1.12b**). Nanoporous films modified with receptor or capturing molecules (listed above)

in the same way as planar films, when exposed to target analyte results in an increase in the local effective refractive index of the nanoporous film inducing a red shift in the interference maxima. Nanoporous films, possess a significantly higher surface area (i.e. more number of receptor molecules on sensing surface) than planar thin films, hence, the changes in local refractive index are substantially higher resulting in larger red shift in the interference spectrum. Therefore, nanoporous thin films based RIfS sensors are much more sensitivity than their planar thin films based counterparts. Also, shift in interference spectrum can be continuously monitored for real-time monitoring of process of infiltration of the pores with proteins, vapours of organic compounds, gas molecules, or solvents. Real-time and in-situ monitoring capability of nanoporous RIfS detection tool is advantageous for determining the mechanism and kinetics of analyte-receptor binding reaction. The interference spectrum can be further resolved to obtain effective optical thickness (OT_{eff}), right hand term "$2n_{eff}L$" in **Eq. (1.5)**, by applying Fast Fourier Transform (FFT) to the spectrum. Applying FFT to reflection interference spectrum and obtaining OT_{eff} provide a single peak in comparison to multiple peaks in the interference spectrum, thus making it easier to follow the changes due to the bio-recognition reaction [111].

1.3.2. RIfS for Sensing and Biosensing

RIfS was initially used for sensing application by G. Gauglitz *et al.* in late 1980s who observed the generation of interference fringe pattern on shining white light on a thin film under normal incidence [106-107]. Gauglitz's group reported on optimization and detection of a large variety of chemical and biological analyte molecules on planar substrates with RIfS. The planar thing films were the substrates of choice with RIfS for Gauglitz's group including silicon dioxide and glass coated with polymer films, metals, and metal oxides [105-108]. They utilized an array of different receptor entities or capturing probes including antibodies, proteins, oligonucleotides hybridization (RNA, DNA, PNA, LNA), aptamers, nanoparticles and so on for studying

bimolecular interactions. These recognition elements capture the target analytes and result in increase in interfacial refractive index leading to shifts in the interference spectrum and effective optical thickness (OT_{eff}, the sensing parameter) of the film. The OT_{eff} can be calculated by plotting a curve between the fringe order (m) and their corresponding wavelength inverse (i.e. wavenumber, $1/\lambda$). The slope of this curve is the OT_{eff} of the substrate as described in **Figure 1.13**. Planar thin films of polymers were utilized by Gauglitz's group for detection of organic solvents for industrial applications as polymer thin films undergo a reversible swelling and deswelling on exposure to such analytes. Planar thin films have been used for RIfS based sensing operations for label-free detection of various target analytes including proteins, DNA, herbicides and hydrocarbons [109-138].

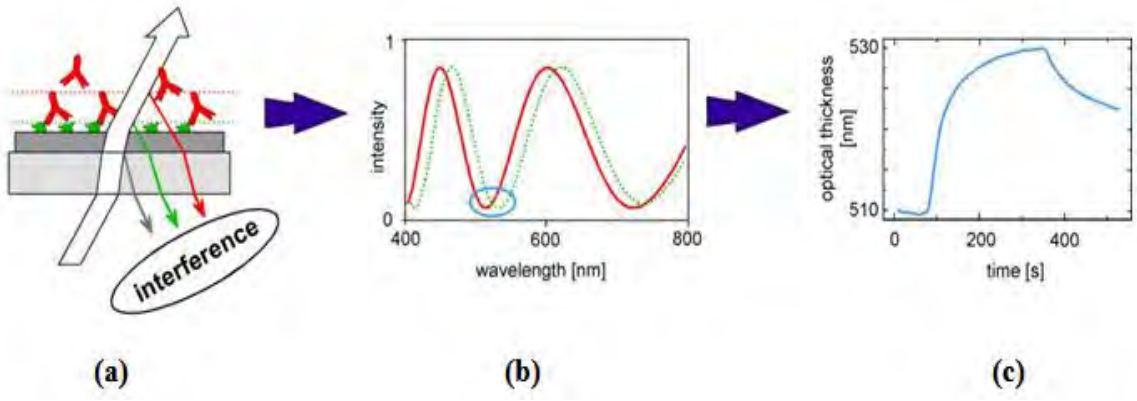

Figure 1.13. (a) Schematic of reflective interference from a planar thin film, (b) generated interference pattern, and (c) optical thickness measurement over time (Source [112]).

They also concentrated some efforts in developing more innovative and complicated RIfS based detection systems using planar thin films. First effort in this direction was to use light emitting diodes (LEDs) as sources and a simple photodiode as detector for a low-cost RIfS setup. They used LEDs of four different colour/wavelengths and were focused on to the planar sensing substrate directly (i.e. without an optical fibre) and the reflected light was picked up by a photodiode mounted above the sample at normal angle. This fibre free RIfS sensor was highly sensitive and was used to monitor the OT_{eff} changes on administration of organic compound over

the sensing substrate surface [139]. A highly complicated and advanced multi-analyte RIfS based sensor was developed using an array of six optical fibres focusing light on six spots on sensing substrate with different surface chemistries. The reflected light is fed to an optical multiplexer which processes the signal from six spots using complex neural network modelling protocols and makes it possible to detect different analytes and their interaction on the sensing spots on the same sensing substrate [140-141]. A new RIfS configuration operating in total internal reflection (TIR) mode was also pioneered by the same group using polymer thin film coated glass substrate. TIR mode RIfS setup was used for detection of proteins and immune-molecules [142-143]. Although, great amount of work was carried out and published by Gauglitz's group, the low surface area and instability of the planer substrate used by this group limits the practical sensing applications of such systems. These issues can easily be overcome using nanoporous thin films (i.e., porous silicon, nanoporous anodic alumina, and titania nanotubes) have emerged as their potential alternative and the first attempt for such system was made by Bjorklund *et al.* who detected organic vaporous and their condensation behaviour inside the pores of porous silicon based interferometer (i.e. thin film) [144].

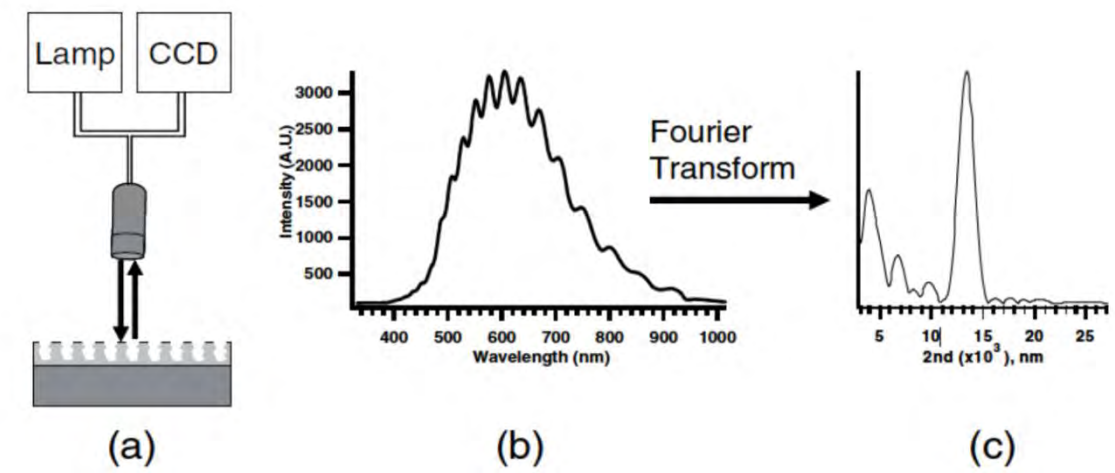

Figure 1.14. (a) Schematic of RIfS from nanoporous substrate, (b) generated interference pattern, and (c) effective optical thickness (EOT) obtained by applying FFT on the interference spectrum (Source [145]).

Sailor and co-workers have exploited porous silicon as a suitable RIfS substrate to develop highly sensitive chemical and bio-sensors (**Figure 1.14**) [145-148]. They have been able to achieve sensitivities of up to 10^{-5} of refractive index unit (RIU) using porous silicon thin films with 80% porosity [149]. Sailor and co-workers have used porous silicon (pSi) thin films very extensively for developing sensors for detection of various target analytes including gases, vapours, proteins, DNA, antibodies, sugars enzymes, cells and so on [149-152]. They were able to achieve a low limit of detection down to 9 fg/mL for detection of DNA hybridization on a complementary DNA immobilized porous silicon substrate [153]. They not only were able to do qualitative and quantitative detection of target analytes but could also determine the binding kinetics of proteins and antibodies by packing the pSi sensing chip in a flow cell [108, 154]. It was demonstrated by that changing the current density during the etching of pSi directly results in changes in its porosity (i.e. refractive index) along the thickness. This ability to modulate the porosity spatially along the length of the pores allows for fabrication of complex pore structures in porous silicon to generate 1D photonic crystals such as rugate filters and Bragg mirrors, and layered pore structures (i.e. stacks of different porosity). Photonic structures like rugate filters display a sharp stop band/reflection peak in optical spectrum along with regular interference fringes. Such structures have been used for development of a variety of optical sensors for detection of vapours, gases, and biomolecules like proteins, sucrose, enzymes, and others [155-161]. Porous silicon rugate filters with both the optical signatures (i.e. reflection peak and interference fringes) have been used for developing internally referenced sensing substrate, which can nullify the noise induced by factors such as bubbles, vibrations and temperature fluctuations. Layered or stacked pSi sensing substrates have been fabricated for up to three stacks and have been extensively studied for multiple innovative sensing applications. For example, a pSi layered structure with two stacks having a high porosity layer on top and a low porosity layer at bottom was prepared by sequentially reducing the current density from high to low during

electrochemical etching of pSi [151, 160, 162]. Due to different porosity both stacks act as individual interferometer and complex interference pattern is observed in reflection spectrum. This complex reflection interference spectrum can be resolved to obtain three peaks corresponding to effective optical thickness of the top, bottom, and the whole (i.e. top + bottom layers) in the FFT plot. Such two layered structures were used to detect selectively large proteins from a mixture of proteins and small sugar molecules. This was achieved due to size-exclusion effect of the bottom layer that does not allow infiltration of large proteins whereas small sugar molecules easily fill both the layers. Therefore, this strategy was employed for selective multiple detection of small and large target analytes at the same time. Also, the bottom layer can act as a reference channel for elimination of noise due to small salt and interfering molecules in the sample mixture. In another study, top layer was immobilized with an enzyme (i.e. a large protein molecule) and the degradation product of a substrate was collected in the bottom layer of low porosity [154]. During this process the top layer (with higher porosity) act as a nanoreactors while the bottom layer acts as a container for concentrating the degradation product. Additionally, advantage of this system is that the process of enzyme immobilization and degradation of substrate in top layer, and collection of degradation product in the bottom layer can be monitored in real-time by their respective peaks in the FFT spectrum [162-163]. They also, fabricated a pSi structure with three layers which was used for time-resolved detection of an array of organic vapours [167]. Furthermore, they demonstrated that composites of pSi with carbon, titania, and other materials can improve the stability of pSi and be used for development of sensors for organic vapours and biological target analytes [156, 165-166]. A few other studies by several groups including Volcker's (Australia), Pacholski's (Germany), Segal's (Israel) and Gooding's (Australia) have also utilized pSi based sensing substrates in combination with RIfS for development of sensors for various target analytes such as proteins, bacteria, aptamers, cells, enzymes and so on [167-179]. Although pSi displays unique and extraordinary capabilities to fabricate complex and innovative optical

structure that have been used for development of highly sensitive, selective, and innovative sensors, this nanoporous material is unstable under chemical and biological environment leading to collapse of the pore structure. The collapse or degradation of pore structure results in decrease in the refractive index over time and hence a drift in the sensor response and instability in the interference signal. This instability of pSi under biological environment encouraged Sailor's group to utilize other nanoporous materials like nanoporous anodic alumina (NAA) and titania nanotube arrays (TiNTs), which are much more chemically and thermally stable than porous silicon [180-181]. They successfully demonstrated application of NAA and TiNTs as effective substrate for fabrication of immunosensors [180]. Furthermore, NAA based interferometric films were utilized by them to understand the capillary condensation based adsorption and desorption of organic vapours inside its pores [182-183].

Note that, NAA offers several advantages over other nanoporous substrates (i.e. porous silicon and titania nanotubes). In this case, NAA present much better chemical and mechanical stability, ease of surface modification, and more controllable and defined nanoporous structure in comparison to pSi and it is much optically active (i.e. better refractive index contrast) than titania nanotubes as well [11-13, 59]. NAA acts as Fabry-Pérot cavity and thus presents well-resolved interference fringe pattern in the RIfS spectrum [181]. Similar to pSi, the interference fringes from NAA can be resolved to obtain effective optical thickness and allow for real-time and in-situ monitoring of binding events of biomolecules and perform label-free optical sensing (**Figure 1.15)**. NAA in combination with RIfS has been used to develop highly sensitive qualitative and quantitative detection systems for analyzing a broad range of analyte molecules including gases, organic molecules and biomolecules [12-13]. Pan *et al.* developed a label-free DNA sensor using RIfS for detection or capturing of target DNA strand on the complementary DNA immobilized inside NAA pores [184]. Alvarez *et al.* described a label-free immunosensor to monitor the

selective capturing of target antigens by the specific antibodies immobilized inside NAA pores using RIfS [181]. A significant change in effective optical thickness takes place only during selective antigen-antibody binding reaction occurring inside NAA pores. An *et al.* optimized the pore geometry of NAA based on pore widening time to obtain the optimal interference signal for development of highly sensitive RIfS sensing systems [185]. The optimization of RIfS signal was carried out by measuring the shift in effective optical thickness of NAA with different pore diameters (different pore widening time) as a function of adsorption of BSA and PSA (prostate specific antigen) antigen inside NAA pores. The final outcome of the study was that the RIfS sensing performance of NAA improves with increasing the pore diameter. Separately, Kumeria *et al.* carried out a comprehensive and cohesive study about optimization of RIfS signal from NAA. In this study, they not only measured the RIfS signal just as a function of pore diameter but also pore length, and surface coatings (i.e. metal deposition) to obtain the most optimum NAA structure for RIfS based sensing platforms [186]. After optimization of NAA structure for Kumeria *et al.* employed this NAA for label-free detection of volatile sulphur compounds (*i.e.*, VSCs: hydrogen sulphide gas) and hydrogen gas in combination with RIfS [187-188]. The selectivity towards VSCs was due to gold coating on the top surface of NAA while platinum metal coating was used for selective adsorption of hydrogen gas. Furthermore, a microfluidics based flow cell was designed by them for the next study to develop a label-free and portable oral malodour (i.e. mostly VSCs due to degradation of sulfur containing amino acids residing on the tongue) [188]. The same combination of microfluidic and NAA-RIfS system was used for detecting and quantifying circulating tumour cells (CTCs) by Kumeria *et al.* [17]. For this study, gold coated NAA sensing substrates were functionalized with anti-EpCAM antibodies which specifically capture the CTCs. The process of capturing CTCs on anti-EpCAM modified NAA was monitored in real-time by following the changes in OT_{eff}. The major advantage of the proposed CTCs detection microchip sensors is that it does not require any pre-enhancement step before

detection step. Detection of CTCs in buffer and human blood was successfully demonstrated for this NAA based microchip sensor. Dronov *et al.* used platinum metal coated NAA as interferometric transducer with high signal to noise ratio and improved sensing properties [189]. The sensing performance of platinum coated NAA was compared with porous silicon substrate and NAA proved to be more sensitive than porous silicon. Recently, Macias *et al.* fabricated a bi-layered NAA stacks and were employed for size exclusion based sensing [190]. This bi-layered NAA substrate generates a complex reflectivity spectrum (similar to pSi). The RIfS signal was observed to be enhanced on coating the top surface of these engineered NAA substrate with gold. The sensing performance was assessed by detecting BSA in the top layer as it does not infiltrate pores in the bottom layer (i.e. due to smaller pore diameter). This system is capable of size exclusion based sensing of large and small molecules by measuring the effective optical thickness peak corresponding to respective layer.

Further development in this field for detection of heavy metal ions and comparing the optical performance of NAA-RIfS sensors with other techniques (i.e. photoluminescence spectroscopy) for detection of amino acid has been carried out by Kumeria and co-workers. The details of these studies are presented in **Chapter 3** and **Chapter 7** of this PhD thesis.

1.3.3. Challenges for NAA based Optical Sensing

Nanoporous substrates provide several advantages in comparison to planar films as high surface area, easy of surface modification, enhanced optical activity and so on. Porous silicon, nanoporous anodic alumina, and titania nanotubes array are the most popular substrates of choice used for optical sensing applications. NAA offers several advantages of the other two substrates such as chemical, physical, and thermal stability, controllable pore structure and surface chemistry, and others. Previously, a number of reports have been presented on NAA based

optical sensors using a variety of detection techniques such as PLS, SPR, SERS, wave-guiding and so on. However, the combination of NAA with the aforementioned techniques is limited for their practical industrial and environmental application. For example, although the NAA based SPR sensors are highly sensitive they are limited by the cost, bulkiness, and requirement of state-of the art optical (e.g. special prisms) setups. Similarly, PLS and SERS based NAA sensors suffer from the same problems in addition to the issues such as inability to carry out real-time measurements, need for precise structural control and noble metal coatings or particles. Hence, there is an immediate need for sensing platforms which can overcome the limitations of the aforementioned sensing techniques. RIfS is an attractive alternative which not only overcomes the mentioned problems but in combination with NAA like porous substrate can be used to make highly selective and sensitive label-free, portable point-of-care sensing systems.

Therefore, for developing a label-free NAA based sensors these key factors should be carefully considered:

1. Pore dimensions and geometry of NAA
2. Surface chemistry of NAA
3. Flow cell design and integration of NAA
4. Target analytes and RIfS sensing setup

1.4. Objectives

The aim of this thesis will be to develop a highly sensitive and portable sensing system based on nanoporous substrate. List of aims of this thesis and specific objectives identified to achieve these aims are provided below.

1. To explore and optimise the structural features of NAA for an effective sensing device. The specific research objectives are:
    - To define the most effective structural geometry for generating intense interference signal from NAA.
    - To study the effect of structural engineering of NAA on the optical reflection signal.
    - To fabricate and optimize optical signatures of 1D photonic structures in NAA for optical sensing.
2. To investigate the surface modification methods for specific and nonspecific type analyte binding inside NAA pores.
    - To modify the surface chemistry of NAA with organo-silanes and metal coatings for selective binding of target analyte.
    - To infiltrate the pores with small molecules such as glucose for nonspecific and adsorption based sensing as a result of spatial refractive index variation.
3. To design and fabricate bulk and microfluidic flow cells and incorporation of NAA and RIfS with these flow cells. The specific development areas are:
    - To design and fabricate bulk and microfluidic flow cells and optimize the flow rates for each depending on the application.
    - To optimize the sensing performance of the NAA sensing device by choosing correct combination of analyte and flow cell (i.e. bulk flow cell for environmental samples and microfluidic flow cell for biological analytes).
4. To detect a series of model analytes of environmental and biomedical relevance. The list includes:
    - Heavy metal ions such as gold and mercury in environmental samples like tap water and water samples taken from River Torrens in South Australia.

- Biological analytes such as amino acids, antibodies, small sugar molecules.

5. To determine sensing performance of NAA based sensing system by determining:
   - The lower limit of detection for each of the analysed analytes.
   - The response time to obtain readable signal on attachment of the target analyte inside the NAA pores
   - The sensitivity and selectivity of NAA based sensor towards a particular analyte.
   - The reproducibility of the sensing performance.
   - The kinetics and mechanism of analyte capture inside the functionalized NAA pores.
6. To the sensing performance of NAA with different structural features and with different sensing techniques. More specifically:
   - To compare the performance of NAA with straight pores and modulated pores (i.e. NAA-RFs) in terms of their sensing parameters.
   - To compare the performance of NAA based sensing system with detection techniques as RIfS and PLs
7. To adapt NAA RIfS sensing system for other applications such as monitoring of drug release from NAA pores in real-time and in-situ under dynamic flow conditions.

1.5. Thesis Structure

This thesis includes 9 chapters. This section provides a short summary of all the chapters included in this thesis and how each chapter achieves a specific objective defined above to develop a highly sensitive NAA based sensing device.

Chapter 1 intends to provide detailed description of sensors and their application in everyday life. Also, the history and extended literature review on sensors, nanoporous anodic alumina, its fabrication, structural engineering, and its surface modification is provided. Details of principle,

setup, and previous studies on reflectometric interference spectroscopy are provided in last section of this chapter.

Chapter 2 gives out details of materials and methods including the anodization process for fabrication of NAA, its surface modification, design of bulk and microfluidic flow cells, and RIfS setup.

Chapter 3 demonstrates the ability of NAA modified with mercapto-silane for selective binding with gold (III) ions and their detection using RIfS. The real-life application of the developed sensor is proven by detecting gold (III) ions in tap water and phosphate buffer.

Chapter 4 presents the a new pseudo-sinusoidal anodization approach for preparation of 1D photonic structures in NAA, known as NAA rugate filters (NAA-RFs). Four different types of NAA-RFs are prepared and optimized based on their sensing performance by pore infiltration (i.e. non-specific binding) with small sugar molecule (i.e. glucose).

Chapter 5 demonstrates the ability of NAA-RFs for detection of heavy metal ions (i.e. ionic mercury). The real-life application of the developed sensor is proven by detecting ionic mercury in tap water and river water (River Torrens, South Australia).

Chapter 6 essentially compares the sensing performance of the NAA with straight pores and NAA with modulated pores (i.e. NAA based Bragg reflectors) by infiltrating the pores with glucose and the most optimum NAA structure is utilized for detection of ionic mercury using mercapto-silane surface modification.

Chapter 7 compares the performance of NAA as a sensing substrate under two sensing techniques (i.e. RIfS and PLS). Here the performance parameters for NAA-RIfS and NAA-PLS

sensors are determined under nonspecific and specific binding conditions of analytes inside NAA pores.

Chapter 8 displays a different application of NAA-RIfS system by monitoring the release of model drug from NAA pores in real-time under dynamic flow conditions when a drug loaded NAA substrate is packed in the specifically designed microfluidic flow cell.

Chapter 9 summarizes the research results for this thesis and provides a perspective for future applications of NAA based optical sensors.

The Appendices provide the peer-reviewed review articles that are relevant to **Chapter 1** and other peer-reviewed Journal and conference articles related to this thesis. **Appendix A** is a recently published article in one of the top journal in material (i.e. Advanced Materials) with impact factor of 15.4. **Appendix B** is a of literature review of NAA, its chemical and optical properties, and RIfS and its applications covering a portion of **Chapter 1**.

1.6. References

1. Kissinger, P. T., Biosensors-a perspective. *Biosensors and Bioelectronics* **2005,** *20*, 2512-2516.

2. Scheller, F. W.; Wollenberger, U.; Warsinke, A.; Lisdat, F., Research and development in biosensors. *Current Opinion in Biotechnology* **2001,** *12*, 35-40.

3. Nakamura, H.; Karube, I., Current research activity in biosensors. *Analytical and bioanalytical chemistry* **2003,** *377*, 446-468.

4. *Biosensors in medical diagnostics - a global strategic business report*; USA., **2013**; p 287.

5. Luong, J. H.; Male, K. B.; Glennon, J. D., Biosensor technology: technology push versus market pull. *Biotechnology advances* **2008,** *26*, 492-500.

6. Cooper, M. A., Label-free screening of bio-molecular interactions. *Analytical and bioanalytical chemistry* **2003,** *377*, 834-842.

7. Spichiger-Keller, U. E., *Chemical sensors and biosensors for medical and biological applications*. John Wiley & Sons: **2008**, DOI: 10.1002/9783527612284.

8. Taylor, R. F., Schultz J. S., Eds. Handbook of chemical and biological sensors. CRC Press, **1996**.

9. Soloman, S., Ed. *Sensors handbook*. McGraw-Hill Inc. **2009**.

10. Fan, X.; White, I. M.; Shopova, S. I.; Zhu, H.; Suter, J. D.; Sun, Y., Sensitive optical biosensors for unlabeled targets: A review. *analytica chimica acta* **2008,** *620*, 8-26.

11. Santos, A.; Kumeria, T.; Losic, D., Nanoporous anodic aluminum oxide for chemical sensing and biosensors. *TrAC Trends in Analytical Chemistry* **2013,** *44*, 25-38.

12. Kumeria, T.; Santos, A.; Losic, D., Nanoporous Anodic Alumina Platforms: Engineered Surface Chemistry and Structure for Optical Sensing Applications. *Sensors* **2014,** *14*, 11878-11918.

13. Santos, A.; Kumeria, T.; Losic, D., Nanoporous Anodic Alumina: A Versatile Platform for Optical Biosensors. *Materials* **2014,** *7*, 4297-4320.

14. Pattnaik, P., Surface plasmon resonance. *Applied biochemistry and biotechnology* **2005,** *126*, 79-92.

15. Homola, J., Ed. Surface plasmon resonance based sensors. Vol. 4. *Springer Science & Business Media*, **2006**.

16. Willets, K. A.; Van Duyne, R. P., Localized surface plasmon resonance spectroscopy and sensing. *Annu. Rev. Phys. Chem.* **2007,** *58*, 267-297.

17. Kumeria, T.; Kurkuri, M. D.; Diener, K. R.; Parkinson, L.; Losic, D., Label-free reflectometric interference microchip biosensor based on nanoporous alumina for detection of circulating tumour cells. *Biosensors and Bioelectronics* **2012,** *35*, 167-173.

18. Masuda, H.; Fukuda, K., Ordered metal nanohole arrays made by a two-step replication of honeycomb structures of anodic alumina. *Science* **1995,** *268*, 1466-1468.

19. Kant, K.; Losic, D., Self-ordering electrochemical synthesis of TiO 2 nanotube arrays: controlling the nanotube geometry and the growth rate. *International Journal of Nanoscience* **2011,** *10*, 55-58.

20. Lehmann, V.; Gösele, U., Porous silicon formation: A quantum wire effect. *Applied Physics Letters* **1991,** *58*, 856-858.

21. Kinard, J. T., Melody B. J., Wheeler D. A., Method of operating process for anodizing valve metals." U.S. Patent No. 6,235,181, **2001**.

22. Ingham, C. J.; ter Maat, J.; de Vos, W. M., Where bio meets nano: the many uses for nanoporous aluminum oxide in biotechnology. *Biotechnology advances* **2012,** *30*, 1089-1099.

23. Bengough, G. D., Struat J. A. *J. Inst. Met.* **1922,** *28*, 66.

24. Bengough, G. D., Stuart J. M., The anodic oxidation of aluminium and its alloys as a protection against corrosion. British Patent 223994, **1923**.

25. Caboni V., Italian Patent 339 232, **1936**.

26. Li, A.; Müller, F.; Birner, A.; Nielsch, K.; Gösele, U., Hexagonal pore arrays with a 50–420 nm interpore distance formed by self-organization in anodic alumina. *Journal of applied physics* **1998,** *84*, 6023-6026.

27. Akahori, H.; Fukushima, T., Study on the Hydration of Alumite by Electron Microscopy and Electron Micro Diffraction. *Journal of Electron Microscopy* **1964,** *13*, 162-171.

28. Thompson, G.; Furneaux, R.; Wood, G.; Richardson, J.; Goode, J., Nucleation and growth of porous anodic films on aluminium. *Nature* **1978,** 272, 433-435.

29. Akahori, H., Electron Microscopic Study of Growing Mechanism of Aluminium Anodic Oxide Film. *Journal of Electron Microscopy* **1961,** *10*, 175-185.

30. Keller, F.; Hunter, M.; Robinson, D., Structural features of oxide coatings on aluminum. *Journal of the Electrochemical Society* **1953,** *100*, 411-419.

31. Shingubara, S., Fabrication of nanomaterials using porous alumina templates. *Journal of Nanoparticle Research* **2003,** *5*, 17-30.

32. Lee, W.; Ji, R.; Gösele, U.; Nielsch, K., Fast fabrication of long-range ordered porous alumina membranes by hard anodization. *Nature materials* **2006,** *5*, 741-747.

33. O'sullivan, J.; Wood, G., The morphology and mechanism of formation of porous anodic films on aluminium. *Proceedings of the Royal Society of* London. *A. Mathematical and Physical Sciences* **1970,** *317*, 511-543.

34. Vasudevan, A. K.; Doherty, R. D., Eds. Aluminum Alloys-Contemporary Research and Applications. Vol. 31, *Elsevier* **2012**.

35. Thompson, G.; Xu, Y.; Skeldon, P.; Shimizu, K.; Han, S.; Wood, G., Anodic oxidation of aluminium. *Philosophical Magazine B* **1987,** *55*, 651-667.

36. Pang, S.; Tamamura, T.; Nakao, M.; Ozawa, A.; Masuda, H., Direct nano-printing on Al substrate using a SiC mold. *Journal of Vacuum Science & Technology B* **1998,** *16*, 1145-1149.

37. Masuda, H.; Yamada, H.; Satoh, M.; Asoh, H.; Nakao, M.; Tamamura, T., Highly ordered nanochannel-array architecture in anodic alumina. *Applied Physics Letters* **1997,** *71*, 2770-2772.

38. Lee, W.; Park, S.-J., Porous anodic aluminum oxide: anodization and templated synthesis of functional nanostructures. *Chemical reviews* **2014,** *114*, 7487-7556.

39. Nielsch, K.; Choi, J.; Schwirn, K.; Wehrspohn, R. B.; Gösele, U., Self-ordering regimes of porous alumina: the 10 porosity rule. *Nano letters* **2002,** *2*, 677-680.

40. Sulka, G. D., Highly ordered anodic porous alumina formation by self-organized anodizing in Nanostructured materials in electrochemistry. *Wiley VCH Verlag GmbH & Co.* **2008**, 1-116.

41. Jessensky, O.; Müller, F.; Gösele, U., Self-organized formation of hexagonal pore arrays in anodic alumina. *Applied Physics Letters* **1998,** *72*, 1173-1175.

42. Schwirn, K.; Lee, W.; Hillebrand, R.; Steinhart, M.; Nielsch, K.; Gösele, U., Self-ordered anodic aluminum oxide formed by H2SO4 hard anodization. *ACS nano* **2008,** *2*, 302-310.

43. Masuda, H.; Yada, K.; Osaka, A., Self-ordering of cell configuration of anodic porous alumina with large-size pores in phosphoric acid solution. *Japanese Journal of Applied Physics* **1998,** *37*, L1340.

44. Masuda, H.; Hasegwa, F.; Ono, S., Self-Ordering of Cell Arrangement of Anodic Porous Alumina Formed in Sulfuric Acid Solution. *Journal of the electrochemical society* **1997,** *144*, L127-L130.

45. Ono, S.; Saito, M.; Asoh, H., Self-ordering of anodic porous alumina formed in organic acid electrolytes. *Electrochimica Acta* **2005,** *51*, 827-833.

46. Surganov, V.; Morgen, P.; Nielsen, J.; Gorokh, G.; Mozalev, A., Study of the initial stage of aluminium anodization in malonic acid solution. *Electrochimica Acta* **1987,** *32*, 1125-1127.

47. Surganov, V.; Gorokh, G., Anodic oxide cellular structure formation on aluminum films in tartaric acid electrolyte. *Materials Letters* **1993,** *17*, 121-124.

48. Chu, S.; Wada, K.; Inoue, S.; Isogai, M.; Katsuta, Y.; Yasumori, A., Large-scale fabrication of ordered nanoporous alumina films with arbitrary pore intervals by critical-potential anodization. *Journal of The Electrochemical Society* **2006,** *153*, B384-B391.

49. Ono, S.; Saito, M.; Ishiguro, M.; Asoh, H., Controlling factor of self-ordering of anodic porous alumina. *Journal of The Electrochemical Society* **2004,** *151*, B473-B478.

50. Mozalev, A.; Mozaleva, I.; Sakairi, M.; Takahashi, H., Anodic film growth on Al layers and Ta–Al metal bilayers in citric acid electrolytes. *Electrochimica acta* **2005,** *50*, 5065-5075.

51. Lee, W.; Schwirn, K.; Steinhart, M.; Pippel, E.; Scholz, R.; Gösele, U., Structural engineering of nanoporous anodic aluminium oxide by pulse anodization of aluminium. *Nature nanotechnology* **2008,** *3*, 234-239.

52. Losic, D.; Lillo, M., Porous alumina with shaped pore geometries and complex pore architectures fabricated by cyclic anodization. *Small* **2009,** *5*, 1392-1397.

53. Santos, A.; Formentín, P.; Pallarès, J.; Ferré-Borrull, J.; Marsal, L. F., Structural engineering of nanoporous anodic alumina funnels with high aspect ratio. *Journal of Electroanalytical Chemistry* **2011,** *655*, 73-78.

54. Nagaura, T.; Takeuchi, F.; Inoue, S., Fabrication and structural control of anodic alumina films with inverted cone porous structure using multi-step anodizing. *Electrochimica Acta* **2008,** *53*, 2109-2114.

55. Nagaura, T.; Takeuchi, F.; Yamauchi, Y.; Wada, K.; Inoue, S., Fabrication of ordered Ni nanocones using a porous anodic alumina template. *Electrochemistry Communications* **2008,** *10*, 681-685.

56. Li, J.; Li, C.; Chen, C.; Hao, Q.; Wang, Z.; Zhu, J.; Gao, X., Facile method for modulating the profiles and periods of self-ordered three-dimensional alumina taper-nanopores. *ACS applied materials & interfaces* **2012,** *4*, 5678-5683.

57. Yanagishita, T.; Kondo, T.; Nishio, K.; Masuda, H., Optimization of antireflection structures of polymer based on nanoimprinting using anodic porous alumina. *Journal of Vacuum Science & Technology B* **2008,** *26*, 1856-1859.

58. Losic, D.; Losic Jr, D., Preparation of porous anodic alumina with periodically perforated pores. *Langmuir* **2009,** *25*, 5426-5431.

59. Jani, A. M. M.; Losic, D.; Voelcker, N. H., Nanoporous anodic aluminium oxide: Advances in surface engineering and emerging applications. *Progress in Materials Science* **2013,** *58*, 636-704.

60. Thompson, G.; Wood, G., *Anodic films on aluminum*. Academic Press. Inc: New York, , 1983, **1983**; p 205-329.

61. Santos, A.; Kumeria, T.; Wang, Y.; Losic, D., In situ monitored engineering of inverted nanoporous anodic alumina funnels: On the precise generation of 3d optical nanostructures. *Nanoscale* **2014,** *6*, 9991-9999.

62. Pitzschel, K.; Moreno, J. M. M.; Escrig, J.; Albrecht, O.; Nielsch, K.; Bachmann, J., Controlled introduction of diameter modulations in arrayed magnetic iron oxide nanotubes. *ACS nano* **2009,** *3*, 3463-3468.

63. Santos, A.; Ferré-Borrull, J.; Pallarès, J.; Marsal, L., Hierarchical nanoporous anodic alumina templates by asymmetric two-step anodization. *physica status solidi (a)* **2011,** *208*, 668-674.

64. Zhu, X.; Liu, L.; Song, Y.; Jia, H.; Yu, H.; Xiao, X.; Yang, X., Oxygen bubble mould effect: Serrated nanopore formation and porous alumina growth. *Monatshefte für Chemie-Chemical Monthly* **2008,** *139*, 999-1003.

65. Li, D.; Zhao, L.; Jiang, C.; Lu, J. G., Formation of anodic aluminum oxide with serrated nanochannels. *Nano letters* **2010,** *10*, 2766-2771.

66. Santos, A.; Vojkuvka, L.; Alba, M.; Balderrama, V. S.; Ferré-Borrull, J.; Pallares, J.; Marsal, L. F., Understanding and morphology control of pore modulations in nanoporous anodic alumina by discontinuous anodization. *physica status solidi (a)* **2012,** *209*, 2045-2048.

67. Martín, J.; Martín-González, M.; Fernández, J. F.; Caballero-Calero, O., Ordered three-dimensional interconnected nanoarchitectures in anodic porous alumina. *Nature communications* **2014,** *5*, DOI:10.1038/ncomms6130.

68. Sulka, G. D.; Hnida, K., Distributed Bragg reflector based on porous anodic alumina fabricated by pulse anodization. *Nanotechnology* **2012,** *23*, 075303.

69. Zheng, W. J.; Fei, G. T.; Wang, B.; De Zhang, L., Modulation of transmission spectra of anodized alumina membrane distributed Bragg reflector by controlling anodization temperature. *Nanoscale research letters* **2009,** *4*, 665-667.

70. Ferré-Borrull, J.; Rahman, M. M.; Pallarès, J.; Marsal, L. F., Tuning nanoporous anodic alumina distributed-Bragg reflectors with the number of anodization cycles and the anodization temperature. *Nanoscale research letters* **2014,** *9*, 1-6.

71. Rahman, M. M.; Marsal, L. F.; Pallarès, J.; Ferré-Borrull, J., Tuning the photonic stop bands of nanoporous anodic alumina-based distributed Bragg reflectors by pore widening. *ACS applied materials & interfaces* **2013,** *5*, 13375-13381.

72. Macias, G.; Ferré-Borrull, J.; Pallarès, J.; Marsal, L. F., 1-D nanoporous anodic alumina rugate filters by means of small current variations for real-time sensing applications. *Nanoscale research letters* **2014,** *9*, 1-6.

73. Yamamoto, Y.; Baba, N.; Tajima, S., Coloured materials and photoluminescence centres in anodic film on aluminium. *Nature* **1981,** *289*, 572-574.

74. Martin, C. R., Nanomaterials: A Membrane-Based Synthetic Approach. *Science* **1994,** *266*, 1961-1966.

75. Szczepanski, V.; Vlassiouk, I.; Smirnov, S., Stability of silane modifiers on alumina nanoporous membranes. *Journal of membrane science* **2006,** *281*, 587-591.

76. Hendren, Z.; Brant, J.; Wiesner, M., Surface modification of nanostructured ceramic membranes for direct contact membrane distillation. *Journal of Membrane Science* **2009,** *331*, 1-10.

77. Odom, D. J.; Baker, L. A.; Martin, C. R., Solvent-extraction and langmuir-adsorption-based transport in chemically functionalized nanopore membranes. *The Journal of Physical Chemistry B* **2005,** *109*, 20887-20894.

78. Velleman, L.; Triani, G.; E vans, P. J.; Shapter, J. G.; Losic, D., Structural and chemical modification of porous alumina membranes. *Microporous and Mesoporous Materials* **2009,** *126*, 87-94.

79. Ku, A. Y.; Ruud, J. A.; Early, T. A.; Corderman, R. R., Evidence of ion transport through surface conduction in alkylsilane-functionalized nanoporous ceramic membranes. *Langmuir* **2006,** *22*, 8277-8280.

80. Popat, K. C.; Mor, G.; Grimes, C. A.; Desai, T. A., Surface modification of nanoporous alumina surfaces with poly (ethylene glycol). *Langmuir* **2004,** *20*, 8035-8041.

81. La Flamme, K. E.; Popat, K. C.; Leoni, L.; Markiewicz, E.; La Tempa, T. J.; Roman, B. B.; Grimes, C. A.; Desai, T. A., Biocompatibility of nanoporous alumina membranes for immunoisolation. *Biomaterials* **2007,** *28*, 2638-2645.

82. Lee, S. W.; Shang, H.; Haasch, R. T.; Petrova, V.; Lee, G. U., Transport and functional behaviour of poly (ethylene glycol)-modified nanoporous alumina membranes. *Nanotechnology* **2005,** *16*, 1335.

83. Vlassiouk, I.; Takmakov, P.; Smirnov, S., Sensing DNA hybridization via ionic conductance through a nanoporous electrode. *Langmuir* **2005,** *21*, 4776-4778.

84. Takmakov, P.; Vlassiouk, I.; Smirnov, S., Application of anodized aluminum in fluorescence detection of biological species. *Analytical and bioanalytical chemistry* **2006,** *385*, 954-958.

85. Yang, Z.; Si, S.; Dai, H.; Zhang, C., Piezoelectric urea biosensor based on immobilization of urease onto nanoporous alumina membranes. *Biosensors and Bioelectronics* **2007,** *22*, 3283-3287.

86. Hobler, C.; Bakowsky, U.; Keusgen, M., A functional immobilization of semiconductor nanoparticles (quantum dots) on nanoporous aluminium oxide. *physica status solidi (a)* **2010,** *207*, 872-877.

87. Largueze, J.-B.; El Kirat, K.; Morandat, S., Preparation of an electrochemical biosensor based on lipid membranes in nanoporous alumina. *Colloids and Surfaces B: Biointerfaces* **2010,** *79*, 33-40.

88. Lau, K. A.; Duran, H.; Knoll, W., In situ characterization of N-carboxy anhydride polymerization in nanoporous anodic alumina. *The Journal of Physical Chemistry B* **2009,** *113*, 3179-3189.

89. Li, P.-F.; Xie, R.; Jiang, J.-C.; Meng, T.; Yang, M.; Ju, X.-J.; Yang, L.; Chu, L.-Y., Thermo-responsive gating membranes with controllable length and density of poly (N-isopropylacrylamide) chains grafted by ATRP method. *Journal of Membrane Science* **2009,** *337*, 310-317.

90. Wang, W.; Li, N.; Li, X.; Geng, W.; Qiu, S., Synthesis of metallic nanotube arrays in porous anodic aluminum oxide template through electroless deposition. *Materials research bulletin* **2006,** *41*, 1417-1423.

91. Sehayek, T.; Lahav, M.; Popovitz-Biro, R.; Vaskevich, A.; Rubinstein, I., Template synthesis of nanotubes by room-temperature coalescence of metal nanoparticles. *Chemistry of materials* **2005,** *17*, 3743-3748.

92. Lahav, M.; Sehayek, T.; Vaskevich, A.; Rubinstein, I., Nanoparticle nanotubes. *Angewandte Chemie International Edition* **2003,** *42*, 5576-5579.

93. Jani, A. M. M.; Anglin, E. J.; McInnes, S. J.; Losic, D.; Shapter, J. G.; Voelcker, N. H., Nanoporous anodic aluminium oxide membranes with layered surface chemistry. *Chemical Communications* **2009,** *21*, 3062-3064.

94. Jani, A. M. M.; Kempson, I. M.; Losic, D.; Voelcker, N. H., Dressing in layers: layering surface functionalities in nanoporous aluminum oxide membranes. *Angewandte Chemie* **2010,** *122*, 8105-8109.

95. Qiu, T.; Zhang, W.; Lang, X.; Zhou, Y.; Cui, T.; Chu, P. K., Controlled Assembly of Highly Raman-Enhancing Silver Nanocap Arrays Templated by Porous Anodic Alumina Membranes. *Small* **2009,** *5*, 2333-2337.

96. Béron, F.; Knobel, M.; Pirota, K. R., Magnetostatic behaviour of antidot arrays under the local influence of nanopillars. *Journal of Physics D: Applied Physics* **2012,** *45*, 505002.

97. Cheow, P.-S.; Ting, E. Z. C.; Tan, M. Q.; Toh, C.-S., Transport and separation of proteins across platinum-coated nanoporous alumina membranes. *Electrochimica Acta* **2008,** *53*, 4669-4673.

98. Nguyen, B. T.; Ting, E. Z. C.; Toh, C.-S., Development of a biomimetic nanoporous membrane for the selective transport of charged proteins. *Bioinspiration & biomimetics* **2008,** *3*, 035008.

99. Béron, F.; Pirota, K. R.; Vega, V.; Prida, V.; Fernández, A.; Hernando, B.; Knobel, M., An effective method to probe local magnetostatic properties in a nanometric FePd antidot array. *New Journal of Physics* **2011,** *13*, 013035.

100. Kumeria, T.; Santos, A., Sensing and biosensing applications of nanoporous anodic alumina. In *Electrochemically engineered nanoporous materials - Methods, properties and applications*, Losic, D.; Santos, A., Eds. Springer International Publishing AG - Germany: Australia, **2015**; Chapter 3.

101. Smith, R. G.; D'Souza, N.; Nicklin, S., A review of biosensors and biologically-inspired systems for explosives detection. *Analyst* **2008,** *133*, 571-584.

102. Kumeria, T.; Parkinson, L.; Losic, D., Bioinspired microchip nanoporous interferometric sensor for sensing and biosensing applications. *Micro and Nanosystems* **2011,** *3*, 290-295.

103. Snow, M. R.; Pring, A.; Self, P.; Losic, D.; Shapter, J., The origin of the color of pearls in iridescence from nano-composite structures of the nacre. *American Mineralogist* **2004,** *89*, 1353-1358.

104. Vukusic, P.; Sambles, J.; Lawrence, C.; Wootton, R., Quantified interference and diffraction in single Morpho butterfly scales. *Proceedings of the Royal Society of London. Series B: Biological Sciences* **1999,** *266*, 1403-1411.

105. Brecht, A.; Gauglitz, G., Optical probes and transducers. *Biosensors and Bioelectronics* **1995,** *10* (9), 923-936.

106. Gauglitz, G., Direct optical sensors: principles and selected applications. *Analytical and bioanalytical chemistry* **2005,** *381*, 141-155.

107. Gauglitz, G., Direct optical detection in bioanalysis: an update. *Analytical and bioanalytical chemistry* **2010,** *398*, 2363-2372.

108. Dancil, K.-P. S.; Greiner, D. P.; Sailor, M. J., A porous silicon optical biosensor: detection of reversible binding of IgG to a protein A-modified surface. *Journal of the American Chemical Society* **1999,** *121*, 7925-7930.

109. Gauglitz, G.; Brecht, A.; Kraus, G.; Mahm, W., Chemical and biochemical sensors based on interferometry at thin (multi-) layers. *Sensors and Actuators B: Chemical* **1993,** *11*, 21-27.

110. Gauglitz, G.; Krause-Bonte, J.; Schlemmer, H.; Matthes, A., Spectral interference refractometry by diode array spectrometry. *Analytical Chemistry* **1988,** *60*, 2609-2612.

111. Bayerbach, S.; Gauglitz, G., Spectral detection in thin-layer chromatography by linear photodiode array spectrometry. *Fresenius' Zeitschrift für analytische Chemie* **1989,** *335*, 370-374.

112. Pröll, F.; Möhrle, B.; Kumpf, M.; Gauglitz, G., Label-free characterisation of oligonucleotide hybridisation using reflectometric interference spectroscopy. *Analytical and bioanalytical chemistry* **2005,** *382*, 1889-1894.

113. Möhrle, B. P.; Köhler, K.; Jaehrling, J.; Brock, R.; Gauglitz, G., Label-free characterization of cell adhesion using reflectometric interference spectroscopy (RIfS). *Analytical and bioanalytical chemistry* **2006,** *384*, 407-413.

114. Dankbar, D. M.; Gauglitz, G., A study on photolinkers used for biomolecule attachment to polymer surfaces. *Analytical and bioanalytical chemistry* **2006,** *386*, 1967-1974.

115. Busche, S.; Kasper, M.; Mutschler, T.; Leopold, N.; Gauglitz, G., Eds. Interaction behaviour of the ultramicroporous polymer Makrolon® by spectroscopic methods In Characterization of Polymer Surfaces and Thin Films, Vol. 132, *Springer*, **2006**, 16-22.

116. Mehlmann, M.; Garvin, A. M.; Steinwand, M.; Gauglitz, G., Reflectometric interference spectroscopy combined with MALDI− TOF mass spectrometry to determine quantitative and qualitative binding of mixtures of vancomycin derivatives. *Analytical and bioanalytical chemistry* **2005,** *382*, 1942-1948.

117. Länge, K.; Herold, M.; Scheideler, L.; Geis-Gerstorfer, J.; Wendel, H.-P.; Gauglitz, G., Investigation of initial pellicle formation on modified titanium dioxide (TiO 2) surfaces by reflectometric interference spectroscopy (RIfS) in a model system. *Dental Materials* **2004,** *20*, 814-822.

118. Hänel, C.; Gauglitz, G., Comparison of reflectometric interference spectroscopy with other instruments for label-free optical detection. *Analytical and bioanalytical chemistry* **2002,** *372*, 91-100.

119. Dieterle, F.; Belge, G.; Betsch, C.; Gauglitz, G., Quantification of the refrigerants R22 and R134a in mixtures by means of different polymers and reflectometric interference spectroscopy. *Analytical and bioanalytical chemistry* **2002,** *374*, 858-867.

120. Birkert, O.; Gauglitz, G., Development of an assay for label-free high-throughput screening of thrombin inhibitors by use of reflectometric interference spectroscopy. *Analytical and bioanalytical chemistry* **2002,** *372*, 141-147.

121. Belge, G.; Beyerlein, D.; Betsch, C.; Eichhorn, K.-J.; Gauglitz, G.; Grundke, K.; Voit, B., Suitability of hyperbranched polyester for sensoric applications–investigation with reflectometric interference spectroscopy. *Analytical and bioanalytical chemistry* **2002,** *374*, 403-411.

122. Tünnemann, R.; Mehlmann, M.; Süssmuth, R. D.; Bühler, B.; Pelzer, S.; Wohlleben, W.; Fiedler, H.-P.; Wiesmüller, K.-H.; Gauglitz, G.; Jung, G., Optical biosensors. Monitoring studies of glycopeptide antibiotic fermentation using white light interference. *Analytical chemistry* **2001,** *73*, 4313-4318.

123. Piehler, J.; Schreiber, G., Fast transient cytokine–receptor interactions monitored in real time by reflectometric interference spectroscopy. *Analytical biochemistry* **2001,** *289*, 173-186.

124. Birkert, O.; Haake, H.-M.; Schütz, A.; Mack, J.; Brecht, A.; Jung, G.; Gauglitz, G., A streptavidin surface on planar glass substrates for the detection of biomolecular interaction. *Analytical biochemistry* **2000,** *282*, 200-208.

125. Sauer, M.; Brecht, A.; Charisse, K.; Maier, M.; Gerster, M.; Stemmler, I.; Gauglitz, G.; Bayer, E., Interaction of chemically modified antisense oligonucleotides with sense DNA: a label-free interaction study with reflectometric interference spectroscopy. *Analytical chemistry* **1999,** *71*, 2850-2857.

126. Rathgeb, F.; Gauglitz, G., Dyeless optical detection of ammonia in the gas phase using pH-responsive polymers with reflectometric interference spectroscopy. *Analytica chimica acta* **1998,** *372*, 333-340.

127. Leipert, D.; Nopper, D.; Bauser, M.; Gauglitz, G.; Jung, G., Investigation of the molecular recognition of amino acids by cyclopeptides with reflectometric interference spectroscopy. *Angewandte Chemie International Edition* **1998,** *37*, 3308-3311.

128. Schmitt, H.-M.; Brecht, A.; Piehler, J.; Gauglitz, G., An integrated system for optical biomolecular interaction analysis. *Biosensors and Bioelectronics* **1997,** *12*, 809-816.

129. Piehler, J.; Brecht, A.; Gauglitz, G.; Zerlin, M.; Maul, C.; Thiericke, R.; Grabley, S., Label-free monitoring of DNA–ligand interactions. *Analytical biochemistry* **1997,** *249*, 94-102.

130. Brecht, A.; Gauglitz, G., Recent developments in optical transducers for chemical or biochemical applications. *Sensors and Actuators B: Chemical* **1997,** *38*, 1-7.

131. Piehler, J.; Brecht, A.; Geckeler, K. E.; Gauglitz, G., Surface modification for direct immunoprobes. *Biosensors and Bioelectronics* **1996,** *11*, 579-590.

132. Piehler, J.; Brecht, A.; Gauglitz, G., Affinity detection of low molecular weight analytes. *Analytical Chemistry* **1996,** *68*, 139-143.

133. Mouvet, C.; Amalric, L.; Broussard, S.; Lang, G.; Brecht, A.; Gauglitz, G., Reflectometric interference spectroscopy for the determination of atrazine in natural water samples. *Environmental science & technology* **1996,** *30*, 1846-1851.

134. Yan, H.; Kraus, G.; Gauglitz, G., Detection of mixtures of organic pollutants in water by polymer film receptors in fibre-optical sensors based on reflectometric interference spectrometry. *Analytica chimica acta* **1995,** *312*, 1-8.

135. Kraus, G.; Brecht, A.; Vasic, V.; Gauglitz, G., Polymer based RIFS sensing: an approach to the indirect measurement of organic pollutants in water. *Fresenius' journal of analytical chemistry* **1994,** *348*, 598-601.

136. Gauglitz, G.; Kraus, G., A reflectometric sensor for ammonia and hydrocarbons. *Fresenius' journal of analytical chemistry* **1993,** *346*, 572-576.

137. Brecht, A.; Ingenhoff, J.; Gauglitz, G., Direct monitoring of antigen-antibody interactions by spectral interferometry. *Sensors and Actuators B: Chemical* **1992,** *6*, 96-100.

138. Brecht, A.; Gauglitz, G.; Nahm, W., Interferometric measurements used in chemical and biochemical sensors. *Analusis* **1992,** *20*, 135-140.

139. Reichl, D.; Krage, R.; Krumme, C.; Gauglitz, G., Sensing of volatile organic compounds using a simplified reflectometric interference spectroscopy setup. *Applied Spectroscopy* **2000,** *54*, 583-586.

140. Gauglitz, G., Multiple reflectance interference spectroscopy measurements made in parallel for binding studies. *Review of scientific instruments* **2005,** *76*, 062224.

141. Birkert, O.; Tünnemann, R.; Jung, G.; Gauglitz, G., Label-free parallel screening of combinatorial triazine libraries using reflectometric interference spectroscopy. *Analytical chemistry* **2002,** *74*, 834-840.

142. Tschmelak, J.; Kumpf, M.; Käppel, N.; Proll, G.; Gauglitz, G., Total internal reflectance fluorescence (TIRF) biosensor for environmental monitoring of testosterone with commercially available immunochemistry: Antibody characterization, assay development and real sample measurements. *Talanta* **2006,** *69*, 343-350.

143. Kröger, K.; Jung, A.; Reder, S.; Gauglitz, G., Versatile biosensor surface based on peptide nucleic acid with label free and total internal reflection fluorescence detection for quantification of endocrine disruptors. *Analytica Chimica Acta* **2002,** *469*, 37-48.

144. Bjorklund, R. B.; Zangooie, S.; Arwin, H., Color changes in thin porous silicon films caused by vapor exposure. *Applied physics letters* **1996,** *69*, 3001-3003.

145. Ghadiri, M. R., Motesharei, K., Lin, S. Y., Sailor, M. J., Dancil, K. P. S., Porous semiconductor-based optical interferometric sensor. U.S. Patent No. 6,248,539, **2001**.

146. Ghadiri, M. R., Sailor, M. J., Motesharei, K., Lin, S. Y., Dancil, K. P. S., Porous semiconductor-based optical interferometric sensor. U.S. Patent No. 6,720,177, **2004**.

147. Ghadiri, M. R. Motesharei, K. Lin, S. Y. Sailor, M. J. Dancil, K. P. S., Porous semiconductor-based optical interferometric sensor. U.S. Patent No. 6,897,965, **2005**.

148. Janshoff, A.; Dancil, K.-P. S.; Steinem, C.; Greiner, D. P.; Lin, V. S.-Y.; Gurtner, C.; Motesharei, K.; Sailor, M. J.; Ghadiri, M. R., Macroporous p-type silicon Fabry-Perot layers. Fabrication, characterization, and applications in biosensing. *Journal of the American Chemical Society* **1998,** *120*, 12108-12116.

149. Alvarez, S. D., Stability and biocompatability of porous silicon and porous alumina for cell and biomolecular sensing. PhD thesis at submitted to univerisyt of California, San Diego, **2008**.

150. Jane, A.; Dronov, R.; Hodges, A.; Voelcker, N. H., Porous silicon biosensors on the advance. *Trends in biotechnology* **2009,** *27*, 230-239.

151. Pacholski, C.; Yu, C.; Miskelly, G. M.; Godin, D.; Sailor, M. J., Reflective interferometric fourier transform spectroscopy: a self-compensating label-free immunosensor using double-layers of porous SiO2. *Journal of the American Chemical Society* **2006,** *128*, 4250-4252.

152. Salem, M.; Sailor, M.; Fukami, K.; Sakka, T.; Ogata, Y., Sensitivity of porous silicon rugate filters for chemical vapor detection. *Journal of Applied Physics* **2008,** *103*, 083516.

153. Lin, V. S.-Y.; Motesharei, K.; Dancil, K.-P. S.; Sailor, M. J.; Ghadiri, M. R., A porous silicon-based optical interferometric biosensor. *Science* **1997,** *278*, 840-843.

154. Orosco, M. M.; Pacholski, C.; Miskelly, G. M.; Sailor, M. J., Protein-Coated Porous-Silicon Photonic Crystals for Amplified Optical Detection of Protease Activity. *Advanced Materials* **2006,** *18*, 1393-1396.

155. Anglin, E. J.; Schwartz, M. P.; Ng, V. P.; Perelman, L. A.; Sailor, M. J., Engineering the chemistry and nanostructure of porous silicon Fabry-Pérot films for loading and release of a steroid. *Langmuir* **2004,** *20*, 11264-11269.

156. Lin, H.; Gao, T.; Fantini, J.; Sailor, M. J., A porous silicon-palladium composite film for optical interferometric sensing of hydrogen. *Langmuir* **2004,** *20*, 5104-5108.

157. Sciacca, B.; Alvarez, S. D.; Geobaldo, F.; Sailor, M. J., Bioconjugate functionalization of thermally carbonized porous silicon using a radical coupling reaction. *Dalton Transactions* **2010,** *39*, 10847-10853.

158. Sohn, H.; Létant, S.; Sailor, M. J.; Trogler, W. C., Detection of fluorophosphonate chemical warfare agents by catalytic hydrolysis with a porous silicon interferometer. *Journal of the American Chemical Society* **2000,** *122*, 5399-5400.

159. Dorvee, J.; Sailor, M. J., A low-power sensor for volatile organic compounds based on porous silicon photonic crystals. *physica status solidi (a)* **2005,** *202*, 1619-1623.

160. Pacholski, C.; Sartor, M.; Sailor, M. J.; Cunin, F.; Miskelly, G. M., Biosensing using porous silicon double-layer interferometers: reflective interferometric Fourier transform spectroscopy. *Journal of the American Chemical Society* **2005,** *127*, 11636-11645.

161. Ruminski, A. M.; Barillaro, G.; Chaffin, C.; Sailor, M. J., Internally referenced remote sensors for HF and Cl2 using reactive porous silicon photonic crystals. *Advanced Functional Materials* **2011,** *21*, 1511-1525.

162. Pacholski, C.; Perelman, L. A.; VanNieuwenhze, M. S.; Sailor, M. J., Small molecule detection by reflective interferometric Fourier transform spectroscopy (RIFTS). *physica status solidi (a)* **2009,** *206*, 1318-1321.

163. Perelman, L. A.; Pacholski, C.; Li, Y. Y.; VanNieuwenhze, M. S.; Sailor, M. J., pH-triggered release of vancomycin from protein-capped porous silicon films. *Nanomedicine* **2008** *3*, 31-43.

164. Kelly, T. L.; Garcia Sega, A.; Sailor, M. J., Identification and quantification of organic vapors by time-resolved diffusion in stacked mesoporous photonic crystals. *Nano letters* **2011,** *11*, 3169-3173.

165. Kelly, T. L.; Gao, T.; Sailor, M. J., Carbon and carbon/silicon composites templated in rugate filters for the adsorption and detection of organic vapors. *Advanced Materials* **2011,** *23*, 1776-1781.

166. Li, J.; Sailor, M. J., Synthesis and characterization of a stable, label-free optical biosensor from TiO 2-coated porous silicon. *Biosensors and Bioelectronics* **2014,** *55*, 372-378.

167. Kilian, K. A.; Böcking, T.; Gaus, K.; Gal, M.; Gooding, J. J., Peptide-modified optical filters for detecting protease activity. *ACS nano* **2007,** *1*, 355-361.

168. Sweetman, M. J.; Voelcker, N. H., Chemically patterned porous silicon photonic crystals towards internally referenced organic vapour sensors. *RSC Advances* **2012,** *2*, 4620-4622.

169. Voelcker, N. H.; Alfonso, I.; Ghadiri, M. R., Catalyzed oxidative corrosion of porous silicon used as an optical transducer for ligand–receptor interactions. *ChemBioChem* **2008,** *9*, 1776-1786.

170. Flavel, B. S.; Sweetman, M. J.; Shearer, C. J.; Shapter, J. G.; Voelcker, N. H., Micropatterned arrays of porous silicon: toward sensory biointerfaces. *ACS applied materials & interfaces* **2011,** *3*, 2463-2471.

171. Ciampi, S.; Böcking, T.; Kilian, K. A.; Harper, J. B.; Gooding, J. J., Click chemistry in mesoporous materials: functionalization of porous silicon rugate filters. *Langmuir* **2008,** *24*, 5888-5892.

172. Guan, B.; Magenau, A.; Kilian, K. A.; Ciampi, S.; Gaus, K.; Reece, P. J.; Gooding, J. J., Mesoporous silicon photonic crystal microparticles: towards single-cell optical biosensors. *Faraday discussions* **2011,** *149*, 301-317.

173. Gupta, B.; Zhu, Y.; Guan, B.; Reece, P. J.; Gooding, J. J., Functionalised porous silicon as a biosensor: emphasis on monitoring cells in vivo and in vitro. *Analyst* **2013,** *138*, 3593-3615.

174. Bonanno, L. M.; Segal, E., Nanostructured porous silicon-polymer-based hybrids: from biosensing to drug delivery. *Nanomedicine* **2011,** *6*, 1755-1770.

175. Massad-Ivanir, N.; Shtenberg, G.; Tzur, A.; Krepker, M. A.; Segal, E., Engineering nanostructured porous SiO2 surfaces for bacteria detection via "Direct Cell Capture". *Analytical chemistry* **2011,** *83*, 3282-3289.

176. Shtenberg, G.; Massad-Ivanir, N.; Moscovitz, O.; Engin, S.; Sharon, M.; Fruk, L.; Segal, E., Picking up the pieces: a generic porous Si biosensor for probing the proteolytic products of enzymes. *Analytical chemistry* **2013,** *85*, 1951-1956.

177. Massad-Ivanir, N.; Shtenberg, G.; Zeidman, T.; Segal, E., Construction and characterization of porous SiO2/hydrogel hybrids as optical biosensors for rapid detection of bacteria. *Advanced Functional Materials* **2010,** *20*, 2269-2277.

178. Urmann, K.; Walter, J. G.; Scheper, T.; Segal, E., Label-Free Optical Biosensors Based on Aptamer-Functionalized Porous Silicon Scaffolds. *Analytical chemistry* **2015,** *87*, 1999–2006.

179. Shtenberg, G.; Massad-Ivanir, N.; Fruk, L.; Segal, E., Nanostructured Porous Si Optical Biosensors: Effect of Thermal Oxidation on Their Performance and Properties. *ACS applied materials & interfaces* **2014,** *6*, 16049-16055.

180. Mun, K.-S.; Alvarez, S. D.; Choi, W.-Y.; Sailor, M. J., A stable, label-free optical interferometric biosensor based on TiO2 nanotube arrays. *Acs Nano* **2010,** *4*, 2070-2076.

181. Alvarez, S. D.; Li, C.-P.; Chiang, C. E.; Schuller, I. K.; Sailor, M. J., A label-free porous alumina interferometric immunosensor. *Acs Nano* **2009,** *3*, 3301-3307.

182. Casanova, F.; Chiang, C.; Li, C.-P.; Roshchin, I.; Ruminski, A.; Sailor, M.; Schuller, I., Effect of surface interactions on the hysteresis of capillary condensation in nanopores. *EPL (Europhysics Letters)* **2008,** *81*, 26003.

183. Casanova, F.; Chiang, C. E.; Li, C.-P.; Roshchin, I. V.; Ruminski, A. M.; Sailor, M. J.; Schuller, I. K., Gas adsorption and capillary condensation in nanoporous alumina films. *Nanotechnology* **2008,** *19*, 315709.

184. Pan, S.; Rothberg, L. J., Interferometric sensing of biomolecular binding using nanoporous aluminum oxide templates. *Nano letters* **2003,** *3*, 811-814.

185. An, H. C.; An, J. Y.; Kim, B.-W., Improvement of sensitivity in an interferometry by controlling pore size on the anodic aluminum oxide chip pore-widening technique. *Korean Journal of Chemical Engineering* **2009,** *26*, 160-164.

186. Kumeria, T.; Losic, D., Controlling interferometric properties of nanoporous anodic aluminium oxide. *Nanoscale research letters* **2012,** *7*, 1-10.

187. Kumeria, T.; Losic, D., Reflective interferometric gas sensing using nanoporous anodic aluminium oxide (AAO). *physica status solidi (RRL)-Rapid Research Letters* **2011,** *5*, 406-408.

188. Kumeria, T.; Parkinson, L.; Losic, D., A nanoporous interferometric micro-sensor for biomedical detection of volatile sulphur compounds. *Nanoscale research letters* **2011,** *6*, 1-7.

189. Dronov, R.; Jane, A.; Shapter, J. G.; Hodges, A.; Voelcker, N. H., Nanoporous alumina-based interferometric transducers ennobled. *Nanoscale* **2011,** *3*, 3109-3114.

190. Macias, G.; Hernández-Eguía, L. P.; Ferré-Borrull, J.; Pallares, J.; Marsal, L. F., Gold-coated ordered nanoporous anodic alumina bilayers for future label-free interferometric biosensors. *ACS applied materials & interfaces* **2013,** *5*, 8093-8098.

CHAPTER 2

DESIGNING and FABRICATION of RIfS SETUP and BULK and MICROFLUIDIC FLOW CELLS

Tushar Kumeria

School of Chemical Engineering, The University of Adelaide, South Australia 5005, Australia

CHAPTER 2: DESIGNING and FABRICATION of RIfS SETUP and BULK and MICROFLUIDIC FLOW CELLS

2.1. Introduction and Objectives

Optical sensors are highly sensitive and precise tools for detection of target analytes. Therefore, it is necessary to exclusively design and fabricate the component for desired and optimal performance. Although, all the components of RIfS optical setup are commercially available, our system takes advantage of its integration of specific components to obtain the best possible performance. Furthermore, the specifically designed flow cells (i.e. both bulk flow cell and microfluidic flow cell) not only allow for integration of NAA with RIfS but also greatly enhance the performance of the prepared optical sensing system. The RIfS optical setup in combination with NAA is the starting point for further research into this field. Therefore, the objective of this chapter (**Chapter 2**) is to define the design, fabrication, and assembly process of RIfS setup and the flow cells (i.e. bulk and microfluidic flow cell). This chapter (**Chapter 2**) also briefly defines the electrochemical setup used for fabrication of NAA by anodization process and the chemical vapour deposition (CVD) setup used for functionalization of NAA with silanes.

2.2. Electrochemical anodization for fabrication of NAA

NAA substrates used for this study were fabricated using a process known as electrochemical anodization, which has been used for industrial applications such as corrosion protection, automobile engineering, metal decoration and others for more than a century now [1-4]. The electrochemical anodization setup for NAA fabrication consists of two electrodes; anode, which is and aluminium (Al) foil and a cathode, which is a platinum wire mesh or a plate. For anodization, high purity Al foil (99.997 %, Goodfellow UK) is cut into circular discs of diameter

16 mm and sonicated in ethanol and water for 15 min individually. The clean Al discs are then packed into a custom made anodization holder (**Figure 2.1**), which offers a back copper contact for electrical connection and a front open window of diameter 12 mm for anodization.

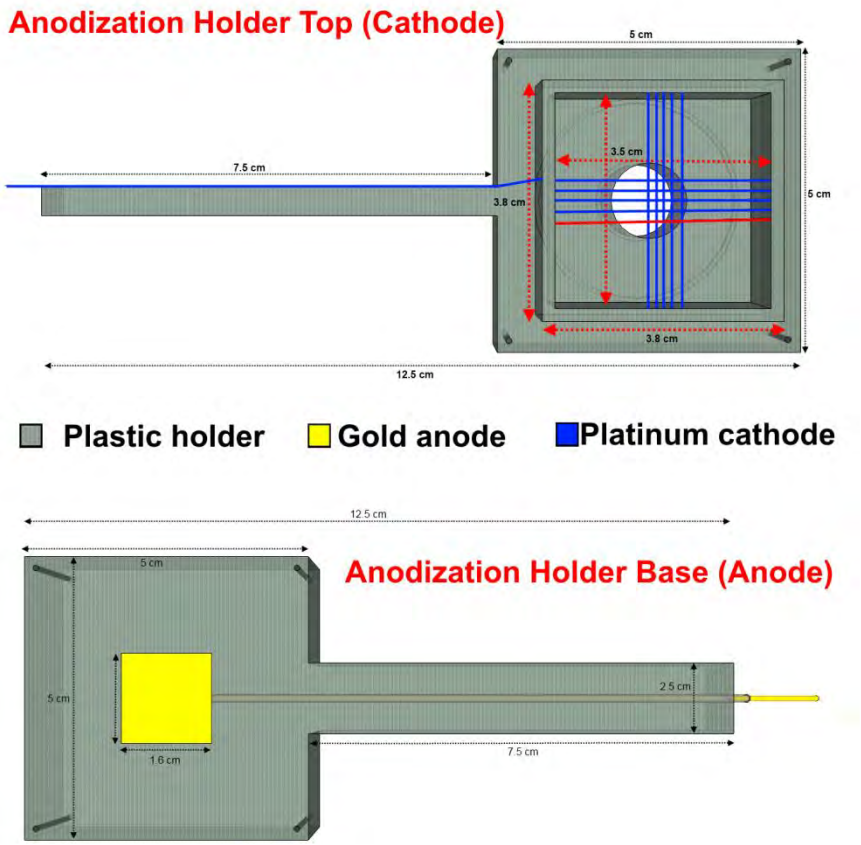

Figure 2.1. Top view of both the parts of anodization holder used for fabrication of NAA substrates (a) Anodization holder top (Cathode). (b) Anodization holder base (Anode).

Packing of Al discs is followed by their electropolishing in a mixture of ethanol and perchloric acid (4:1, *v*:*v*) at 20 V for 3 min. The electropolished Al discs are then subjected to a two-step electrochemical anodization process in aqueous acid electrolyte (mostly oxalic acid or sulphuric acid or phosphoric) solution using the setup described in **Figure 2.2**. The Al disc holder was made out of poly-acrylic polymer sheet by cutting and milling. The pore geometry of

NAA is highly dependent on the electrochemical anodization conditions (i.e. type of acid, purity of Al foil, anodization voltage, current, and temperature and so on), hence, it is necessary to design and optimize its geometry for particular application.

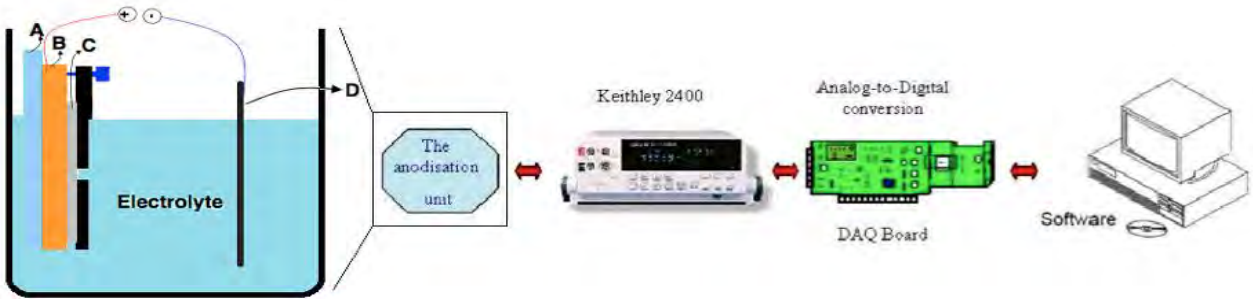

Figure 2.2. A schematic diagram of the electrochemical anodization setup including an anodization unit, a power supply, an analogue to digital converter card connecting the power supply to a computer. The anodization unit consists of the following parts; A, plastic holder with a window; B; back metal contact; C, Al foil; D, platinum counter electrode.

The electrolyte temperature during the anodization process is maintained in a double jacket beaker, which allows for flow of coolant liquid between the two layers for cooling the electrolyte (**Figure 2.3a**). The coolant liquid used here is a mixture of ethylene glycol and water (9:1, *v*:*v*), which is cooled and circulated using a fluid chiller and circulator (**Figure 2.3b**). The potential during the anodization was applied using and Agilent N5724 power supply, which is controlled by a custom made Labview program.

NAA samples with straight pore (used in **Chapter 3, 7, and 8**), prepared for this PhD study were anodized using aqueous oxalic acid electrolyte at potentiostatic mode under mild anodization conditions (described in **Chapter 1**). During the two-step anodization process, the first anodized layer (anodized at 40 V for 20 h and 6ºC) is selectively chemically etched to obtain Al substrate with a hexagonally organized pit like pattern. These hexagonally organized pits act as the nucleation site during second anodization step for growth of hexagonally organized pores. The length of NAA pores was controlled by anodization time depending upon the application [1-4].

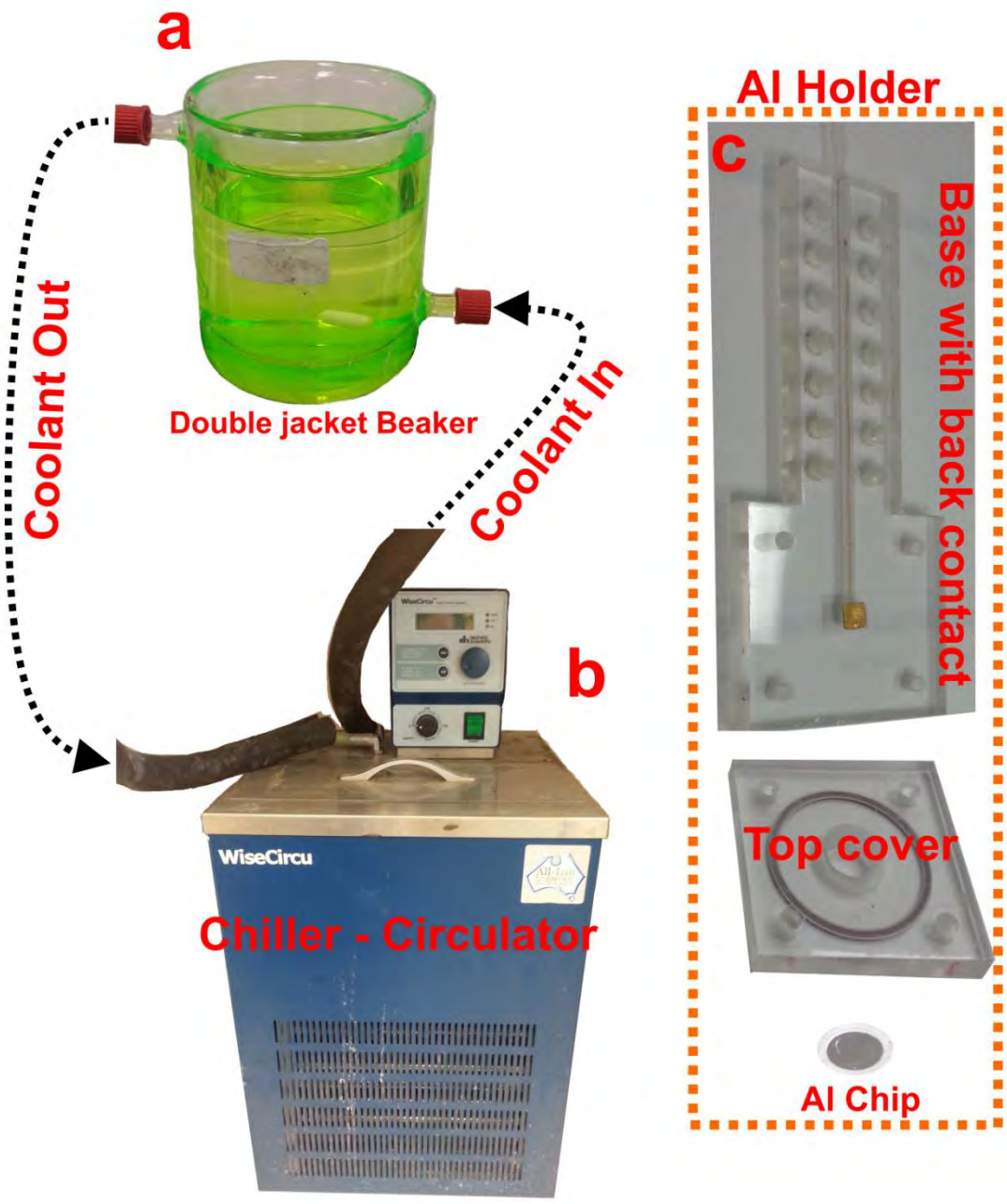

Figure 2.3. (a) Anodization beaker with double jacket which allows for maintain a constant electrolyte temperature. (b) Chiller circulator used for cooling and circulating the coolant around the anodization beaker. (c) Digital photograph of the anodization holder along with an Al chip.

NAA samples periodically modulated pores (i.e. NAA rugate filter photonic structures), were prepared using a novel anodization process. In this process, Al discs were cleaned and sonicated in ethanol and water, followed by electropolishing as for NAA with straight pores. The electropolished Al discs were then first anodized and subsequently subjected to removal of first

anodized layer selectively under same conditions as NAA with straight pores to obtain pre-patterned Al discs. The pre-patterned Al discs were subsequently anodized using psuedosinusoidal voltage profiles (described in details in **Chapter 4, 5, and 6**). This pseudo-sinusoidal anodization voltage profile provides periodic modulation of pore diameter along the thickness of NAA layer.

2.3. Functionalization of NAA with silanes using CVD process

Functionalization of NAA surface is one of the main step in fabrication of nanopore based optical sensors [4]. Functionalization provides NAA capabilities to specifically and selectively capture target molecule, which is monitored by the RIfS optical system. NAA samples were mainly functionalized with silanes (with amine and thiol terminal groups) using a chemical vapour deposition (CVD) process in a glass desiccator heated in a conventional oven. A digital photograph of the CVD setup is provided in **Figure 2.4**.

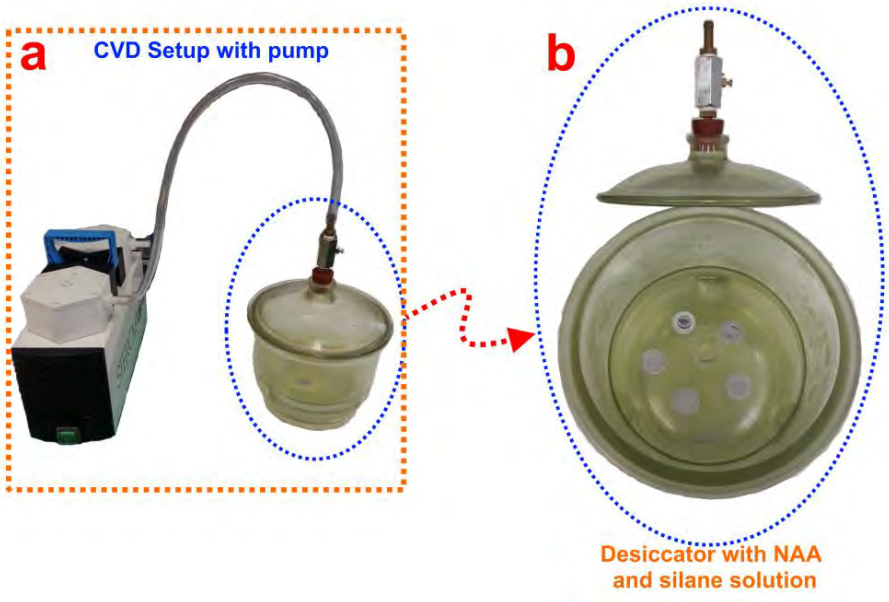

Figure 2.4. Digital photographs of (a) CVD setup used for silanization of NAA sensing substrates. (b) open desiccator showing configuration of NAA sensing substrates and silane solution.

2.4. Design and fabrication of bulk and microfluidic flow cells

Flow cells are an essential part of the optical sensing setup. Flow cells allow for real time monitoring attachment of analyte molecules to the capture probes immobilised on the NAA sensing substrate. Real-time monitoring presents several advantages over batch processing based sensing approach (i.e. signal only measured in the beginning and at the end of the analyte attachment process) such as ability to monitor the analyte-receptor binding process as it occurs, extensive data points for better understanding the binding kinetics and so on. The design of flow cell is highly critical for target sensing application. For example, bulk flow cell (i.e. large total analyte volume required) is more suitable for applications where analytes molecules are abundantly present in the sample solution and are not expensive. Therefore, bulk flow cells are more suitable for environmental and industrial sensing applications [5]. On the other hand, a microfluidic cell, requires low analyte molecule (in nano to micro litter range), are more suitable for application in which target analytes are scarce in the sample solution and are highly expensive (i.e. limited available amount). For these reasons, microfluidic flow cells are more suitable for detection of target analytes of biological origin as they are extremely complex to prepare and the synthesis process is highly time and cost intensive. Therefore, a bulk flow cell and a microfluidic cell were designed and fabricated to cover environmental, industrial as well as biomedical sensing applications, respectively.

The bulk flow cell designed and fabricated for thesis not only accommodates the NAA sensing substrate but also allows for real-time monitoring of sensing reaction in combination with RIfS. A schematic of the bulk flow cell is provided in **Figure 2.5a**. The bulk flow cell used in this thesis (**Chapter 3, 4, 5, 6, and 7**) consists of two parts, a support base and a top cover, which are clamped together by stainless screws. The support base sits under NAA sensing substrate preventing it from tilting or bending, whereas the top cover is drilled with inlet and

outlet ports for analyte transport over NAA sensing substrate. A viton® O-ring is used to seal the two parts together and create a working volume for flow analyte solution over NAA sensing substrate packed in the cell. The Bulk flow cell was constructed in poly-acrylic plastic (i.e. plexi glass) due to its low optical scattering and ease of process ability. A digital photograph of the bulk flow cell is provided in **Figure 2.5b**.

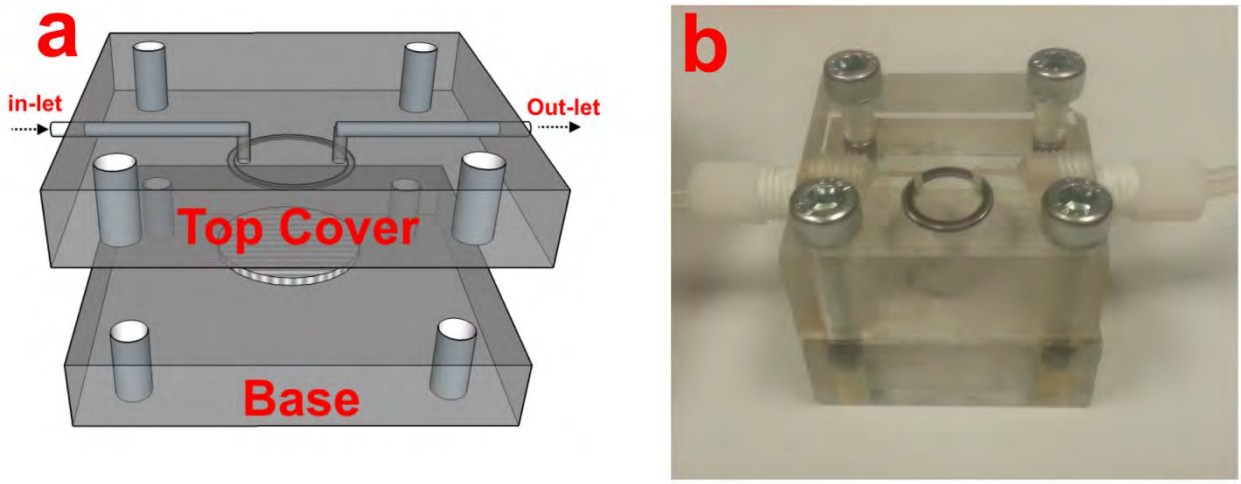

Figure 2.5. Design and scheme of the bulk flow cell used in this thesis presented as (a) A schematic. (b) A digital photograph (Used for studies presented in **Chapter 3, 4, 5, 6,** and **7**).

The microfluidic flow cell used in this thesis consists of two halves which can be sealed during use by a stainless steel clamp. This microfluidic flow cell is bondless type making it re-usable for multiple sensing experiments. Similar to the bulk flow cell the micro fluidic cell has a base and a top cover. The top cover for the microfluidic flow cell is made of borosilicate glass with 0.5 mm diameter holes drilled for inlet and outlet port. The base chip supports the micro channel (100 µm wide and 100 µm deep) that deliver the analyte fluid to a square cavity (1.6 x 1.6 mm^2 and 400 µm deep) which accommodates NAA sensing substrate (approximately 300 µm thick). This leaves a further 100 µm space between the NAA sensing substrate and borosilicate glass lid where analyte fluid could pass. Micropillar mixers present before the sensing substrate cavity ensure even delivery and distribution of fluid over the whole NAA sensing substrate [6-8]. A schematic of the base chip for the microfluidic cell is provided in **Figure**

2.6a. The microstructures were formed in solid poly-(methyl methacrylate) (PMMA) by the hot-embossing process using a brass stamp, machined by CNC micromachining (Supermill-2M, Kira), at 4.3 MPa at 130 °C using a hot embosser-substrate bonder (EVG, 520-HE). The stainless steel clamp was designed in such a way that it ensured complete sealing of the two halves and provided a window for focusing the RIfS optical probe onto NAA sensing substrate for optical measurements. A digital photograph of the completely packed microfluidic cell is provided in **Figure 2.6b**. The analytes were delivered to NAA sensing substrate using a syringe pump (Fusion Touch, Chemyx, UK) connected to flow cells by silicon tubing. The flow rates for different experiments were optimized and controlled accordingly.

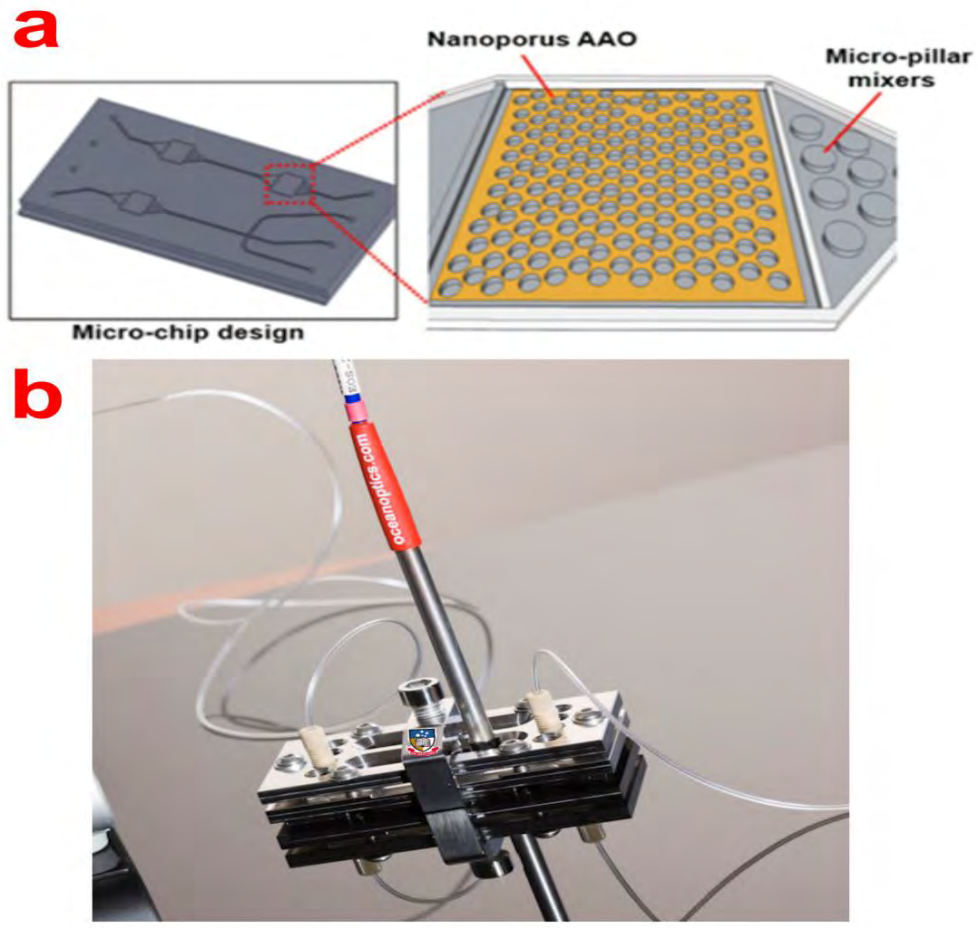

Figure 2.6. (a) Schematic showing the design of the microfluidic flow cell used in this thesis with a zoom on the cavity holding the NAA sensing substrate. (b) A digital photograph of the packed microfluidic cell fitted with the optical probe (Used for study presented in **Chapter 8**).

2.5. RIfS setup for optical sensing measurements

The RIfS optical setup used throughout this thesis consists of a halogen white light source (HL 1LL, Ocean Optics, USA) connected to one end of a bifurcated optical probe (R400-7 Vis-NIR, Ocean Optics, USA) that carries the light and focuses it on NAA sensing substrate. The reflected light is collected by the collection fibers in the same probe and is transferred to a miniature spectrometer (USB4000 VIS-NIR, Ocean Optics, USA) through the other bifurcated end. The white light is sharply focused on NAA sensing substrate illuminating a spot of 2 mm in diameter by a collimating lens connected at the end of the probe using a custom designed fitting (made from plastic). A digital photograph of the RIfS setup, which fits on an A4 sheet of paper, is shown in **Figure 2.7**. The optical reflection data from the miniature spectrometer is acquired by software package from Ocean Optics (SpectraSuit) in wavelength range 400 to 1000 nm. This software package allows to control the integration time, saving interval, and measurement averaging for optimal signal collection and post processing. The collected optical reflection spectrum for sensing experiments are processed in Igor Pro (Wavemetrics, USA) to calculate effective optical thickness, which used has been used as the sensing parameter in this thesis.

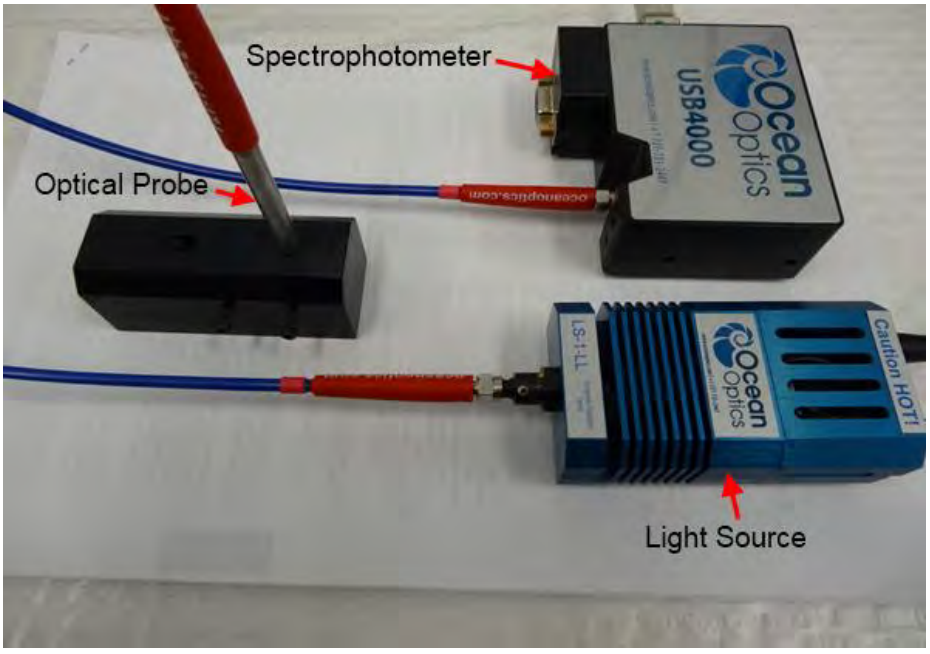

Figure 2.7. Photograph of the complete RIfS setup that is smaller than an A4 size sheet of paper .

Note that, the RIfS probe held vertically using a micro manipulator arm to focus light on NAA sensing substrate at a normal angle. The micromanipulator arm allows for precisely and accurately focusing the light onto desired area of NAA sensing substrate. Notice that, RIfS optical setup is highly susceptible to external vibrations that result in large noise in the RIfs signal. Therefore, the whole RIfS sensing setup was fixed on an anti-vibration table with optical bench to clamp various optical assemblies.

2.6. References

1. Masuda, H.; Hasegwa, F.; Ono, S., Self-Ordering of Cell Arrangement of Anodic Porous Alumina Formed in Sulfuric Acid Solution. *Journal of the electrochemical society* **1997,** *144* (5), L127-L130.

2. Masuda, H.; Fukuda, K., Ordered metal nanohole arrays made by a two-step replication of honeycomb structures of anodic alumina. *Science* **1995,** *268* (5216), 1466-1468.

3. Losic, D.; Velleman, L.; Kant, K.; Kumeria, T.; Gulati, K.; Shapter, J. G.; Beattie, D. A.; Simovic, S., Self-ordering electrochemistry: a simple approach for engineering nanopore and nanotube arrays for emerging applications, *Australian Journal of Chemistry* **2011**,64, 294-301

4. Jani, A. M. M.; Losic, D.; Voelcker, N. H., Nanoporous anodic aluminium oxide: Advances in surface engineering and emerging applications. *Progress in Materials Science* **2013,** *58* (5), 636-704.

5. Dancil, K.-P. S.; Greiner, D. P.; Sailor, M. J., A porous silicon optical biosensor: detection of reversible binding of IgG to a protein A-modified surface. *Journal of the American Chemical Society* **1999,** *121* (34), 7925-7930.

6. Kumeria, T.; Kurkuri, M. D.; Diener, K. R.; Parkinson, L.; Losic, D., Label-free reflectometric interference microchip biosensor based on nanoporous alumina for detection of circulating tumour cells. *Biosensors and Bioelectronics* **2012,** *35* (1), 167-173.

7. Kumeria, T.; Parkinson, L.; Losic, D., A nanoporous interferometric micro-sensor for biomedical detection of volatile sulphur compounds. *Nanoscale research letters* **2011,** *6* (1), 1-7.

8. Kumeria, T.; Losic, D., Reflective interferometric gas sensing using nanoporous anodic aluminium oxide (AAO). *physica status solidi (RRL)-Rapid Research Letters* **2011,** *5* (10-11), 406-408.

CHAPTER 3

ULTRASENSITIVE NANOPOROUS INTERFEROMETRIC SENSOR for LABEL-FREE DETECTION of GOLD (III) IONS

Tushar Kumeria

School of Chemical Engineering, The University of Adelaide South Australia 5005, Australia

This chapter is based on the following peer-reviewed article:

T. Kumeria, A. Santos, D. Losic "Ultrasensitive nanoporous interferometric sensors for label-free detection of gold (III) ions", *ACS Applied materials & interfaces*, 2013, **5**, 11783.

Statement of Authorship

Ultrasensitive nanoporous interferometric sensors for label-free detection of gold (III) ions. *ACS Applied materials & interfaces*, 2013, **5**, 11783.

Tushar Kumeria (Candidate)

Under supervision of D. Losic and A. Santos, I developed, designed, and performed the experiments, interpreted and processed the data and wrote the manuscript for submission.

Signed Date:10/04/2015

Abel Santos

I acted as secondary supervisor for the candidate and aided in development and design of the experiments and evaluation of manuscript for submission. I give consent for Tushar Kumeria to present this paper for examination towards the Doctorate of philosophy.

Signed Date: 10/04/2015

Dusan Losic

I acted as primary supervisor of the candidate and aided in evaluation of experimental design and manuscript for submission. I give consent for Tushar Kumeria to present this paper for examination towards the Doctorate of philosophy

Signed Date: 10/04/2015

ACS APPLIED MATERIALS & INTERFACES

Research Article

www.acsami.org

Ultrasensitive Nanoporous Interferometric Sensor for Label-Free Detection of Gold(III) Ions

Tushar Kumeria, Abel Santos, and Dusan Losic*

School of Chemical Engineering, The University of Adelaide, Adelaide, South Australia, 5005, Australia

Supporting Information

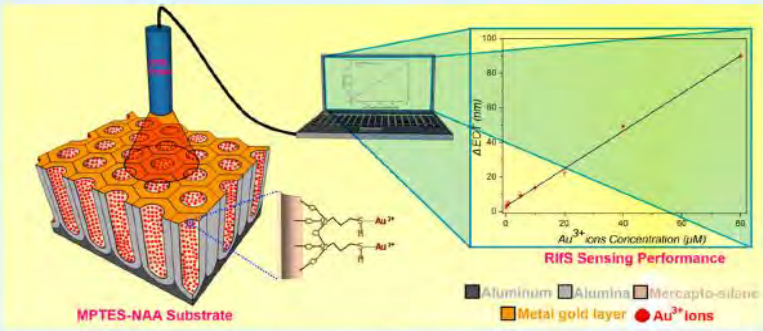

ABSTRACT: In this study, we present an ultrasensitive sensor based on nanoporous anodic alumina (NAA) for detection of gold(III) ions (Au^{3+} ions) using reflectometric interference spectroscopy (RIfS). Nanoporous anodic alumina, prepared by two-step electrochemical anodization, was functionalized with 3-mercaptopropyl-tirethoxysilane (MPTES) in order to selectively detect Au^{3+} ions. Thus prepared, MPTES-NAA sensors were exposed to different concentrations of Au^{3+} ions ranging from 0.1 to 750 μM and the changes in the effective optical thickness (ΔEOT) were monitored in real-time. The linear range of these Au^{3+} sensors was from 0.1 to 80 μM, with a lower detection limit of 0.1 μM of Au^{3+} ions. Furthermore, the specificity of these MPTES-NAA sensors was validated by sequential exposure to 40 μM solutions of Fe^{3+}, Mg^{2+}, Co^{2+}, Cu^{2+}, Ni^{2+}, Ag^{+}, and Pb^{2+}, resulting in negligible changes in EOT as compared to the same concentration of Au^{3+} ions. Detection of Au^{3+} ions in complex and environmentally and biologically relevant solvents such as tap water and phosphate buffer solution (PBS) was also successfully carried out in order to demonstrate the real-life application of these sensors. Finally, the binding isotherm for Au^{3+} ions and thiol (SH) group of MPTES-NAA system was determined by fitting the changes in EOT to Freundlich and Langmuir isotherm models.

KEYWORDS: *nanoporous anodic alumina, reflectometric interference, gold(III) ions, optical sensing, chemical functionalization*

1. INTRODUCTION

In the past decade, the use of gold and gold-based salts has grown very rapidly because of its unique properties (e.g., chemical activity, stability, ability to form functional nanoparticles, etc.). In particular, gold and its salts play key roles in mining, mineral processing, chemistry, medicine, electronics, and biology. For instance, gold is employed in chemistry for catalysis and synthesis of nanomaterials such as nanowires, nanotubes, nanorods, and nanomembranes.[1−4] Gold is a basic element used in many critical components of electronic devices as it fulfills all the electronic requirements better than any other metal (e.g., high corrosion resistance, thermal stability, electrical conductivity, etc.). It is worth stressing that these electronic devices expose these gold-based components to environmental conditions in two ways: either during processing/manufacturing or at the end of their life-cycle, when they are deposited in the dump yard. Under these conditions, gold can leach to soil and underground water by several ways.[5,6] Another important application of gold is in medicine where gold-based drugs are used to treat a broad variety of diseases, including asthma, malaria, cancer, HIV, arthritis, and brain lesions.[7−10] Moreover, gold nanoparticles obtained by reduction of gold ions are used for sensing, drug/gene delivery, and bioimaging.[11−14] Notice that metallic gold is proven to be highly biocompatible and considerably stable in biological conditions.[15,16] Nevertheless, some studies have demonstrated that metallic gold can be chemically oxidized to ionic states by strong oxidants, which are present in environmental and biological conditions.[17,18] These ionic gold species (i.e., Au^{+} and Au^{3+}) are highly reactive and potentially toxic to humans.[19] As for this, it is worth noting that gold salts such as gold chloride cause serious damage to liver, kidneys, and the peripheral nervous system.[20] Particularly, Au^{3+} ions, which are known to bind tightly to DNA and several enzymes leading to DNA cleavage, can degenerate into

Received: August 17, 2013
Accepted: October 14, 2013
Published: October 14, 2013

Scheme 1. Schematic Diagram of RIfS-NAA Sensing System for Detection of Gold Ions on Mercapto-Silane Modified Nanoporous Anodic Alumina[a]

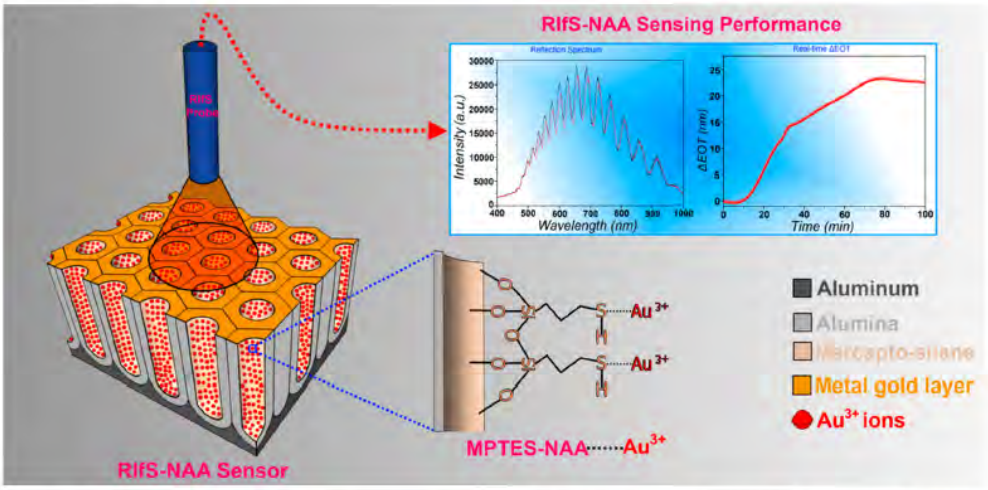

[a]An optical fiber probe shines light on the MPTES-NAA substrate surface to obtain reflective interference fringe pattern and real-time RIfS response curve for Au^{3+} ions detection.

disruption of nervous systems.[21,22] In addition, cytotoxicity of gold nanoparticles to human cells is also a debatable issue.[23]

Therefore, since the use of gold species, in ionic or nanoparticle form, is on the rise in medicine, mining, mineral processing, chemical, electronic, and catalysis industries, more efficient, accurate, sensitive, cost-competitive, and versatile detection systems must be implemented in order to address the toxic effects associated with different gold species present in environmental and biological samples (e.g., water or blood). Traditionally, heavy metals, including gold species, are detected by means of analytical techniques such as UV−visible and fluorescence spectroscopy, atomic absorption spectroscopy (AAS), atomic fluorescence microscopy (AFS), and inductively coupled plasma mass spectroscopy (ICP-MS).[24] Recently, surface plasmon resonance (SPR) and photoluminescence spectroscopy (PLS) have also been extensively applied in detection of gold species by means of several specific probes by taking advantage of alkynophilicity of gold.[21,22,26−30] Although these techniques provide highly sensitive analyses, they require complex and time-consuming sample preparation steps in addition to expensive and sophisticated instrumentation, skilled operators, large sample volume, destruction of sample, and inability to do real-time measurements.[25] Consequently, new sensing methods are required for overcoming the above-mentioned drawbacks and developing ultrasensitive and fast gold sensors for environmental and biological applications.

In this scenario, optical detection methods have emerged as an outstanding alternative as a result of their high sensitivity, low cost, real-time and point-of-care detection, and ease of miniaturization.[31,32] Thus, a label-free sensing platform for real-time detection of gold(III) ions is considered to be an attractive alternative to current sensing techniques used to detect gold ions. Among these optical techniques, reflectometric interference spectroscopy (RIfS) is a simple optical method of detection based on thin film interference of white light.

The principle of RIfS is the Fabry−Pérot interference phenomenon, which results in appearance of alternate fringe maxima and minima (i.e., fringes) in the reflection spectrum when white light is reflected from top and bottom interfaces of an air-thin film system.[33] Notice that these well-resolved fringes follow the Fabry−Pérot relationship (eq 1), from which the effective optical thickness (EOT) can be calculated.

$$\mathrm{EOT} = m\lambda = 2n_{\mathrm{eff}}L \quad (1)$$

where m is the fringe order in the RIfS spectrum, of which the maximum is located at the wavelength λ, n_{eff} is the effective refractive index of the film, and L its physical thickness. Therefore, any change in n_{eff} or L results in a variation in the fringe pattern (i.e., shift of fringes in the RIfS spectrum) and thus a change in the optical thickness, which forms the basis of RIfS sensing system.[31,33] Thus far, many studies have reported about the RIFs based detection of a broad range of analytes (e.g., proteins, antigens, environmental pollutants, tumor cells, organic compounds, etc.) by using thin polymer films or inorganic nanoporous films (e.g., porous silicon, nanoporous alumina, and nanotubular titania).[34−41] In particular, integration of RIfS with nanoporous substrates results in improvement of sensing characteristics as these nanopores act as containers for analytes, enhancing the optical signal from the analyte molecules immobilized onto these nanoporous films.[42−44] As for this, nanoporous anodic alumina (NAA) provides highly controllable and designable porous geometry, tunable surface chemistry, biocompatibility, chemical and thermal stability, easy and scalable fabrication process, and stable optical activity.[45] These properties make NAA as an emerging and outstanding substrate for RIfS sensing.[45] NAA-based RIfS sensing platforms have already been proven for highly sensitive and specific detection of proteins/antibodies, volatile organic/sulfur compounds (e.g., ethanol, acetone, hydrogen sulfide, etc.), nucleic acids (DNA), and circulating tumor cells.[31,38,40,43−46] However, to the best of our knowledge, so far no study has reported about the detection of gold ions using RIfS or any other sensing technique combined with NAA substrates.

Herein, we present a highly sensitive, selective, and label-free optical sensor for detection of gold(III) ions (Au^{3+} ions) on mercapto-silane modified NAA combined with RIfS. NAA

constants. Parameters $1/K_L\Delta EOT_m$ and $1/\Delta EOT_m$ can be obtained by the intercept and slope of a plot between $[Au^{3+}]/\Delta EOT_e$ and $[Au^{3+}]$, respectively.

As for the Freundlich isotherm, this is given by eq 3.

$$\log(\Delta EOT_m) = \log K_f + \frac{1}{n}\log[Au^{3+}] \quad (3)$$

where ΔEOT_e is the change in EOT at equilibrium, $[Au^{3+}]$ is the concentration of Au^{3+} ions, and K_f and n are characteristic constants. Values of log K_f and $1/n$ can be determined, respectively, by the intercept and slope of a plot between $\log(\Delta EOT_e)$ and $\log[Au^{3+}]$. Mathematical derivation for all the above equations is provided in the Supporting Information.

3. RESULTS AND DISCUSSION

3.1. Structural Characterization and Chemical Analysis of NAA. As reported previously, the structural characteristics of NAA are critical to its reflective interference properties and sensing performance.[39] Scanning electron microscopy (SEM) imaging was performed to confirm that desired nanoporous layer was obtained. Figure 1 shows typical SEM images of NAA structure prepared by the two-step electrochemical anodization process. Figure 1a presents a SEM image of top surface of NAA, which clearly shows hexagonally organized pores with diameters of 35 ± 5 nm with an inset digital photograph of an NAA sensor. SEM characterization performed after MPTES modifications inside nanopores and gold deposition on the top NAA surface did not show any change in the pore geometry (Figure S1, Supporting Information). The cross-sectional SEM image of NAA provided in Figure 1b reveals perfectly straight and vertically aligned cylindrical pores, which are closed at the bottom side by an oxide barrier layer. The pore length in the resulting NAA samples was 4.5 ± 0.2 μm, which is an optimal length for RIfS in accordance with our previous work.[39]

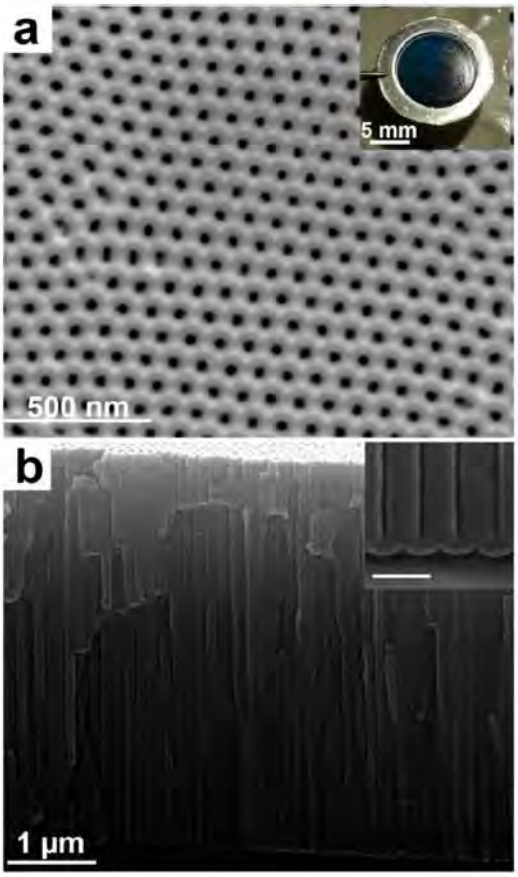

Figure 1. SEM images of typical NAA substrates used for RIfS Au^{3+} ions sensing. (a) Top view showing hexagonally arranged pores with inset digital photograph of MPTES-NAA sensor. (b) Cross-sectional view of the same NAA sample with straight cylindrical pores with inset image showing closed pores at the bottom by an oxide barrier layer (scale bar = 100 nm).

These NAA samples were modified with MPTES to obtain thiol functional groups on the alumina surface for specific detection of gold(III) ions. FTIR spectroscopy data shown in Figure 2 prove the silanization of NAA. Whereas FTIR peaks at

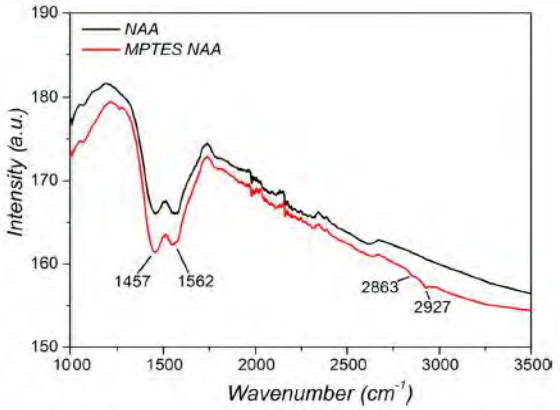

Figure 2. FTIR spectra of as-produced NAA and MPTES modified NAA.

1460 and 1570 cm^{-1} are associated with nanoporous anodic alumina, the appearance of additional peaks at 2929 and 2869 cm^{-1} corresponds to asymmetric and symmetric vibrations of methylene ($-CH_2-$) group of propyl chain, respectively. This confirms the presence of thiol terminal groups of MPTES molecules on the NAA surface.[49,50] Furthermore, SEM images obtained after MPTES surface functionalization and ultrathin gold coating show that the NAA samples maintain their porous structure (Figure S1, Supporting Information).

3.2. Detection of Au^{3+} Ions on MPTES-Modified NAA. NAA modified with MPTES was used as a sensing substrate for detection of Au^{3+} ions. Figure 3a shows a typical example of interference pattern obtained by shining white light on MPTES-NAA surface. This figure also shows the red-shift of the interference fringe pattern on exposure of MPTES-NAA sensor chip to Au^{3+} ions ($[Au^{3+}] = 40$ μM). To resolve this red-shift in interference pattern, FFT was applied and EOT calculated. This parameter (EOT) was used as the sensing parameter for detection of Au^{3+} ions. Figure 3b presents a real-time monitoring plot of ΔEOT by RIfS using a MPTES-NAA sensor for detection of 20 μM Au^{3+} ions solution in ultrapure water. Notice that, as was mentioned previously, a stable ΔEOT baseline was first obtained with ultrapure water for 10 min followed by injection of the analyte solutions. When this MPTES-NAA sample was exposed to the analyte solution, a rapid and sharp increase was observed initially, which slowed down progressively to achieve a stable value of 24 nm in

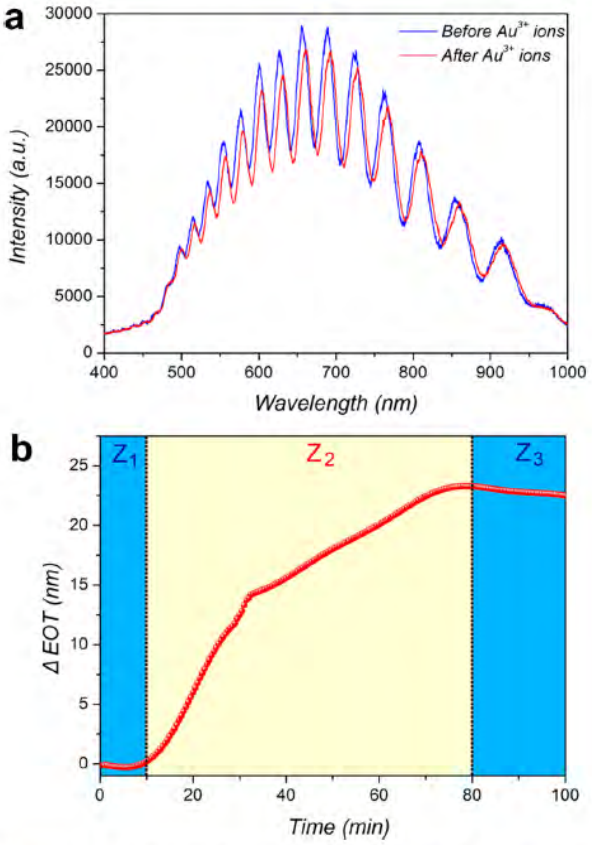

Figure 3. Detection performance of Au^{3+} ions by RIfS using the proposed MPTES-NAA sensor. (a) Optical interference spectrum of MPTES-NAA sensor before and after exposure to gold(III) ions. (b) Real-time detection curve of 20 μM Au^{3+} ions solution in ultrapure water consisting of three zones: (Z_1) ultrapure water for baseline; (Z_2) 20 μM aqueous solution of Au^{3+} ions; and (Z_3) rinse with ultrapure water.

ΔEOT. This confirmed the attachment of Au^{3+} ions to thiol terminals of MPTES molecules present on the surface inside NAA pores. It is worthwhile mentioning that after achieving the equilibrium ΔEOT value, on rinsing the MPTES-NAA sensor with ultrapure water, the observed ΔEOT value decreased slightly to 22 nm and remained stable throughout. This slight decrease and formation of another baseline at 22 nm in ΔEOT is associated with the removal of nonspecifically bound Au^{3+} ions. Similar trend in ΔEOT was observed in all the concentrations above 5 μM, while lower concentrations showed a more linear trend with time. Therefore, the total increase in ΔEOT is a result of an increase in the effective refractive index of the effective medium (i.e., MPTES-NAA sensor) related to the stable attachment of Au^{3+} ions on the inner surface of NAA pores. Notice that the average response time of the proposed RIfS-based gold(III) ions sensor to reach 90% (t_{90}) of the stable ΔEOT value was 40 $\pm$ 8 min for all the measured Au^{3+} ion concentrations (0.1−750 μM), which is either comparable or better than the response times of fluorescence and SPR-based metal ion detection systems. Furthermore, we also observed that the time required for ΔEOT to reach the equilibrium value increased by decreasing the concentration of Au^{3+} ions in analyte solutions.

The sensor performance as a function of the analyte concentration is shown in Figure 4a. This calibration curve

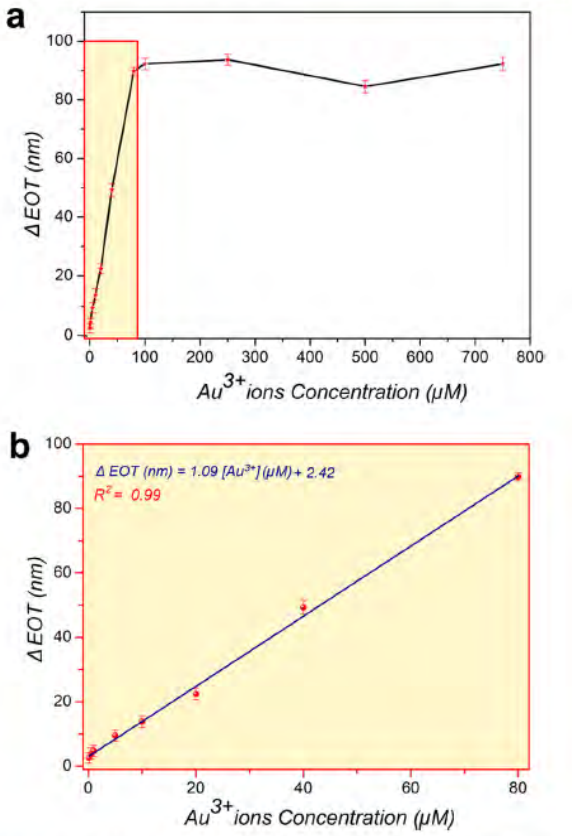

Figure 4. (a) ΔEOT as a function of the concentration of Au^{3+} ions on MPTES-NAA sensors throughout the complete concentration range of 0.1−750 μM. (b) Magnified view of red rectangle (yellow background) shown in (a), which corresponds to the calibration curve for the linear range of Au^{3+} ions detection.

obtained from RIfS measurements correlates the effective optical thickness change and the concentration of gold(III) ions in the analyte solution. Twelve different concentrations in a broad range of 4 orders of magnitude (i.e., 0.1−750 μM) of Au^{3+} ions were analyzed in order to characterize linear and saturation range of the proposed MPTES-NAA sensing device. Figure 4a clearly shows that ΔEOT value tends to saturate at concentrations above 80 μM. This suggests saturation of all possible binding sites (i.e., thiol terminal groups) for Au^{3+} ions on the MPTES-NAA substrate. A linear relationship between ΔEOT and Au^{3+} ions concentration was observed within the concentration range of 0.1−80 μM (i.e., 0.019−15.736 ppm (ppm = parts per million)), which is presented in Figure 4a (red rectangle). A linear regression fit of the linear range is presented in Figure 4b along with the resulting fitting equation. This calibration curve can be used to quantify the concentration of Au^{3+} ions in an aqueous solution from the effective optical thickness change provided by the proposed sensing platform. Notice that this result demonstrates that qualitative analyses to determine the presence/absence of gold(III) ions in the sample are possible within the studied concentration range (i.e., 0.1−750 μM) using the proposed MPTES-NAA sensor. However,

quantitative detection of gold(III) ions can only be performed in the concentration range 0.1 to 80 μM. The dynamic linear range of the proposed sensor is very broad (i.e., 0.1−80 μM: three orders of magnitude in concentration) which is better than that of most gold(III) ion sensors reported previously.[26−29] Furthermore, a linear relation between Au^{3+} concentration and change in EOT can be obtained 25 min after starting the Au^{3+} ion measurement, showing a reasonable analytical performance for a concentration range of 0.1−80 μM of gold(III) ions (Figure S2, Supporting Information).

It is worth noting that this MPTES-NAA-based RIfS detection system was able to detect 0.1 μM of Au^{3+} ions in aqueous solution, with a limit of detection (LOD) lower than 0.1 μM. Hence, the LOD of the proposed RIfS sensing system is lower than that of most of the previously reported fluorescence-based systems for quantifying Au^{3+} ions.[26−29] This detection limit depends on several parameters and can be improved by several ways: by increasing the density of binding SH groups on the pore surface by surface functionalization using organic compounds consisting multiple mercapto groups (i.e., −SH) or by further optimization of the pore structure by increasing the active surface area and enhancing the optical signal and by structural engineering of NAA sensor chip. Mercapto-silane functionality was specifically chosen because the thiol functional group is known to bind selectively and specifically to certain metal ions, including Au^{3+} ions. A control experiment was carried out in order to confirm the selective binding of Au^{3+} ions through thiol groups on MPTES-NAA. To this end, an unmodified NAA substrate (i.e., without mercapto-silane) was consecutively exposed to 20, 40, and 80 μM aqueous solutions of gold(III) ions (Figure S3, Supporting Information). A change in EOT of approximately 5.78, 6.45, and 6.71 nm was observed for 20, 40, and 80 μM aqueous solutions of Au^{3+} ions, respectively. Notice that, when exposed to 20 μM, 5.78 nm change in EOT was observed, while subsequent subjection to 40 and 80 μM only resulted in 6.45 and 6.71 nm of change in EOT, respectively. This could be explained by nonspecific and fast adsorption of Au^{3+} ions onto inherently negatively charged NAA.

3.3. Selectivity of MPTES-NAA toward Au^{3+} Ions. Selectivity of the proposed MPTES-NAA system was analyzed by two sets of experiments. First, a selectivity test was carried out by exposing a MPTES-NAA sensor to 40 μM aqueous solutions of Fe^{3+}, Mg^{2+}, Co^{2+}, Cu^{2+}, Ni^{2+}, Ag^{+}, and Pb^{2+} ions in a succession followed by 20 μM Au^{3+} ions. These interfering metal ions are selected as common ions in natural water solutions and ions that have low (Fe, Mg) and high (Ag) affinity toward mercapto groups. Figure 5 shows a bar graph plot of ΔEOT for the aforementioned aqueous ionic solutions. The highest nonspecific change in EOT was observed for Ag^{+} and Pb^{2+} analytes (~5.67 and 5.63 nm, respectively) followed by Mg^{2+}, Ni^{2+}, Co^{2+}, Fe^{3+}, and Cu^{2+}. However, when the same sample was exposed to a 20 μM aqueous solution of Au^{3+} ions, a significant change in EOT of more than 20 nm was observed. This result proves that the MPTES-NAA sensor is highly selective toward gold(III) ions.

The second selectivity test was carried out by exposing the MPTES modified NAA sensor to a 1:1 mixture of Pb^{2+} and Ag^{+} (i.e., mix-1), Au^{3+} and Pb^{2+} (i.e., mix-2), and Au^{3+} and Ag^{+} (i.e., mix-3) (Figure 5). Exposure of the MPTES-NAA sensor to mix-1 resulted in a practically negligible RIfS response (i.e., EOT change) of approximately 5.47 nm, while mix-2 and mix-3 resulted in approximately 21.23 and 22.41 nm, respectively.

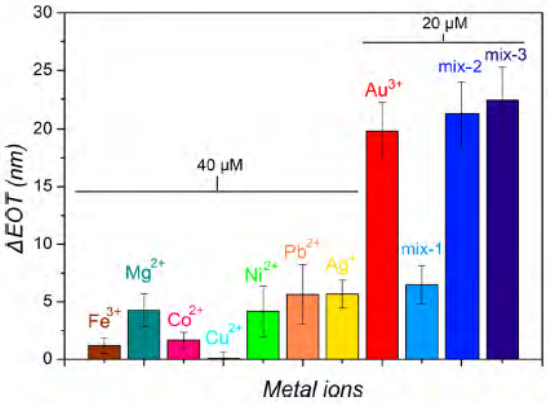

Figure 5. Bar graph chart showing the effective optical thickness change of the proposed RIfS sensing system based on MPTES modified NAA sensor after exposure to several aqueous metal ion solutions, the concentration of which was 2 times (40 μM) higher than that for Au^{3+} ions, which was 20 μM, and different binary mixtures (i.e., mix-1: Pb^{2+} and Ag^{+}, mix-2: Au^{3+} and Pb^{2+}, and mix-3: Au^{3+} and Ag^{+}) having a 20 μM final concentration of each metal ion in each mix.

These results again demonstrate the capability of the proposed RIfS system based on NAA functionalized with specific ligands, which has an outstanding performance for label-free and highly selective detection of gold(III) ions even in solutions composed of multiple metal ions. These results motivated us for detecting gold(III) ions in complex solvents as tap water and phosphate buffer solution in order to explore its practical applications.

3.4. Detection of Au^{3+} Ions in Environmental and Biological Scenarios. To analyze the performance of the proposed optical RIfS sensor in a real-life application, a 40 μM solution of gold(III) ions was prepared in tap water and phosphate buffer solution. The 40 μM solution of gold(III) ions prepared in ultrapure water was used as a control. As for RIfS measurements for an environmental sample as tap water, first, a baseline was obtained with tap water followed by injection of gold(III) ions solution prepared in tap water. Similarly, for detection of gold(III) ions in a biological environment, a baseline with PBS was first obtained for 10 min and then a 40 μM solution of gold(III) ions in PBS was flowed. RIfS response for gold(III) ions in tap water and PBS was found to be approximately 42.85 and 44.83 nm, respectively. This response is slightly lower in comparison to 49.28 nm for the same concentration of gold(III) ions in ultrapure water (Figure 6). This lower response and higher standard error can be associated with the number of nonspecific adsorption of other ionic species present in these complex solutions (i.e., tap water and PBS) and reduced actual concentration of Au^{3+} ions due to their interaction with impurities and compounds present in these complex solvents, which reduce their binding affinity toward thiol group. In addition, a real-time RIfS response curve for 40 μM Au^{3+} ions in ultrapure water and tap water is provided in Figure S4 (Supporting Information), showing that the latter presented a more noisy signal compared to the former. This can be ascribed to the presence of various metallic, ionic, molecular, and organic impurities present in tap water. Therefore, the proposed MPTES-NAA sensor proved its capability for label-free detection of gold(III) ions in real-life samples.

3.5. Binding Isotherms for Au^{3+} Binding to Thiol Groups of MPTES-NAA. Langmuir and Freundlich binding

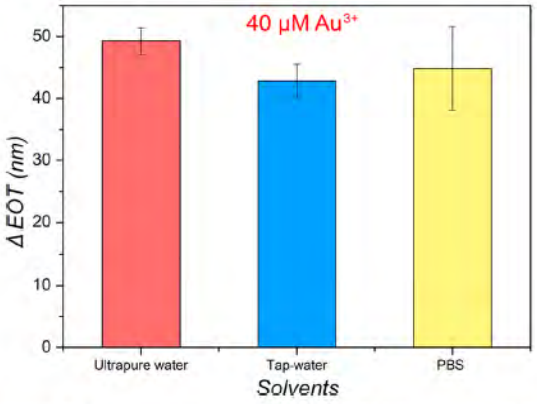

Figure 6. RIfS response on exposing a MPTES-NAA sensor to 40 μM Au^{3+} ions solution prepared in ultrapure water, tap water, and PBS.

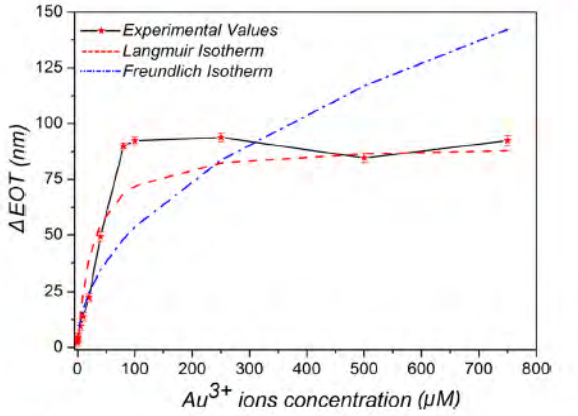

Figure 7. Langmuir and Freundlich binding isotherm fittings and experimental values for binding of Au^{3+} ions to thiol groups on MPTES modified NAA surface.

isotherm models were used to describe the binding mechanism of Au^{3+} ions onto thiol groups present on the MPTES-modified surface of NAA. These data were fitted to the aforementioned eqs 2 and 3 (Experimental Section) to discern which of these binding isotherms explains the binding mechanism of gold(III) ions in the proposed optical sensors. On the one hand, the Langmuir isotherm is more suitable for flat surfaces and it considers the number of binding sites to be constant throughout the reaction. On the other hand, the Freundlich isotherm is a more suitable model for binding on rough surfaces and it assumes that the binding sites increase with the concentration of analyte molecules (i.e., $[Au^{3+}]$). The calculated constant values for both isotherm models and their corresponding correlation factors are given in Table 1. These

Table 1. Characteristic Constants and Correlation Coefficients for Langmuir and Freundlich Binding Isotherms for Detection of Gold(III) Ions in the Proposed Optical Biosensors

Langmuir isotherm			Freundlich isotherm		
ΔEOT_m (nm)	K_L (μM^{-1})	R^2	n	K_f	R^2
94.34	3.70×10^{-2}	0.99	2.05	5.75	0.93

results denote that the binding mechanism of gold(III) ions to the thiol groups present on the sensor surface follows a Langmuir isotherm model, which has a better fitting than Freundlich isotherm, according to the R^2 values.

Figure 7 presents a graphic of the obtained Langmuir and Freundlich isotherms along with the experimental data, which were observed to fit better to a Langmuir isotherm model with a fitting efficiency of 93% in comparison to 61% of a Freundlich isotherm model. This suggests that the attachment of Au^{3+} ions is similar to monolayer sorption, which was expected as the number of binding sites in the sensing platform remains constant throughout and the inner surface of pores in NAA is flat and fairly smooth.

Therefore, the above-mentioned results have demonstrated the application of MPTES-NAA chips for capturing and label-free detection of gold(III) ions with a broad linear range and a low limit of detection in ultrapure water and complex solvent systems such as tap water and PBS.

4. CONCLUSIONS

In summary, we have demonstrated the capability of reflective interference spectroscopy combined with nanoporous anodic alumina substrates modified with mercaptro-silane to carry out label-free detection of gold(III) ions. Gold(III) ion solutions with a broad range of concentrations (i.e., 0.1−750 μM) were detected on these optical sensors. The linear detection range of the proposed system was measured to be 0.1−80 μM with a lower limit of detection of 0.1 μM. Highly selective detection of gold(III) ions was achieved through thiol functionalities on MPTES-NAA, which showed negligible RIfS response on exposure to aqueous solutions of Fe^{3+}, Mg^{2+}, Co^{2+}, Cu^{2+}, Ni^{2+}, Ag^{+}, and Pb^{2+} ions (at 40 μM concentration). Furthermore, the RIfS-MPTES-NAA sensing system was capable of selectively detecting gold(III) ions in binary mixtures of different metal ions (i.e., 1:1, 40 μM/40 μM, Pb^{2+} and Ag^{+}, Au^{3+} and Pb^{2+}, and Au^{3+} and Ag^{+}). The real-life application of this RIfS-based sensing platform for detection of gold(III) ions was proven by successful detection of 40 μM Au^{3+} ions in tap water and PBS. At last, the fitting results for binding isotherms reveal that the binding mechanism of gold(III) ions to thiol terminals inside the NAA pores follows a Langmuir isotherm model. In this study, gold(III) ions have been used as a model ion but the proposed RIfS sensing system based on NAA can be considered as a generic concept as it can be modified at will by changing the surface chemistry (i.e., chemical ligand) on the surface inside the NAA pores. Therefore, the proposed sensors can be used to selectively detect any other metal ion, including heavy and toxic metal ones, which are of high interest for environmental control and biomedical applications.

■ ASSOCIATED CONTENT

Supporting Information

Further details about SEM images of NAA after MPTES-silanization, real-time response curves for concentrations in linear detection range and calibration curve for fast measurements, control experiment with unmodified NAA, and Langmuir and Freundlich binding isotherm models. This material is available free of charge via the Internet at http://pubs.acs.org.

AUTHOR INFORMATION

Corresponding Author

*E-mail: dusan.losic@adelaide.edu.au.

Author Contributions

The manuscript was written through contributions of all authors. All authors have given approval to the final version of the manuscript.

Notes

The authors declare no competing financial interest.

ACKNOWLEDGMENTS

Authors acknowledge the financial support provided by the Australian Research Council (DP 120101680, FT 110100711) and the School of Chemical Engineering – The University of Adelaide. We are also thankful to Prof. M. J. Sailor (UCSD) for providing FFT analysis software. We thank the workshop staff from the School of Chemical Engineering, particularly Mr. Jason Peak, Mr. Michael Jung, and Mr. Jeffrey Hiorns, for assistance with the fabrication of the flow cell for RIfS.

REFERENCES

(1) Rosi, N. L.; Mirkin, C. A. *Chem. Rev.* 2005, *105*, 1547−1562.
(2) Wang, Z.; Ma, L. *Coord. Chem. Rev.* 2009, *253*, 1607−1618.
(3) Li, Z.; Brouwer, C.; He, C. *Chem. Rev.* 2008, *108*, 3239−3265.
(4) Gorin, D. J.; Toste, F. D. *Nature* 2007, *446*, 395−403.
(5) Ishikawa, S.; Suyama, K.; Arihara, K.; Itoh, M. *Bioresour. Technol.* 2002, *81*, 201−206.
(6) Ngah, W. S. W.; Liang, K. H. *Ind. Eng. Chem. Res.* 1999, *38*, 1411−1414.
(7) Ott, I. *Coord. Chem. Rev.* 2009, *253*, 1670−1681.
(8) Mohamed, A. A.; Chen, J.; Bruce, A. E.; Bruce, M. R.; Krause Bauer, J. A.; Hill, D. T. *Inorg. Chem.* 2003, *42*, 2203−2205.
(9) Shaw, C. F. *Chem. Rev.* 1999, *99*, 2589−2600.
(10) Messori, L.; Marcon, G. *Met. Ions Biol. Syst.* 2004, *41*, 279−304.
(11) Sardar, R.; Funston, A. M.; Mulvaney, P.; Murray, R. W. *Langmuir* 2009, *25*, 13840−13851.
(12) Murphy, C. J.; Gole, A. M.; Stone, J. W.; Sisco, P. N.; Alkilany, A. M.; Goldsmith, E. C.; Baxter, S. C. *Acc. Chem. Res.* 2008, *41*, 1721−1730.
(13) Tsoutsi, D.; Guerrini, L.; Hermida-Ramon, H. M.; Giannini, V.; Liz-Marzán, L. M.; Wei, A.; Alvarez-Puebla, R. A. *Nanoscale* 2013, *5*, 5841−5846.
(14) Gómez-Graña, S.; Pérez-Juste, J.; Alvarez-Puebla, R. A.; Guerrero-Martínez, A.; Liz-Marzán, L. M. *Adv. Opt. Mater.* 2013, *7*, 477−481.
(15) Goodman, C. M.; McCusker, C. D.; Yilmaz, T.; Rotello, V. M. *Bioconjugate Chem.* 2004, *15*, 897−900.
(16) Nyarko, E.; Hara, T.; Grab, D. J.; Habib, A.; Kim, Y.; Nikolskaia, O.; Fukuma, T.; Tabata, M. *Chem.-Biol. Interact.* 2004, *148*, 19−25.
(17) Goebel, C.; Kubicka-Muranyi, M.; Tonn, T.; Gonzalez, J.; Gleichmann, E. *Arch. Toxicol.* 1995, *69*, 450−459.
(18) Parkinson, J.; Sadler, P. *Chem. Commun.* 1999, 1359−1360.
(19) Habib, A.; Tabata, M. J. *Inorg. Biochem.* 2004, *98*, 1696−1702.
(20) Park, J.; Choi, S.; Kim, T.-I.; Kim, Y. *Analyst* 2012, *137*, 4411−4414.
(21) Kundu, A.; Layek, R. K.; Kuila, A.; Nandi, A. K. *ACS Appl. Mater. Interfaces* 2012, *4*, 5576−5582.
(22) Yang, Y.; Yin, C.; Huo, F.; Chao, J. *RSC Adv.* 2013, *3*, 9637−9640.
(23) Connor, E. E.; Mwamuka, J.; Gole, A.; Murphy, C. J.; Wyatt, M. D. *Small* 2005, *1*, 325−327.
(24) Butler, O. T.; Cook, J. M.; Harrington, C. F.; Hill, S. J.; Rieuwerts, J.; Miles, D. L. *J. Anal. At. Spectrom.* 2007, *22*, 187−221.
(25) Hung, Y.-L.; Hsiung, T.-M.; Chen, Y.-Y.; Huang, Y.-F.; Huang, C.-C. *J. Phys. Chem. C* 2010, *114*, 16329−16334.
(26) Egorova, O. A.; Seo, H.; Chatterjee, A.; Ahn, K. H. *Org. Lett.* 2009, *12*, 401−403.
(27) Do, J. H.; Kim, H. N.; Yoon, J.; Kim, J. S.; Kim, H.-J. *Org. Lett.* 2010, *12*, 932−934.
(28) Dong, M.; Wang, Y.-W.; Peng, Y. *Org. Lett.* 2010, *12*, 5310−5313.
(29) Zhang, J. F.; Zhou, Y.; Yoon, J.; Kim, J. S. *Chem. Soc. Rev.* 2011, *40*, 3416−3429.
(30) Yang, Y.-K.; Lee, S.; Tae, J. *Org. Lett.* 2009, *11*, 5610−5613.
(31) Kumeria, T.; Kurkuri, M. D.; Diener, K. R.; Parkinson, L.; Losic, D. *Biosens. Bioelectron.* 2012, *35*, 167−173.
(32) Gauglitz, G. *Anal. Bioanal. Chem.* 2005, *381*, 141−155.
(33) Gauglitz, G.; Brecht, A.; Kraus, G.; Mahm, W. *Sens. Actuators, B* 1993, *11*, 21−27.
(34) Lin, V. S.-Y.; Motesharei, K.; Dancil, K.-P. S.; Sailor, M. J.; Ghadiri, M. R. *Science* 1997, *278*, 840−843.
(35) Dancil, K.-P. S.; Greiner, D. P.; Sailor, M. J. *J. Am. Chem. Soc.* 1999, *121*, 7925−7930.
(36) Janshoff, A.; Dancil, K.-P. S.; Steinem, C.; Greiner, D. P.; Lin, V. S.-Y.; Gurtner, C.; Motesharei, K.; Sailor, M. J.; Ghadiri, M. R. *J. Am. Chem. Soc.* 1998, *120*, 12108−12116.
(37) Gauglitz, G. *Anal. Bioanal. Chem.* 2010, *398*, 2363−2372.
(38) Kumeria, T.; Losic, D. *Phys. Status Solidi RRL* 2011, *5*, 406−408.
(39) Kumeria, T.; Losic, D. *Nanoscale Res. Lett.* 2012, *7*, 1−10.
(40) Kumeria, T.; Parkinson, L.; Losic, D. *Nanoscale Res. Lett.* 2011, *6*, 1−7.
(41) Losic, D.; Velleman, L.; Kant, K.; Kumeria, T.; Gulati, K.; Shapter, J. G.; Beattie, D. A.; Simovic, S. *Aust. J. Chem.* 2011, *64*, 294−301.
(42) Schwartz, M. P.; Alvarez, S. D.; Sailor, M. *J. Anal. Chem.* 2007, *79*, 327−334.
(43) Kumeria, T.; Gulati, K.; Santos, A.; Losic, D. *ACS Appl. Mater. Interfaces* 2013, *5*, 5436−5442.
(44) Santos, A.; Kumeria, T.; Losic, D. *Anal. Chem.* 2013, *85*, 7904−7911.
(45) Santos, A.; Kumeria, T.; Losic, D. *Trends Anal. Chem.* 2013, *44*, 25−38.
(46) Pan, S.; Rothberg, L. J. *Nano Lett.* 2003, *3*, 811−814.
(47) Masuda, H.; Fukuda, K. *Science* 1995, *268*, 1466−1468.
(48) Zhang, F.; Sautter, K.; Larsen, A. M.; Findley, D. A.; Davis, R. C.; Samha, H.; Linford, M. R. *Langmuir* 2010, *26*, 14648−14654.
(49) Shiraki, H.; Kimura, Y.; Ishii, H.; Ono, S.; Itaya, K.; Niwano, M. *Appl. Surf. Sci.* 2004, *237*, 369−373.
(50) Wang, J.; Yang, S.; Liu, X.; Ren, S.; Guan, F.; Chen, M. *Appl. Surf. Sci.* 2004, *221*, 272−280.

SCHOOL OF CHEMICAL ENGINEERING

THE UNIVERSITY of ADELAIDE

Supporting Information

Ultrasensitive Nanoporous Interferometric Sensor for Label-free Detection of Gold (III) Ions

*Tushar Kumeria, Abel Santos, Dusan Losic**

School of Chemical Engineering, The University of Adelaide, SA 5005, Australia

Losic Group

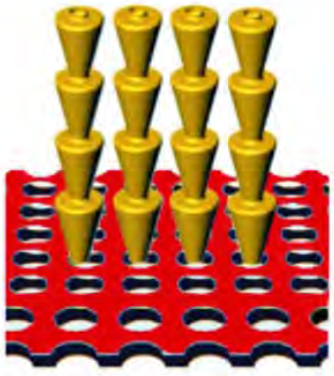

NanoTech Research

Ultrasensitive Nanoporous Interferometric Sensor for Label-free Detection of Gold (III) Ions

1) SEM images of NAA after mercapto-silane modification and ultra-thin gold layer deposition

Scanning electron microscopy was used to investigate the changes in structure of nanoporous anodic alumina (NAA) after surface modification with 3-mercaptopropyl-triethoxysilane (MPTES) followed by coating of an ultra-thin layer (4-5 nm) of gold metal. **Figure S1** shows a SEM image of the top surface of NAA after MPTES modification and metal gold deposition. No change in pore geometry and structure of NAA was observed, confirming that our samples were suitable for detection of Au^{3+} ions inside the pores of MPTES-NAA substrate.

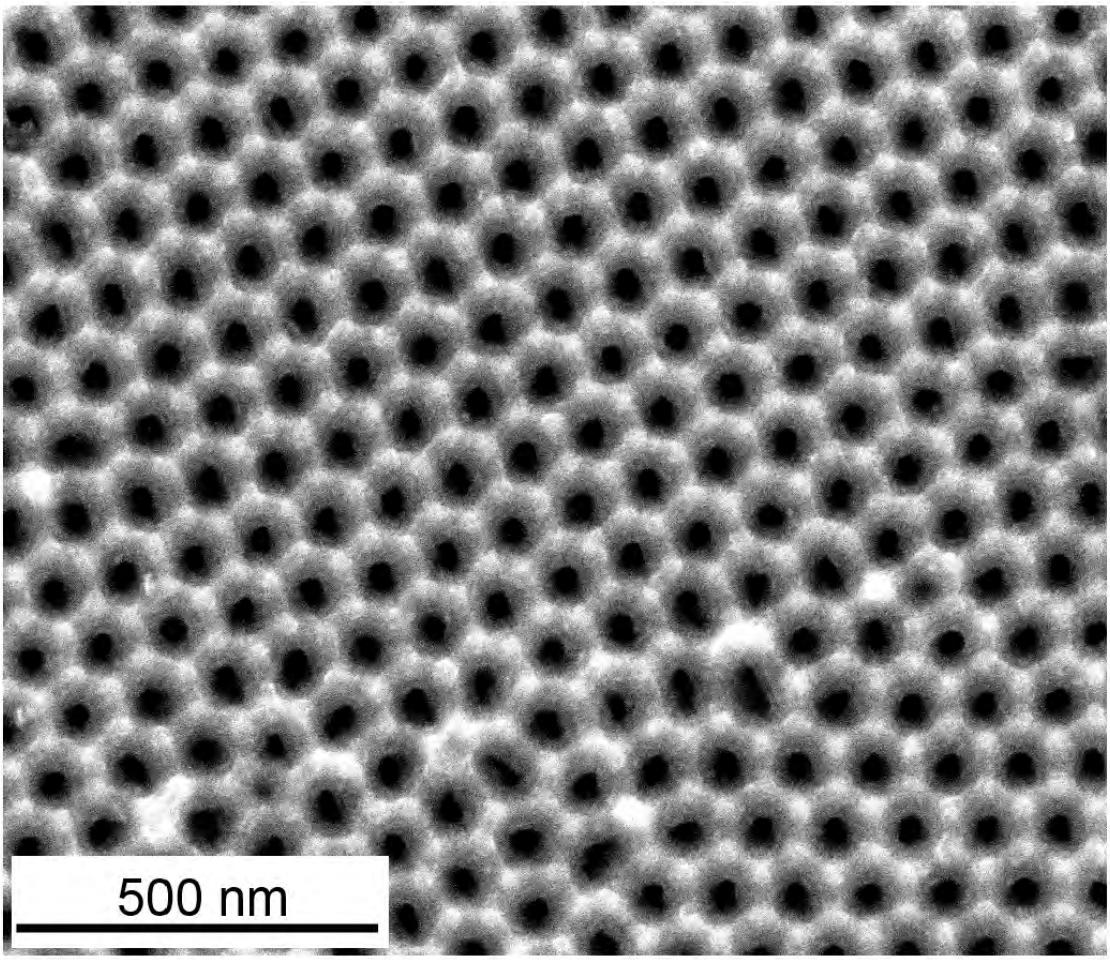

Figure S1. SEM image of the top surface of NAA after modification with MPTES and deposition of an ultra-thin metal gold layer.

2) Real-time RIfS response and calibration curve for rapid measurements

Real-time response of RIfS for different concentrations of Au^{3+} ions ranging from 0.1 to 80 µM till 30 min is presented in **Figure S2 a**. Notice that, *ΔEOT* change for different concentrations with time increases linearly, which could be used to preapare a calibration curve for situations requiring quick measurements for in-field applications. A calibration curve correlating changes in *EOT* with different concentrations is provided in **Figure S2 b**. It is worth stressing that this calibration curve could prove usefull where rapid results are required and knowing accurate concentration is not so important (i.e. qualitative detection).

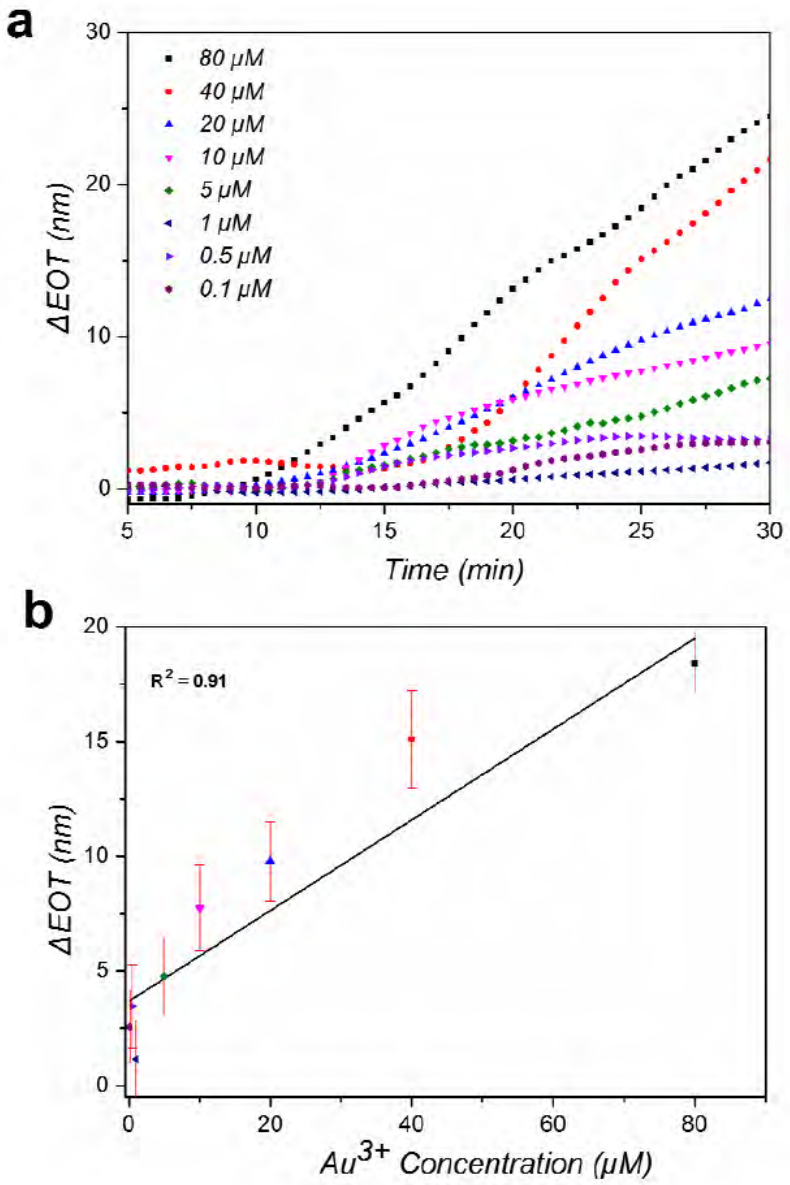

Figure S2. RIfS response of MPTES-NAA sensor for detection of Au^{3+} ions a) Real-time detection curve for eight different concentrations of Au^{3+} ions solutions in ultrapure water for 30 minutes of measurements. b) ΔEOT as a function of the concentration of Au^{3+} ions on MPTES-NAA sensors for concentration range 0.1-80 μM at time 25 min after starting the mearurement process .

3) Selectivity/control experiment with unmodified NAA

To confirm that the attachment of Au^{3+} ion to MPTES-NAA was due to binding between thiol groups of MPTES functionalities, we carried out a control experiment by exposing an unmodified NAA (i.e. without MPTES functionalization) to three different concentrations of gold (III) ions in aqueous solution. **Figure S3** presents the real-time RIfS response for gold ion attachment to an unmodified NAA substrate. An insignificant change in *EOT* was measured for 20 µM, 40 µM, and 80 µM aqueous solutions of gold ions on unmodified NAA in comparison to a MPTES-modified NAA substrate.

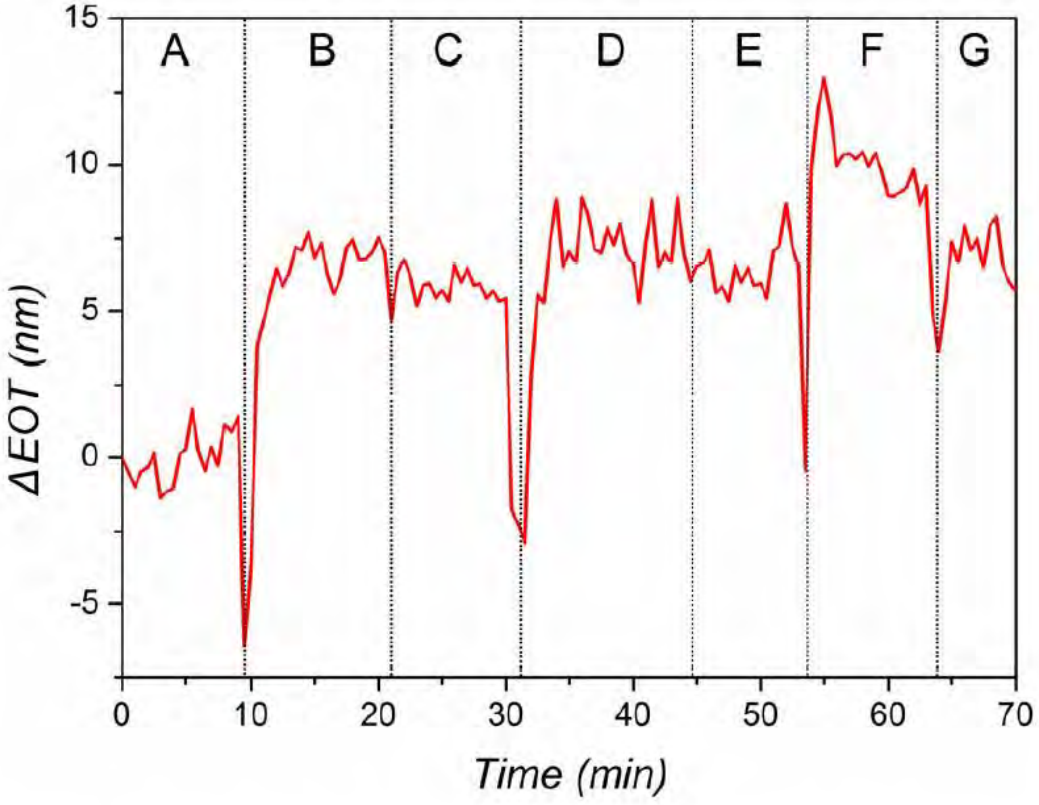

Figure S3 A real-time response curve for detection of Au^{3+} ions on an unmodified NAA substrate (control). The different regions in the figure are: A) baseline with ultrapure water; B) 20 µM Au^{3+} ion solution; C) rinse with ultrapure water; D) 40 µM Au^{3+} ion solution; E) rinse with ultrapure water; F) 80 µM Au^{3+} ion solution; and G) rinse with ultrapure water.

4) Real-time RIfS response for detection of gold ions in tap-water

Real-life application of our sensing system was demonstrated by detecting gold ions in tap-water (40 μM). **Figure S4** provides the real-time response for detection of gold ions in tap-water and ultrapure water. It is clearly visible that the binding curve was noisier for detection of gold ions in tap-water as compared to ultrapure water. Furthermore, the final equilibrium change in *EOT* value was slightly lower as well.

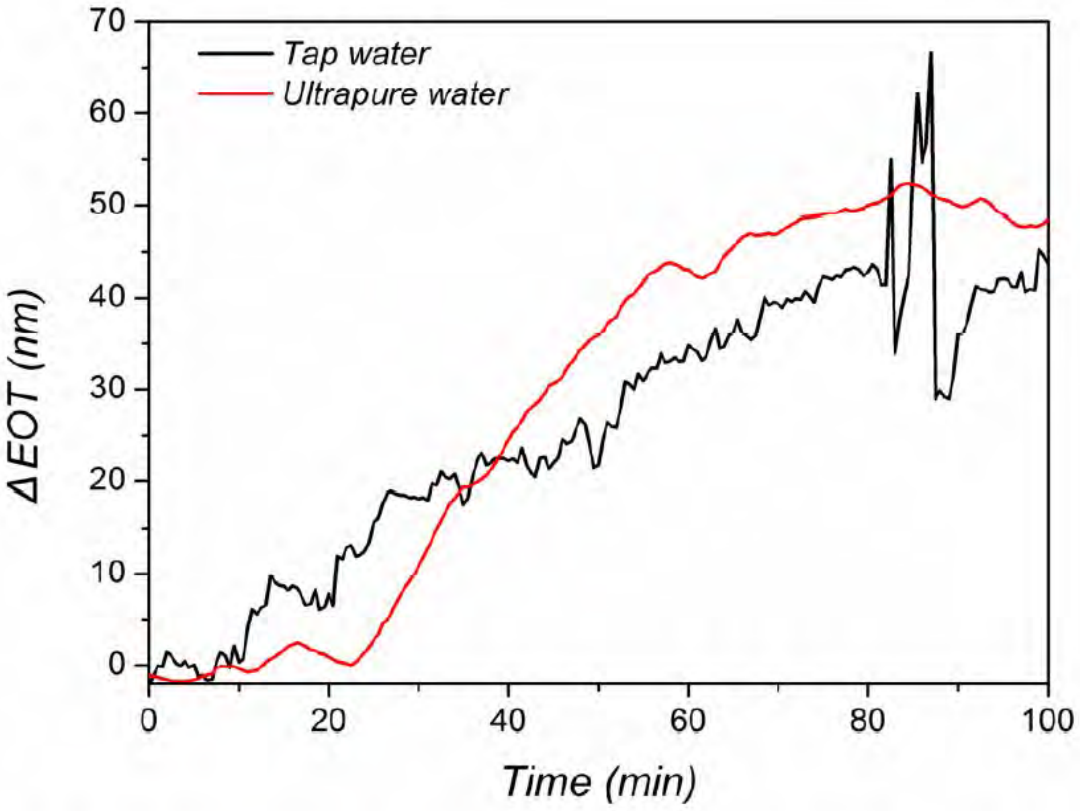

Figure S4 Real-time RIfS response curve of MPTES-NAA sensor for detection of gold ions (con 40uM) in tap-water and ultrapure water solutions.

5) Mathematical derivation of binding isotherms

Isotherm models used to describe the binding of Au^{3+} ions on thiol ligands of MPTES-NAA were the Freundlich and Langmuir isotherms, which were used to fit the experimental data. The binding reaction of Au^{3+} ions onto thiol groups of MPTES modified NAA surface can be defined by the expression.

$$SH + [Au^{3+}] \underset{Kd}{\overset{Ka}{\rightleftarrows}} Au - SH \quad (1)$$

Where, SH represents the available thiol groups on NAA surface, $[Au^{3+}]$ represents the concentration of free gold ions in solution, and Au – SH represents the surface-bound thiol gold-thiol complex while k_a and k_d are the association and dissociation constants, respectively.[1,2]

The equilibrium binding constant is defined as:

$$K_L = \frac{Au-SH}{SH[Au^{3+}]} \quad (2)$$

This equation can be rearranged as:

$$Au - SH = SH[Au^{3+}]K_L \quad (3)$$

SH is an unknown quantity, but it can be expressed in terms of product formed and thus substituted in eq. (3):

$$Au - SH = K_L((Au - SH_{max}) - (Au - SH))[Au^{3+}] \quad (4)$$

where $Au - SH_{max}$ is the maximum number of available binding sites, which are constant and equal to the number of SH terminal available on the NAA substrate initially. Since a number of studies have proved that the change in effective optical thickness (*EOT*) is proportional to the total number of adsorbed molecules, Au – SH is proportional to ΔEOT_e

(equilibrium value of *ΔEOT* for a given $[Au^{3+}]$) and, similarly, $Au-SH_{max}$ is proportional to ΔEOT_{max}. Then, after replacing and rearranging eq. (4), we get:

$$\Delta EOT_e = K_L \Delta EOT_{max}[Au^{3+}] - K_L \Delta EOT_e[Au^{3+}] \quad (5)$$

Further rearrangement of the above equation provides us:

$$\frac{[Au^{3+}]}{\Delta EOT_e} = \frac{1}{K_L \Delta EOT_{max}} + \frac{[Au^{3+}]}{\Delta EOT_{max}} \quad (6)$$

Eq. (6) represents a very common form of Langmuir equation and the parameters $\frac{1}{K_L \Delta EOT_{max}}$ and $\frac{1}{\Delta EOT_{max}}$ can be obtained by the intercept and slope of a plot between $\frac{[Au^{3+}]}{\Delta EOT_e}$ and $[Au^{3+}]$.

Freundlich isotherm (FI) model expression is an exponential equation.[2] This model is more suitable for describing binding on rough surfaces and it assumes that the binding sites increase with increasing the analyte concentration ($[Au^{3+}]$ in our case). In contrast, the Langmuir isotherm is more suitable for flat and smooth surfaces and it considers the number of binding sites to be constant throughout the reaction.

The empirical Freundlich equation based on sorption onto a rough surface is given by eq. (7):

$$Au-SH = K_f [Au^{3+}]^{1/n} \quad (7)$$

Where K_f and 1/n are related to the binding capacity of surface SH groups and binding intensity, respectively. Similar to eq. 4, we can replace $Au-SH$ with ΔEOT_e as reported by other groups. In this way, the change in *EOT* is directly proportional to the number of surface bound species. So, eq. 7 can be rewritten as:

$$\Delta EOT_e = K_f [Au^{3+}]^{1/n} \quad (8)$$

$$Ln(\Delta EOT_e) = logK_f + \frac{1}{n} log[Au^{3+}] \quad (9)$$

Values of $logK_f$ and $\frac{1}{n}$ can be determined respectively by the intercept and slope of a plot between $Ln(\Delta EOT_e)$ and $log[Au^{3+}]$.

REFERENCES

1. Schwartz, M. P.; Alvarez, S. D.; Sailor, M. J., Porous SiO_2 interferometric biosensor for quantitative determination of protein interactions: binding of protein A to immunoglobulins derived from different species. *Anal. Chem.* **2007,** 79, 327-334.

2. Chen, Z.; Ma, W.; Han, M., Biosorption of nickel and copper onto treated alga *Undaria pinnatifida*: Application of isotherm and kinetic models. *J. Haz. Mater.* **2008,** 155, 327-333.

CHAPTER 4

STRUCTURAL and OPTICAL NANOENGINEERING of NANOPOROUS ANODIC ALUMINA RUGATE FILTERS for REAL-TIME AND LABEL-FREE BIOSENSING APPLICATIONS

Tushar Kumeria

School of Chemical Engineering, The University of Adelaide South Australia 5005, Australia

This chapter is based on the following peer-reviewed article:

T. Kumeria, M. M. Rahman, A. Santos, J.Ferre-Borrull, L. F. Marsal, D. Losic "Structural and Optical Nanoengineering of Nanoporous Anodic Alumina Rugate Filters for Real-Time and Label-Free Biosensing Applications" *Analytical Chemistry*, 2014, **86**, 1837.

Statement of Authorship

Structural and Optical Nanoengineering of Nanoporous Anodic Alumina Rugate Filters for Real-Time and Label-Free Biosensing Applications. *Analytical Chemistry*, 2014, **86**, 1837.

Tushar Kumeria (Candidate)

Under supervision of D. Losic and A. Santos, I developed, designed, and performed the experiments, interpreted and processed the data and contributed in writing the manuscript for submission.

Signed Date:10/04/2015

Abel Santos

I acted as secondary supervisor for the candidate and aided in development and design of the experiments, and writing and evaluation of manuscript for submission. I give consent for Tushar Kumeria to present this paper for examination towards the Doctorate of philosophy.

Signed Date: 10/04/2015

Dusan Losic

I acted as primary supervisor of the candidate and aided in evaluation of experimental design and manuscript for submission. I give consent for Tushar Kumeria to present this paper for examination towards the Doctorate of philosophy

Signed Date: 10/04/2015

Mahbub M. Rahman

I acted as a collaborator (from Universitat Rovira i Virgili, Spain) on this work and provided the process for anodization of Al to produce NAA rugate filters evaluation of manuscript for submission. I give consent for Tushar Kumeria to present this paper for examination towards the Doctorate of philosophy

Signed Date: 30/03/2015

Joseph Ferre-Borrull

I acted as a collaborator (from Universitat Rovira i Virgili, Spain) and supervisor of M. M. Rahman and aided in development of Labview program used for anodization of Al for producing NAA rugate filters evaluation of manuscript for submission. I give consent for Tushar Kumeria to present this paper for examination towards the Doctorate of philosophy

Signed Date: 30/03/2015

Luis. F. Marsal

I acted as a collaborator (from Universitat Rovira i Virgili, Spain) and supervisor of M. M. Rahman and aided in designing and evaluation of experiments and manuscript for submission. I give my consent for Tushar Kumeria to present this paper for examination towards the Doctorate of Philosophy.

Signed Date: 30/03/2015

analytical chemistry

Article

pubs.acs.org/ac

Structural and Optical Nanoengineering of Nanoporous Anodic Alumina Rugate Filters for Real-Time and Label-Free Biosensing Applications

Tushar Kumeria,[†] Mohammad Mahbubur Rahman,[†,‡] Abel Santos,*[,†] Josep Ferré-Borrull,[‡] Lluís F. Marsal,[‡] and Dusan Losic[†]

[†]School of Chemical Engineering, The University of Adelaide, Engineering North Building, 5005 Adelaide, Australia

[‡]Departament d'Enginyeria Electrònica, Elèctrica i Automàtica, Universitat Rovira i Virgili, Avda Països Catalans 26, 43007 Tarragona, Spain

Supporting Information

ABSTRACT: In this study, we report about the structural engineering and optical optimization of nanoporous anodic alumina rugate filters (NAA-RFs) for real-time and label-free biosensing applications. Structurally engineered NAA-RFs are combined with reflection spectroscopy (RfS) in order to develop a biosensing system based on the position shift of the characteristic peak in the reflection spectrum of NAA-RFs ($\Delta\lambda_{peak}$). This system is optimized and assessed by measuring shifts in the characteristic peak position produced by small changes in the effective medium (i.e., refractive index). To this end, NAA-RFs are filled with different solutions of D-glucose, and the $\Delta\lambda_{peak}$ is measured in real time by RfS. These results are validated by a theoretical model (i.e., the Looyenga–Landau–Lifshitz model), demonstrating that the control over the nanoporous structure makes it possible to optimize optical signals in RfS for sensing purposes. The linear range of these optical sensors ranges from 0.01 to 1.00 M, with a low detection limit of 0.01 M of D-glucose (i.e., 1.80 ppm), a sensitivity of 4.93 nm M^{-1} (i.e., 164 nm per refractive index units), and a linearity of 0.998. This proof-of-concept study demonstrates that the proposed system combining NAA-RFs with RfS has outstanding capabilities to develop ultrasensitive, portable, and cost-competitive optical sensors.

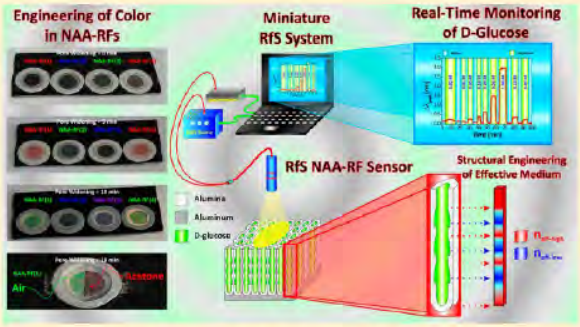

A fast and accurate analysis can become a crucial factor to diagnose and minimize some diseases, monitor levels of environmental pollutants, or control bioengineering processes at an opportune time, when a suitable therapy or action can be implemented. Nevertheless, there is still an important lack of accurate, fast, simple, cost-competitive, and portable analytical systems suitable for medical diagnosis, environmental analysis, and industrial applications. As for this, some nanoporous materials have demonstrated an outstanding sensing performance when combined with different optical techniques. Optical signals from analyte molecules immobilized onto these nanoporous networks are enhanced as compared with solid thin films as a result of their large specific surface area (i.e., multiplier effect). Some examples of these techniques are surface plasmon resonance,[1−3] localized surface plasmon resonance,[4−6] waveguiding spectroscopy,[7−10] surface-enhanced Raman scattering spectroscopy (SERS),[11−15] photoluminescence spectroscopy (PLS),[16−18] reflectometric interference spectroscopy (RIfS),[19−25] and reflection spectroscopy (RfS).[26,27] Some of the aforementioned optical techniques can be implemented in small, portable, and cost-competitive spectrometers (e.g., RIfS, RfS, PLS, etc.), enabling the development of cost-efficient and portable analytical systems.[28−30]

Amid the nanoporous materials used as sensing platforms, porous silicon (pSi) and nanoporous anodic alumina (NAA) are particularly interesting as they are not only optically active and biocompatible materials[31,32] but also their nanopores can work as containers and size-exclusive and chemical-surface-selective filters for a broad range of analytes. Typically, pSi and NAA are obtained by electrochemical etching/anodization of silicon and aluminum, respectively. Therefore, whereas their nanoporous structure can be accurately designed by structural engineering through the etching/anodization parameters, further specific surface chemistry functionalization endows pSi and NAA with chemical selectivity toward analytes of interest in complex mixtures.[16,17,21,22,33−36] Notably, engineering the nanopores of pSi and NAA makes it possible to modify the effective medium of these nanoporous materials and thus produce a variety of optically active platforms sensitive toward changes in the

Received: November 25, 2013
Accepted: January 13, 2014
Published: January 13, 2014

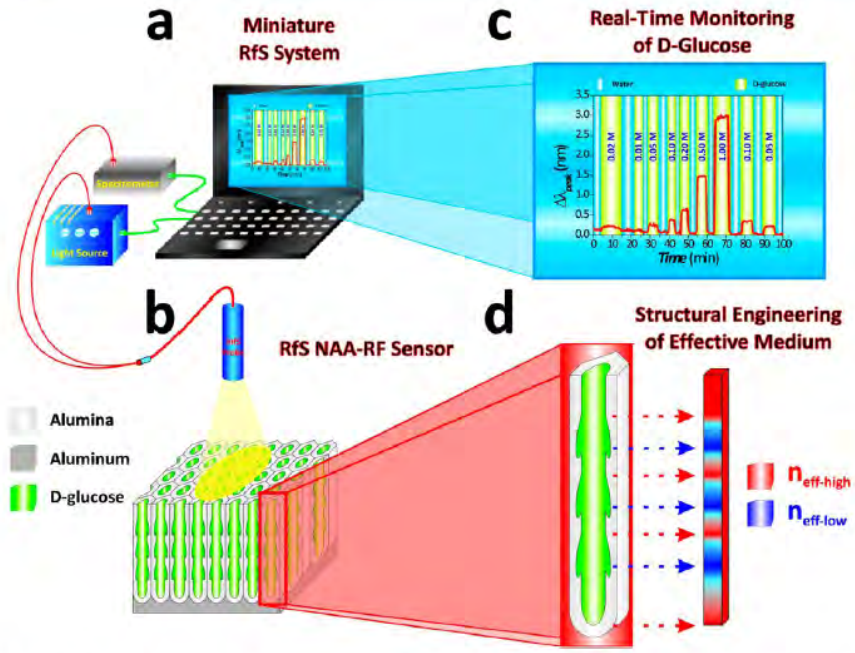

Figure 1. Scheme of proposed optical system for detection of analytes by combining NAA-RFs and RfS. (a) Miniature RfS system composed of notebook, light source, spectrometer, and optical probe. (b) Optical sensing platform based on NAA-RFs. (c) Real-time monitoring of D-glucose by the proposed NAA-RF/RfS system. (d) Structural engineering of pore geometry in NAA to design the effective medium of rugate filters in depth.

effective refractive index of the nanoporous structure (e.g., omnidirectional mirrors, microcavities, distributed Bragg reflectors, waveguides, rugate filters, etc.). These platforms can be implemented as substrates for optical sensing systems when combined with different techniques (e.g., SERS, PLS, RIfS, RfS, etc.). Thus far, pSi has been extensively used to develop optical nanostructures as a result of its outstanding optical properties and versatility in terms of pore geometry.[37−40] Nonetheless, pSi needs to be chemically passivated to provide stable optical signals and is limited by its poor mechanical stability.[26] In contrast, NAA presents stable optical signals without further passivation, it can be fabricated at industrial scale, its surface chemistry can be tuned ad libitum by many well-established protocols, and it is a mechanically stable material able to withstand high pressures.[18] Among the above-mentioned optical nanostructures, rugate filters are nanostructures in which the effective refractive index is modified in depth in a sinusoidal or pseudosinusoidal fashion. This modification of the effective refractive index leads to an enhanced reflection of light in some narrow regions of the UV−vis−NIR spectrum (i.e., stop bands), which can be determined by engineering the structure of the nanoporous material. In contrast to other optical filters, rugate filters provide equidistant and well-defined isolated peaks in the reflection spectrum without sidebands. These peaks can be used as the base to develop highly sensitive optical sensors as any change in the effective medium of the nanoporous structure (i.e., effective refractive index) is translated into a shift in the position of the characteristic reflection peak (i.e., $\Delta\lambda_{peak}$—sensing principle). As for the base material, rugate filters based on NAA, in contrast to commonly used pSi rugate filters, could provide many advantages, including industrial scalability and a cost-competitive fabrication process, stable optical signals throughout without further passivation, selective surface chemistry by functionalization with cost-competitive and stable chemicals through well-established protocols, and mechanical/thermal stability. To the best of our knowledge, however, no studies have reported about the structural engineering of optical rugate filters based on NAA and the analysis of their optical properties for developing optical sensing systems.

Herein, in this scenario, we report on the structural and optical engineering of rugate filters based on NAA combined with RfS. Figure 1 shows a schematic diagram of the proposed RfS system combined with NAA-RFs. Four different types of rugate filters are produced by electrochemical anodization of aluminum foils through four distinct pseudosinusoidal anodization profiles. Subsequently, the optical characteristics of these nanoporous platforms is assessed by measuring shifts in the characteristic peak position produced by small changes in the effective medium. To this end, the effective refractive index of theses NAA-RFs is systematically modified by filling their nanopores with aqueous solutions of D-glucose. This process is carried out in a flow cell, which makes it possible to monitor the sensing parameter (i.e., $\Delta\lambda_{peak}$) in real-time. From this, we establish the most sensitive rugate filter structure by analyzing such parameters as the sensitivity, low limit of detection and linearity. Moreover, experimental data are validated by the Looyenga−Landau−Lifshitz model, which is typically used to describe the effective medium of complex nanoporous structures. The obtained results demonstrate that structurally optimized nanoporous structures combined with optical techniques can enhance the sensing performance of current analytical methods, enabling the development of portable, accurate, fast, and cost-effective analytical systems for medical, environmental, or industrial applications.

EXPERIMENTAL SECTION

Materials. Aluminum (Al) foils of thickness 0.32 mm and purity 99.9997% were supplied by Goodfellow Cambridge Ltd. (U.K.). Oxalic acid ($C_2H_2O_4$), phosphoric acid (H_3PO_4), hydrochloric acid (HCl), ethanol (C_2H_5OH), perchloric acid ($HClO_4$), chromium trioxide (CrO_3), copper(II) chloride ($CuCl_2$), and D-glucose ($C_6H_{12}O_6$) were purchased from Sigma-Aldrich (Australia) and used without further processing. Ultrapure water Option Q–Purelabs (Australia) was used for preparing all the solutions used in this study.

Fabrication of NAA-RFs. Nanoporous anodic alumina rugate filters were prepared by anodizing high purity Al chips through a modified two-step electrochemical anodization process.[41−44] Briefly, Al chips 1.5 cm in diameter were first sonicated in ethanol (EtOH) and distilled water for 15 min each and dried under a nitrogen stream. These chips were electropolished prior to anodization in a mixture of EtOH and $HClO_4$ 4:1 (v/v) at 20 V and 5 °C for 3 min. After this, the first anodization step was carried out in a 0.3 M aqueous solution of $H_2C_2O_4$ at 40 V and 8 °C for 20 h. Next, the resulting NAA layer was dissolved by wet chemical etching in a solution of 0.2 M chromic acid (H_2CrO_4) and 0.4 M H_3PO_4 at 70 °C for 3 h. Finally, the second anodization step was performed in the same acid electrolyte at 8 °C. In this step, however, four different pseudosinusoidal anodization profiles under potentiostatic conditions controlled by total charge were used to generate four different types of rugate filters. Once the anodization process finished, the remaining aluminum substrate was selectively removed from the backside of these Al chips by wet chemical etching through an etching mask in a saturated solution of hydrochloric acid and cupric chloride ($HCl/CuCl_2$). In some experiments, a pore-widening process was performed by wet chemical etching in an aqueous solution of H_3PO_4 5 wt % at 35 °C. Notice that the second anodization step was controlled specifically to yield rugate filters that satisfy all mathematical and structural requirements for generating an optimized reflection spectrum in RfS.

Optical RfS System. Real-time measurements of the reflection spectrum of nanoporous anodic alumina rugate filters were carried out using a RfS system combined with a flow cell. Briefly, this system is composed of a bifurcated optical probe, one arm of which conducts and focuses white light from a source with a tungsten lamp (LS-1LL, Ocean Optics, U.S.A.) on the surface of NAA-RFs with an illumination spot of 2 mm in diameter. The reflected light from this spot is collected by the collection fiber assembled in the same optical probe and transferred to a miniature spectrophotometer (USB 4000, Ocean Optics, U.S.A.). UV–vis optical spectra were acquired in the 400–1000 nm wavelength range, and spectral data were saved at intervals of 30 s with an integration time of 100 ms and 50 average measurements (i.e., time between two consecutive scans = 5 s). After collection, RfS spectra were processed by measuring the shift in the position of the reflection peak $\Delta\lambda_{peak}$ in Igor Pro library (Wavemetrics, U.S.A.). $\Delta\lambda_{peak}$ was used as the optical parameter, and its changes were monitored in real time when the different analyte solutions of D-glucose were flowed through the system. These solutions produced changes in the effective medium of the NAA-RFs and thus shifts in the position of the characteristic peak of each rugate filter.

Flow Cell and Injection of Analyte Solutions. The optical characteristics of the NAA-RFs were assessed by packing them in a custom-designed and fabricated flow cell. Real-time optical measurements in the flow cell were carried out at a flow rate of 400 μL min^{-1}, which was maintained by a peristaltic pump (BT100–2J, LongerPump, U.S.A.). Note that a stable baseline with ultrapure water (i.e., solvent) was established for 10 min prior to injection of the different analyte solutions into the flow cell. After filling the nanopores of NAA-RFs with the different analyte solutions of D-glucose, sharp changes in $\Delta\lambda_{peak}$ took place as a result of the effective refractive index change.

Structural Characterization of NAA-RFs. The structural characteristics of the different types of NAA-RFs were established from SEM images acquired through a field emission gun scanning electron microscope (FEG-SEM FEI Quanta 450). These images were subsequently analyzed by the standard image processing package ImageJ (public domain program developed at the RSB of the NIH).[45]

Unless otherwise indicated, all the aforementioned experiments were repeated three times with freshly prepared rugate filters, and the obtained values of the different characteristic parameters were statistically treated by calculating averages and standard deviations.

RESULTS AND DISCUSSION

Fabrication of Optical NAA Rugate Filters. As previously mentioned, nanoporous anodic alumina rugate filters were prepared by anodizing aluminum chips through a modified two-step anodization process under potentiostatic conditions. In this process, a first anodization step was performed at 40 V and 8 °C for 20 h in an aqueous solution of $H_2C_2O_4$ in order to pattern the aluminum surface and obtain hexagonally arranged nanopores. Then, the second anodization step was carried out using the same acid electrolyte but applying a pseudosinusoidal voltage profile controlled by total charge (Q) (i.e., integrated current passed through the system).[46,47] Four different anodization profiles were used to produce four different types of rugate filters based on NAA (i.e., NAA-RF(1), NAA-RF(2), NAA-RF(3), and NAA-RF(4)). The anodization conditions and a generalized form of pseudosinusoidal anodization profile employed in this study to fabricate NAA-RFs are summarized in Table 1 and Figure S1 (Supporting Information), respectively. To fabricate type NAA-RF(1), the second anodization step was started at 20 V (V_0) and lasted until a charge of 1 C flowed through the system (Q_0). After this, a cyclic pseudosinusoidal anodization stage was started. Each cycle of this stage consisted of a linear increasing voltage ramp from 20 to 50 V at a rate of 0.5 V s^{-1} (R_{up}) and a subsequent linear decreasing voltage ramp from 50 to 20 V at a rate of −0.01 V s^{-1} (R_{down}). This cycle was repeated 150 times and finished by an interval at 20 V for a charge of 1 C and subsequent decreasing voltage ramp from 20 to 0 V at a rate of −0.001 V s^{-1} (final-A). In the case of type NAA-RF(2), the cyclic pseudosinusoidal anodization stage was directly started at 50 V. In each cycle of this stage, the voltage was kept constant at 50 V for a total charge of 1 C. Subsequently, voltage was decreased to 20 V by a linear

Table 1. Characteristic Parameters of Pseudosinusoidal Anodization for Each Type of Nanoporous Anodic Alumina Rugate Filter Produced in This Study

label	Q_0 (C)	V_0 (V)	Q_{s0} (C)	number of cycles	final step
NAA-RF(1)	1	20	0	150	final-A
NAA-RF(2)	0	50	1	150	final-B
NAA-RF(3)	1	20	1	100	final-A
NAA-RF(4)	1	20	0	150	final-C

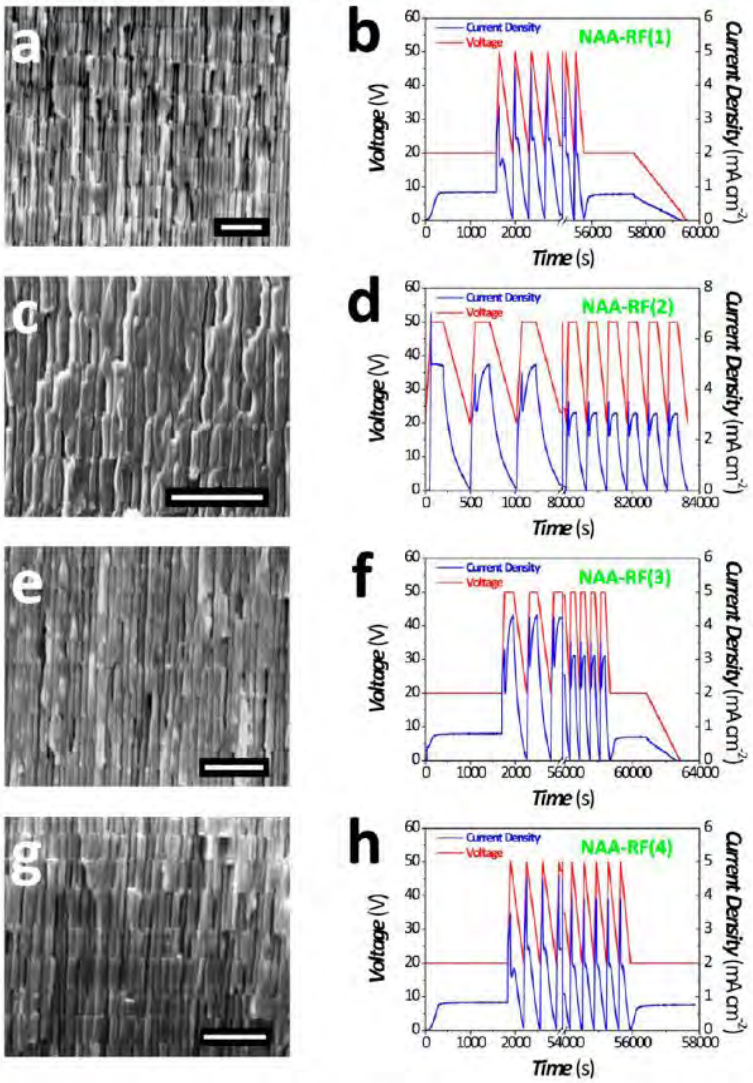

Figure 2. Cross-section SEM images and pseudosinusoidal anodization profiles of NAA-RFs produced in this study (scale bars =1 μm). (a,b) NAA-RF(1). (c,d) NAA-RF(2). (e,f) NAA-RF(3). (g,h) NAA-RF(4).

decreasing voltage ramp at a rate of −0.01 V s^{-1}. Then, voltage was increased up to 50 V by a linear increasing voltage ramp at a rate of 0.5 V s^{-1}. This cycle was repeated 150 times and directly finished at 20 V at the end of the last cycle (final-B). To produce rugate filters of type NAA-RF(3), we used the same anodization profile than for NAA-RF(1) but reducing the number of cycles to 100. Finally, rugate filters of type NAA-RF(4) were produced by the same anodization profile as that used for NAA-RF(1), but the cyclic pseudosinusoidal stage was finished at a constant voltage of 20 V for a total charge of 2 C (final-C).

Notice that the anodization of aluminum is an electrochemical process controlled by the flow of ionic species (i.e., OH^-, O^{2-}, Al^{3+}, etc.) through the oxide barrier layer located at the pore bottom tips.[48] For this reason, the decreasing voltage ramp was set as the fastest possible without blocking of the anodization process. This anodization approach makes it possible to generate a variety of optically active nanostructures and engineer the effective medium of NAA in depth as the anodization profile is translated into the pore geometry of NAA.[49,50]

Structural Characterization and Optical Properties of NAA Rugate Filters. *Structure and Optical Properties of NAA-RFs.* Pore geometry in NAA-RFs can be defined as progressive and continuous increments and decrements of the pore diameter in depth, the periods of which are established by the anodization profile. Figure 2 summarizes a set of cross-section FEG-SEM images of the resulting rugate filters along with the corresponding anodization profiles. These show how the effective medium is engineered in depth by oscillating the anodization voltage in a pseudosinusoidal fashion. NAA-RFs present cylindrical pore geometry from top to bottom with modified pore diameter, which allows analyte molecules to flow without obstructions inside the nanoporous structure.

Likewise in pSi, these NAA rugate filters presented different colors depending on the anodization profile, the pore-widening time, and the medium filling the pores. Figure 3 compiles a set of

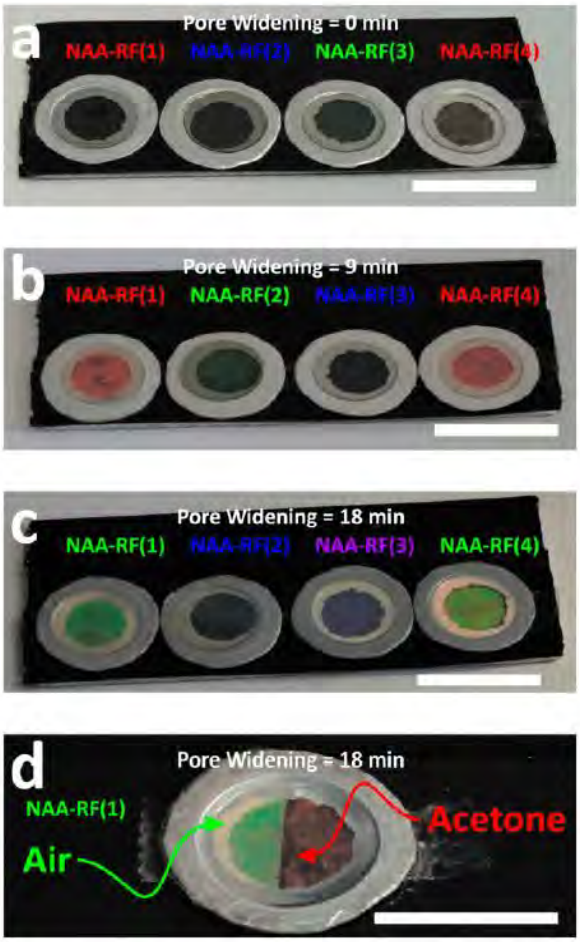

Figure 3. Set of digital photographs of NAA-RFs produced in this study and their color change as a result of the effective medium change. (a) NAA-RFs without pore widening. (b) NAA-RFs after 9 min of pore widening. (c) NAA-RFs after 18 min of pore widening. For (a–c), scale bar = 1.5 cm. (d) NAA-RF(1) after 18 min of pore widening and partially filling its nanopores with air and acetone (scale bar = 1.0 cm).

digital images showing this phenomenon, which is certainly useful in order to develop visual colorimetric sensing systems. For instance, NAA-RF(1) changes its color from slightly reddish (Figure 3a), to intense red (Figure 3b), and to intense green (Figure 3c) after different pore-widening times (i.e., 0, 9, and 18 min, respectively). Furthermore, as Figure 3d shows, a noticeable change in color (e.g., from intense green to intense red) takes place when the nanoporous network of NAA-RFs is filled with a different medium (e.g., acetone). This reveals that nanoporous anodic alumina rugate filters are extremely sensitive optical nanostructures toward any change in the effective medium (i.e., effective refractive index), which is the basic principle of optical sensors. Detailed information in this regard is included in Videos S1–S4 (Supporting Information).

Reflection Spectrum and Sensing Principle of NAA-RFs. After fabrication, the optical characteristics of the resulting NAA-RFs were assessed by measuring the shift in the characteristic peak position as a result of changes in the effective refractive index, which were achieved by filling the nanopores with different media (i.e., air, water, ethanol, and aqueous solutions of D-glucose). Notice that an increment of the effective refractive index of the rugate filter structure leads to a red shift in the reflection peak position (i.e., shift toward longer wavelengths). This process was carried out in a flow cell, and shifts in the reflection peak position were monitored in real time by reflection spectroscopy. Figure 4 shows an example of reflection spectrum

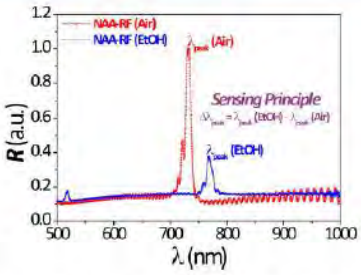

Figure 4. Reflection spectrum of a NAA-RF in air and ethanol showing the sensing principle used in nanoporous anodic alumina rugate filters combined with RfS ($\Delta\lambda_{peak} = \lambda_{peak}$ (EtOH) $- \lambda_{peak}$ (air)).

of a nanoporous anodic alumina rugate filter obtained by shining white light on its surface and the red shift in the reflection peak position ($\Delta\lambda_{peak}$) after filling its nanopores with ethanol. Although the peak position is shifted toward longer wavelengths as a result of the refractive index increment, its intensity is dramatically reduced as a result of light absorption by the ethanol filling the pores of the rugate filter structure. For this reason, $\Delta\lambda_{peak}$ was used as the sensing parameter in the proposed optical system.

Optical Sensitivity of NAA-RFs toward Changes in the Effective Refractive Index. Using the aforementioned sensing principle, the most sensitive rugate filter structure toward changes in the effective refractive index was established by measuring $\Delta\lambda_{peak}$ in reflection spectroscopy after filling their nanopores with different aqueous solutions of D-glucose, the concentration of which ranged from 0.01 to 1.00 M (i.e., modification of refractive index from 1.333 to 1.363). D-Glucose molecules were selected as model molecules because of their importance in clinical analysis and food technology. To this end, first, ultrapure water was injected into the flow cell, and a stable baseline was recorded for 10 min. After this, the corresponding analyte solution of D-glucose was injected into the flow cell, and a red shift in λ_{peak} was observed as a result of the effective refractive index change. Next, ultrapure water was flowed again, and $\Delta\lambda_{peak}$ decreased to the previous baseline value as D-glucose molecules were not specifically immobilized onto the NAA pores. This process was repeated for all the above-mentioned solutions, and $\Delta\lambda_{peak}$ was studied as a function of the analyte concentration (i.e., effective refractive index) in the different rugate filters analyzed in this study. The obtained results are shown in Figures 5 and 6, and the optical parameters of each rugate filter are summarized in Table 2. From this test, we found out that the most sensitive rugate filter structure toward changes in the effective refractive index produced by D-glucose molecules was NAA-RF(2), which presented a sensitivity (S) of 4.93 ± 0.08 nm M^{-1} (i.e., 164 nm per refractive index units), a limit of detection (LOD) of 0.01 M (i.e., refractive index 1.333), and a linearity (R^2) of 0.998 (Table 2).

Furthermore, the optical performance of these rugate filters was assessed after widening the pore diameter and repeating the aforementioned process by filling the nanopores with analyte

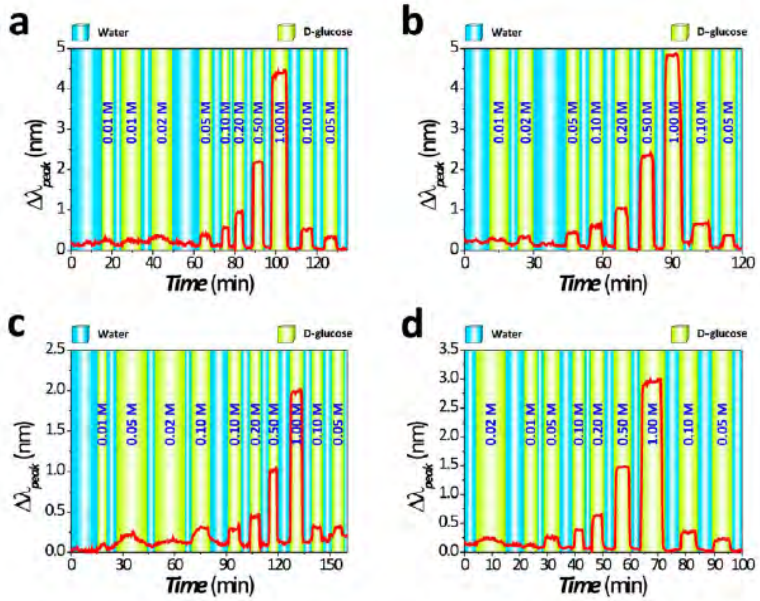

Figure 5. Depicts the $\Delta\lambda_{peak}$ analysis of real-time and in situ monitoring of D-glucose levels in the proposed optical biosensing system combining RfS with four types of NAA-RFs. (a) NAA-RF(1). (b) NAA-RF(2). (c) NAA-RF(3). (d) NAA-RF(4).

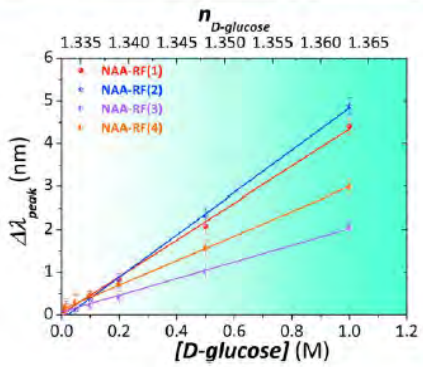

Figure 6. Optical optimization and fitting lines used to establish the characteristic sensing parameters of the different NAA-RFs fabricated in this study when detecting D-glucose levels in real time and in situ by RfS.

Table 2. Characteristic Sensing Parameters of the Different NAA-RFs Fabricated in This Study for Detection of Different Levels of D-Glucose in Real-Time by RfS

label	S^a (nm M^{-1})	S^b (nm RIU^{-1})	LOD^c (M)	R^2
NAA-RF(1)	4.31 ± 0.09	144 ± 3	0.010	0.997
NAA-RF(2)	4.93 ± 0.08	164 ± 3	0.010	0.998
NAA-RF(3)	2.87 ± 0.07	96 ± 2	0.010	0.996
NAA-RF(4)	1.95 ± 0.07	65 ± 2	0.015	0.991

^{a}S and ^{b}S = sensitivity expressed in units of reflection peak position shift ($\Delta\lambda_{peak}$) per concentration of analyte in M and units of refractive index (RIU), respectively. ^{c}LOD = Lower analyte concentration out of the standard deviation of the fitting lines shown in Figure 6.

solutions of D-glucose. From this test, we established that an increase in the pore diameter (i.e., porosity) enhances the sensitivity of NAA-RFs toward changes in the effective refractive index, and the optimal pore-widening time was 18 min (Supporting Information Figure S2).

Effective Media Model for NAA-RFs. To evaluate and validate the experimental results obtained in our study, we used an effective medium model for optical rugate filters. The Looyenga–Landau–Lifshitz (3L) model describes the average effective refractive index of complex nanoporous structures. Previous studies have demonstrated that the 3L model is more reliable than others (e.g., Maxwell-Garnett, Bruggeman, etc.) to describe complex nanoporous structures.[51] Furthermore, the 3L model can be easily implemented to describe systems containing multiple components, what is extremely useful for optical modeling purposes.

In this case, the Looyenga–Landau–Lifshitz model adapted to NAA-RFs can be expressed by eq 1.[51,52]

$$n_{eff-NAA-RF}^{2/3} = f_{Al_2O_3} n_{Al_2O_3}^{2/3} + f_{medium} n_{medium}^{2/3} \quad (1)$$

where $n_{eff-NAA-RF}$, $n_{Al_2O_3}$, n_{medium}, $f_{Al_2O_3}$, and f_{medium} are the effective refractive index of the NAA-RF, the refractive index of pure alumina, the refractive index of the medium filling the nanopores, and the volume fraction of alumina and medium filling the nanopores, respectively.

In addition to this, the reflection of light in each period of a rugate filter follows the Fabry–Pérot relationship, which is provided by eq 2.

$$\lambda_{NAA-RF} = 2n_{eff-NAA-RF} d_{NAA-RF} \cos\theta \quad (2)$$

where λ_{NAA-RF}, d_{NAA-RF}, and $\cos\theta$ are the reflection peak position in the reflection spectrum, the oscillation in-depth period of the refractive index in the rugate filter, and the angle of incidence of light, respectively.

Given that $f_{Al_2O_3} + f_{medium} = 1$ and $\theta = 0°$ in RfS, eq 1 can be reorganized as eq 3.

$$\lambda_{NAA-RF}^{2/3} = (2d_{NAA-RF})^{2/3}(1 - f_{medium}) n_{Al_2O_3}^{2/3} + (2d_{NAA-RF})^{2/3} f_{medium} n_{medium}^{2/3} \quad (3)$$

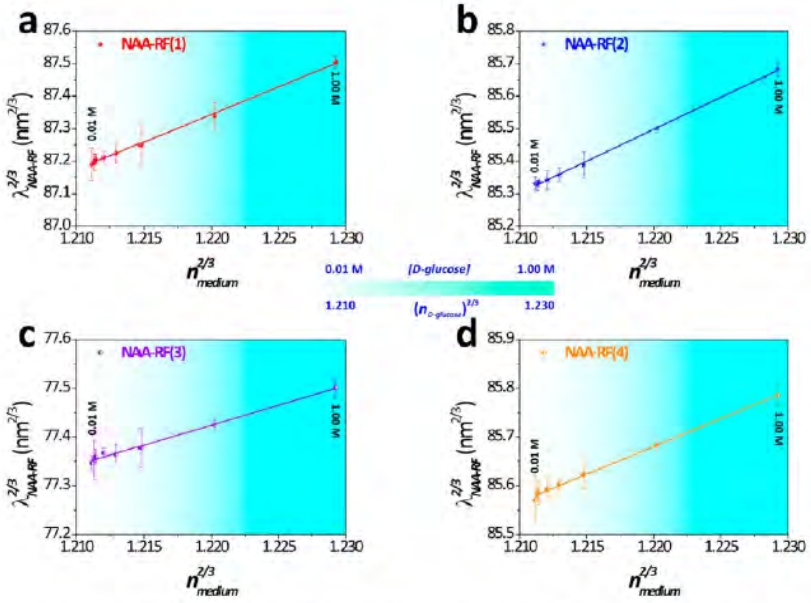

Figure 7. Looyenga–Landau–Lifshitz model describing the effective medium change in the different NAA-RFs produced in this study as a function of different levels of D-glucose molecules. (a) NAA-RF(1). (b) NAA-RF(2). (c) NAA-RF(3). (d) NAA-RF(4).

Table 3. Effective Structural Parameters of NAA-RFs Fabricated in This Study Obtained from the Looyenga–Landau–Lifshitz Model Used to Describe the Effective Media in Complex Nanoporous Materials

label	$(2d_{NAA-RF})^{2/3} f_{medium}$ (nm$^{2/3}$)	$(2d_{NAA-RF})^{2/3}(1-f_{medium})\, n^{2/3}_{Al_2O_3}$ (nm$^{2/3}$)	d_{NAA-RF} (nm)	f_{medium} (%)
NAA-RF(1)	16.98 ± 0.34	66.63 ± 0.42	256 ± 4	26 ± 1
NAA-RF(2)	19.64 ± 0.34	61.54 ± 0.41	252 ± 2	31 ± 4
NAA-RF(3)	8.17 ± 0.29	67.46 ± 0.35	246 ± 3	18 ± 3
NAA-RF(4)	11.40 ± 0.26	71.77 ± 0.32	210 ± 4	15 ± 2

Therefore, considering that $n_{Al_2O_3} = 1.670$,[18] the effective structural parameters of the different NAA-RFs (i.e., d_{NAA-RF} and f_{medium}) can be estimated by a linear fitting between the peak position ($\lambda^{2/3}_{NAA-RF}$) and the refractive index of the medium ($n^{2/3}_{medium}$) filling the nanopores. To this end, we used the experimental data obtained from the aforementioned sensing experiments detecting different concentrations of D-glucose. Figure 7 and Table 3 summarize the obtained results. These show that the most sensitive rugate filter toward changes in the effective medium is the structure NAA-RF(2), which presents a higher volume fraction medium filling the nanopores (f_{medium}). These results are in good agreement with the experimental data obtained in our study, demonstrating that the effective medium in complex nanoporous structures such as nanoporous anodic alumina rugate filters can be described by the 3L model.

■ CONCLUSIONS

In this study, we have reported on the structural engineering and optical performance of nanoporous anodic alumina rugate filters produced by electrochemical anodization of aluminum. Four different types of NAA-RFs were fabricated by modifying the anodization conditions, enabling the structural engineering of the effective medium of NAA-RFs in depth. Subsequently, these nanoporous platforms were combined with reflection spectroscopy in order to assess the optical characteristics of the resulting nanostructures through changes in the effective medium of the rugate filters. This was accomplished by measuring shifts in the characteristic peak position with the effective refractive index change, which was achieved by detecting different levels of D-glucose molecules (i.e., different refractive indexes). The obtained results revealed that the most sensitive NAA-RF structure toward changes in the effective refractive index was NAA-RF(2), which presented a low limit of detection of 0.01 M (i.e., refractive index of 1.333), a sensitivity of 4.93 nm M^{-1} (i.e., 164 nm per refractive index units), and a linearity of 0.998.

This analysis established that the sensing characteristics rely strongly upon the structure of the rugate filter, making it possible to enhance the sensing performance by tuning the nanoporous structure of NAA-RFs. This enables the development of more efficient optical biosensors for particular analytical purposes. Furthermore, the experimental results were validated and verified by a theoretical model (i.e., Looyenga–Landau–Lifshitz model) used to describe the effective medium of complex nanoporous materials. Therefore, this study contributes to the understanding and development of optimized optical biosensors based on structurally engineered nanoporous anodic alumina platforms with enhanced optical signals. As a result of its outstanding properties (i.e., cost-competitive price, portability, easy operation, accuracy, velocity, etc.), the proposed optical biosensing system is envisaged for developing portable and low-cost systems with applications in clinical, environmental, and food technology analyses.

dx.doi.org/10.1021/ac500069f | Anal. Chem. 2014, 86, 1837–1844

■ ASSOCIATED CONTENT

Supporting Information

Information about the anodization conditions used to fabricate NAA-RFs, and the effect of the pore widening over the sensitivity of NAA-RFs, and additional videos showing the real-time color change of these NAARFs when filling their pores with different solvents. This material is available free of charge via the Internet at http://pubs.acs.org.

■ AUTHOR INFORMATION

Corresponding Author

*E-mail: abel.santos@adelaide.edu.au. Fax: +61 8 8303 4373. Tel.: +61 8 8313 1535. Web page: http://www.adelaide.edu.au/directory/abel.santos.

Author Contributions

T.K., M.M.R., and A.S. contributed equally to this work. The manuscript was written through contributions of all authors. All authors have given approval to the final version of the manuscript.

Notes

The authors declare no competing financial interest.

■ ACKNOWLEDGMENTS

The authors thank the support provided by the Australian Research Council (ARC) through the grant nos. DP120101680, FT110100711, and DE140100549, the Spanish Ministerio de Economía y Competitividad through the grant no. TEC2012-34397, and the Generalitat de Catalunya through the grant no. 2009-SGR-549. Furthermore, the authors thank Mr. Jason Peak, Mr. Michael Jung, and Mr. Jeffrey Hiorns from the mechanical workshop of the School of Chemical Engineering (University of Adelaide) for their help and support with the fabrication of the experimental setups used in this study and the Adelaide Microscopy (AM) centre for FEG-SEM characterization.

■ REFERENCES

(1) Green, R. J.; Frazier, R. A.; Shakeshe, K. M.; Davies, M. C.; Roberts, C. J.; Tendler, S. J. B. *Biomaterials* **2000**, *21*, 1823−1835.
(2) Koutsioubas, A. G.; Spiliopoulos, N.; Anastassopoulos, D.; Vradis, A. A.; Priftis, G. D. *J. Appl. Phys.* **2008**, *103*, 094521.
(3) Dhathathreyan, A. *J. Phys. Chem. B* **2011**, *115*, 6678−6682.
(4) Hiep, H. M.; Yoshikawa, H.; Tamiya, E. *Anal. Chem.* **2010**, *82*, 1221−1227.
(5) Anker, J. N.; Hall, W. P.; Lyandres, O.; Shah, N. C.; Zhao, J.; Van Duyne, R. P. *Nat. Mater.* **2008**, *7*, 442−453.
(6) Yeom, S. H.; Kim, O. G.; Kang, B. H.; Kim, K. J.; Yuan, H.; Kwon, D. H.; Kim, H. R.; Kang, S. W. *Opt. Express* **2011**, *19*, 22882−22891.
(7) Fan, Y.; Hotta, K.; Yamaguchi, A.; Teramae1, N. *Opt. Express* **2012**, *20*, 12850−12859.
(8) Hotta, K.; Yamaguchi, A.; Teramae, N. *ACS Nano* **2012**, *6*, 1541−1547.
(9) Lau, K. H. A.; Tan, L. S.; Tamada, K.; Sander, M. S.; Knoll, W. *J. Phys. Chem. B* **2004**, *108*, 10812−10818.
(10) Lau, K. H. A.; Duran, H.; Knoll, W. *J. Phys. Chem. B* **2009**, *113*, 3179−3189.
(11) Lang, X.; Qiu, T.; Zhang, W.; Yin, Y.; Chu, P. K. *J. Phys. Chem. C* **2011**, *115*, 24328−24333.
(12) Ko, H.; Tsukruk, V. V. *Small* **2008**, *4*, 1980−1984.
(13) Ji, N.; Ruan, W.; Wang, C.; Lu, Z.; Zhao, B. *Langmuir* **2009**, *25*, 11869−11873.
(14) Velleman, L.; Bruneel, J. L.; Guillaume, F.; Losic, D.; Shapter, J. G. *Phys. Chem. Chem. Phys.* **2011**, *13*, 19587−19593.
(15) Kondo, T.; Miyazaki, H.; Nishio, K.; Masuda, H. *J. Photochem. Photobiol. A* **2011**, *221*, 199−203.
(16) Santos, A.; Kumeria, T.; Losic, D. *Anal. Chem.* **2013**, *85*, 7904−7911.
(17) Santos, A.; Macías, G.; Ferré-Borrull, J.; Pallarès, J.; Marsal, L. F. *ACS Appl. Mater. Interfaces* **2012**, *4*, 3584−3588.
(18) Santos, A.; Balderrama, V. S.; Alba, M.; Formentín, P.; Ferré-Borrull, J.; Pallarès, J.; Marsal, L. F. *Adv. Mater.* **2012**, *24*, 1050−1054.
(19) Lin, V. S. Y.; Motesharei, K.; Dancil, K. P. S.; Sailor, M. J.; Ghadiri, M. R. *Science* **1997**, *278*, 840−843.
(20) Jane, A.; Dronov, R.; Hodges, A.; Voelcker, N. H. *Trends Biotechnol.* **2009**, *27*, 230−239.
(21) Alvarez, S. D.; Li, C. P.; Chiang, C. E.; Schuller, I. K.; Sailor, M. J. *ACS Nano* **2009**, *3*, 3301−3307.
(22) Kumeria, T.; Losic, D. *Nanoscale Res. Lett.* **2012**, *7*, 88.
(23) Casanova, F.; Chiang, C. E.; Li, C. P.; Roshchin, I. V.; Ruminski, A. M.; Sailor, M. J.; Schuller, I. K. *Nanotechnology* **2008**, *19*, 315709.
(24) Kumeria, T.; Kurkuri, M. D.; Diener, K. R.; Parkinson, L.; Losic, D. *Biosens. Bioelectron.* **2012**, *35*, 167−173.
(25) Kumeria, T.; Losic, D. *Phys. Status Solidi RRL* **2011**, *5*, 406−408.
(26) Li, Y. Y.; Cunin, F.; Link, J. R.; Gao, T.; Betts, R. E.; Reiver, S. H.; Chin, V.; Bhatia, S. N.; Sailor, M. J. *Science* **2003**, *299*, 2045−2047.
(27) Cunin, F.; Schemedake, T. A.; Link, J. R.; Li, Y. Y.; Koh, J.; Bhatia, S. N.; Sailor, M. J. *Nat. Mater.* **2002**, *1*, 39−41.
(28) Ocean Optics Spectrometers. http://www.oceanoptics.com/Products/spectrometers.asp (Accessed 11, 2013).
(29) Avantes Spectrometers. http://www.avantes.com/Spectometers/Four-lines-of-Spectrometers.html (Accessed 11, 2013).
(30) Horiba Spectrometers. http://www.horiba.com/scientific/products/oem-mini-ccd-spectrometers/ccd-pda-spectrometers/ (Accessed 11, 2013).
(31) Canham, L. T. *Adv. Mater.* **1995**, *7*, 1033−1037.
(32) La Flamme, K. E.; Popat, K. C.; Leoni, L.; Markiewicz, E.; LaTempa, T. J.; Roman, B. B.; Grimes, C. A.; Desai, T. A. *Biomaterials* **2007**, *28*, 2638−2645.
(33) Kumeria, T.; Parkinson, L.; Losic, D. *Nanoscale Res. Lett.* **2011**, *6*, 634.
(34) Pacholsky, C.; Sartor, M.; Sailor, M. J.; Cunin, F.; Miskelly, G. M. *J. Am. Chem. Soc.* **2005**, *127*, 11636−11645.
(35) Pacholsky, C.; Yu, C.; Miskelly, G. M.; Godin, D.; Sailor, M. J. *J. Am. Chem. Soc.* **2006**, *128*, 4250−4252.
(36) Orosco, M. M.; Pacholsky, C.; Sailor, M. J. *Nat. Nanotechnol.* **2009**, *4*, 255−258.
(37) Pavesi, L.; Dubos, P. *Semicond. Sci. Technol.* **1997**, *12*, 570−575.
(38) Pellegrini, V.; Tredicucci, A.; Mazzoleni, C.; Pavesi, L. *Phys. Rev. B: Condens. Matter Mater. Phys.* **1995**, *52*, R14328−R14331.
(39) Pavesi, L.; Guardini, R.; Mazzoleni, C. *Solid State Commun.* **1996**, *97*, 1051−1053.
(40) Ilyas, S.; Böcking, T.; Kilian, K.; Reece, P. J.; Gooding, J. J.; Gaus, K.; Gal, M. *Porous Opt. Mater.* **2007**, *29*, 619−622.
(41) Masuda, H.; Fukuda, K. *Science* **1995**, *268*, 1466−1468.
(42) Masuda, H.; Hasegwa, F. J. *Electrochem. Soc.* **1997**, *144*, L127−L130.
(43) Masuda, H.; Yada, K.; Osaka, A. *Jpn. J. Appl. Phys.* **1998**, *37*, L1340−L1342.
(44) Nielsch, K.; Choi, J.; Schwirn, K.; Wehspohn, R. B.; Gösele, C. *Nano Lett.* **2002**, *2*, 677−680.
(45) Abràmoff, M. D.; Magalhaes, P. J.; Ram, S. J. *Biophotonics Int.* **2004**, *11*, 36−42.
(46) Santos, A.; Formentín, P.; Pallarès, J.; Ferré-Borrull, J.; Marsal, L. F. *J. Electroanal. Chem.* **2011**, *655*, 73−78.
(47) Rahman, M. M.; Garcia-Caurel, E.; Santos, A.; Marsal, L. F.; Pallarès, J.; Ferré-Borrull, J. *Nanoscale Res. Lett.* **2012**, *7*, 474.
(48) Jessensky, O.; Müller, F.; Gösele, U. *Appl. Phys. Lett.* **1998**, *72*, 1173−1175.
(49) Losic, D.; Lillo, M.; Losic, D., Jr. *Small* **2009**, *5*, 1392−1397.
(50) Lee, W.; Kim, J. C.; Gösele, U. *Adv. Funct. Mater.* **2009**, *19*, 1−7.
(51) Alekseev, S. A.; Lysenko, V.; Zaitsev, V. N.; Barbier, D. *J. Phys. Chem. C* **2007**, *111*, 15217−15222.
(52) Spanier, J. E.; Herman, I. P. *Phys. Rev. B: Condens. Matter Mater. Phys.* **2000**, *61*, PRB 61 10 437−PRB 61 10 450.

SCHOOL OF CHEMICAL ENGINEERING | THE UNIVERSITY of ADELAIDE

UNIVERSITAT ROVIRA I VIRGILI

Supporting Information

Structural and Optical Nanoengineering of Nanoporous Anodic Alumina Rugate Filters for Real-Time and Label-Free Biosensing Applications

Tushar Kumeria[1], Mohammad Mahbubur Rahman[1,2], Abel Santos[1]*, Josep Ferré-Borrull[2], Lluís F. Marsal[2] and Dusan Losic[1]

[1] School of Chemical Engineering – The University of Adelaide, Adelaide, Australia
[2] Departament d'Enginyeria Electrònica, Elèctrica i Automàtica – Universitat Rovira i Virgili, Tarragona, Spain

***E-Mail:** abel.santos@adelaide.edu.au

Losic Group

NanoTech Research

NePhos Nanoelectronic and Photonic Systems

Structural and Optical Nanoengineering of Nanoporous Anodic Alumina Rugate Filters for Real-Time and Label-Free Biosensing Applications

S1. Pseudosinusoidal Anodization for Preparing NAA-RFs

NAA-RFs were prepared by anodizing aluminum chips through a modified two-step anodization process, the second step of which consisted of a pseudosinusoidal voltage profile controlled by total charge (Q) (i.e. integrated current passed through the system). Figure S1 shows a generalized form of pseudosinusoidal anodization profile. This step starts at a given voltage (V_0) and lasts until a given charge (Q_0) flows through the system. After this, a cyclic pseudosinusoidal anodization process with multiple cycles is started. Each cycle of this process consists of three phases:

i) A linear increasing voltage ramp from 20 to 50 V at a rate of 0.5 V s^{-1} (R_{up}).

ii) An interval at 50 V for a given charge (Q_{50}).

iii) A linear decreasing voltage ramp from 50 to 20 V at a rate of -0.01 V s^{-1} (R_{down}).

Notice that this anodization process was finished in three different ways, depending on the type of NAA-RF:

Final-A) Stop at the end of the decreasing voltage ramp in phase (iii).

Final-B) Final interval at a constant voltage of 20 V for a charge of 2 C.

Final-C) Final interval at 20 V for a charge of 1 C and subsequent decreasing voltage ramp from 20 to 0 V at a rate of -0.001 V s^{-1}.

This electrochemical anodization approach enables the engineering of the nanoporous structure of NAA in order to generate a broad range of optically active nanostructures (e.g. optical rugate filters).

Structural and Optical Nanoengineering of Nanoporous Anodic Alumina Rugate Filters for Real-Time and Label-Free Biosensing Applications

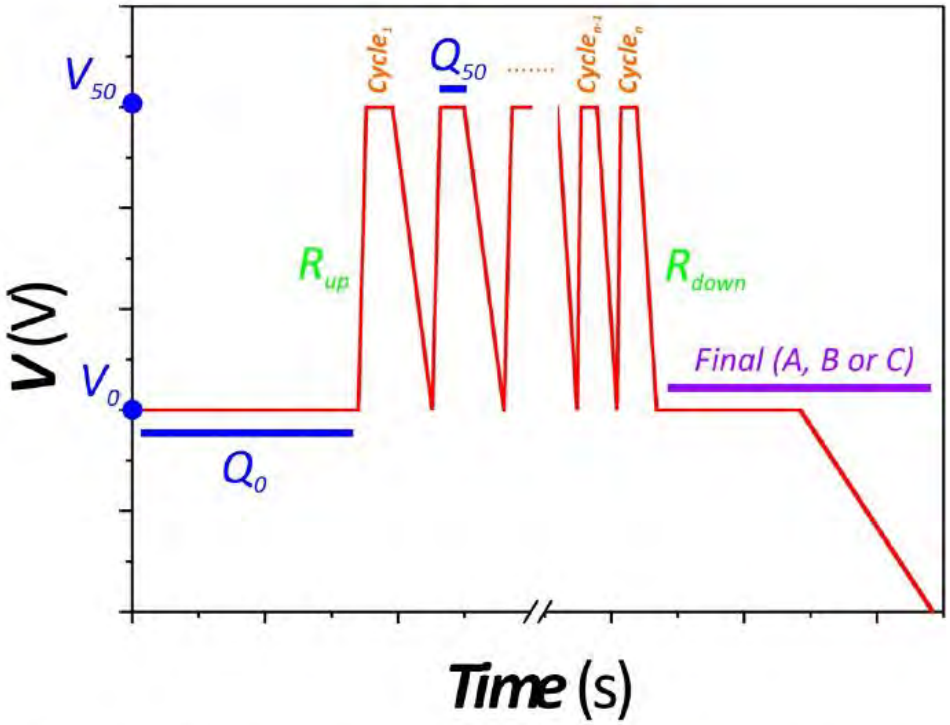

Figure S1. Generalized form of pseudosinusoidal anodization profile with characteristic parameters (V_0, Q_0, V_{50}, Q_{50}, R_{up}, R_{down}, *Cycle*, and *Final*) employed to produce NAA-RFs in this study.

Structural and Optical Nanoengineering of Nanoporous Anodic Alumina Rugate Filters for Real-Time and Label-Free Biosensing Applications

S2. Effect of Pore Widening over Sensitivity of NAA-RFs

The sensing performance of the different NAA-RFs produced in this study was assessed after widening the pore diameter and filling the nanopores with different aqueous solutions of D-glucose under non-specific adsorption conditions. From this test, we established that an increase in the pore diameter (i.e. porosity) enhances the sensitivity of the NAA-RF and the optimal pore widening time for all the NAA-RFs produced in this study was 18 min. An example of this is shown in **Figure S2**.

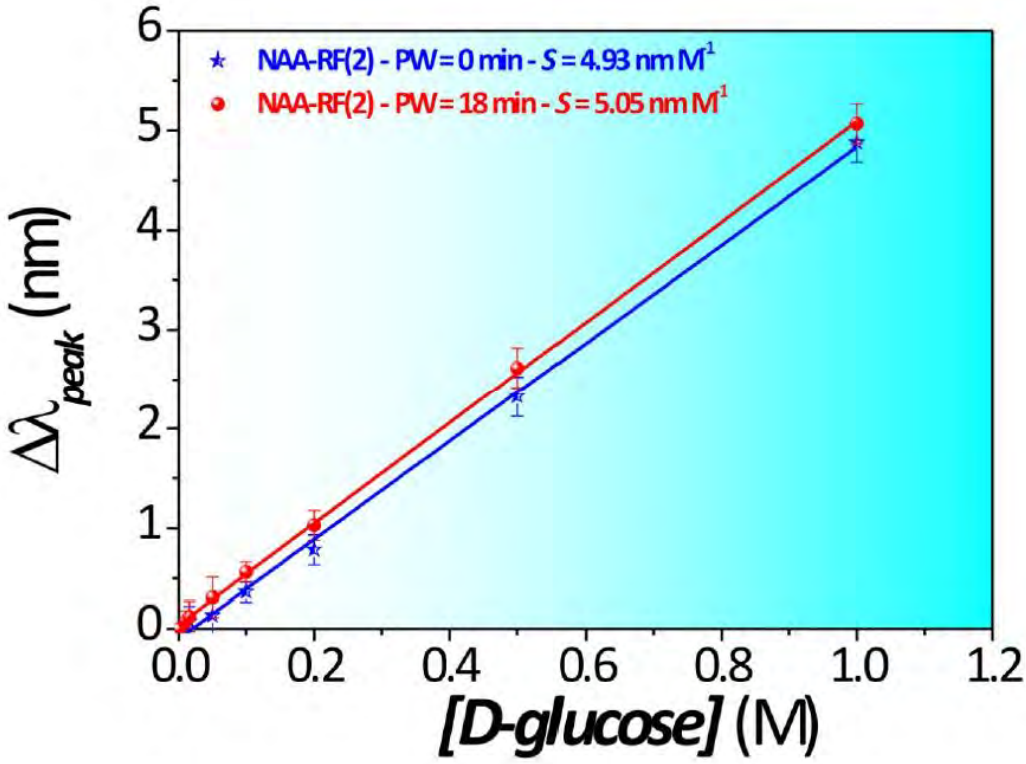

Figure S2. Optical performance of NAA-RF(2) for detection of D-glucose under non-specific adsorption conditions before and after a pore widening of 18 min. †S = Sensitivity expressed in units of reflectivity peak position change ($\Delta\lambda_{peak}$) per concentration of analyte in M (i.e. slope of linear fitting).

S3. Videos

These additional videos show the change in color of the different NAA-RFs after filling their pores with acetone. That phenomenon is associated with the effective medium change. Notice that these nanostructures recover the original color after acetone is evaporated. An electronic copy of these videos is provided along with each copy of the thesis.

Video S1. Change in color of the different NAA-RFs without pore widening after infiltrating their nanopores with acetone.

Video S2. Change in color of the different NAA-RFs with 9 min of pore widening after infiltrating their nanopores with acetone.

Video S3. Change in color of the different NAA-RFs with 18 min of pore widening after infiltrating their nanopores with acetone.

Video S4. Partial change in color of NAA-RF(1) with 18 min of pore widening after infiltrating their nanopores with acetone. Notice that one half of that sample was covered with transparent tape in order for avoiding the infiltration of its nanopores with acetone.

CHAPTER 5

NANOPOROUS ANODIC ALUMINA RUGATE FILTERS for SENSING OF IONIC MERCURY: TOWARD ENVIRONMENTAL POINT-of-ANALYSIS SYSTEMS

Tushar Kumeria

School of Chemical Engineering, The University of Adelaide South Australia 5005, Australia

This chapter is based on the following peer-reviewed article:

T. Kumeria, M. M. Rahman, A. Santos, J. Ferre-Borrull, L. F. Marsal, D. Losic "Nanoporous anodic alumina rugate filters for sensing of ionic mercury: Toward environmental point-of-analysis systems" *ACS Applied Materials & Interfaces*, 2014, **6**, 12971.

Statement of Authorship

Nanoporous anodic alumina rugate filters for sensing of ionic mercury: Toward environmental point-of-analysis systems. *ACS Applied Materials & Interfaces*, 2014, **6**, 12971.

Tushar Kumeria (Candidate)

Under supervision of D. Losic and A. Santos, I developed, designed, and performed the experiments, interpreted and processed the data and contributed in writing the manuscript for submission.

Signed Date:10/04/2015

Abel Santos

I acted as secondary supervisor for the candidate and aided in development and design of the experiments, and writing and evaluation of manuscript for submission. I give consent for Tushar Kumeria to present this paper for examination towards the Doctorate of philosophy.

Signed Date: 10/04/2015

Dusan Losic

I acted as primary supervisor of the candidate and aided in evaluation of experimental design and manuscript for submission. I give consent for Tushar Kumeria to present this paper for examination towards the Doctorate of philosophy

Signed Date:10/04/2015

Mahbub M. Rahman

I acted as a collaborator (from Universitat Rovira i Virgili, Spain) on this work and provided the process for anodization of Al to produce NAA rugate filters evaluation of manuscript for submission. I give consent for Tushar Kumeria to present this paper for examination towards the Doctorate of philosophy

Signed Date: 30/03/2015

Joseph Ferre-Borrull

I acted as a collaborator (from Universitat Rovira i Virgili, Spain) and supervisor of M. M. Rahman and aided in development of Labview program used for anodization of Al for producing NAA rugate filters evaluation of manuscript for submission. I give consent for Tushar Kumeria to present this paper for examination towards the Doctorate of philosophy

Signed Date: 30/03/2015

Luis. F. Marsal

I acted as a collaborator (from Universitat Rovira i Virgili, Spain) and supervisor of M. M. Rahman and aided in designing and evaluation of experiments and manuscript for submission. I give my consent for Tushar Kumeria to present this paper for examination towards the Doctorate of Philosophy.

Signed Date: 30/03/2015

ACS APPLIED MATERIALS & INTERFACES

Research Article

www.acsami.org

Nanoporous Anodic Alumina Rugate Filters for Sensing of Ionic Mercury: Toward Environmental Point-of-Analysis Systems

Tushar Kumeria,[†] Mohammad Mahbubur Rahman,[†,‡] Abel Santos,*[,†] Josep Ferré-Borrull,[‡] Lluís F. Marsal,[‡] and Dusan Losic[†]

[†]School of Chemical Engineering, The University of Adelaide, Adelaide, SA 5005, Australia

[‡]Departament d'Enginyeria Electrònica, Elèctrica i Automàtica, Universitat Rovira i Virgili, Avda Països Catalans 26, 43007 Tarragona, Spain

Supporting Information

ABSTRACT: Herein, we present an ultrasensitive, cost-competitive, and portable optical sensing system for detecting ionic mercury in environmental water. This analytical system combines structurally engineered and chemically modified nanoporous anodic alumina rugate filters (NAA-RFs) with reflection spectroscopy (RfS). The sensing performance of the proposed system is assessed through several tests, establishing its sensing performance (i.e., linear working range from 1 to 100 μM of Hg^{2+}, low limit of detection 1 μM of Hg^{2+} ions (i.e., 200 ppb), and sensitivity of 0.072 nm μM^{-1}), chemical selectivity (i.e., exposure to different metal ions Co^{2+}, Mg^{2+}, Ni^{2+}, Cu^{2+}, Pb^{2+}, Fe^{3+}, Ca^{2+}, Cr^{6+}, and Ag^{+}) and metal ions binding mechanism (i.e., fitting to Langmuir and Freundlich isotherm models). Furthermore, the detection of Hg^{2+} ions in tap and environmental water (River Torrens) is successfully carried out, demonstrating the suitability of this system for developing environmental point-of-analysis systems.

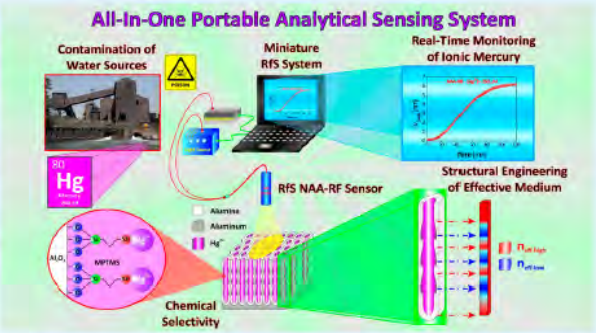

KEYWORDS: *nanoporous anodic alumina, reflection spectroscopy, optical rugate filters, mercury ions, selective surface chemistry, environmental water*

1. INTRODUCTION

Mercury emissions and releases produced by anthropogenic and natural sources have been accumulated in the natural environment by tropospheric cycling since the industrialization period in the 19th century.[1] Mercury can damage the immune and nervous systems, produce genetic mutations in developing embryos and affect motion coordination, touch, taste, and sight in adults.[2] Recently, worldwide concerns about mercury have been expressed by UNEP through a legally binding convention directed at controlling, monitoring and reducing mercury pollution at global scale.[3] In that regard, the development of ultrasensitive, handy, and cost-competitive sensors for monitoring levels of mercuric pollutants in water sources can enable effective actions to reduce levels of ionic mercury at opportune time, assessing risks for human populations and the environment.[1] Inorganic mercury(II) ions (Hg^{2+}) are the largest mercuric pollutants in environmental water and sources must be monitored throughout. Traditionally, atomic absorption spectroscopy (AAS) and gas chromatography (GC) have been used for this purpose since they can detect traces of ionic mercury (i.e., up to 10^{-7} wt % = 100 ppb; ppb = parts per billion).[4,5] More recently, surface enhanced Raman spectroscopy and plasmon enhanced vibrational spectroscopy have demonstrated outstanding sensing performances when detecting Hg^{2+} concentrations below 1 ppt (i.e., 10^{-12} wt % = 1 ppt; ppt = parts per trillion).[6−8] However, these techniques are expensive and require samples to be chemically treated before the analysis is performed, making it cost-intensive, laborious, and complicated. These limitations can be overcome by miniature spectrometers, which provide not only portability but also outstanding performances in terms of sensitivity, accuracy, and versatility. Amid the different optical techniques, reflection spectroscopy (RfS) has demonstrated competent capabilities in terms of limit of detection, accuracy and versatility for different sensing applications.[9−12] Moreover, RfS can be implemented in miniature spectrometers, reducing both costs and time consumed by current analytical techniques and enabling the development of portable point-of-analysis systems for detecting low levels of mercury in the site of interest (e.g., water sources).[13,14] RfS is an optical technique based on the constructive reflection of white light with a thin film, which can be combined with nanoporous structures such as porous silicon (PSi) and nanoporous anodic alumina (NAA). PSi and NAA are nanoporous materials that can confine, guide,

Received: May 12, 2014
Accepted: July 8, 2014
Published: July 8, 2014

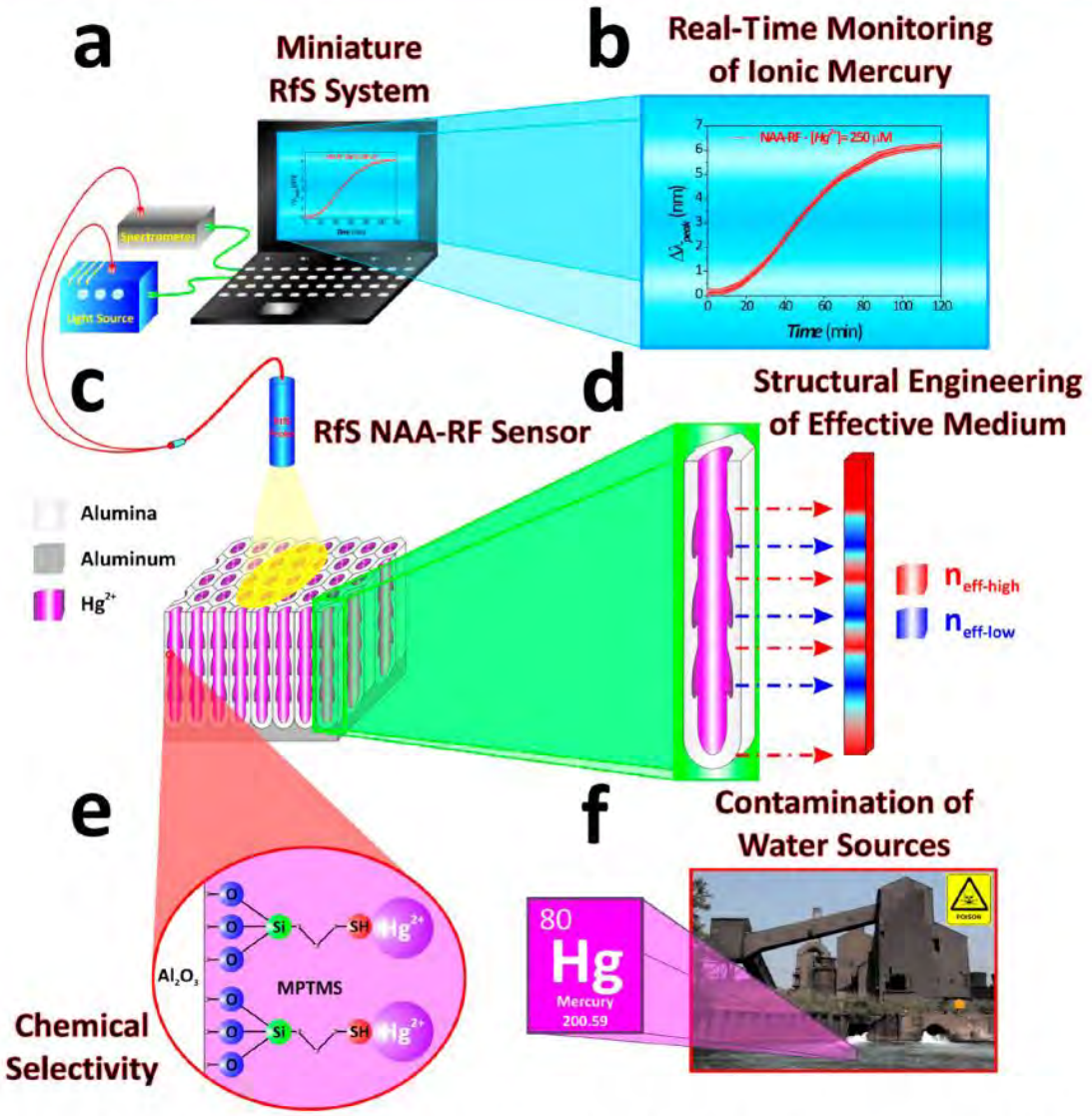

Figure 1. Scheme of proposed optical system for sensing Hg^{2+} in environmental water by combining RfS with structurally engineered and chemically modified NAA-RFs. (a) Miniature RfS system composed of notebook, light source, spectrometer, and optical probe. (b) Real-time monitoring of ionic mercury by RfS+NAA-RF system. (c) Optical sensing platform based on chemically modified NAA-RFs. (d) Structural engineering of effective medium in NAA-RFs. (e) Surface chemical selectivity by functionalization with MPTMS. (f) Real-time and label-free analysis of environmental water sources.

reflect and transmit light. Furthermore, their nanopores can be used as containers to accommodate molecules as well as chemical and physical filters for analytes. These properties can be achieved by engineering their nanoporous structure and changing their surface chemistry via functionalization, respectively.[15−24] Pore geometry in PSi and NAA can be structurally engineered by the etching/anodization parameters. Therefore, the effective medium of these nanoporous materials can be designed to produce a broad range of optically active structures (e.g., distributed Bragg reflectors, omnidirectional mirrors, rugate filters, waveguides, microcavities, etc.). For instance, rugate filters are optical nanostructures with effective refractive index modified in a sinusoidal or pseudosinusoidal manner in depth. These nanostructures present well-defined stop bands, where light is efficiently reflected in some narrow regions of the UV−visible−NIR spectrum. These stop bands can be established by tuning the pore geometry, yielding equidistant and well-defined isolated peaks in the reflection spectrum without sidebands. These peaks can be readily used to develop highly sensitive and selective optical sensors given that changes in the effective medium are translated into shifts in the position of the characteristic reflection peak of the optical rugate filter (i.e., sensing principle). Thus far, many studies have demonstrated that PSi is an excellent material to develop rugate filters.[18−27] Nonetheless, it is worth stressing that rugate filters based on NAA could offer many advantages; tunable pore geometry, cost-efficient, and scalable fabrication process and chemical and mechanical stability. NAA has been intensively

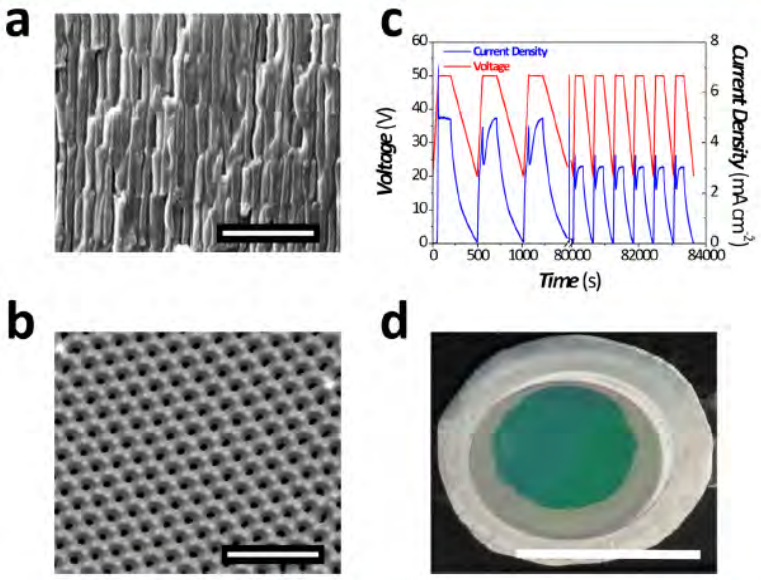

Figure 2. Fabrication and structural characteristics of NAA-RFs. (a) Cross-section SEM image of NAA-RFs fabricated in this study (scale bar = 1 μm). (b) Top-view SEM image of NAA-RFs (scale bar =500 nm). (c) Pseudosinusoidal anodization profile of NAA-RFs produced in this study. (d) Digital photography of NAA-RFs used in this study (scale bar = 1 cm).

used during the last years for a broad range of applications such as solar energy,[28,29] template synthesis,[30−34] and biosensing.[35−37]

In this scenario, we present for the first time an innovative portable and cost-competitive sensing system that combines chemically modified nanoporous anodic alumina rugate filters (NAA-Rfs) with RfS for sensing Hg^{2+} ions in environmental water. Figure 1 illustrates the proposed point-of-analysis system, which combines NAA-RFs and RfS for detecting Hg^{2+}.

2. EXPERIMENTAL SECTION

2.1. Materials. Aluminum (Al) foils of thickness 0.32 mm and purity 99.9997% were supplied by Goodfellow Cambridge Ltd. (UK). Oxalic acid ($C_2H_2O_4$), phosphoric acid (H_3PO_4), hydrochloric acid (HCl), ethanol (C_2H_5OH), acetone ($(CH_3)_2CO$), perchloric acid ($HClO_4$), hydrogen peroxide (H_2O_2), chromium trioxide (CrO_3), 3-(mercaptopropyl)-trimethoxysilane (MPTMS), cobalt(II) chloride ($CoCl_2$), magnesium(II) chloride ($MgCl_2$), nickel(II) sulfate ($NiSO_4$), copper(II) chloride ($CuCl_2$), lead(II) nitrate ($Pb(NO_3)_2$), iron(III) chloride ($FeCl_3$), calcium(II) chloride ($CaCl_2$), silver(I) nitrate ($AgNO_3$), and mercury(II) chloride ($HgCl_2$) were obtained from Sigma-Aldrich (Australia) and used as received. All solutions used in this study were prepared with ultrapure water Option Q-Purelabs (Australia).

2.2. Fabrication of NAA-RFs. Anodization of high purity Al foils by a modified two-step anodization process yields nanoporous anodic alumina rugate filters.[38−41] First, Al chips 1.5 cm in diameter were sonicated in ethanol (EtOH) and distilled water for 15 min each and dried under nitrogen stream. Then. aluminum chips were electropolished in a mixture of EtOH and $HClO_4$ 4:1 (*v*/*v*) at 20 V and 5 °C for 3 min. Subsequently, the first anodization step was conducted in a 0.3 M solution of $H_2C_2O_4$ at 40 V and 8 °C for 20 h and the resulting NAA was selectively removed by chemically etching in a mixture of 0.2 M chromic acid (H_2CrO_4) and 0.4 M H_3PO_4 at 70 °C for 3 h. After that, the second anodization step was carried out using the same acid electrolyte at 8 °C. In this step, however, a pseudosinusoidal anodization profile was applied. This step was not controlled by time but by total charge. Note that the remaining aluminum substrate was removed from the bottom side of these Al chips by chemical etching in mixture of hydrochloric acid and cupric chloride (HCl/$CuCl_2$). Finally, the nanoporous structure was widened by wet chemical etching in H_3PO_4 5 wt % at 35 °C for 18 min.

2.3. Functionalization of NAA-RFs. NAA-RFs were modified with MPTMS to chemically functionalize the inner surface of nanopores with thiol functional groups. Silanization was carried out through a well-established protocol reported elsewhere.[42] Briefly, hydroxyl groups (−OH) were generated on the inner surface of NAA-RFs by treatment with H_2O_2 30 wt % for 10 min at 85 °C. Then, NAA-RFs were dried under nitrogen stream prior to functionalization via chemical vapor deposition of MPTMS at 135 °C for 3 h. Physisorbed MPTMS molecules were removed from the surface of MPTMS-functionalized NAA-RFs by washing with acetone and water. Silanization was verified by Fourier transform infrared spectroscopy (FTIR, Nicolet 6700, Thermo Fisher Scientific, Australia) in the spectral range from 1000 to 3500 cm^{-1} (Figure S1, Supporting Information).

2.4. Optical RfS System. RfS spectra of NAA-RFs were acquired in real-time using a RfS system combined with a flow cell. This system consists of a bifurcated optical probe that conducts white light from a tungsten source (LS-1LL, Ocean Optics, USA) and focus it on NAA-RFs. The reflected light is collected by the collection fiber, which is assembled in the same optical probe. Finally, the reflected light is collected in a miniature spectrophotometer (USB 4000, Ocean Optics, USA). UV−visible optical spectra were acquired in the 400−1000 nm wavelength range. Spectral data were saved at intervals of 30 s with an integration time of 100 ms and 50 average measurements (i.e., time between two consecutive scans = 5 s). After collection, RfS spectra were processed by measuring the shift in the position of the reflection peak ($\Delta\lambda_{peak}$) in Igor Pro library (Wavemetrics, USA). $\Delta\lambda_{peak}$ was used as the sensing parameter and its changes were monitored in real-time to follow the binding of Hg^{2+} ions to thiol functional groups of MPTMS functionalities inside the NAA-RFs used in this study.

2.5. Flow Cell and Injection of Analyte Solutions. Sensing experiments were carried out by packing MPTMS-modified NAA-RFs in a flow cell based on acrylic plastic, through which the different analyte solutions were flowed by a peristaltic pump (BT100-2J, LongerPump, U.S.A.) at a constant flow rate of 400 μL min^{-1}. Prior to injection of the different analyte solutions, a stable baseline with the corresponding solvent (i.e., ultrapure, tap or River Torrens' water) was obtained for 10 min. The binding between Hg^{2+} ions and thiol functional groups inside the pores of MPTMS-modified NAA-RFs

produced shifts in $\Delta\lambda_{peak}$, which lasted until the available thiol groups on the inner surface of NAA-RFs were saturated with Hg^{2+} ions.

2.6. Chemical Selectivity Tests. The chemical selectivity of the proposed sensing system toward Hg^{2+} ions was assessed by exposing a MPTMS-modified NAA-RF sensor to 2 mM aqueous solutions of nine different metal ions (i.e., Co^{2+}, Mg^{2+}, Ni^{2+}, Cu^{2+}, Pb^{2+}, Fe^{3+}, Ca^{2+}, Cr^{6+}, and Ag^{+}), which was followed by a solution of Hg^{2+} ions with a fifty-fold lower concentration (i.e., 40 μM).

2.7. Applicability of RfS Combined with NAA-RFs for Real-Life Applications. To demonstrate the capability of the proposed sensing system for real-life environmental applications, MPTMS-modified NAA-RFs were analyzed when detecting Hg^{2+} ions (i.e., 5 and 40 μM) in tap and River Torrens' water. Whereas tap water was directly collected from the laboratory sink (SA Water, South Australia, Adelaide), environmental water was first collected from the River Torrens (Adelaide, South Australia, Australia) and thus filtered with a paper filter to remove any particulate. Water from these sources was used as a solvent for preparing 5 and 40 μM Hg^{2+} solutions used in these tests.

2.8. Structural Characterization of NAA-RFs. NAA-RFs were structurally characterized by analyzing SEM images, which were acquired by field emission gun scanning electron microscopy (FEG-SEM FEI Quanta 450).

Note that all the aforementioned experiments were repeated three times using freshly produced NAA-RFs.

3. RESULTS AND DISCUSSION

3.1. Fabrication of Optical NAA Rugate Filters. NAA-RFs were produced by anodization of Al foils following a modified two-step process. The second anodization step of this process consisted in a pseudosinusoidal voltage profile controlled by total charge (Q).[43,44] This process started at 20 V and, subsequently, the voltage was increased from 20 to 50 V at a rate of 0.5 V s^{-1}. After this, the anodization voltage was kept constant at 50 V for a charge of 1 C. Next, the anodization voltage was reduced from 50 to 20 V by a linear decreasing ramp at a rate of −0.01 V s^{-1}. This cycle was repeated 150 times. The anodization process was finished at the end of the decreasing voltage ramp of the last cycle. Note that anodization of aluminum is controlled by the flow of ionic species (i.e., OH^{-}, O^{2-}, Al^{3+}, etc.) across the oxide barrier layer at the pore bottom tips.[45] This electrochemical process enables the generation of optical nanostructures by engineering the effective medium in depth. This makes it possible to produce nanoporous platforms suitable for developing optical sensing systems. Figures 2a and b show top and cross-section views scanning electron microscopy (SEM) images of the resulting NAA-RFs. This reveals how the pore structure is engineered in depth by the anodization profile. Figure 2c presents the pseudosinusoidal anodization profile used in this study to produce NAA-RFs with optimal RfS signal. It is worthwhile mentioning that these NAA-RFs presented green color as a result of the reflected light. Figure 2d shows a digital photography of a NAA-RF demonstrating this optical phenomenon.

3.2. Optical Sensing Performance of NAA-RFs for Detection of Ionic Mercury. *3.2.1. Sensing Principle.* As mentioned before, in NAA-RFs, an increment of the effective medium yields a red shift in the reflection peak position (i.e., shift toward longer wavelengths = sensing principle). The sensing performance of these nanostructures was assessed by measuring shifts in the reflection peak position as a result of mercury ions binding. This process was monitored in real-time by RfS. Supporting Information Figure S2 shows an example of reflection spectrum of a NAA-RF in RfS obtained by shining white light on its surface and the red shift in $\Delta\lambda_{peak}$ before and after filling its nanopores with ethanol.

3.2.2. Real-Time Monitoring of Hg^{2+}. A set of NAA-RFs was chemically modified with MPTMS, which is an organosilane with thiol functional terminal (−SH), to endow NAA-RFs with chemical selectivity toward Hg^{2+} ions.[42] It is well-known that thiol groups have strong affinity for mercury ions. In particular, thiols are known as mercaptans becaue of their ability for mercury capture, forming a strong coordination complex with Hg^{2+}. Figure 3a presents an example of real-time monitoring of

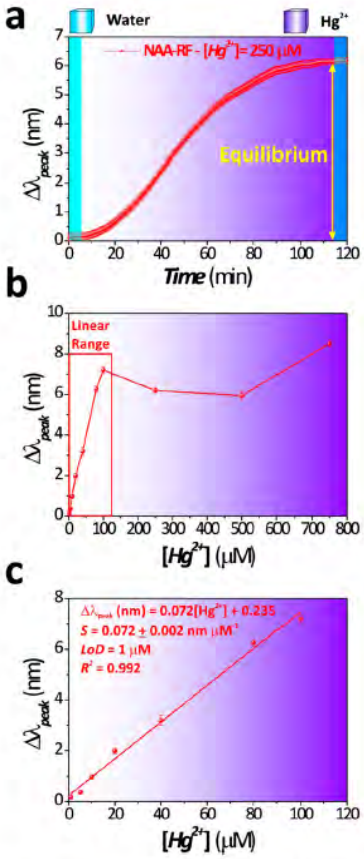

Figure 3. Sensing performance of the proposed sensing system for real-time detection of ionic mercury in ultrapure water. (a) Example of real-time monitoring of $\Delta\lambda_{peak}$ for [Hg^{2+}] = 250 μM. (b) $\Delta\lambda_{peak}$ as a function of analyte concentration from 1 to 750 μM. (c) Linear range of the proposed NAA-RF sensor, calibration curve and sensing parameters (i.e., from 1 to 100 μM). S = Sensitivity expressed in units of $\Delta\lambda_{peak}$ per concentration of analyte in mM. LoD = Low analyte concentration out of the standard deviation of the fitting line. R^2 = Linearity.

$\Delta\lambda_{peak}$ by RfS for detection of 250 μM Hg^{2+} in ultrapure water. It is worth noting that a stable $\Delta\lambda_{peak}$ baseline was first obtained with ultrapure water for 10 min, which was followed by injection of the analyte solution into the flow cell. After this, a sharp shift of approximately 6 nm in λ_{peak} was observed when the MPTMS-modified NAA-RF was exposed to the analyte solution. This confirmed the binding of Hg^{2+} ions to thiol terminals of MPTMS molecules present on NAA-RF pores. Stress that, after $\Delta\lambda_{peak}$ achieved a stable value, ultrapure water

Table 1. Characteristic Constants and Correlation Coefficients for Langmuir and Freundlich Binding Isotherm Models Obtained for the Immobilization and Detection of Mercury Ions in the Proposed Optical Sensing System

Langmuir model			Freundlich model		
$\Delta\lambda^{m}_{peak}$ (nm)	K_L (μM^{-1})	R^2	K_f (mg g^{-1})	n^{-1}	R^2
8.3 ± 0.7	0.015 ± 0.007	0.942	0.23 ± 0.02	0.61 ± 0.08	0.875

was flowed again through the flow cell in order to remove nonspecifically bound Hg^{2+} ions. Then, $\Delta\lambda_{peak}$ remained stable at that value throughout. In this way, we ensured that the total shift in $\Delta\lambda_{peak}$ was a result of an increase in the effective medium of the MPTMS-modified NAA-RF, which is associated with a stable binding of Hg^{2+} ions over the inner surface of NAA-RFs. Following this procedure and using $\Delta\lambda_{peak}$ as the sensing parameter, we assessed the performance of the proposed system for detecting ionic mercury in ultrapure water as a function of the analyte concentration (i.e., $[Hg^{2+}]$). To this end, $[Hg^{2+}]$ was modified from 1 to 750 μM and $\Delta\lambda_{peak}$ was monitored in real-time for each of these samples. From this, we obtained a calibration curve that correlates $\Delta\lambda_{peak}$ with $[Hg^{2+}]$. Ten different concentrations of Hg^{2+} ions within 3 orders of magnitude (i.e., from 1 to 750 μM) were evaluated to establish the linear and saturation range of the proposed sensing device. Figure 3b shows that $\Delta\lambda_{peak}$ saturates at concentrations above 100 μM. This suggests that the binding sites (i.e., thiol terminal groups) for Hg^{2+} ions on the MPTMS-modified NAA-RFs get saturated of mercury ions above that concentration. A linear relationship between $\Delta\lambda_{peak}$ and $[Hg^{2+}]$, however, was observed from 1 to 100 μM (i.e., from 200 ppb to 20 ppm; ppm = parts per million). A linear fitting of $\Delta\lambda_{peak}$ with the analyte concentration within this concentration range is presented in Figure 3c along with the resulting fitting equation and the sensing parameters. This calibration curve can be used to quantify concentrations of Hg^{2+} ions in aqueous solutions by measuring $\Delta\lambda_{peak}$ in the proposed sensing system, which presents a sensitivity (S) of 0.072 nm μM^{-1}, a low limit of detection (LoD) of 1 μM and a linearity (R^2) of 0.992 within a broad analyte concentration range (i.e., from 1 to 100 μM).

3.2.3. Isotherm Models for Binding of Hg^{2+} Ions over MPTMS-Modified NAA-RFs. The obtained results were fitted to Langmuir and Freundlich isotherm models to figure out the kinetics binding mechanism between Hg^{2+} ions and thiol groups on the inner surface of chemically functionalized NAA-RFs.[46] A complete mathematical derivation for these isotherm models is provided in the Supporting Information.

Langmuir isotherm model for the studied process is given by eq 1.

$$\frac{[Hg^{2+}]}{\Delta\lambda^{e}_{peak}} = \frac{1}{K_L \Delta\lambda^{m}_{peak}} + \frac{[Hg^{2+}]}{\Delta\lambda^{m}_{peak}} \quad (1)$$

where $\Delta\lambda^{e}_{peak}$ is the shift in the reflection peak position at equilibrium (see Figure 3a) and K_L and $\Delta\lambda^{m}_{peak}$ are characteristic constants.

Therefore, $1/(K_L\Delta\lambda^{m}_{peak})$ and $1/(\Delta\lambda^{m}_{peak})$ can be obtained by a linear fitting between $\Delta\lambda^{e}_{peak}$ and $[Hg^{2+}]$.

As for the Freundlich isotherm model adapted to the binding of mercury ions, this is given by eq 2.

$$\log(\Delta\lambda^{e}_{peak}) = \log(K_f) + \frac{1}{n}\log([Hg^{2+}]) \quad (2)$$

where K_f and n are characteristic constants.

Hence, values of $\log(K_f)$and $1/n$ can be estimated by the intercept and slope of a linear fitting between $\log(\Delta\lambda^{e}_{peak})$ and $\log([Hg^{2+}])$, respectively.

Note that, while Langmuir isotherm model describes flat surfaces considering constant the number of binding sites throughout the reaction (i.e., functional groups on the inner surface of NAA-RF), Freundlich isotherm model characterizes rough surfaces, assuming that the number of binding sites increases with the concentration of analyte molecules (i.e., $[Hg^{2+}]$). To throw light on this question, experimental data were fitted to both isotherm models and their characteristic constants calculated. The obtained results and the correlation factors are summarized in Table 1. The fitting parameters reveal that the binding mechanism between mercury ions and thiol groups on the surface of NAA-RFs can be described by a Langmuir isotherm model. Supporting Information Figure S3 shows a graphic of the obtained Langmuir and Freundlich isotherm models. It was observed that the experimental data fitted better to a Langmuir isotherm model. These results indicate that the binding of Hg^{2+} ions in the sensing platform follows a monolayer sorption mechanism.

Finally, an additional control test was carried out to demonstrate that changes in $\Delta\lambda_{peak}$ were exclusively associated with selective binding of Hg^{2+} ions to thiol groups. To this end, an as-produced NAA-RF (i.e., NAA-RF without MPTMS functionalization) was exposed to a 40 μM aqueous solution of Hg^{2+} ions (Figure S4, Supporting Information). These results demonstrate that changes in $\Delta\lambda_{peak}$ for NAA-RFs without MPTMS functionalization are negligible as compared to NAA-RFs functionalized with MPTMS.

3.2.4. Chemical Selectivity of NAA-RFs toward Hg^{2+}. The chemical selectivity of the presented optical sensing system was analyzed by a series of selectivity tests, in which a MPTMS-modified NAA-RF was exposed to a succession of 2 mM aqueous solutions of Co^{2+}, Mg^{2+}, Ni^{2+}, Cu^{2+}, Pb^{2+}, Fe^{3+}, Ca^{2+}, Cr^{6+}, and Ag^{+} ions, which are common ions present in environmental water. This was followed by final injection of an aqueous solution of 40 μM Hg^{2+} ions. These interfering metal ions were selected as common ions in environmental water, which present low (i.e., Fe^{3+} and Mg^{2+}) and high (i.e., Ag^{+}) affinity toward thiol functional groups. Figure 4a shows a bar graph of $\Delta\lambda_{peak}$ for the aforementioned test. This demonstrates that the highest nonspecific change in $\Delta\lambda_{peak}$ was observed for Ag^{+} and Cu^{2+} analytes (i.e., 1.52 ± 0.04 and 0.66 ± 0.01 nm, respectively). However, when the same sample was exposed to a 40 μM aqueous solution of Hg^{2+} (i.e., concentration 50 times lower), a sharp change in $\Delta\lambda_{peak}$ of 3.20 ± 0.20 nm was observed. This result proves that the proposed optical sensing system is highly selective toward ionic mercury in complex mixtures of metal ions.

3.2.5. Detection of Hg^{2+} in Tap and Environmental Water. To assess the suitability of the proposed optical sensing system for detecting ionic mercury in real-life environmental applications, two model solutions of Hg^{2+} (i.e., 5 and 40 μM) were prepared in tap water (i.e., SA Water, Adelaide) and environmental water collected from a local river (i.e., River

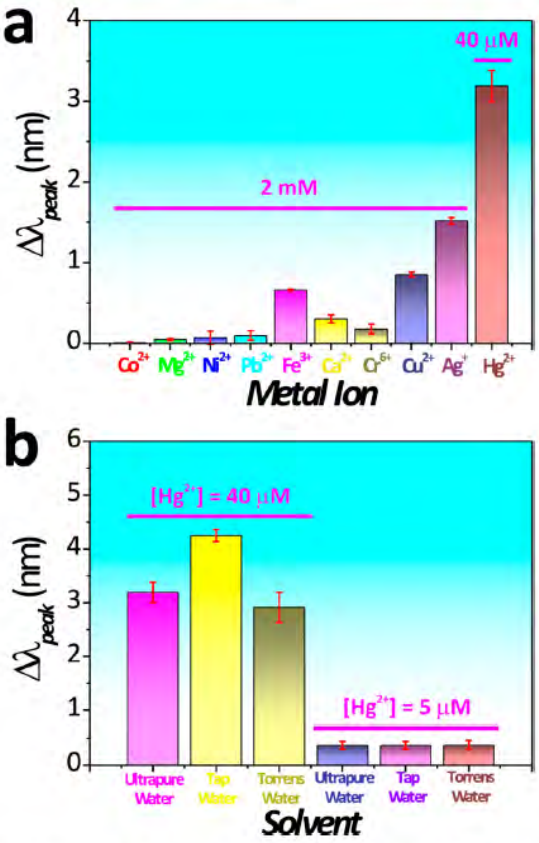

Figure 4. Chemical selectivity and real-life application of the proposed optical sensing system. (a) Bar graph chart showing $\Delta\lambda_{peak}$ after exposure to aqueous solutions of different metal ions. (b) Bar graph chart showing $\Delta\lambda_{peak}$ on exposing a MPTMS-modified NAA-RFs to 5 and 40 μM Hg^{2+} solutions prepared in ultrapure, tap and River Torrens' water, respectively.

Torrens, Adelaide). It is worth mentioning that in these experiments 5 and 40 μM aqueous solutions of Hg^{2+} prepared in ultrapure water were used as control samples. Moreover, a stable baseline was first obtained with the corresponding solvent (i.e., ultrapure, tap or River Torrens' water) for 10 min. After this, the analyte solutions of Hg^{2+} prepared in these solvents were injected into the flow cell. These solvents were also flowed at the end of these processes in order for obtaining the total change in $\Delta\lambda_{peak}$ associated with specific binding of mercury ions to thiol groups. The obtained results revealed that $\Delta\lambda_{peak}$ for 40 μM solutions of Hg^{2+} ions prepared in tap and River Torrens' water were 4.25 ± 0.11 and 2.91 ± 0.28 nm, respectively. This response is slightly higher and lower, respectively, as compared to 3.19 ± 0.19 nm for the same concentration of Hg^{2+} in ultrapure water (i.e., control sample) (Figure 4b). This slight difference in response could be associated with interactions from organic impurities and ionic compounds present in these complex solvents, which interfere slightly the binding affinity between Hg^{2+} ions and thiol functional groups. This difference in $\Delta\lambda_{peak}$, however, became smaller when the concentration of analyte was reduced to 5 μM. In that case, $\Delta\lambda_{peak}$ was the same for all these samples, 0.37 ± 0.07 nm. Examples of real-time RfS response curves for 40 μM Hg^{2+} ions in ultrapure and River Torrens' water are shown in Supporting Information Figure S5. This result verifies that the proposed optical system combined with MPTMS-modified NAA-RFs is able to carry out real-time and label-free detection of ionic mercury in environmental samples without further chemical treatments.

4. CONCLUSIONS

In summary, this study has demonstrated the capability of reflection spectroscopy combined with structurally engineered and chemically modified nanoporous anodic alumina rugate filters for real-time and label-free detection of ionic mercury in complex mixtures of metallic ions and environmental samples (i.e., tap and River Torrens' water). For the first time, NAA-RFs were structurally engineered and chemically modified to produce optical nanostructures with optimized effective medium for sensing applications. Chemical selectivity toward Hg^{2+} ions was achieved through thiol functional groups on MPTMS-modified NAA-RFs. The linear working range of the proposed system for detection of ionic mercury was from 1 to 100 μM, with a low limit of detection of 1 μM (i.e., 200 ppb) and a sensitivity of 0.072 nm μM^{-1}. Furthermore, the binding mechanism of Hg^{2+} ions to thiol functional groups inside the NAA-RF was found to follow a Langmuir isotherm model. Finally, the proposed RfS optical sensing system was capable of selectively detecting mercury ions in complex mixtures of metal ions and environmental samples (i.e., tap and River Torrens water). Although the obtained results are certainly promising and demonstrate the potential capabilities of the proposed system, these reveal that the performance of the proposed system is slightly above the highest mercury levels in drinking water established by the US environmental protection agency (EPA), which is 2 ppb. Nevertheless, it is worth stressing that there is a broad margin to improve the performance of the proposed system by enhancing the surface chemistry and structure of NAA rugate filters. For instance, different functional groups (e.g., oligonucleotides, oligopeptides, etc.) have shown better sensing performances than traditional thiol chemistry by providing more significant changes in the effective refractive index of the sensing platform when mercury ions are immobilized onto the nanoporous network.

The promising sensing performance of the proposed system along with its cost-competitive and scalable fabrication process of its sensing platforms (i.e., NAA-RFs) and portability make it an excellent alternative to current analytical techniques. This system could be at the base of future point-of-analysis systems for monitoring of the quality of environmental water in situ.

■ ASSOCIATED CONTENT

Supporting Information

Further information about FTIR spectra of MPTMS-modified NAA-RFs, the sensing principle of the proposed system, a complete mathematical derivation of Langmuir and Freundlich binding isotherms models, and a control test comparing as-produced and chemically modified NAA-RFs. This material is available free of charge via the Internet at http://pubs.acs.org.

■ AUTHOR INFORMATION

Corresponding Author

*Phone: +61 8 8313 1535. Fax: +61 8 8303 4373. E-mail: abel.santos@adelaide.edu.au. Web page: http://www.adelaide.edu.au/directory/abel.santos.

Author Contributions

T.K., M.M.R., and A.S. contributed equally to this work. The manuscript was written through contributions of all authors. All authors have given approval to the final version of the manuscript.

Notes

The authors declare no competing financial interest.

■ ACKNOWLEDGMENTS

This research was supported by the Australian Research Council (ARC) through the grants number FT110100711 and DE14010054, the Spanish Ministerio de Economía y Competitividad through the grant number TEC2012-34397 and the Generalitat de Catalunya through the grant number 2014 SGR 1344. Authors thank Mr. Jason Peak, Mr. Michael Jung, and Mr. Jeffrey Hiorns from the mechanical workshop of the School of Chemical Engineering (UoA) for their help and support with the fabrication of the experimental set-ups used in this study and the Adelaide Microscopy (AM) centre for FEG-SEM characterisation.

■ ABBREVIATIONS

NAA-RFs, nanoporous anodic alumina rugate filters
pSi, porous silicon
RfS, reflection spectroscopy
S, sensitivity
LoD, limit of detection

■ REFERENCES

(1) UNEP Chemicals Branch. In *UNEP Global Mercury Assessment 2013: Sources, Emissions, Releases and Environmental Transport*; UNEP: Geneva, Switzerland, 2013.
(2) Risher, J.; DeWoskin, R. In *Toxicological Profile for Mercury*; U.S. Department of Health and Human Services, Public Health Service, Agency for Toxic Substances and Disease Registry: Atlanta, GA, U.S.A., 1999.
(3) Kohler, P. M.; Morgera, E.; Ripley, K.; Schabus, N.; Tsioumani, E. Summary of The Fifth Session of The Intergovernmental Negotiating Committee to Prepare a Global Legally Binding Instrument on Mercury. *ENB* 2013, *28*, 1−25.
(4) Hatch, W. R.; Ott, W. L. Determination of Sub-Microgram Quantities of Mercury by Atomic Absorption Spectrophotometry. *Anal. Chem.* 1968, *40*, 2085−2087.
(5) Bloom, N.; Fitzgerald, W. F. Determination of Volatile Mercury Species at The Pictogram Level by Low-Temperature Gas Chromatography with Cold-Vapour Atomic Fluorescence Detection. *Anal. Chim. Acta* 1988, *208*, 151−161.
(6) Zhang, L.; Chang, H.; Hirata, A.; Wu, H.; Xue, Q. K.; Chen, M. Nanoporous Gold Based Optical Sensor for Sub-ppt Detection of Mercury Ions. *ACS Nano* 2013, *7*, 4595−4600.
(7) Ma, W.; Sun, M.; Xu, L.; Wang, L.; Kuang, H.; Xu, C. A SERS Active Gold Nanostar Dimer for Mercury Ion Detection. *Chem. Commun.* 2013, *49*, 4989−4991.
(8) Hoang, C. V.; Oyama, M.; Saito, O.; Aono, M.; Nagao, T. Monitoring The Presence of Ionic Mercury in Environmental Water by Plasmon-Enhanced Infrared Spectroscopy. *Sci. Rep.* 2013, *3*, 1175 −1−3.
(9) Lin, V. S. Y.; Motesharei, K.; Dancil, K. P. S.; Sailor, M. J.; Ghadiri, M. R. A Porous Silicon-Based Optical Interferometric Biosensor. *Science* 1997, *278*, 840−843.
(10) Santos, A.; Kumeria, T.; Losic, D. Optically Optimized Photoluminescent and Interferometric Biosensors Based on Nanoporous Anodic Alumina: A Comparison. *Anal. Chem.* 2013, *85*, 7904−7911.
(11) Santos, A.; Balderrama, V. S.; Alba, M.; Formentín, P.; Ferré-Borrull, J.; Pallarès, J.; Marsal, L. F. Nanoporous Anodic Alumina Barcodes: Toward Smart Optical Biosensors. *Adv. Mater.* 2012, *24*, 1050−1054.
(12) Kumeria, T.; Losic, D. Controlling Interferometric Properties of Nanoporous Anodic Aluminium Oxide. *Nanoscale Res. Lett.* 2012, *7*, 88−1−10.
(13) Wang, G. L.; Zhu, X. Y.; Jiao, H. J.; Dong, Y. M.; Li, Z. J.; Li, Z. J. Ultrasensitive and Dual Functional Colorimetric Sensors for Mercury (II) Ions and Hydrogen Peroxide Based on Catalytic Reduction Property of Silver Nanoparticles. *Biosens. Bioelectron.* 2012, *31*, 337−342.
(14) Wang, G. L.; Xu, X. F.; Cao, L. H.; He, C. H.; Li, Z. J.; Zhang, C. Mercury(II)-Stimulated Oxidase Mimetic Activity of Silver Nanoparticles as a Sensitive and Selective Mercury(II) Sensor. *RSC Adv.* 2014, *4*, 5867−5872.
(15) Pacholski, C.; Sartor, M.; Sailor, M. J.; Cunin, F.; Miskelly, G. M. Biosensing Using Porous Silicon Double-Layer Interferometers: Reflective Interferometric Fourier Transform Spectroscopy. *J. Am. Chem. Soc.* 2005, *127*, 11636−11645.
(16) Pacholski, C.; Yu, C.; Miskelly, G. M.; Godin, D.; Sailor, M. J. Reflective Interferometric Fourier Transform Spectroscopy: A Self-Compensating Label-Free Immunosensor Using Double-Layers of Porous SiO_2. *J. Am. Chem. Soc.* 2006, *128*, 4250−4252.
(17) Orosco, M. M.; Pacholski, C.; Sailor, M. J. Real-Time Monitoring of Enzyme Activity in a Mesoporous Silicon Double Layer. *Nat. Nanotechnol.* 2009, *4*, 255−258.
(18) Pavesi, L.; Dubos, P. Random Porous Silicon Multilayers: Application to Distributed Bragg Reflectors and Interferential Fabry-Pérot Filters. *Semicond. Sci. Technol.* 1997, *12*, 570−575.
(19) Pellegrini, V.; Tredicucci, A.; Mazzoleni, C.; Pavesi, L. Enhanced Optical Properties in Porous Silicon Microcavities. *Phys. Rev. B: Condens. Matter Mater. Phys.* 1995, *52*, R14 328−R14 328.
(20) Pavesi, L.; Guardini, R.; Mazzoleni, C. Porous Silicon Resonant Cavity Light Emitting Diodes. *Solid State Commun.* 1996, *97*, 1051−1053.
(21) Cunin, F.; Schemedake, T. A.; Link, J. R.; Li, Y. Y.; Koh, J.; Bhatia, S. N.; Sailor, M. J. Biomolecular Screening with Encoded Porous-Silicon Photonic Crystals. *Nat. Mater.* 2002, *1*, 39−41.
(22) Ilyas, S.; Böcking, T.; Kilian, K.; Reece, P. J.; Gooding, J. J.; Gaus, K.; Gal, M. Porous Silicon Based Narrow Line-Width Rugate Filters. *Opt. Mater.* 2007, *29*, 619−622.
(23) Kilian, K. A.; Böcking, T.; Ilyas, S.; Gaus, K.; Jessup, W.; Gal, M.; Gooding, J. J. Forming Antifouling Organic Multilayers on Porous Silicon Rugate Filters towards In Vivo/Ex Vivo Biophotonic Devices. *Adv. Funct. Mater.* 2007, *17*, 2884−2890.
(24) Li, Y. Y.; Cunin, F.; Link, J. R.; Gao, T.; Betts, R. E.; Reiver, S. H.; Chin, V.; Bhatia, S. N.; Sailor, M. J. Polymer Replicas of Photonic Porous Silicon for Sensing and Drug Delivery Applications. *Science* 2003, *299*, 2045−2047.
(25) Shang, Y.; Wang, X.; Xu, E.; Tong, C.; Wu, J. Optical Ammonia Gas Sensor Based on a Porous Silicon Rugate Filter Coated with Polymer-Supported Dye. *Anal. Chim. Acta* 2011, *685*, 58−64.
(26) Chapron, J.; Alekseev, S. A.; Lysenko, V.; Zaitsev, V. N.; Barbier, D. Analysis of Interaction between Chemical Agents and Porous Si Nanostructures Using Optical Sensing Properties of Infra-Red Rugate Filters. *Sens. Actuators, B* 2007, *120*, 706−711.
(27) Pacholski, C.; Sailor, M. J. Sensing with Porous Silicon Double Layers: A General Approach for Background Suppression. *Phys. Status Solidi C* 2007, *4*, 2088−2092.
(28) Mubeen, S.; Singh, N.; Lee, J.; Stucky, G. D.; Moskovits, M.; McFarland, E. W. Synthesis of Chemicals Using Solar Energy with Stable Photoelectrochemically Active Heterostructures. *Nano Lett.* 2013, *13*, 2110−2115.
(29) Ghrib, M.; Ouertani, R.; Gaidi, M.; Khedher, N.; Salem, M. B.; Ezzaouia, H. Effect of Annealing on Photoluminescence and Optical Properties of Porous Anodic Alumina Films Formed in Sulfuric Acid for Solar Energy Applications. *Appl. Surf. Sci.* 2012, *258*, 4995−5000.
(30) Sulka, G. D.; Brozózka, A.; Liu, L. Fabrication of Diameter-Modulated and Ultrathin Porous Nanowires in Anodic Aluminium Oxide Templates. *Electrochim. Acta* 2011, *56*, 4972−4979.

(31) Claussen, J. C.; Wickner, M. M.; Fisher, T. S.; Porterfield, D. M. Transforming the Fabrication and Biofunctionalization of Gold Nanoelectrode Arrays into Versatile Electrochemical Glucose Biosensors. *ACS Appl. Mater. Interfaces* **2011**, *3*, 1765−1770.
(32) Sun, L.; Zhang, L.; Liang, C.; Yuan, Z.; Zhang, Y.; Xu, W.; Zhang, J.; Chen, Y. Chitosan Modified Fe^0 Nanowires in Porous Anodic Alumina and Their Application for The Removal of Hexavalent Chromium from Water. *J. Mater. Chem.* **2011**, *21*, 5877−5880.
(33) Franklin, A. D.; Janes, D. B.; Claussen, J. C.; Fisher, T. S.; Sands, T. D. Independently Addressable Fields of Porous Anodic Alumina Embedded in SiO_2 on Si. *Appl. Phys. Lett.* **2008**, *92*, No. 013122.
(34) Rana, K.; Kucukayan-Dogu, G.; Bengu, E. Growth of Vertically Aligned Carbon Nanotubes over Self-Ordered Nano-Porous Alumina Films and Their Surface Properties. *Appl. Surf. Sci.* **2012**, *258*, 7112−7117.
(35) Zhang, Z.; Wang, Q.; Li, G. Fabrication of Novel Nanoporous Array Anodic Alumina Solid-Phase Microextraction Fiber Coating and Its Potential Application for Headspace Sampling of Biological Volatile Organic Compounds. *Anal. Chim. Acta* **2012**, *727*, 13−19.
(36) Claussen, J. C.; Hengenius, J. B.; Wickner, M. M.; Fisher, T. S.; Umulis, D. M.; Porterfield, D. M. Effects of Carbon Nanotube-Tethered Nanosphere Density on Amperometric Biosensing: Simulation and Experiment. *J. Phys. Chem. C* **2011**, *115*, 20896−20904.
(37) Kumeria, T.; Rahman, M. M.; Santos, A.; Ferré-Borrull, J.; Marsal, L. F.; Losic, D. Structural and Optical Nanoengineering of Nanoporous Anodic Alumina Rugate Filters for Real-Time and Label-Free Biosensing Applications. *Anal. Chem.* **2014**, *86*, 1837−1844.
(38) Masuda, H.; Fukuda, K. Ordered Metal Nanohole Arrays Made by a Two-Step Replication of Honeycomb Structures of Anodic Alumina. *Science* **1995**, *268*, 1466−1468.
(39) Masuda, H.; Hasegwa, F. J. Self-Ordering of Cell Arrangement of Anodic Porous Alumina Formed in Sulfuric Acid Solution. *Electrochem. Soc.* **1997**, *144*, L127−L 130.
(40) Masuda, H.; Yada, K.; Osaka, A. Self-Ordering of Cell Configuration of Anodic Porous Alumina with Large-Size Pores in Phosphoric Acid Solution. *Jpn. J. Appl. Phys.* **1998**, *37*, L 1340−L1342.
(41) Nielsch, K.; Choi, J.; Schwirn, K.; Wehspohn, R. B.; Gösele, U. Self-Ordering Regimes of Porous Alumina: The 10% Porosity Rule. *Nano Lett.* **2002**, *2*, 677−680.
(42) Md Jani, A. M.; Kempson, I. M.; Losic, D.; Voelcker, N. H. Dressing in Layers: Layering Surface Functionalities in Nanoporous Aluminum Oxide Membranes. *Angew. Chem., Int. Ed.* **2010**, *49*, 7933−7937.
(43) Santos, A.; Formentín, P.; Pallarès, J.; Ferré-Borrull, J.; Marsal, L. F. Structural Engineering of Nanoporous Anodic Alumina Funnels with High Aspect Ratio. *J. Electroanal. Chem.* **2011**, *655*, 73−78.
(44) Rahman, M. M.; Garcia-Caurel, E.; Santos, A.; Marsal, L. F.; Pallarès, J.; Ferré-Borrull, J. Effect of The Anodization Voltage on The Pore-Widening Rate of Nanoporous Anodic Alumina. *Nanoscale Res. Lett.* **2012**, *7*, 474−1−7.
(45) Jessensky, O.; Müller, F.; Gösele, U. Self-Organized Formation of Hexagonal Pore Arrays in Anodic Alumina. *Appl. Phys. Lett.* **1998**, *72*, 1173−1175.
(46) Schwartz, M. P.; Alvarez, S. D.; Sailor, M. J. Porous SiO_2 Interferometric Biosensor for Quantitative Determination of Protein Interactions: Binding of Protein A to Immunoglobulins Derived from Different Species. *Anal. Chem.* **2007**, *79*, 327−334.

Supporting Information

Nanoporous Anodic Alumina Rugate Filters for Sensing of Ionic Mercury: Toward Environmental Point-of-Analysis Systems

Tushar Kumeria[1], Mohammad Mahbubur Rahman[1,2], Abel Santos[1]*, Josep Ferré-Borrull[2], Lluís F. Marsal[2] and Dusan Losic[1]

[1] School of Chemical Engineering – The University of Adelaide, Adelaide, Australia
[2] Departament d'Enginyeria Electrònica, Elèctrica i Automàtica – Universitat Rovira i Virgili, Tarragona, Spain

***E-Mail:** abel.santos@adelaide.edu.au

Nanoporous Anodic Alumina Rugate Filters for Sensing of Ionic Mercury: Toward Environmental Point-of-Analysis Systems

S1. Validation of Surface Chemistry Functionalisation by FTIR

A MPTMS-modified NAA-RF was analyzed by Fourier transform IR (FTIR) spectroscopy (**Figure S1**). To this end, the remaining aluminium substrate was removed from the NAA-RF backside by wet chemical etching in a saturated solution of (HCl / $CuCl_2$). Notice that the FTIR spectrum of an as-produced NAA-RF was used as a background. FTIR spectra were collected in a FTIR spectrometer (Nexus 6700 Nicolet ThermoFisher). The number of scans was set to 32 with a resolution of 4 cm^{-1}. All spectra were collected in the range 900-4000 cm^{-1} in transmission mode. FTIR spectroscopy data prove the silanization of NAA-RFs. While FTIR peaks at 1460 and 1556 cm^{-1} are associated with nanoporous anodic alumina, the appearance of additional peaks at 2545, 2885 and 2945 cm^{-1} correspond to thiol (–SH) and asymmetric and symmetric vibrations of methylene (-CH_2-) group of propyl chain, respectively. This confirms the presence of MPTMS molecules on the NAA surface.[S1, S2]

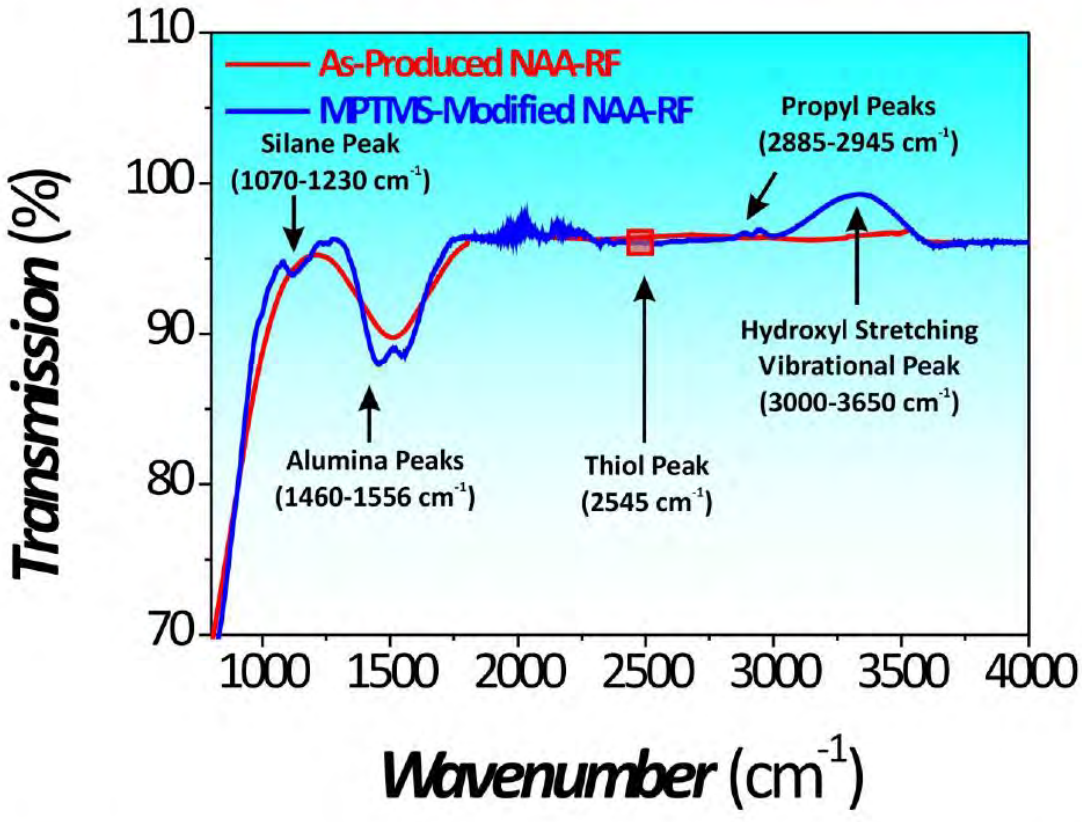

Figure S1. Transmission FTIR spectrum of a MPTMS-modified NAA-RF demonstrating the MPTMS functionalisation.

Nanoporous Anodic Alumina Rugate Filters for Sensing of Ionic Mercury: Toward Environmental Point-of-Analysis Systems

S2. Optical Sensing Principle of NAA-RFs

In this study, the reflection peak position shift ($\Delta\lambda_{peak}$) in the reflection spectrum of NAA-RFs was used as the sensing principle of the proposed system. This analysis can be performed in a flow cell and shifts in the reflection peak position can be monitored in real-time by RfS. **Figure S2** shows an example of this optical principle. It is observed a notorious red shift in the reflection peak position after filling its nanopores with ethanol.

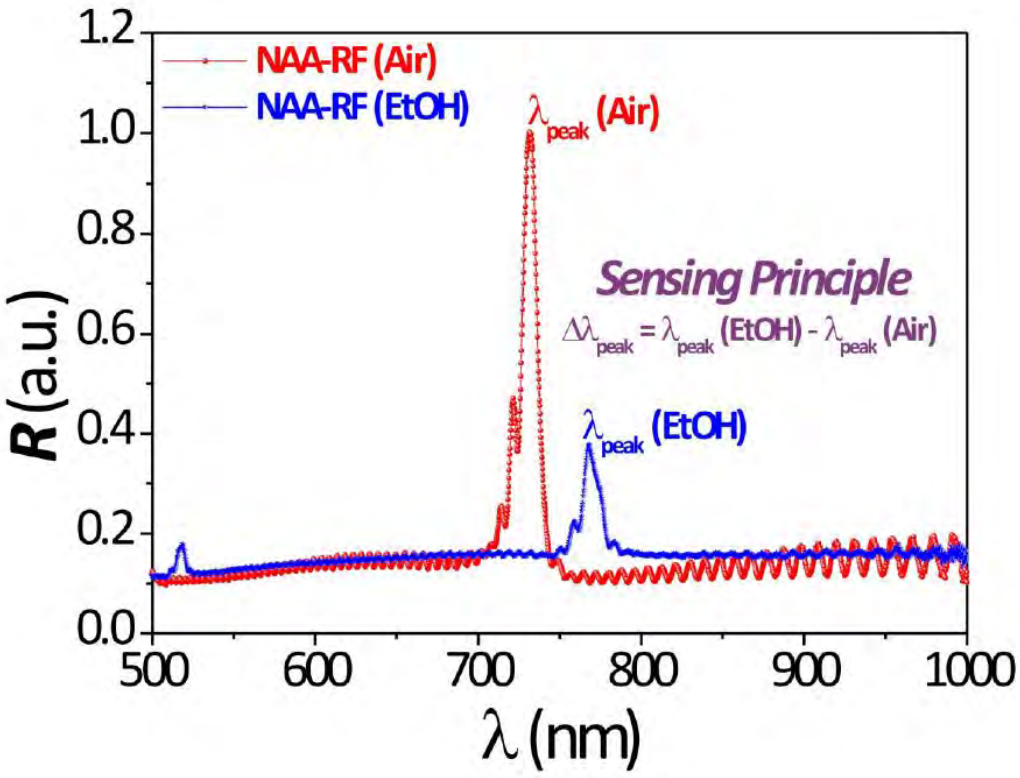

Figure S2. Reflection spectrum of a NAA-RF in air and ethanol showing the sensing principle used in nanoporous anodic alumina rugate filters combined with RfS ($\Delta\lambda_{peak} = \lambda_{peak}$(EtOH) - λ_{peak}(Air)).

Nanoporous Anodic Alumina Rugate Filters for Sensing of Ionic Mercury: Toward Environmental Point-of-Analysis Systems

S3. Mathematical Derivation of Langmuir and Freundlich Binding Isotherms Models

Langmuir and Freundlich isotherm models were used to describe the binding of Hg^{2+} ions on thiol functional groups of MPTMS-modified NAA-RFs. To this end, the experimental data obtained from these experiments were fitted to the above-mentioned models. As for this, notice that the binding reaction of Hg^{2+} ions to thiol functional groups of MPTMS can be defined by **Equation S1**.

$$2R-SH + Hg^{2+} \underset{Kd}{\overset{Ka}{\longleftrightarrow}} R-S-Hg-S-R + 2H^{+} \quad \text{(S1)}$$

where, R–SH represents the available thiol functional groups on the inner surface of NAA-RFs, Hg^{2+} represents the concentration of free mercury ions in the analyte solution, R–S–Hg–S–R is the bound mercury-thiol complex and K_a and K_d are the association and dissociation constants, respectively.[S3]

Considering that $\Delta\lambda_{peak}$ is proportional to the total number of adsorbed molecules of Hg^{2+}, R–S–Hg–S–R is proportional to $\Delta\lambda^{e}_{peak}$, which is the equilibrium value of $\Delta\lambda_{peak}$ for a given [Hg^{2+}]. Similarly, R–SH is proportional to $\Delta\lambda^{m}_{peak}$, which is the maximum value of $\Delta\lambda_{peak}$ for the available binding sites in the NAA-RF surface. Then, after replacing and rearranging **Equation S1**, we obtain **Equation S2**.

$$\Delta\lambda^{e}_{peak} = \Delta\lambda^{m}_{peak} K_L [Hg^{2+}] - \Delta\lambda^{e}_{peak} K_L [Hg^{2+}] \quad \text{(S2)}$$

Further rearrangement of **Equation S2** yields **Equation S3**.

$$\frac{[Hg^{2+}]}{\Delta\lambda^{e}_{peak}} = \frac{1}{\Delta\lambda^{m}_{peak} K_L} + \frac{[Hg^{2+}]}{\Delta\lambda^{m}_{peak}} \quad \text{(S3)}$$

Equation S3 represents a very common form of Langmuir isotherm model adapted for binding Hg^{2+} of with thiol functional groups on the MPTMS-modified surface of NAA-RFs. Therefore, the parameters $1/(K_L \Delta\lambda^{m}_{peak})$ and $1/\Delta\lambda^{m}_{peak}$ can be obtained by a linear fitting between the total shift in the reflection peak position at equilibrium (i.e. end of binding process) and the concentration of mercury ions.

Nanoporous Anodic Alumina Rugate Filters for Sensing of Ionic Mercury: Toward Environmental Point-of-Analysis Systems

Freundlich isotherm model is more suitable for describing binding of molecules on rough surfaces and it assumes that the binding sites increase with increasing the analyte concentration (i.e. $[Hg^{2+}]$ in our case).

The empirical Freundlich equation is given by **Equation S4**.

$$R-S-Hg-S-R = K_f[Hg^{2+}]^{1/n} \quad \text{(S4)}$$

where K_f and 1/n are characteristics constants related to the binding capacity of surface SH groups and the binding intensity, respectively.

Similar to **Equation S2**, R–S–Hg–S–R can be replaced by $\Delta\lambda^e_{peak}$. In this way, the shift in the reflection peak position is directly proportional to the number of surface bound species. Therefore, **Equation S4** can be rewritten as **Equations S5** and **S6**.

$$\Delta\lambda^e_{peak} = K_f[Hg^{2+}]^{1/n} \quad \text{(S5)}$$

$$Log(\Delta\lambda^e_{peak}) = Log(K_f) + \frac{1}{n}Log([Hg^{2+}]) \quad \text{(S6)}$$

Equation S6 represents a very common form of Freundlich isotherm model, the different parameter of which can be obtained by a linear fitting. Values of $Log(K_f)$ and $1/n$ can be estimated by the intercept and slope of a linear fitting between $Log(\Delta\lambda^e_{peak})$ and $Log([Hg^{2+}])$, respectively.

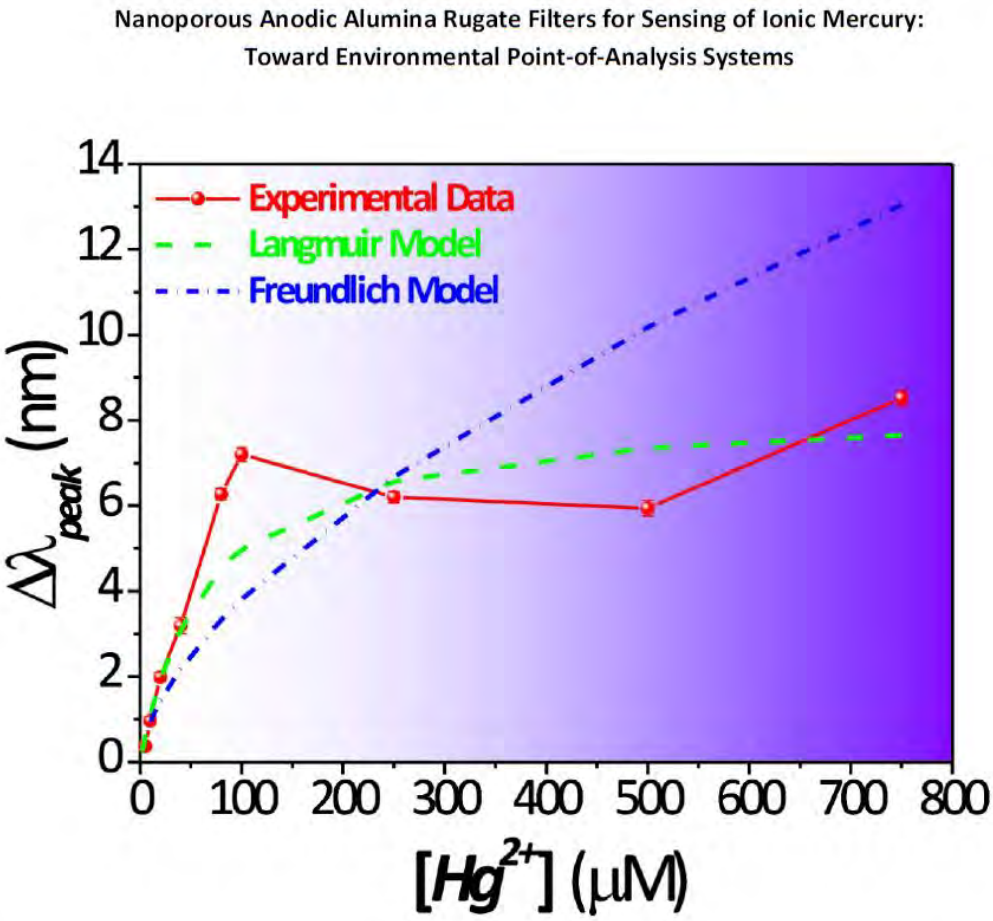

Figure S3. Langmuir and Freundlich binding isotherm fittings and experimental values for binding of Hg^{2+} ions to thiol functional groups on MPTMS-modified NAA-RFs.

Nanoporous Anodic Alumina Rugate Filters for Sensing of Ionic Mercury: Toward Environmental Point-of-Analysis Systems

S4. Control Experiment with Unmodified NAA-RFs

A control experiment was carried out by exposing an as-produced NAA-RF (i.e. NAA-RF without MPTMS functionalisation) to an analyte solution of ionic mercury in ultrapure water. This experiment was performed to confirm that the detection of Hg^{2+} ions is exclusively associated with thiol functional groups of MPTMS functionalities. **Figure S4** presents the real-time RfS response for ionic mercury detection in as-produced and chemically modified NAA-RFs. Notice that a stable base line in ultrapure water was first obtained. This result confirms that a negligible change in $\Delta\lambda_{peak}$ was measured for a 80 μM aqueous solution of mercury ions on an as-produced NAA-RF in comparison to a MPTMS-modified NAA-RF.

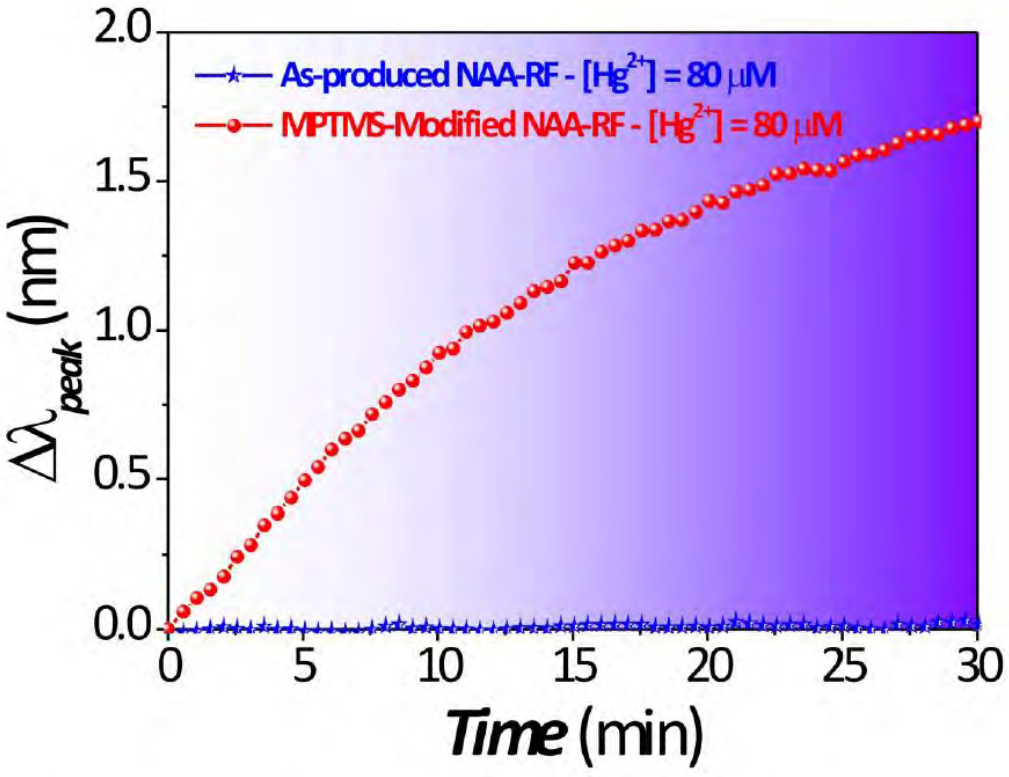

Figure S4. Comparison of chemical selectivity of as-produced and MPTMS-modified NAA-RFs towards a 80 μM aqueous solution of Hg^{2+}.

Nanoporous Anodic Alumina Rugate Filters for Sensing of Ionic Mercury: Toward Environmental Point-of-Analysis Systems

S5. Real-Time Optical Sensing of Hg^{2+} in Environmental Water

A comparison of real-time RfS response curves for 40 μM Hg^{2+} ions in ultrapure and River Torrens' water is shown in **Figure S5**.

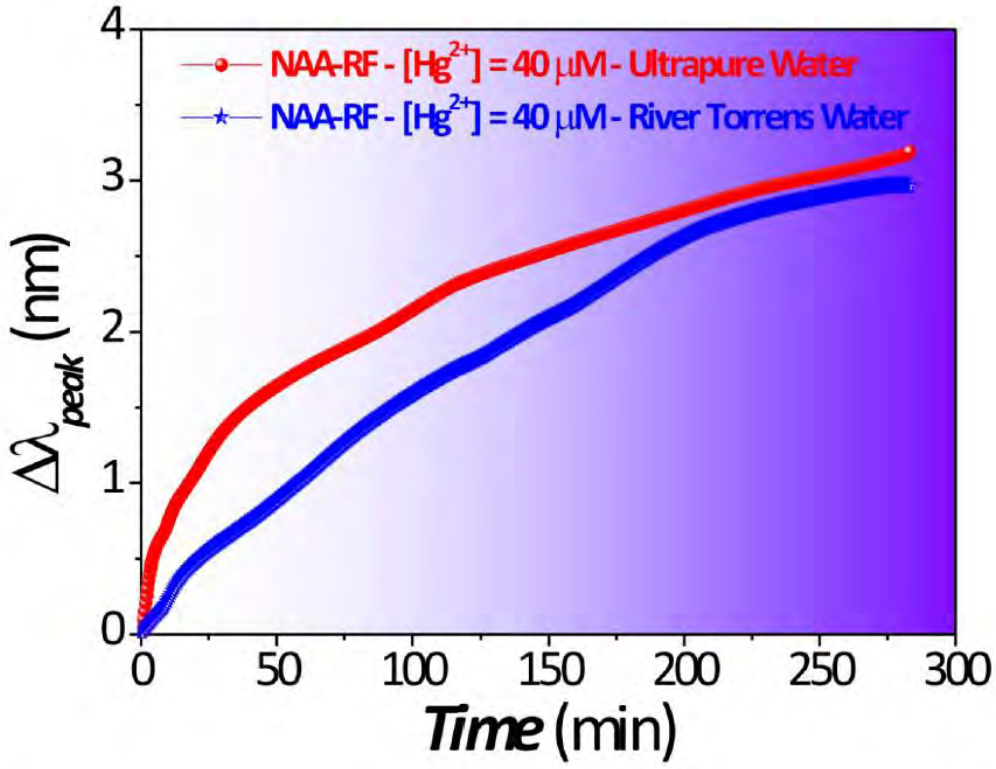

Figure S5. Real-time monitoring of 40 μM Hg^{2+} analyte solutions prepared in ultrapure and River Torrens' water showing the real-life application of the proposed sensing system

S6. References

S1. H. Shiraki, Y. Kimura, H. Ishii, S. Ono, K. Itaya and M. Niwano, *Appl. Surf. Sci.*, 2004, **237**, 369.

S2. J. Wang, S. Yang, X. Liu, S. Ren, F. Guan and M. Chen, *Appl. Surf. Sci.*, 2004, **221**, 272.

S3. Z. Chen, W. Ma and M. Han, *J. Haz. Mater.*, 2008, **155**, 327.

CHAPTER 6

ADVANCED STRUCTURAL DESIGN of NANOPOROUS PHOTONIC STRUCTURES: MODULATING NANOPORE ARCHITECTURE to ENHANCE SENSING PROPERTIES

Tushar Kumeria

School of Chemical Engineering, The University of Adelaide South Australia 5005, Australia

This chapter is based on the following peer-reviewed article:

T. Kumeria, A. Santos, M. M. Rahman, J. Ferre-Borrull, L. F. Marsal, D. Losic "Advanced structural design of nanoporous photonic structures: Modulating nanopore architecture to enhance sensing properties" *ACS Photonics,* 2014, **1**, 1298.

Statement of Authorship

Advanced structural design of nanoporous photonic structures: Modulating nanopore architecture to enhance sensing properties. *ACS Photonics*, 2014, **1**, 1298.

Tushar Kumeria (Candidate)

Under supervision of D. Losic and A. Santos, I developed, designed, and performed the experiments, interpreted and processed the data and contributed in writing the manuscript for submission.

Signed Date:10/04/2015

Abel Santos

I acted as secondary supervisor for the candidate and aided in development and design of the experiments, and writing and evaluation of manuscript for submission. I give consent for Tushar Kumeria to present this paper for examination towards the Doctorate of philosophy.

Signed Date: 10/04/2015

Dusan Losic

I acted as primary supervisor of the candidate and aided in evaluation of experimental design and manuscript for submission. I give consent for Tushar Kumeria to present this paper for examination towards the Doctorate of philosophy

Signed Date: 10/04/2015

Mahbub M. Rahman

I acted as a collaborator (from Universitat Rovira i Virgili, Spain) on this work and provided the process for anodization of Al to produce NAA rugate filters evaluation of manuscript for submission. I give consent for Tushar Kumeria to present this paper for examination towards the Doctorate of philosophy

Signed Date: 30/03/2015

Joseph Ferre-Borrull

I acted as a collaborator (from Universitat Rovira i Virgili, Spain) and supervisor of M. M. Rahman and aided in development of Labview program used for anodization of Al for producing NAA rugate filters evaluation of manuscript for submission. I give consent for Tushar Kumeria to present this paper for examination towards the Doctorate of philosophy

Signed Date: 30/03/2015

Luis. F. Marsal

I acted as a collaborator (from Universitat Rovira i Virgili, Spain) and supervisor of M. M. Rahman and aided in designing and evaluation of experiments and manuscript for submission. I give my consent for Tushar Kumeria to present this paper for examination towards the Doctorate of Philosophy.

Signed Date: 30/03/2015

ACS Photonics

Article

pubs.acs.org/journal/apchd5

Advanced Structural Engineering of Nanoporous Photonic Structures: Tailoring Nanopore Architecture to Enhance Sensing Properties

Tushar Kumeria,[†,§] Abel Santos,[*,†,§] Mohammad Mahbubur Rahman,[†,‡] Josep Ferré-Borrull,[‡] Lluís F. Marsal,[‡] and Dusan Losic[†]

[†]School of Chemical Engineering, The University of Adelaide, Adelaide, SA 5005, Australia

[‡]Departament d'Enginyeria Electrònica, Elèctrica i Automàtica, Universitat Rovira i Virgili, Avda Països Catalans 26, 43007 Tarragona, Spain

Supporting Information

ABSTRACT: In this study, we demonstrate that an optimal design of the pore geometry and shape of sensing platforms based on nanoporous anodic alumina (NAA) photonic structures is critical to develop optical sensors with improved capabilities. To this end, two types of NAA photonic structures featuring different pore geometries (i.e., pore lengths and diameters) and shapes (i.e., straight and modulated pores) were produced, and their optical characteristics were assessed systematically by reflectometric interference spectroscopy. The geometric features (i.e., pore lengths, diameters, and shapes) were systematically modified in order to establish the optimization paths for the sensitivity, low limit of detection, and linearity of these optical sensing platforms. The obtained results reveal that an optimal design of these nanoporous photonic structures can enhance their sensitivity, achieve a lower limit of detection, and improve their linearity for both nonspecific and specific detection of analytes. Therefore, as this study demonstrates, the rational design of optical nanoporous sensing platforms is critical in the development of reliable, sensitive, robust, inexpensive, and portable optical systems for a broad range of sensing applications.

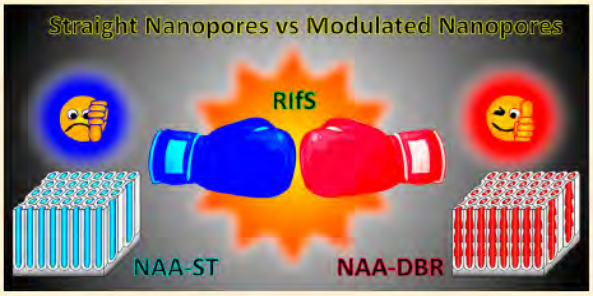

KEYWORDS: *nanoporous anodic alumina, photonics, structural engineering, pore geometry, reflectometric interference spectroscopy*

Currently, optical sensing devices are present in more places of our ordinary lives than ever before. As an example, the advent of smart phones has devised a plethora of new possibilities toward the development of all-in-one analytical devices for real-life applications, which could range from water quality analysis (e.g., detection of levels of heavy metal ions in water) to self-diagnosis (e.g., quantification of levels of glucose in blood).[1−4] Although this technology is still at its beginnings, more exciting developments are expected to be done in the next years. Before this technology becomes feasible and reliable, however, more extensive fundamental research must be carried out in order to make individual components efficient, reliable, sensitive, selective, and inexpensive.

Basically, an optical sensor is composed of a light source, where the optical wave is generated, a sensing platform, where the interaction between light and matter takes place, and a detector, which measures the optical signal shift (i.e., sensing principle).[5] Among these components, the sensing platform plays a critical role as light interacts with analyte molecules present in its effective medium, producing quantifiable changes in the characteristic optical signal of the sensing platform. Subsequently, these changes can be quantitatively (concentration) and/or qualitatively (spectral signature) estimated by the detector. Typically, sensing platforms are based on optically active or passive materials, the function of which is to guide, reflect, absorb, transmit, emit, or enhance the incident light emitted by the source. As far as the different materials used to develop optical sensing platforms is concerned, nanomaterials have enabled the development of highly sensitive and sophisticated systems such as surface-enhanced Raman spectroscopy (SERS), surface plasmon resonance spectroscopy (SPR), localized surface plasmon resonance spectroscopy (LSPR) and others.[6−15] These optical techniques can achieve detection limits as low as single molecules through the amplification of electromagnetic fields generated by the excitation of localized surface plasmons.[16] Another example of a sensitive optical technique extensively used to develop optical sensors is reflectometric interference spectroscopy (RIfS).[17−19] RIfS relies on the constructive interference of reflected light, which takes place when a white light beam interacts with a thin

Received: August 27, 2014
Published: November 17, 2014

   dx.doi.org/10.1021/ph500316u | *ACS Photonics* 2014, 1, 1298−1306

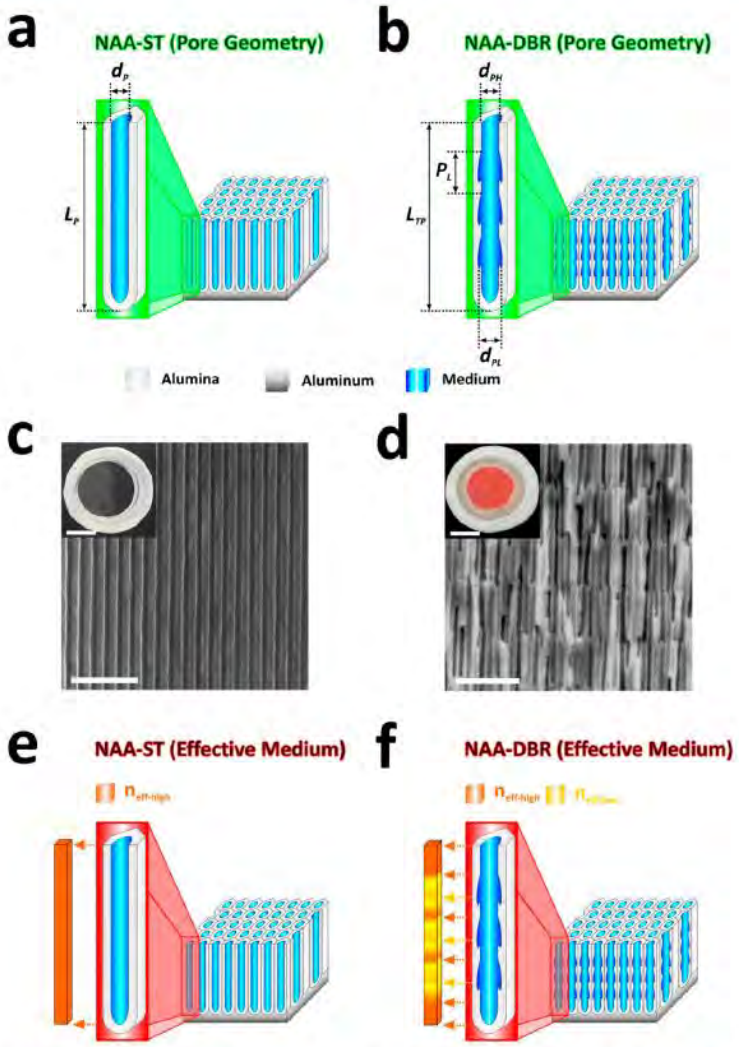

Figure 1. Structural and optical characteristics of photonic structures based on nanoporous anodic alumina. (a, b) Illustrations depicting the representative geometric features of NAA-ST and NAA-DBR platforms, respectively. (c, d) Cross-section SEM images of NAA-ST and NAA-DBR photonic structures, respectively (scale bars = 500 nm). The insets show digital images of these photonic structures after the aluminum substrate was selectively removed from the back side by chemical etching (scale bar = 0.5 cm). (e, f) Schemes showing the relationship between the effective medium and the pore geometry in NAA-ST and NAA-DBR platforms, respectively.

film. This optical technique, which is typically implemented into low-cost miniature spectrometers, can be combined with nanoporous materials such as nanoporous anodic alumina (NAA) in order to develop highly sensitive and reliable optical sensing systems.[20−23] NAA is a nanoporous material produced by electrochemical anodization of aluminum and presents many interesting advantages for the development of optical sensing platforms.[24−28] Some assets of NAA are a cost-competitive and industrially scalable fabrication process, stable optical signals without passivation, controllable and versatile pore geometry, chemical and physical stability, mechanical robustness, easy chemical functionalization, and the capability to guide, reflect, transmit, emit, and enhance incident light by engineering its nanoporous structure through different anodization approaches.[29,30] For these reasons, NAA has been recently envisaged for the development of low-cost, portable, and highly sensitive optical sensing platforms featuring up-to-the-minute capabilities.[31−33] Regardless of the recent use of NAA as a sensing platform, more extensive fundamental research must be carried out in order to establish the optimization paths toward NAA photonic structures with improved optical properties for sensing applications.

Herein we present a detailed study assessing the optical characteristics and sensing performances of two types of NAA photonic structures featuring different pore geometries and shapes. Our study demonstrates that the sensing properties of these photonic structures can be substantially improved by engineering their nanoporous structure.

RESULTS AND DISCUSSION

Fabrication and Structural Characterization of NAA Photonic Structures. Figure 1 illustrates the structures of the two different types of NAA sensing platforms assessed in this study, which were fabricated by electrochemical anodization of aluminum chips under potentiostatic conditions. The former

type of NAA photonic structure, straight NAA (NAA-ST), was produced by anodizing aluminum chips at constant voltage through a symmetric two-step anodization approach.[24−28] NAA-ST samples featured straight cylindrical nanopores from top to bottom and thus constant effective refractive index (n_{eff}) along the nanopores. The latter type of NAA photonic structure, NAA distributed Bragg reflector (NAA-DBR), featured a modulated pore diameter in depth and was produced by a pseudosinusoidal anodization profile (i.e., shifting between high and low anodization voltages) through a modified two-step approach reported elsewhere.[34,35] These NAA photonic structures presented a modulated effective refractive index in depth that was switched between high ($n_{eff\text{-}high}$, low anodization voltage) and low ($n_{eff\text{-}low}$, high anodization voltage) by means of the anodization profile. More detailed information on the fabrication processes of the NAA-ST and NAA-DBR platforms is included in Methods and Figure S1 in the Supporting Information.

The pore lengths of NAA-ST and NAA-DBR platforms were set to four different values (i.e., 30, 35, 40, and 45 μm) by modifying the time of the second anodization step (t_{AN}). It should be noted that in the case of NAA-DBR these pore lengths corresponded to 125, 150, 175, and 200 periods, respectively. Furthermore, the nanopores of as-produced NAA-ST and NAA-DBR platforms were widened by wet chemical etching to obtain four different pore diameters, which corresponded to four different pore widening time lengths (i.e., t_{PW} = 0, 8, 16, and 24 min). Therefore, a total of 16 samples of each type of NAA structure were used in this study, allowing us to assess the sensing characteristics of these photonic structures as a function of their pore geometry and shape within the aforementioned range of geometric features. As far as the different geometric features of these platforms is concerned, whereas the structure of NAA-ST can be defined by the pore length (L_P) and the pore diameter (d_P), the geometric features of NAA-DBR are the total pore length (L_{TP}), the pore diameters, which vary periodically from big to small according to the periodic high and low effective refractive indexes, respectively (d_{PH} with $n_{eff\text{-}high}$ and d_{PL} with $n_{eff\text{-}low}$), and the period length (P_L) (Figure 1a,b). The different geometric characteristics of the NAA-ST and NAA-DBR platforms were established by scanning electron microscopy (SEM) image analysis, and Table 1 summarizes the relationships between fabrication parameters and geometric features.[36]

Table 1. Fabrication Parameters and Geometric Features of NAA-ST and NAA-DBR Photonic Structures Assessed in This Study

NAA-ST			
t_{AN} (h)	L_P (μm)	t_{PW} (min)	d_P (nm)
9.5	30 ± 1	0	21 ± 2
11.3	35 ± 1	8	31 ± 1
13.0	40 ± 1	16	44 ± 2
14.5	45 ± 1	24	56 ± 1

NAA-DBR					
period	L_{PT} (μm)	P_L (nm)	t_{PW} (min)	d_{PH} (nm)	d_{PL} (nm)
125	30 ± 1	171 ± 14	0	18 ± 3	30 ± 4
150	35 ± 1	171 ± 14	8	21 ± 4	38 ± 6
175	40 ± 1	171 ± 14	16	31 ± 3	49 ± 4
200	45 ± 1	171 ± 14	24	42 ± 3	69 ± 9

Figure 1c,d shows cross-section SEM images of the resulting NAA-ST and NAA-DBR structures as well as digital images of these NAA photonic structures. Figure 1c reveals that the NAA-ST structures featured cylindrical nanopores from top to bottom and were transparent, allowing light to pass through so that objects behind were distinctly seen (Figure 1c inset). However, as Figure 1d shows, NAA-DBR platforms presented periodically modulated pore diameters in depth and had red color due to structural coloring associated with light reflection phenomenon (Figure 1d inset).[37] It is worthwhile to note that the structure of the NAA-DBR platform can be tuned in order to reflect light at specific wavelengths within the visible light range.[38] This can be achieved by applying different anodization profiles and by pore widening, which are translated into the nanoporous structure of the photonic platform and thus into its effective refractive index (Figure 1e,f).

Sensing Principles and Optical Assessment of NAA-ST and NAA-DBR Photonic Structures. *Sensing Principles.* Figure 2a,b depicts the sensing principles of NAA-ST and NAA-DBR platforms after their nanopores were infiltrated with water and ethanol. It is well-known that an increment of the effective medium of nanoporous films leads to a red shift in their RIfS spectra (i.e., a shift toward longer wavelengths). In the case of NAA-ST platforms, this shift can be quantified by means of the effective optical thickness change (ΔOT_{eff}), which can be calculated by applying a fast Fourier transform (FFT) to the RIfS spectrum.[39−41] As far as the sensing principle in NAA-DBR platforms is concerned, this is based on changes in the characteristic reflection peak position ($\Delta\lambda_{peak}$) in their RIfS spectra.[42,43] In our study, we used these sensing principles in order to evaluate the optical characteristics of these photonic structures and find the optical optimization paths toward NAA platforms with optimized properties for sensing purposes in the UV−vis range. It should be noted that in the context of our study, the optical optimization paths for the sensing characteristics of NAA-ST and NAA-DBR structures were established using a total of 16 samples of each type of NAA photonic structure.

Optical Assessment under Nonspecific Adsorption Conditions. To assess the optical properties of the NAA-ST and NAA-DBR photonic platforms under nonspecific adsorption conditions, we modified the effective medium of these nanoporous structures by infiltrating their nanopores with different aqueous solutions of glucose ($C_6H_{12}O_6$) (i.e., 0.01, 0.05, 0.1, 0.2, 0.5, and 1.0 M), which provided different levels of refractive index (i.e., 1.333, 1.334, 1.336, 1.339, 1.349, and 1.363 refractive index units (RIU), respectively). In this process, the RIfS spectra of these NAA platforms were monitored in real time using a flow cell combined with a RIfS system (Figure 2c). Glucose solutions were flowed through the flow cell, where the NAA platforms were placed, and changes in the effective medium of these photonic structures produced shifts in their RIfS spectra. These changes, monitored in real time, were recorded and converted into ΔOT_{eff} and $\Delta\lambda_{peak}$, which were subsequently assessed in order to establish and compare the different optical characteristics of NAA-ST and NAA-DBR photonic structures, respectively. Examples of real-time monitoring of ΔOT_{eff} and $\Delta\lambda_{peak}$ are included in Figure S2 in the Supporting Information.

Figure 3 summarizes the obtained results, showing the linear fits between the optical parameters (i.e., ΔOT_{eff} and $\Delta\lambda_{peak}$ for the NAA-ST and NAA-DBR platforms, respectively) and the refractive indexes of glucose solutions as a function of the pore

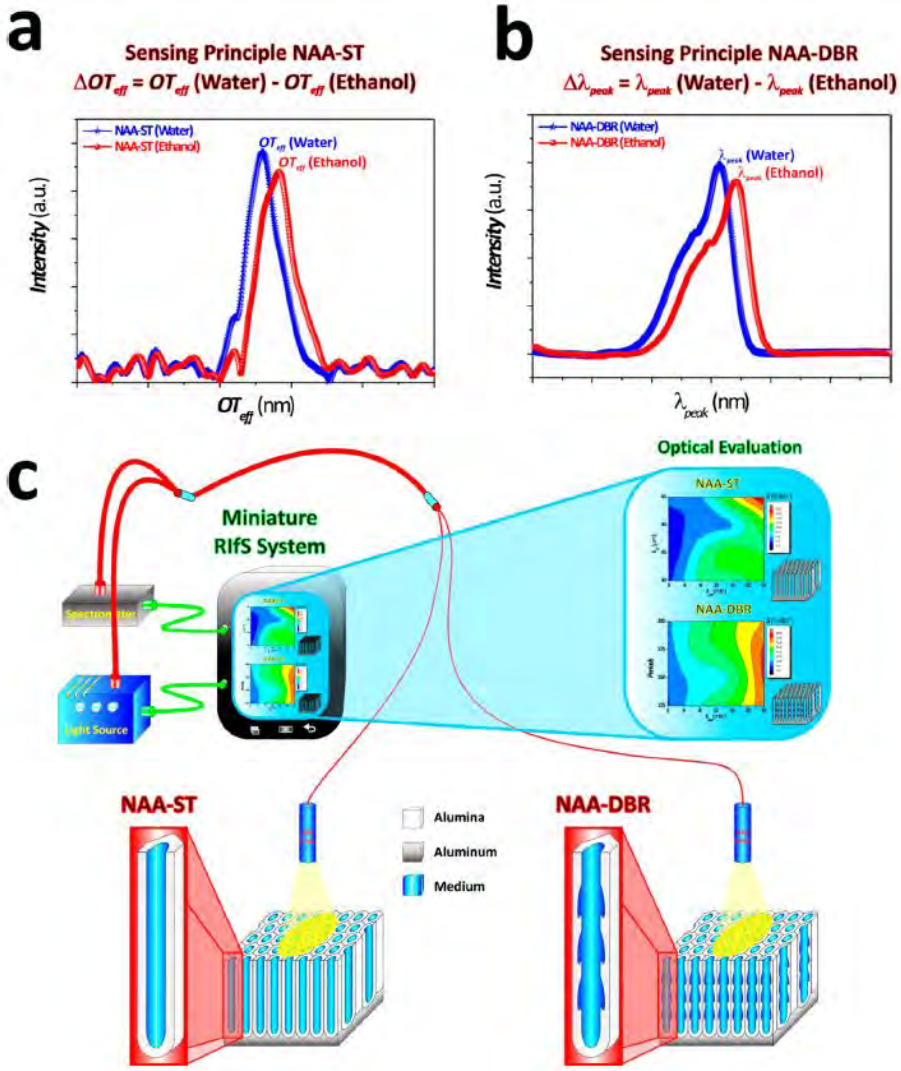

Figure 2. Sensing principles and experimental setup used in this study to assess the optical characteristics of NAA photonic structures. a-b) Sensing principles of NAA-ST and NAA-DBR photonic structures in RIfS based on changes in the effective optical thickness (ΔOT_{eff}) and shifts in the characteristic peak position ($\Delta\lambda_{peak}$), respectively. c) Experimental optical setup composed of tablet, light source, spectrometer, optical probes and NAA photonic structures.

length (i.e., the number of periods for NAA-DBR platforms) and the pore widening time. At first sight it is observed that the sensitivity of these photonic structures (i.e., the slope of the linear fit) increases with the pore widening time (i.e., bigger pores). In order to gain insight into these results, find out the optimization paths, and provide an objective comparison between these two photonic structures, we expressed changes in OT_{eff} and λ_{peak} in terms of percentage. Figure 4 presents contour plots of the different sensing characteristics (i.e., sensitivity (S), low limit of detection (LoD), and linearity (R^2)) of NAA-ST and NAA-DBR platforms along with the optimization paths for each of these parameters. Likewise in a topographic map, each optimization path was established by following the path with the highest slope between the lowest and highest values of the corresponding sensing parameter. Table 2 summarizes the geometric characteristics of these NAA-ST and NAA-DBR platforms, presenting the most optimal optical characteristics obtained from this analysis.

Figure 4a,b shows the dependence of the sensitivity on the pore length (i.e., number of cycles for NAA-DBR platforms) and the pore widening time for NAA-ST and NAA-DBR platforms, respectively. It is observed that in terms of sensitivity the two photonic structures present similar patterns of dependence with these geometric features. In other words, the lines between color fields are closer to each other in a similar manner and the distribution of color fields is fairly homogeneous in both cases, indicating that S changes smoothly with the pore geometry. Nevertheless, the sensitivity of NAA-DBR platforms (i.e., 34.35 ± 1.16% RIU^{-1}) is almost 2-fold higher than that of NAA-ST platforms (i.e., 18.42 ± 0.35% RIU^{-1}). Furthermore, the white arrows in Figure 4a,b depict the sensitivity optimization paths in NAA-ST and NAA-DBR photonic structures. From this, we established the highest sensitivities for NAA-ST and NAA-DBR platforms, which were achieved at (L_P = 45 ± 1 μm ; t_{PW} = 24 min) and (L_{TP} = 40 ± 1 μm (175 periods); t_{PW} = 24 min), respectively.

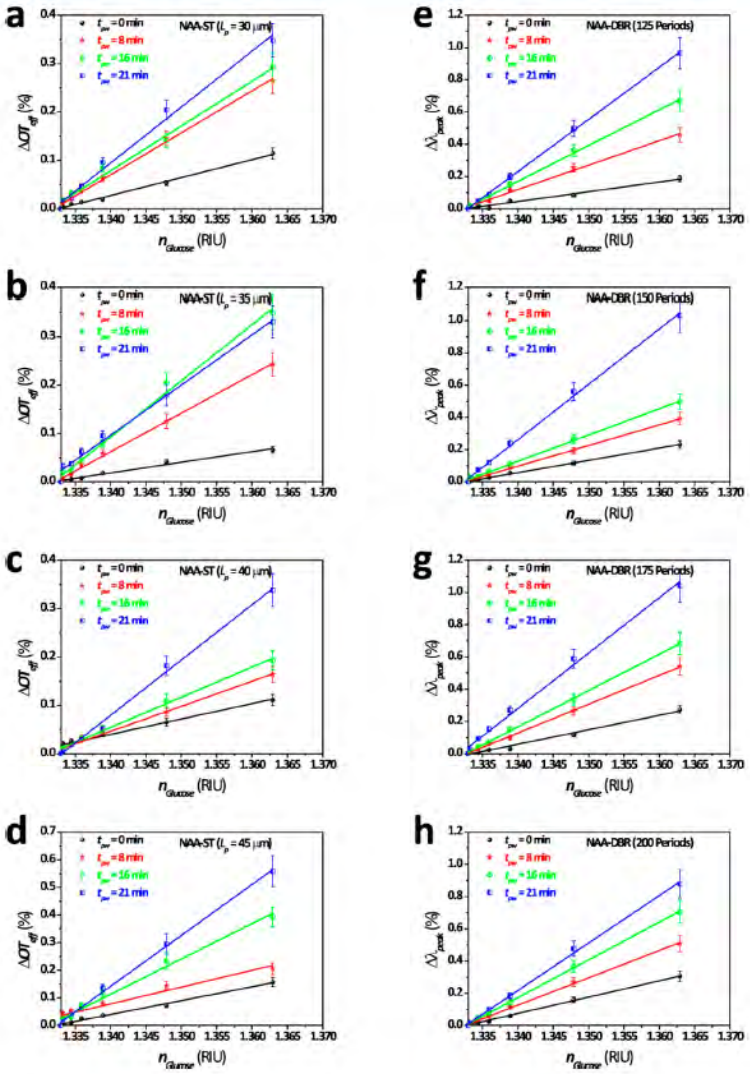

Figure 3. Optical assessment of (a–d) NAA-ST and (e–h) NAA-DBR photonic structures by measuring ΔOT_{eff} and $\Delta\lambda_{peak}$, respectively, as functions of the geometric characteristics and the refractive index of glucose solutions.

As far as the low limit of detection is concerned, Figure 4c,d illustrates the dependence of LoD (calculated as 3σ and expressed in RIU) on the pore length and the pore widening time for NAA-ST and NAA-DBR photonic structures, respectively. These contour plots show that both NAA structures present primary and secondary optimization paths and that the dependence of the LoD on the geometric features of NAA-ST and NAA-DBR is much more heterogeneous than that shown for S (i.e., heterogeneous distribution of color fields). In the case of NAA-ST platforms, the lowest LoD value (i.e., 0.084 RIU) is achieved at (L_P = 45 ± 1 μm; t_{PW} = 24 min), with a secondary minimum of LoD (i.e., 0.103 RIU) at (L_P = 30 ± 1 μm; t_{PW} = 8 min). For NAA-DBR platforms, the lowest LoD value (i.e., 0.040 RIU) is obtained at (L_{TP} = 30 ± 1 μm (125 periods); t_{PW} = 24 min), with a secondary LoD minimum (i.e., 0.052 RIU) at (L_{TP} = 45 ± 1 μm (200 periods); t_{PW} = 16 min). Again, these results verify that NAA-DBR photonic structures can achieve much lower LoD than NAA-ST platforms.

Figure 4e,f depicts the relationship between the linearity and the pore geometry for NAA-ST and NAA-DBR platforms, respectively. As in the case of the LoD, these contour plots reveal that both NAA platforms present primary and secondary optimization paths and a heterogeneous distribution of color fields with the geometric features. The highest linearity in NAA-ST platforms (i.e., 0.998) is achieved at (L_P = 45 ± 1 μm; t_{PW} = 24 min), with a secondary maximum (i.e., 0.997) at (L_P = 35 ± 1 μm; t_{PW} = 8 min). In the case of NAA-DBR photonic structures, R^2 achieves its highest value (i.e., 0.999) at (L_{TP} = 45 ± 1 μm (200 periods); t_{PW} = 8 min), with a secondary maximum (i.e., 0.999) at (L_{TP} = 40 ± 1 μm (175 periods); t_{PW} = 0 min). Although both sensing platforms present excellent linearity, these results verify that NAA-DBR platforms are slightly more linear than NAA-ST platforms.

Optical Assessment under Specific Adsorption Conditions. Finally, NAA-ST and NAA-DBR photonic platforms were assessed when detecting mercury ions (Hg^{2+}) in water under specific adsorption conditions. To this end, the surface of these

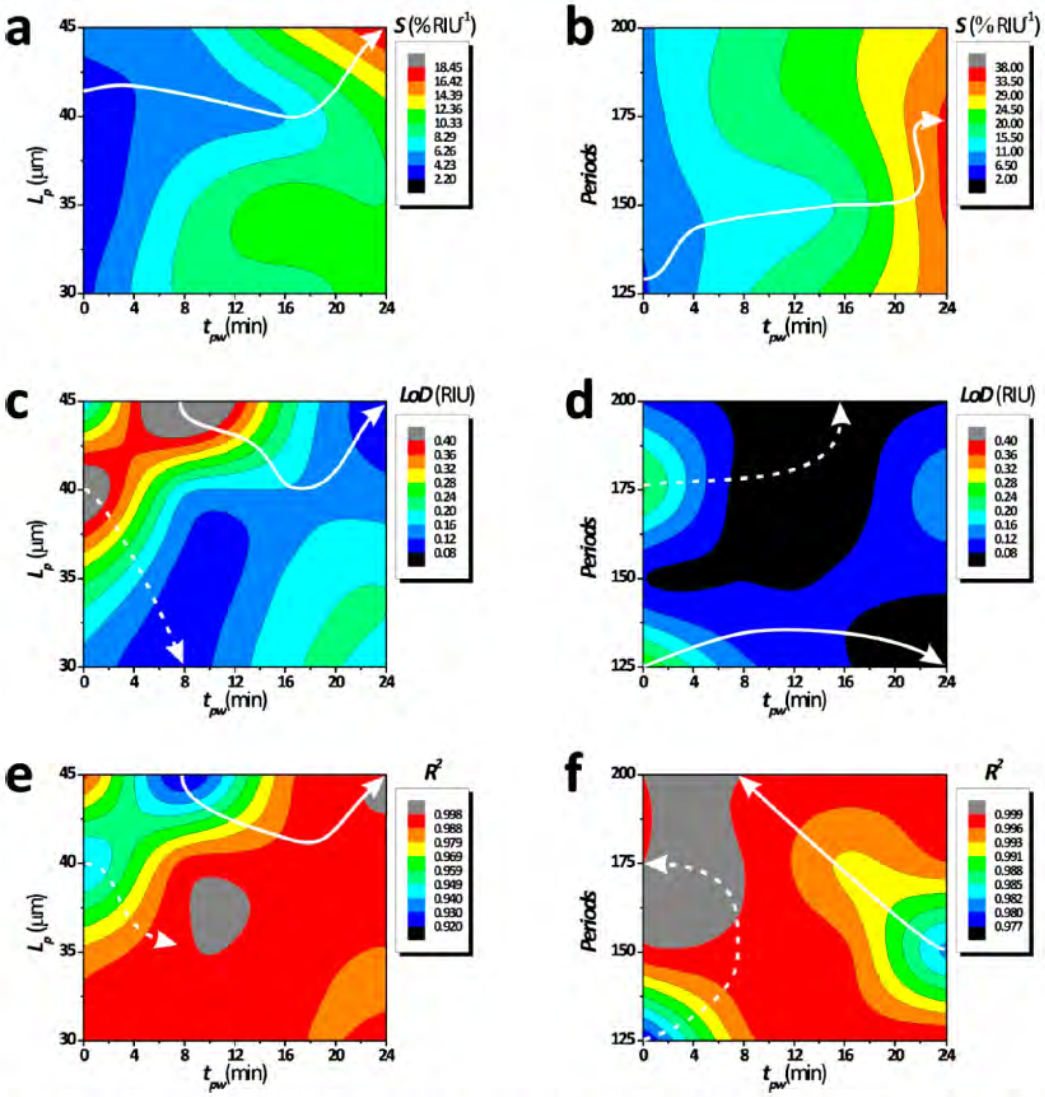

Figure 4. Contour plots showing the optical optimization paths for sensitivity (S), low limit of detection (LoD), and linearity (R^2) in (a, c, e) NAA-ST and (b, d, f) NAA-DBR photonic structures as assessed by RIfS: (a, b) sensitivity in terms of change in sensing parameter (i.e., ΔOT_{eff} or $\Delta\lambda_{peak}$), expressed in percentage per refractive index unit; (c, d) low limit of detection, calculated as 3σ and expressed in refractive index units; (e, f) linearity, calculated as the correlation coefficient. White arrows denote the different optimization paths for S, LoD, and R^2 (solid lines = primary optimization paths and dashed lines = secondary optimization paths).

Table 2. Summary of Geometric and Optical Characteristics of NAA-ST and NAA-DBR Photonic Structures with the Best Optical Performance

optical platform	optical parameter	value	geometric features
NAA-ST	S	18.42 ± 0.35 % RIU^{-1}	L_P = 45 ± 1 μm; d_P = 56 ± 1 nm
NAA-DBR	S	34.35 ± 1.16 % RIU^{-1}	L_{TP} = 40 ± 1 μm (175 periods); d_{PH} = 42 ± 3 nm; d_{PL} = 69 ± 9 nm
NAA-ST	LoD	0.084 RIU	L_P = 45 ± 1 mm ; d_P = 56 ± 1 nm
NAA-DBR	LoD	0.040 RIU	L_{TP} = 30 ± 1 μm (125 periods); d_{PH} = 42 ± 3 nm; d_{PL} = 69 ± 9 nm
NAA-ST	R^2	0.998	L_P = 45 ± 1 mm; d_P = 56 ± 1 nm
NAA-DBR	R^2	0.999	L_{TP} = 45 ± 1 μm (200 periods); d_{PH} = 21 ± 4 nm; d_{PL} = 38 ± 6 nm

NAA structures was functionalized via silanization with thiol functional groups through a well-established protocol reported elsewhere[44] (see Methods). This modification endowed these sensing platforms with chemical selectivity toward ionic mercury, which was achieved by the affinity between thiol groups and mercury ions (Figure 5a). Six different concentrations of mercury ions were used in this study (i.e., 1, 5, 10, 20, 40, and 80 μM), and the geometric features of the photonic platforms assessed in this study were set to L_P = 35 ± 1 μm and d_P = 44 ± 2 nm for NAA-ST and L_{TP} = 35 ± 1 μm (150

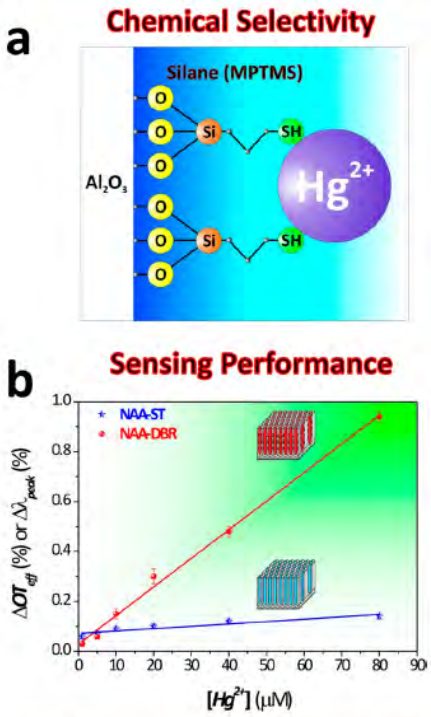

Figure 5. Optical assessment of NAA-ST and NAA-DBR photonic structures by RIfS in detection of mercury ions (Hg^{2+}) in water. (a) Scheme illustrating the surface chemistry modification using thiol chemistry to endow NAA-ST and NAA-DBR photonic structures with chemical selectivity toward ionic mercury. (b) Calibration curves showing the sensing performance of NAA-ST and NAA-DBR photonic structures as a function of the analyte concentration ($[Hg^{2+}]$).

periods), d_{PH} = 31 ± 3 nm, and d_{PL} = 49 ± 4 nm for NAA-DBR. As Figure 5b shows, the sensing performance of NAA-DBR photonic structures was found to be significantly better than that of NAA-ST platforms. Table 3 summarizes the

Table 3. Summary of the Sensing Characteristics of NAA-ST and NAA-DBR Photonic Structures Assessed for the Detection of Ionic Mercury in Water

optical platform	S (% μM^{-1})[a]	LoD (μM)	R^2
NAA-ST	0.0009 ± 0.0002	22.82	0.854
NAA-DBR	0.0115 ± 0.0004	4.20	0.994

[a]Sensitivity expressed in terms of the change in the corresponding sensing parameter (i.e., ΔOT_{eff} or $\Delta\lambda_{peak}$) in units of percentage per analyte concentration unit.

obtained results, which reveal that whereas NAA-DBR photonic structures present a sensitivity of 0.0115 ± 0.0004% μM^{-1}, NAA-ST structures have a 12-fold lower sensitivity of 0.0009 ± 0.0002% μM^{-1}. Furthermore, the low limit of detection of NAA-ST platforms (i.e., 22.82 μM/4.56 ppm) is almost 5-fold higher than that of NAA-DBR photonic structures (i.e., 4.20 μM/0.84 ppm). Finally, it was found that NAA-DBR structures present a more linear response with the analyte concentration (i.e., 0.994) than NAA-ST structures (i.e., 0.854). It is worthwhile to note that the lower limit of detection of these sensing platforms is higher than that established by the U.S. Environmental Protection Agency for drinking water (i.e., 2 ppb). However, we want to stress that the objective of our study was to demonstrate the ability of these photonic platforms to detect analytes under specific adsorption conditions. In that respect, there are many surface chemistry approaches that could enhance the sensing capabilities of these platforms. As an example, it has been demonstrated that different functional molecules (e.g., peptides, DNA, oligonucleotides, etc.) can provide much higher sensitivity than that of traditional thiol chemistry through bigger changes in the effective medium of the sensing platforms.[45,46]

■ CONCLUSION

In this study, we have demonstrated that an optimal design of the pore geometry and shape of photonic structures based on nanoporous anodic alumina can provide enhanced optical properties, which are fundamental requisites for the development of optical sensors with improved capabilities for broad sensing applications. The effects of the pore geometry and shape of two types of NAA photonic structures on their optical characteristics were systematically assessed. Furthermore, optimization paths for the sensitivity, low limit of detection, and linearity of these NAA photonic platforms were established and assessed under nonspecific and specific adsorption conditions for two different types of analytes.

The development of sensitive, reliable, robust, stable, cost-competitive, portable, and selective optical sensing systems requires photonic sensing platforms to have improved optical properties. This study has demonstrated that it is possible to enhance the sensitivity, low limit of detection, and linearity of these NAA photonic structures by engineering their nanopores. Undoubtedly, this reveals the importance of an optimized design of sensing platforms in the development of future sensing systems.

■ METHODS

Materials. High-purity (99.9997%) aluminum foils with a thickness of 0.32 mm were supplied by Goodfellow Cambridge Ltd. (UK). Oxalic acid ($C_2H_2O_4$), phosphoric acid (H_3PO_4), hydrochloric acid (HCl), ethanol (C_2H_5OH), perchloric acid ($HClO_4$), hydrogen peroxide (H_2O_2), chromium trioxide (CrO_3), 3-(mercaptopropyl)trimethoxysilane (MPTMS), D-glucose ($C_6H_{12}O_6$), and mercury(II) chloride ($HgCl_2$) were supplied by Sigma-Aldrich (Australia) and used without further purification. Aqueous solutions used in this study were prepared with ultrapure water (Option Q—Purelabs, Australia).

Fabrication of NAA-ST and NAA-DBR Photonic Structures. Prior to anodization, circular Al substrates with a diameter of 1.5 cm were cleaned under sonication in ethanol (EtOH) and distilled water for 15 min each. Subsequently, aluminum chips were electropolished in a 4:1 (v/v) mixture of EtOH and $HClO_4$ at 20 V and 5 °C for 3 min. After electropolishing, the first anodization step was carried out in a 0.3 M aqueous solution of $H_2C_2O_4$ at 40 V and 6 °C for 20 h. Then the resulting NAA layer was chemically removed in a mixture of 0.2 M chromic acid (H_2CrO_4) and 0.4 M H_3PO_4 at 70 °C for 3 h in order to pattern the aluminum surface and enable the growth of self-organized nanopores from top to bottom. As far as the second anodization step is concerned, two different electrochemical approaches were used to produce NAA-ST and NAA-DBR photonic platforms. Whereas the former type was produced by anodization under the

aforementioned conditions (i.e., 0.3 M $H_2C_2O_4$ at 40 V and 6 °C), the latter type was fabricated using the same conditions but applying a pseudosinusoidal anodization profile. This profile was started by an increasing voltage ramp from 20 to 50 V at a rate of 0.5 V s^{-1}. Then, the process was continued at 50 V for a charge of 1 C. Subsequently, the anodization voltage was linearly reduced from 50 to 20 V at a rate of −0.01 V s^{-1}. In the case of NAA-ST platforms, the second anodization step was controlled by time in order to produce NAA-ST platforms with thicknesses of 30, 35, 40, and 45 μm. However, in the case of NAA-DBR photonic structures, this anodization step was controlled by the number of cycles (i.e., 125, 150, 175, and 200 cycles), which corresponded to thicknesses of 30, 35, 40, and 45 μm, respectively. Finally, the remaining aluminum substrate was removed from the back side by wet etching in a mixture of hydrochloric acid and cupric chloride ($HCl/CuCl_2$), and the nanopores of NAA-ST and NAA-DBR photonic structures were widened by wet chemical etching in 5 wt % H_3PO_4 at 35 °C.

RIfS Setup. The optical characteristics of NAA-ST and NAA-DBR photonic structures were assessed using a RIfS system combined with a flow cell through which the different solutions of glucose and mercury ions were flowed by a peristaltic pump (BT100-2J, LongerPump, USA) at a constant flow rate of 400 μL min^{-1}. Briefly, this optical system was composed of a bifurcated optical probe that conducted and focused white light from a tungsten source (LS-1LL, Ocean Optics, USA). Light reflected from NAA-ST and NAA-DBR platforms was collected by the collection fiber, which was assembled around the optical probe and conducted the reflected light to a miniature spectrophotometer (USB 4000, Ocean Optics, USA). RIfS spectra in the 400−1000 nm wavelength range were acquired in real time and saved at intervals of 30 s with an integration time of 100 ms and 50 average measurements. These spectra were subsequently processed in Igor Pro library (Wavemetrics, USA).

Chemical Functionalization of NAA-ST and NAA-DBR Photonic Structures. The inner surfaces of the nanopores of NAA-ST and NAA-DBR photonic platforms were chemically modified with MPTMS following a well-established silanization protocol. Prior to functionalization, the number of hydroxyl groups (−OH) on the inner surfaces of NAA platforms was increased by boiling these nanoporous substrates in 30 wt % H_2O_2 for 10 min at 90 °C. After this, NAA platforms were dried under a nitrogen stream and functionalized via chemical vapor deposition of MPTMS at 135 °C for 3 h. Subsequently, NAA platforms were washed with acetone and water in order to remove physisorbed MPTMS molecules.

Structural Characterization of NAA-ST and NAA-DBR Photonic Structures. The morphologies and structures of NAA-ST and NAA-DBR platforms were characterized by SEM image analysis from images acquired using a field-emission-gun scanning electron microscope (FEG-SEM FEI Quanta 450).

■ ASSOCIATED CONTENT

Supporting Information

Further information on the anodization profiles used to produce NAA-ST and NAA-DBR photonic platforms and examples of real-time monitoring of ΔOT_{eff} and $\Delta\lambda_{peak}$ after infiltration with different glucose solutions. This material is available free of charge via the Internet at http://pubs.acs.org.

■ AUTHOR INFORMATION

Corresponding Author

*Phone: +61 8 8313 1535. Fax: +61 8 8303 4373. E-mail: abel.santos@adelaide.edu.au. Web: http://www.adelaide.edu.au/directory/abel.santos.

Author Contributions

§T.K. and A.S. contributed equally to this work and carried out the experimental part of this study. The resulting data were analyzed by all authors, and the manuscript was written through contributions of all authors. All authors have given approval to the final version of the manuscript.

Notes

The authors declare no competing financial interest.

■ ACKNOWLEDGMENTS

This research was supported by the Australian Research Council (ARC) through Grants DE14010054 and FT110100711, the Spanish Ministerio de Economía y Competitividad through Grant TEC2012-34397, and the Generalitat de Catalunya through the Grant 2014 SGR 1344. The authors also thank the School of Chemical Engineering (UoA) and Adelaide Microscopy (AM).

■ REFERENCES

(1) Wei, Q.; Nagi, R.; Sadeghi, K.; Feng, S.; Yan, E.; Ki, S. J.; Caire, R.; Tseng, D.; Ozcan, A. Detection and Spatial Mapping of Mercury Contamination in Water Samples Using a Smart-Phone. *ACS Nano* **2014**, *8*, 1121−1129.

(2) Wei, Q.; Qi, H.; Luo, W.; Tseng, D.; Ki, S. J.; Wan, Z.; Göröcs, Z.; Bentolila, L. A.; Wu, T. T.; Sun, R.; Ozcan, A. Fluorescent Imaging of Single Nanoparticles and Viruses on a Smart Phone. *ACS Nano* **2013**, *7*, 9147−9155.

(3) Khatua, S.; Orrit, M. Toward Single-Molecule Microscopy on a Smart Phone. *ACS Nano* **2013**, *7*, 8340−8343.

(4) Ayas, S.; Cupallari, A.; Ekiz, O. O.; Kaya, Y.; Dana, A. Counting Molecules with a Mobile Phone Camera Using Plasmonic Enhancement. *ACS Photonics* **2014**, *1*, 17−26.

(5) Homola, J.; Yee, S. S.; Gauglitz, G. Surface Plasmon Resonance Sensors: Review. *Sens. Actuators, B* **1999**, *54*, 3−15.

(6) Ji, N.; Ruan, W.; Wang, C.; Lu, Z.; Zhao, B. Fabrication of Silver Decorated Anodic Aluminum Oxide Substrate and Its Optical Properties on Surface-Enhanced Raman Scattering and Thin Film Interference. *Langmuir* **2009**, *25*, 11869−11873.

(7) Zhan, Z.; Lei, Y. Sub-100-nm Nanoparticle Arrays with Perfect Ordering and Tuneable and Uniform Dimensions Fabricated by Combining Nanoimprinting with Ultrathin Alumina Mambrane Technique. *ACS Nano* **2014**, *8*, 3862−3868.

(8) Dhathathreyan, A. Real-Time Monitoring of Invertase Activity Immobilized in Nanoporous Aluminum Oxide. *J. Phys. Chem. B* **2011**, *115*, 6678−6682.

(9) Hiep, H. M.; Yoshikawa, H.; Tamiya, E. Interference Localized Surface Plasmon Resonance Nanosensor Tailored for the Detection of Specific Biomolecular Interactions. *Anal. Chem.* **2010**, *82*, 1221−1227.

(10) Kim, D. K.; Kerman, K.; Saito, M.; Sathuluri, R. R.; Endo, T.; Yamamura, S.; Kwon, Y. S.; Tamiya, E. Label-Free DNA Biosensor Based on Localized Surface Plasmon Resonance Coupled with Interferometry. *Anal. Chem.* **2007**, *79*, 1855−1864.

(11) Yeom, S. H.; Kim, O. G.; Kang, B. H.; Kim, K. J.; Yuan, H.; Kwon, D. H.; Kim, H. R.; Kang, S. W. Highly Sensitive Nano-Porous Lattice Biosensor Based on Localized Surface Plasmon Resonance and Interference. *Opt. Express* **2011**, *19*, 22882−22891.

(12) Lau, K. H. A.; Duran, H.; Knoll, W. In Situ Characterization of *N*-Carboxy Anhydride Polymerization in Nanoporous Anodic Alumina. *J. Phys. Chem. B* **2009**, *113*, 3179−3189.

(13) Hotta, K.; Yamaguchi, A.; Teramae, N. Nanoporous Waveguide Sensor with Optimized Nanoarchitectures for Highly Sensitive Label-Free Biosensing. *ACS Nano* **2012**, *6*, 1541−1547.
(14) Lau, K. H. A.; Tan, L. S.; Tamada, K.; Sander, M. S.; Knoll, W. Highly Sensitive Detection of Processes Occurring inside Nanoporous Anodic Alumina Templates: A Waveguide Optical Study. *J. Phys. Chem. B* **2004**, *108*, 10812−10818.
(15) Fan, Y.; Hotta, K.; Yamaguchi, A.; Teramae, N. Enhanced Fluorescence in a Nanoporous Waveguide and Its Qualitative Analysis. *Opt. Express* **2012**, *20*, 12850−12859.
(16) Lee, S. J.; Guan, Z.; Xu, H.; Moskovits, M. Surface-Enhanced Raman Spectroscopy and Nanogeometry: The Plasmonic Origin of SERS. *J. Phys. Chem. C* **2007**, *111*, 17985−17988.
(17) Albrecht, C.; Kaeppel, N.; Gauglitz, G. Two Immunoassay Formats for Fully Automated CRP Detection in Human Serum. *Anal. Bioanal. Chem.* **2008**, *391*, 1845−1852.
(18) Leopold, N.; Busche, S.; Gauglitz, G.; Lendl, B. IR Absorption and Reflectometric Interference Spectroscopy (RIfS) Combined to a New Sensing Approach for Gas Analytes Absorbed into Thin Polymer Films. *Spectrochim. Acta, Part A* **2009**, *72*, 994−999.
(19) Orosco, M. M.; Pacholski, C.; Sailor, M. J. Real-Time Monitoring of Enzyme Activity in a Mesoporous Silicon Double Layer. *Nat. Nanotechnol.* **2009**, *4*, 255−258.
(20) Alvarez, S. D.; Li, C. P.; Chiang, C. E.; Schuller, I. K.; Sailor, M. J. A Label-Free Porous Alumina Interferometric Immunosensor. *ACS Nano* **2009**, *3*, 3301−3307.
(21) Dronov, R.; Jane, A.; Shapter, J. G.; Hodges, A.; Voelcker, N. H. Nanoporous Alumina-Based Interferometric Transducers Ennobled. *Nanoscale* **2011**, *3*, 3109−3114.
(22) Kumeria, T.; Santos, A.; Losic, D. Ultrasensitive Nanoporous Interferometric Sensor for Label-Free Detection of Gold(III) Ions. *ACS Appl. Mater. Interfaces* **2013**, *5*, 11783−11790.
(23) Santos, A.; Kumeria, T.; Losic, D. Optically Optimized Photoluminescent and Interferometric Biosensors Based on Nanoporous Anodic Alumina: A Comparison. *Anal. Chem.* **2013**, *85*, 7904−7911.
(24) Masuda, H.; Fukuda, K. Ordered Metal Nanohole Arrays Made by a Two-Step Replication of Honeycomb Structures of Anodic Alumina. *Science* **1995**, *268*, 1466−1468.
(25) Masuda, H.; Hasegwa, F.; Ono, S. Self-Ordering of Cell Arrangement of Anodic Porous Alumina Formed in Sulfuric Acid Solution. *J. Electrochem. Soc.* **1997**, *144*, L127−L130.
(26) Masuda, H.; Yada, K.; Osaka, A. Self-Ordering of Cell Configuration of Anodic Porous Alumina with Large-Size Pores in Phosphoric Acid Solution. *Jpn. J. Appl. Phys.* **1998**, *37*, L1340−L1342.
(27) Nielsch, K.; Choi, J.; Schwirn, K.; Wehspohn, R. B.; Gösele, U. Self-Ordering Regimes of Porous Alumina: The 10% Porosity Rule. *Nano Lett.* **2002**, *2*, 677−680.
(28) Lee, W.; Ji, R.; Gösele, U.; Nielsch, K. Fast Fabrication of Long-Range Ordered Porous Alumina Membranes by Hard Anodization. *Nat. Mater.* **2006**, *5*, 741−747.
(29) Schwirn, K.; Lee, W.; Hillebrand, R.; Steinhart, M.; Nielsch, K.; Gösele, U. Self-Ordered Anodic Aluminum Oxide Formed by H_2SO_4 Hard Anodization. *ACS Nano* **2008**, *2*, 302−310.
(30) Lee, W.; Schwirn, K.; Steinhart, M.; Pippel, E.; Scholz, R.; Gösele, U. Structural Engineering of Nanoporous Anodic Aluminium Oxide by Pulse Anodization of Aluminium. *Nat. Nanotechnol.* **2008**, *3*, 234−239.
(31) Santos, A.; Kumeria, T.; Losic, D. Nanoporous Anodic Aluminum Oxide for Chemical Sensing and Biosensors. *TrAC, Trends Anal. Chem.* **2013**, *44*, 25−38.
(32) Kumeria, T.; Santos, A.; Losic, D. Nanoporous Anodic Alumina Platforms: Engineered Surface Chemistry and Structure for Optical Sensing Applications. *Sensors* **2014**, *14*, 11878−11918.
(33) Santos, A.; Kumeria, T.; Losic, D. Nanoporous Anodic Alumina: A Versatile Platform for Optical Biosensors. *Materials* **2014**, *7*, 4297−4320.
(34) Kumeria, T.; Santos, A.; Rahman, M. M.; Ferré-Borrull, J.; Marsal, L. F.; Losic, D. Nanoporous Anodic Alumina Rugate Filters for Sensing of Ionic Mercury: Toward Environmental Point-of-Analysis Systems. *ACS Appl. Mater. Interfaces* **2014**, *6*, 12971−12978.
(35) Rahman, M. M.; Marsal, L. F.; Pallarès, J.; Ferré-Borrull, J. Tuning the Photonic Stop Bands of Nanoporous Anodic Alumina-Based Distributed Bragg Reflectors by Pore Widening. *ACS Appl. Mater. Interfaces* **2013**, *5*, 13375−13381.
(36) Abràmoff, M. D.; Magalhaes, P. J.; Ram, S. J. Image Processing with ImageJ. *Biophotonics Int.* **2004**, *11*, 36−42.
(37) Yisen, L.; Yi, C.; Zhiyuan, L.; Xing, H.; Yi, L. Structural Coloring of Aluminum. *Electrochem. Commun.* **2011**, *13*, 1336−1339.
(38) Kumeria, T.; Rahman, M. M.; Santos, A.; Ferré-Borrull, J.; Marsal, L. F.; Losic, D. Structural and Optical Nanoengineering of Nanoporous Anodic Alumina Rugate Filters for Real-Time and Label-Free Biosensing Applications. *Anal. Chem.* **2014**, *86*, 1837−1844.
(39) Santos, A.; Balderrama, V. S.; Alba, M.; Formentín, P.; Ferré-Borrull, J.; Pallarès, J.; Marsal, L. F. Nanoporous Anodic Alumina Barcodes: Toward Smart Optical Biosensors. *Adv. Mater.* **2012**, *24*, 1050−1054.
(40) Pacholski, C.; Sartor, M.; Sailor, M. J.; Cunin, F.; Miskelly, G. M. Biosensing Using Porous Silicon Double-Layer Interferometers: Reflective Interferometric Fourier Transform Spectroscopy. *J. Am. Chem. Soc.* **2005**, *127*, 11636−11645.
(41) Pacholski, C.; Yu, C.; Miskelly, G. M.; Godin, D.; Sailor, M. J. Reflective Interferometric Fourier Transform Spectroscopy: A Self-Compensating Label-Free Immunosensor Using Double-Layers of Porous SiO_2. *J. Am. Chem. Soc.* **2006**, *128*, 4250−4252.
(42) Kilian, K. A.; Lai, L. M. H.; Magenau, A.; Cartland, S.; Böcking, T.; Girolamo, N. D.; Gal, M.; Gaus, K.; Gooding, J. J. Smart Tissue Culture: In Situ Monitoring of the Activity of Protease Enzymes Secreted from Live Cells Using Nanostructured Photonic Crystals. *Nano Lett.* **2009**, *9*, 2021−2025.
(43) Kilian, K. A.; Böcking, T.; Gaus, K.; Gal, M.; Gooding, J. J. Peptide-Modified Optical Filters for Detecting Protease Activity. *ACS Nano* **2007**, *1*, 355−361.
(44) Jani, A. M. Md.; Kempson, I. M.; Losic, D.; Voelcker, N. H. Dressing in Layers: Layering Surface Functionalities in Nanoporous Aluminum Oxide Membranes. *Angew. Chem., Int. Ed.* **2010**, *49*, 7933−7937.
(45) Hoang, C. V.; Oyama, M.; Saito, O.; Aono, M.; Nagao, T. Monitoring the Presence of Ionic Mercury in Environmental Water by Plasmon-Enhanced Infrared Spectroscopy. *Sci. Rep.* **2013**, *3*, No. 1175.
(46) Zhang, L.; Chang, H.; Hirata, A.; Wu, H.; Xue, Q. K.; Chen, M. Nanoporous Gold Based Optical Sensor for Sub-ppt Detection of Mercury Ions. *ACS Nano* **2013**, *7*, 4595−4600.

Supporting Information

Advanced Structural Engineering of Nanoporous Photonic Structures: Tailoring Nanopore Architecture to Enhance Sensing Properties

Tushar Kumeria[1], Abel Santos[1]*, Mohammad Mahbubur Rahman[1,2], Josep Ferré-Borrull[2], Lluís F. Marsal[2] and Dusan Losic[1]

[1] School of Chemical Engineering – The University of Adelaide, Adelaide, Australia
[2] Departament d'Enginyeria Electrònica, Elèctrica i Automàtica – Universitat Rovira i Virgili, Tarragona, Spain

***E-Mail:** abel.santos@adelaide.edu.au

Number of Pages = 3
Number of Figures = 2
Number of Tables = 0

S1. Anodization profiles used to produce NAA-ST and NAA-RF platforms

Figures S1a and b illustrates the anodization profiles applied to produce NAA-ST and NAA-RF platforms. Whereas NAA-ST platforms were produced by anodization at constant voltage, NAA platforms were fabricated by a pseudosinusoidal anodization profile, in which the anodization profile was shifted between high and low anodization voltages.

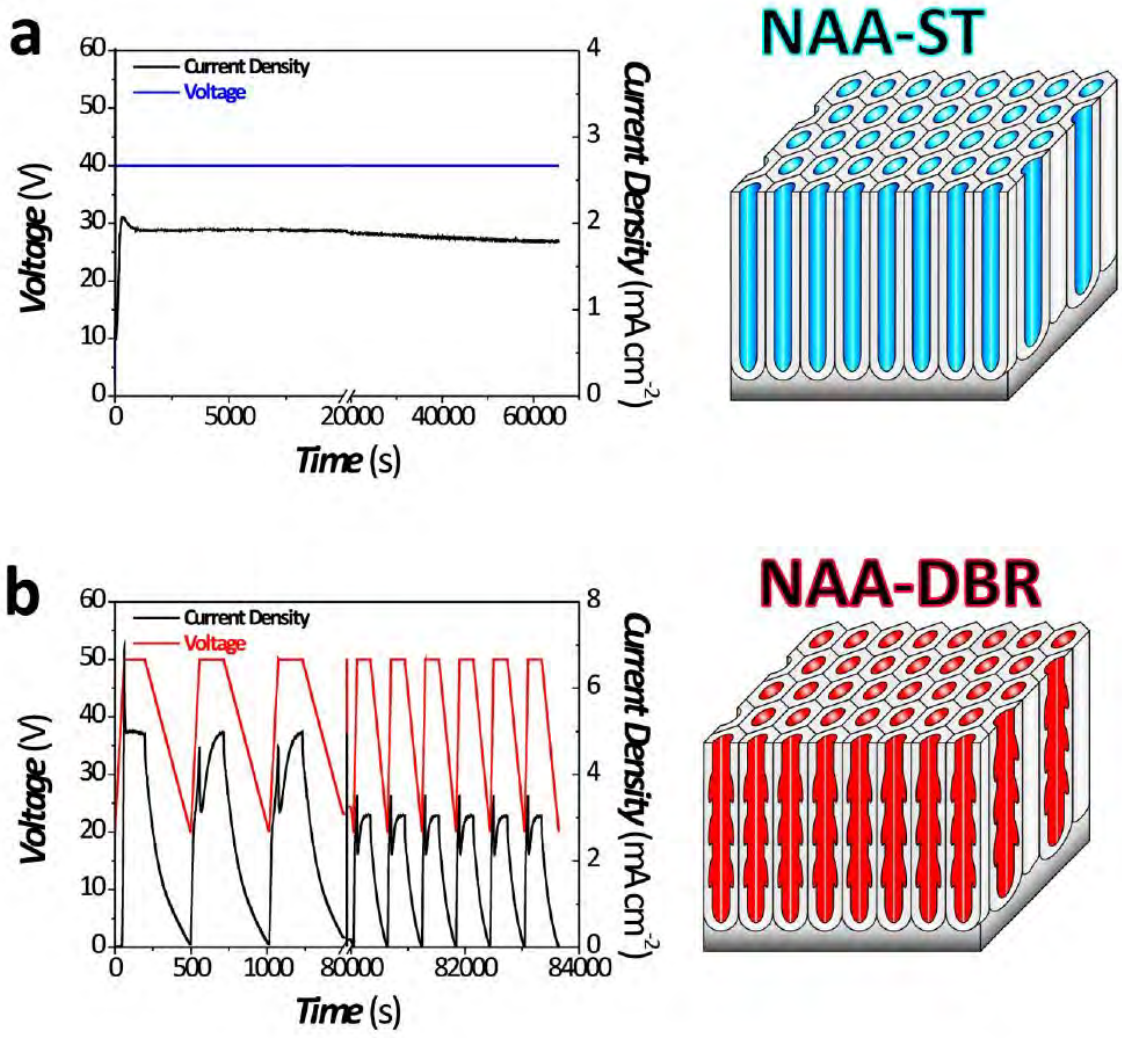

Figure S1. Anodization profiles and structural illustrations of (a) NAA-ST and (b) NAA-RF platforms.

S2. Real-time monitoring of changes in ΔOT_{eff} and $\Delta\lambda_{peak}$ in NAA-ST and NAA-RFs platforms

The optical properties of NAA-ST and NAA-RF platforms were assessed in real-time by changing the effective medium of these nanoporous structures. To this end, their nanopores were infiltrated with different aqueous solutions of glucose from 0.01 to 1.00 M (**Figure S2**). Then, changes in the effective medium of these nanoporous platforms produced changes in ΔOT_{eff} and $\Delta\lambda_{peak}$, which were used as the sensing parameters.

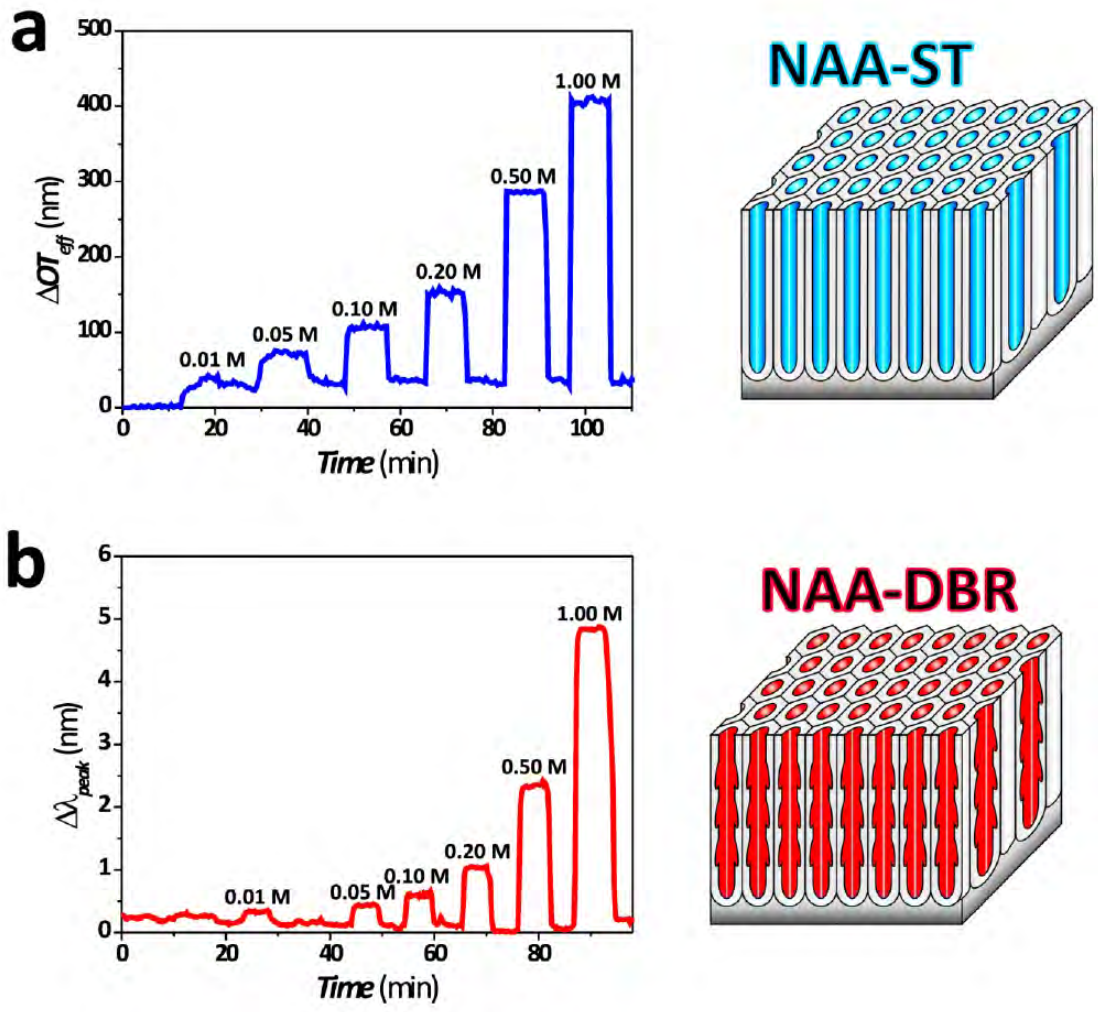

Figure S2. Examples of real-time monitoring of the effective medium change in NAA-ST and NAA-RF platforms as a result of infiltration of glucose solutions of different concentrations.

CHAPTER 7

OPTICALLY OPTIMIZED PHOTOLUMINESCENT and INTERFEROMETRIC BIOSENSORS BASED on NANOPOROUS ANODIC ALUMINA: A COMPARISON

Tushar Kumeria

School of Chemical Engineering, The University of Adelaide South Australia 5005, Australia

This chapter is based on the following peer-reviewed article:

A. Santos, **T. Kumeria**, D. Losic "Optically optimized photoluminescent and interferometric biosensors based on nanoporous anodic alumina: a comparison" *Analytical Chemistry*, 2013, **85**, 7904.

Statement of Authorship

Optically optimized photoluminescent and interferometric biosensors based on nanoporous anodic alumina: a comparison. *Analytical Chemistry*, 2013, **85**, 7904.

Tushar Kumeria (Candidate)

Under supervision of D. Losic and A. Santos, I developed and performed a part of the experiments, and contributed towards interpretation and processing of the data, and writing the manuscript for submission.

Signed Date:10/04/2015

Abel Santos

I acted as secondary supervisor for the candidate and aided in development and design of the experiments, and writing and evaluation of manuscript for submission. I give consent for Tushar Kumeria to present this paper for examination towards the Doctorate of philosophy.

Signed Date: 10/04/2015

Dusan Losic

I acted as primary supervisor of the candidate and aided in evaluation of experimental design and manuscript for submission. I give consent for Tushar Kumeria to present this paper for examination towards the Doctorate of philosophy

Signed Date: 10/04/2015

analytical chemistry

Article

pubs.acs.org/ac

Optically Optimized Photoluminescent and Interferometric Biosensors Based on Nanoporous Anodic Alumina: A Comparison

Abel Santos, Tushar Kumeria, and Dusan Losic*

School of Chemical Engineering, The University of Adelaide, Adelaide, SA 5005 Australia

Supporting Information

ABSTRACT: Herein, we present a comparative study about the sensing performance of optical biosensors based on photoluminescence spectroscopy (PLS) and reflectometric interference spectroscopy (RIfS) combined with nanoporous anodic alumina (NAA) platforms when detecting different analytes under distinct adsorption conditions. First, NAA platforms are structurally engineered in order for optimizing the optical signals obtained by PLS and RIfS. Then, the most optimal NAA platforms combined with PLS and RIfS are quantitatively compared by detecting two different analytes: D-glucose and L-cysteine under nonspecific and specific adsorption conditions, respectively. The obtained results demonstrate that such parameters as the analyte nature and adsorption conditions play a direct role in the sensing performance of these platforms. However, as this study demonstrates, PLS-NAA platforms are more sensitive than RIfS-NAA ones. The former shows better linearity (i.e., proportional change in the sensing parameter with analyte concentration), higher sensitivity toward analytes (i.e., sharper change in the sensing parameter with analyte concentration), and lower limit of detection (i.e., minimum detectable concentration of analyte).

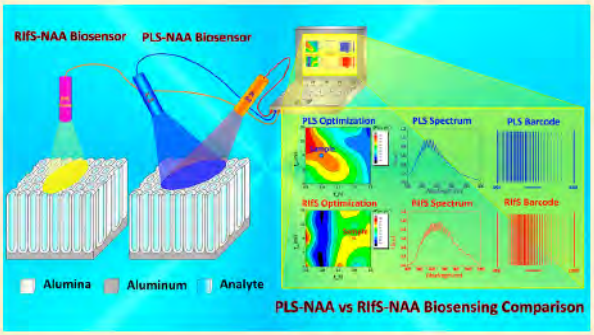

Ultrasensitive optical biosensors can accurately detect small concentrations of analyte in milliseconds without sample contamination or deterioration as the sensing principle is based on the interaction between light and analyzed sample.[1−3] So far, such optical techniques as photoluminescence spectroscopy (PLS),[4−7] surface plasmon resonance,[8−10] localized surface plasmon resonance,[11−13] wave-guiding spectroscopy,[14−17] surface-enhanced Raman scattering spectroscopy,[18−22] and reflectometric interference spectroscopy (RIfS)[23−29] have demonstrated outstanding biosensing performances in terms of limit of detection, accuracy, resolution, versatility, and reading velocity. Among these optical biosensing techniques, PLS and RIfS offer many interesting advantages as they can be implemented in small and cost-competitive portable spectrometers, enabling the development of in situ monitoring systems and reducing ostensibly the costs and time consumed by current clinical or industrial analytical techniques.[30] PLS relies upon the ability of materials to absorb photons of a given energy state from a source (i.e., excitation) and emit photons at a lower energy state as a result of that excitation (i.e., emission).[4,7] RIfS is based on the constructive reflection of white light as a result of the interference between a white light beam and a thin film.[25,26] Notice that PLS and RIfS can be combined with such nanoporous structures as porous silicon (PSi) and nanoporous anodic alumina (NAA), which have proved to be two excellent biosensing platforms. PSi and NAA are two optically active materials, the pores of which not only play a role as reservoirs or containers for analytes but also act as selective filters for different substances by size-exclusion or surface chemistry selectivity. These properties can be achieved by structural engineering of the pore geometry and surface chemistry functionalization, respectively.[4,26,31−33] Moreover, the optical signal from analyte molecules immobilized onto these nanoporous platforms is more intense than that obtained from nonporous thin films because of their large specific surface area (i.e., more analyte molecules are immobilized in these nanoporous structures than in flat ones). Several groups have exploited these advantages of PSi and NAA combined with RIfS in order for developing ultrasensitive biosensing platforms for a broad range of analytes and biological events (e.g., antibody−antigen bindings, enzyme−substrate digestions, drug loading and release, etc.) and applications (e.g., biosensors, nanoreactors, drug releasing nanochips, etc.).[23,25,27,31−38] More recently, we put forward another biosensing system that combines PLS and NAA platforms, which has shown excellent and promising biosensing performances for different analytes.[4,7] It is worth stressing that, when combined with nanoporous platforms, both sensing techniques are based on the same sensing principle, the Fabry−Pérot effect. This optical phenomenon is translated into an amplification of the PLS and RIfS signals from the nanoporous platforms due to strong enhancement of the emitted/reflected light at wavelengths corresponding to the optical modes of the Fabry−Pérot cavity

Received: May 29, 2013
Accepted: July 17, 2013
Published: July 17, 2013

formed by the system film−surrounding medium. As a result, PLS and RIfS spectra show abundant, well-resolved, and narrow oscillations/fringes, which constitute the base of the sensing principle of these techniques. Furthermore, these optical signals can be converted into optical barcodes, which act as exclusive and unique fingerprints of different analytes and thus can be implemented in computerized databases for automated clinical or industrial analysis (Figure 1).[4,7]

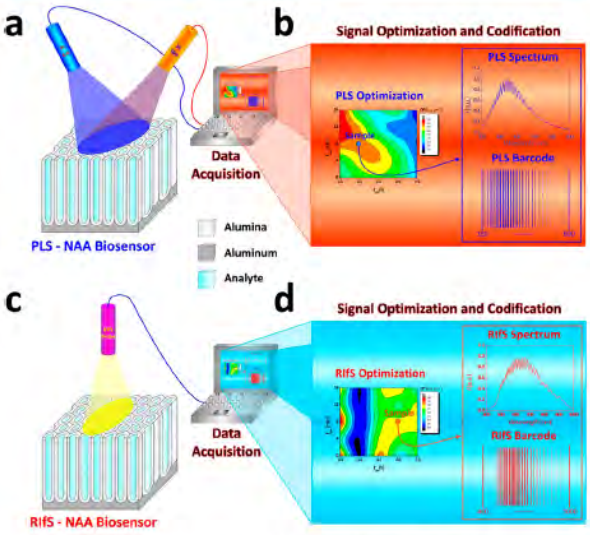

Figure 1. Schematic diagram of PLS-NAA and RIfS-NAA biosensing platforms. (a) PLS-NAA sensing platform. (b) Optimization and conversion of each PLS-NAA spectrum into an optical barcode. (c) RIfS-NAA sensing platform. (d) Optimization and conversion of each RIfS-NAA spectrum into an optical barcode.

The wavelength of each oscillation/fringe maximum in these spectra can be calculated by the Fabry−Pérot relationship (eq 1):

$$OT_{eff} = 2n_{eff}L\cos\theta = m\lambda \quad (1)$$

where OT_{eff} is the effective optical thickness; n_{eff} is the effective refractive index of the film; L is the film thickness; m is the order of the oscillation/fringe in the PLS or RIfS spectrum, the maximum of which is located at the wavelength λ; and θ is the angle of incidence. Therefore, different analytes can be detected and quantified when they are immobilized over a thin film through changes in its effective optical thickness (ΔOT_{eff}). This can be obtained after applying a fast Fourier transform (FFT) to the PLS and RIfS spectra, resulting in a FFT spectrum with a Gaussian-like peak, the center of which indicates the OT_{eff} of the Fabry−Pérot cavity. Notice that, when combined with nanoporous platforms, PLS and RIfS signals are directly dependent on the nanoporous structure (i.e., effective refractive index of the nanoporous matrix). Hence, this enables the optical optimization of these signals by structural engineering of the nanoporous structure, which can be achieved by the etching/anodization parameters in the case of PSi and NAA, respectively. In other words, a particular nanoporous structure will provide a more intense and well-resolved OT_{eff} peak, which will be more sensitive for analytical purposes.

Amid the above-mentioned nanoporous structures, NAA is thought to be an excellent platform to develop ultrasensitive optical biosensors as a result of its unique set of properties (e.g., biocompatibility, optical activity, well-defined and versatile porous structure, chemical and thermal stability, optical signal stability without further passivation or modification, etc.).[39] NAA is an optically active substrate that can be combined with such real-time and in situ optical spectroscopic techniques as PLS and RIfS. Notice that the sensing performance of these biosensing platforms relies upon the optical technique, the nanoporous platform, the analyte molecules, and its adsorption conditions. Nevertheless, to our knowledge, no comparison studies have assessed the biosensing performance and capabilities of PLS and RIfS combined with NAA platforms when detecting different analytes under distinct adsorption conditions.

Hence, more studies need to be carried out in order to establish which conditions make the optical performance of these biosensing platforms optimal for different analytes. This will enable the design and development of more efficient optical biosensors for particular analytical purposes in medicine and industry.

In this scenario, to address this question, we present a comparison study between photoluminescent and interferometric biosensing based on NAA platforms when detecting different analytes under two distinct adsorption conditions. To this end, first, PLS and RIfS signals from NAA platforms are optically optimized to provide intense and well-resolved spectra by structural engineering of the NAA pores. Then, the most optimal NAA platforms combined with PLS and RIfS are analyzed when detecting two analytes under different adsorption conditions, namely (i) D-glucose under nonspecific adsorption conditions and (ii) L-cysteine under specific adsorption conditions. The analysis of such sensing features as linearity (i.e., proportional change in the effective optical thickness with analyte concentration), sensitivity (i.e., change in the effective optical thickness with analyte concentration), and lower limit of detection (i.e., minimum detectable concentration of analyte) allows us to demonstrate that such parameters as the detection principle, the nanoporous platform, the analyte properties and its adsorption conditions through the nanoporous matrix have a direct effect over the optical performance of these biosensing platforms.

■ EXPERIMENTAL SECTION

Preparation of NAA Platforms. High purity aluminum (Al) foils were anodized by the two-step process reported elsewhere.[40−43] Briefly, Al chips of 1.5 cm in diameter were sonicated in ethanol (EtOH) and distilled water for 15 min and subsequently dried under nitrogen stream. Before anodizing, Al chips were electropolished in a mixture of ethanol (EtOH) and perchloric acid ($HClO_4$) 4:1 (v:v) at 20 V and 5 °C for 3 min. Then, the first anodization step was carried out in an aqueous solution of 0.3 M oxalic acid ($H_2C_2O_4$) at 40 V and 6 °C for 20 h. Next, the resulting NAA layer was removed by wet chemical etching in a mixture of 0.2 M chromic acid (H_2CrO_4) and 0.4 M phosphoric acid (H_3PO_4) for 3 h at 70 °C. After this, the second anodization step was performed under the same anodization conditions. Whereas the pore length was controlled by the anodization time of this step, the pore diameter was widened by a wet chemical etching in an aqueous solution of H_3PO_4 5 wt % at 35 °C after anodizing.

PLS and RIfS Signals Optimization. To optimize PLS and RIfS signals obtained from NAA platforms (i.e., range of pore geometries within which PLS and RIfS spectra present well-resolved oscillations/fringes), the anodization time (t_{an}) and

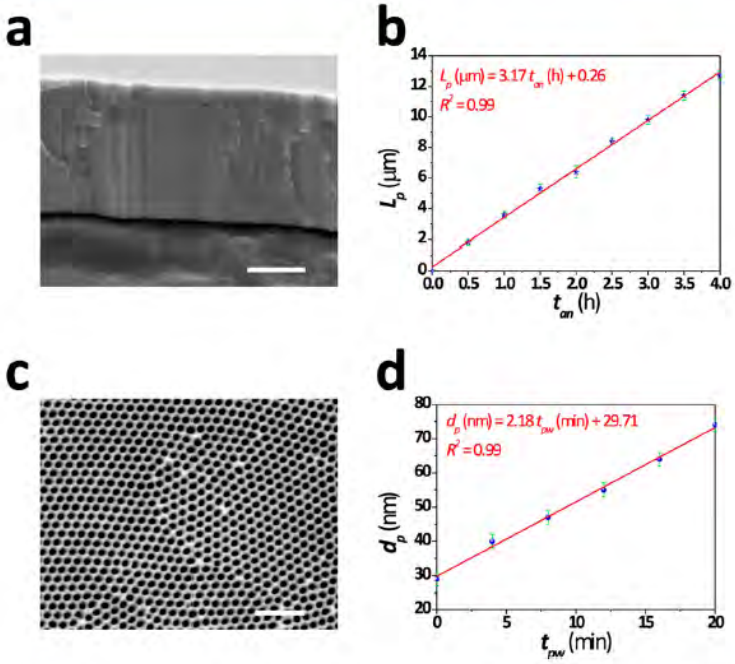

Figure 2. Geometric characteristics of NAA platforms as a function of the fabrication parameters. (a) Cross-section view SEM image of a NAA platform at t_{an} = 2.0 h (scale bar = 2.5 μm). (b) Calibration curve establishing a linear relationship between the pore length and the anodization time ($L_p - t_{an}$). (c) Top view SEM image of a NAA platform at t_{pw} = 12 min (scale bar = 500 nm). (d) Calibration curve establishing the relationship between the pore diameter and the pore widening time ($d_p - t_{pw}$).

the pore widening time (t_{pw}) were each set to five values (i.e., 0.5, 1.0, 1.5, 2.0, and 2.5 h and 0, 4, 8, 12, and 16 min, respectively). So, a total of 50 different NAA samples (i.e., 25 for each sensing platform: 25 PLS-NAA and 25 RIfS-NAA) were fabricated and subsequently analyzed. Figure 1 shows schemes of both experimental setups used in this study as well as an example of structural optimization and barcode implementation of PLS and RIfS signals. The fabrication conditions and the geometric characteristics of the resulting NAA platforms are summarized in Table S1 and Figure S1 (Supporting Information). These measurements were repeated three times, and the obtained results were statistically treated by calculating averages and experimental errors.

Glucose Sensing Performance by Optimized PLS-NAA and RIfS-NAA Platforms under Nonspecific Adsorption Conditions. The sensing performance of the most optimal NAA platforms in PLS and RIfS established by means of the above-mentioned optimization process was analyzed by detecting D-glucose ($C_6H_{12}O_6$) under nonspecific adsorption conditions. To this end, NAA platforms were placed in a spin coater (WS-650 Laurell Technologies Corporation), and 0.5 mL of D-glucose solution were poured on them. That solution was left over the samples for 10 min in order to infiltrate the NAA pores with glucose solution. After this, these samples were spun at 2000 rpm for 1 min to remove the supernatant. Finally, these infiltrated samples were thermally treated at 100 °C for 10 min in order to evaporate the remaining water. It is worth noting that such a thermal treatment did not alter the physical and chemical properties of the NAA platforms and D-glucose molecules. Six different aqueous solutions of D-glucose were used in order to establish the limit of detection and linearity of these sensing platforms with glucose concentration (i.e., 0.01, 0.05, 0.10, 0.20, 0.55, and 1.20 M). These experiments were repeated three times, and the obtained results were averaged and the experimental errors estimated.

Peptide Sensing Performance by Optimized PLS-NAA and RIfS-NAA Platforms under Specific Adsorption Conditions. Finally, the most optimal NAA platforms in PLS and RIfS established from the aforementioned optimization process were analyzed when detecting L-cysteine ($C_3H_7NO_2S$) under specific adsorption conditions. Before specific peptide adsorption, NAA platforms were functionalized through a well-established protocol reported elsewhere.[4,44−46] Briefly, as-produced NAA samples were hydroxylated through immersion in a hydrogen peroxide solution (H_2O_2) 30 wt % for 10 min at 85 °C and subsequently dried under nitrogen stream.

Then, these hydroxylated NAA samples were functionalized by chemical vapor deposition of 3-aminopropyltriethoxysilane (APTES) at 110 °C for 2.5 h. Next, these samples were washed with distilled water, and the amine group of APTES was activated by incubation in an aqueous solution of 2.5 vol % glutaraldehyde (GTA) at room temperature for 10 min. Finally, after washing these activated NAA platforms with distilled water, the peptide adsorption was conducted by dipping these activated NAA platforms into the corresponding L-cysteine solution for 10 min. Eight different aqueous solutions of L-cysteine were used in order to establish the limit of detection, sensitivity, and linearity of these biosensing platforms with peptide concentration (i.e., 0.005, 0.020, 0.035, 0.050, 0.065, 0080, 0.095, and 0.100 M). To guarantee the reliability of these biosensors, all these experiments were repeated three times and the obtained results were statistically treated by calculating averages and experimental errors. Furthermore, the functionalization protocol was validated through fluorescein isothiocyanate (FITC) visual test (Figure S2, Supporting Information). This was carried out by dipping a functionalized-activated NAA

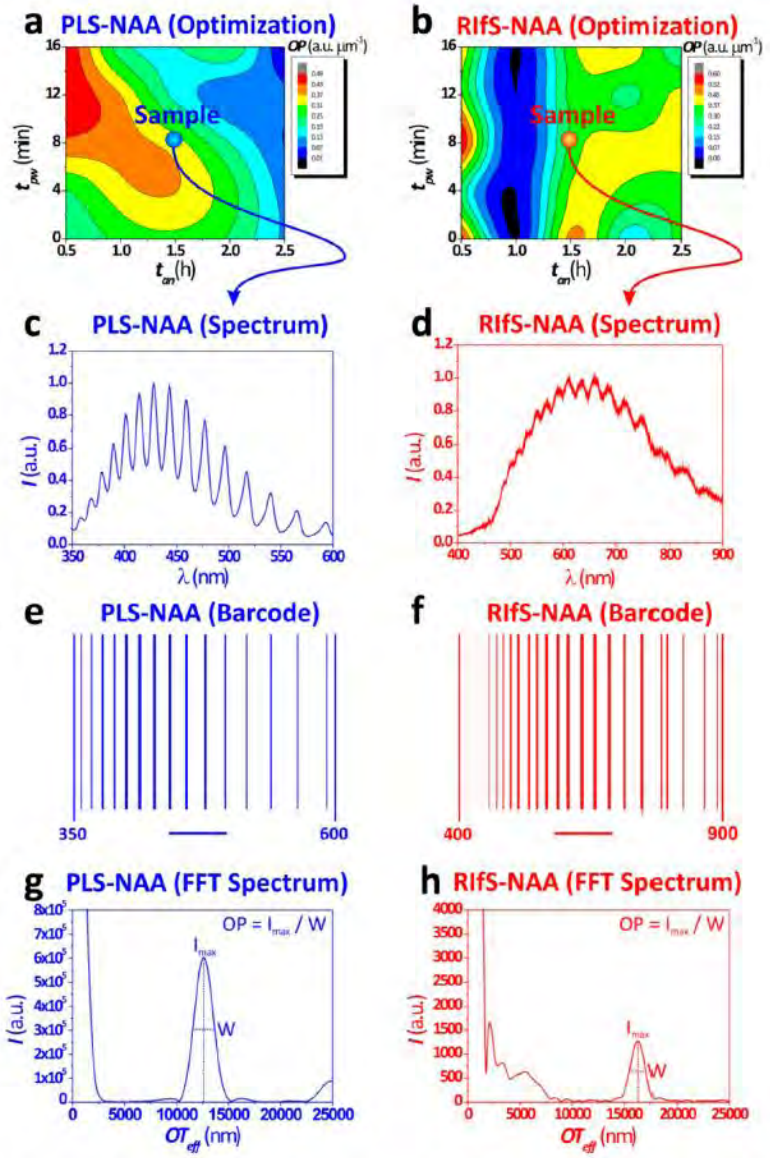

Figure 3. Optical optimization process of PLS-NAA and RIfS-NAA platforms. (a, b) Contour plots summarizing the optimization process of PLS and RIfS signals from NAA platforms through the parameter OP. (c, d) Example of PLS and RIfS spectra for samples fabricated at t_{an} = 1.5 h and t_{pw} = 8 min. (e, f) Example of barcode generation from the PLS and RIfS spectra shown in c and d, respectively. (g, h) Effective optical thickness spectra obtained from the PLS and RIfS spectra shown in c and d after applying fast Fourier transform and definition of parameter OP.

platform and a nonfunctionalized-activated NAA platform into an aqueous solution of FITC 200 μg mL^{-1} for 2 h at room temperature and subsequent washing with distilled water.

Optical and Structural Characterization. PLS measurements were performed in a spectrofluorometer (Fluoromax-4 Horiba Jobin Yvon) equipped with a Xe lamp used as the excitation light source at room temperature. The excitation wavelength (λ_{ex}) was set to 320 nm with a slit size of 5 nm and an angle of incidence/emission of 40° (i.e., θ = 40°), and the spectral range was 350−600 nm. A set of preliminary experiments was performed to find the most optimal conditions of PLS emissions from NAA platforms in this experimental setup.

RIfS measurements were performed in a setup composed of a Y-junction optical fiber probe connected to a miniature spectrometer. One end of that optical probe was connected to a tungsten halogen light source (Ocean Optics LS-1LL) and the other one to the spectrophotometer (Ocean Optics USB 4000). The common end of that probe was used to focus white light from the source and collect the reflected light from NAA platforms at normal incidence (i.e., θ = 0°). The obtained data were collected from an illuminated circular spot of 2 mm in diameter, and the spectral range was 400−900 nm. Finally, the effective optical thickness (OT_{eff}) was obtained by applying fast Fourier transform to the PLS and RIfS spectra in Igor Pro library (Wavemetrics). The effective optical thickness change (ΔOT_{eff}) was calculated as the difference of OT_{eff} in each

sample expressed in percentage before and after adsorption of the analyzed analyte (Table S2 and Figure S3, Supporting Information). The structural characteristics of NAA platforms such as the pore length and its diameter were established from scanning electron microscopy (SEM) images acquired through a scanning electron microscope (FEG-SEM FEI Quanta 450). These images were subsequently analyzed by the standard image processing package ImageJ (public domain program developed at the RSB of the NIH).[47] NAA platforms infiltrated with D-glucose and L-cysteine were also analyzed through Fourier transform infrared (FT-IR) spectroscopy (Figure S4, Supporting Information). FT-IR spectra were collected from NAA platforms without aluminum substrate in a FT-IR spectrometer (Nicolet 6700 ThermoFisher). The number of scans was set to 32 with a resolution of 4 cm^{-1}. All spectra were collected in the 4000−1500 cm^{-1} range in transmission mode.

Notice that, unless otherwise indicated, all the aforementioned experiments were repeated three times with freshly prepared NAA samples and the obtained values were statistically treated by calculating averages and experimental errors.

■ RESULTS AND DISCUSSION

Structural Analysis of NAA Platforms. The geometric characteristics of the different NAA platforms used in this study were established by SEM image analysis. The obtained results revealed that the pore lengths and diameters in the different NAA platforms ranged from 1.8 ± 0.2 to 12.7 ± 0.3 μm and from 29 ± 2 to 74 ± 2 nm, respectively. These results are summarized in Table S1 (Supporting Information). Figure 2 shows two examples of SEM images of NAA platforms and the calibration curves obtained from the above-mentioned image analysis, which demonstrate a linear relationship between the pore length and its diameter and the anodization and pore widening time, respectively. These make it possible to tune at will the pore geometry in NAA and thus the optical properties of the sensing platforms. Furthermore, Figure S1 (Supporting Information) compiles a set of SEM images of top and cross-section views of the most representative NAA platforms featuring different pore lengths and diameters.

Optical Optimization of PLS-NAA and RIfS-NAA Platforms. As was previously commented, the sensing parameter used in PLS-NAA and RIfS-NAA platforms is the effective optical thickness (OT_{eff}). This optical parameter makes it possible to establish the amount of analyte through its changes in the range of linear performance of these biosensors (i.e., range within which the effective optical thickness change is directly proportional to the analyte concentration). It is worthwhile mentioning that OT_{eff} changes as a result of modifications in the effective medium within the NAA pores, which are generated when analyte molecules are immobilized through the nanoporous structure. This parameter can be estimated by applying FFT to the PLS and RIfS spectra. The result is a Gaussian-like peak, the most representative parameters of which are its maximum height and width at half of that height.

Therefore, to establish the most optimal NAA platform, we used the parameter OP, which is defined as the ratio between the maximum peak intensity and its width at half of the intensity value calculated from the FFT spectra obtained from the PLS and RIfS spectra (i.e., effective optical thickness peak) (Figure S5, Supporting Information). It is worth stressing that the highest OP value indicates the most optimal NAA platform in PLS and RIfS as the higher the intensity and the narrower the OT_{eff} peak in the FFT spectrum the most sensitive the NAA platform. In other words, shifts of the OT_{eff} peak in the FFT spectrum will be more noticeable if that peak is narrow and intense. Figure 3 shows the optimization process for the different sensing platforms analyzed in this study (i.e., PLS-NAA and RIfS-NAA). Parts a and b of Figure 3 show contour plots representing the optimization process of the parameter OP. As a first result, these plots reveal that RIfS-NAA platforms are more dependent on the pore geometry than PLS-NAA ones as the lines between different OP values (i.e., color fields) are closer to each other (i.e., higher gradient of OP as a function of the geometric characteristics in the NAA platforms). Furthermore, it is observed that the distribution of color fields is more homogeneous in PLS-NAA platforms, indicating that OP changes smoothly in these platforms when the pore geometry is modified. Figure 3a demonstrates that OP in PLS-NAA platforms decreases homogeneously with the pore length and its diameter. However, as Figure 3b indicates, this is slightly different for RIfS-NAA platforms as the OP parameter changes heterogeneously with the pore geometry. This can indicate that PLS signals are more stable than RIfS ones when the pore geometry in NAA is modified.

The obtained results revealed that the most optimal NAA platform in PLS is that obtained after 0.5 h of anodization (i.e., L_p = 1.8 ± 0.2 μm) and 12 min of pore widening (i.e., d_p = 55 ± 2 nm). As for the most sensitive platform for RIfS signals, this corresponds to that sample obtained after 0.5 h of anodization (i.e., L_p = 1.8 ± 0.2 μm) and 8 min of pore widening (i.e., d_p = 47 ± 2 nm). These results are summarized in Table 1. Notice that the values of the OP parameter

Table 1. Most Optimal NAA Sensing Platforms for PLS and RIfS Obtained through the Parameter OP along with Their Fabrication Conditions and Geometric Characteristics

		anodization conditions		pore geometry	
sensing platform	OP (a.u. μm^{-1})	t_{an} (h)	t_{pw} (min)	L_p (μm)	d_p (nm)
PLS-NAA	0.488 ± 0.003	0.5	12	1.8 ± 0.2	55 ± 2
RIfS-NAA	0.597 ± 0.002	0.5	8	1.8 ± 0.2	47 ± 2

calculated from PLS and RIfS signals cannot be directly compared as the intensity values obtained from these optical techniques are not absolute but relative. To gain insight into this issue, compare objectively both optical biosensing platforms, and understand the different aspects of these biosensing techniques, several tests were carried out, namely (i) detection of D-glucose under nonspecific adsorption conditions and (ii) detection of L-cysteine under specific adsorption conditions. It is worthwhile noting that such parameters as the analyte properties and its adsorption conditions are critical aspects to develop more sensitive and selective optical biosensors based on NAA with an optimal sensing performance for specific analytical purposes.

Glucose Sensing Performance by Optimized PLS-NAA and RIfS-NAA Platforms. From the above-mentioned optimization process, we established the most sensitive NAA platforms in PLS and RIfS (i.e., samples obtained after 0.5 h of anodization and 12 and 8 min of pore widening, respectively). After this, we studied the performance of these optical biosensing platforms when detecting glucose under nonspecific

adsorption conditions at different concentrations. Glucose is a monosaccharide that is absorbed directly into the bloodstream during digestion. This carbohydrate is used by cells as metabolic intermediate and primary source of energy. From the analytical point of view, glucose is a common medical analyte measured in blood samples from many clinical patients. A high level of glucose in the bloodstream may be a sign of diabetes mellitus. Figure 4a and Table 2 summarize the

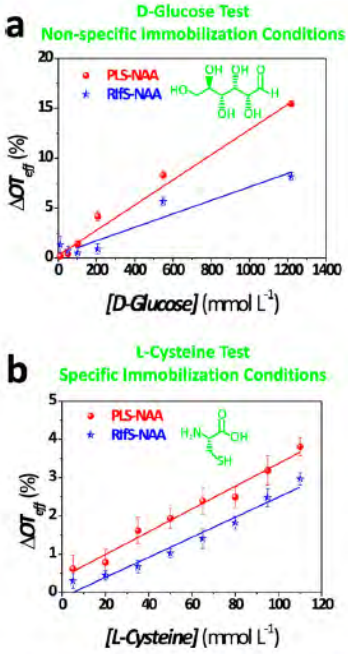

Figure 4. Optical performance of PLS-NAA and RIfS-NAA sensing platforms when detecting D-glucose and L-cysteine under nonspecific and specific adsorption conditions, respectively. (a) Effective optical thickness change of PLS-NAA and RIfS-NAA with D-glucose concentration. (b) Effective optical thickness change of PLS-NAA and RIfS-NAA with L-cysteine concentration.

obtained results. It was found out that the platform PLS-NAA is much more sensitive for glucose than the RIfS-NAA one. Whereas the former had a limit of detection (LoD) for glucose of 0.01 M and sensitivity (S) of 0.013 ± 0.001% mM^{-1}, the latter had 0.1 M and 0.007 ± 0.001% mM^{-1} for LoD and S, respectively. It is noteworthy that the sensitivity parameter S used in this study corresponds to the slope of the linear fitting obtained for each biosensing platform within the linear range (i.e., range within which the effective optical thickness change is linear with the analyte concentration). Furthermore, the linearity (R^2) of PLS-NAA platforms was found to be much better than that of RIfS-NAA ones (Table 2).

Peptide Sensing Performance by Optimized PLS-NAA and RIfS-NAA Platforms. Another set of optimized NAA platforms was used to study the performance of these optical biosensors when detecting L-cysteine at different concentrations under specific adsorption conditions. L-Cysteine is a semi-essential amino acid that can be biosynthesized by the human body. Its thiol side chain participates in enzymatic reactions, acting as a nucleophile. This peptide is also used as a food additive (E920) and can work as preventative for certain negative effects derived from alcohol consumption, including liver damage and hangover. Figure 4b and Table 2 compile the obtained results, which denote that the platform PLS-NAA is slightly more sensitive for L-cysteine than the RIfS-NAA one. Both sensing platforms presented the same LoD for cysteine (i.e., 0.005 M), whereas the former and the latter had sensitivities of 0.029 ± 0.002 and 0.026 ± 0.002% mM^{-1}, respectively. Finally, it was established that both biosensing platforms provide a comparable linear performance (Table 2).

From these results just mentioned above, it was established that photoluminescent biosensors based on nanoporous anodic alumina platforms are more sensitive toward D-glucose and L-cysteine under nonspecific and specific adsorption conditions, respectively. However, as this study demonstrates, the performance of these biosensors not only depends on the sensing platform but also upon the properties of the analyte molecules and the adsorption conditions through the nanoporous matrix. Notice that the infiltration and subsequent adsorption of biomolecules through the NAA network lead to an increase in the effective optical thickness. For a given nanoporous matrix, the magnitude of that change and thus the sensitivity of the sensor relies upon four main factors, namely (i) the size of the analyte molecules, (ii) the optical characteristics of the analyte molecules (i.e., degree to which the analyte molecules increase the refractive index of the effective medium in the nanoporous matrix), (iii) the chemical or physical interaction between analyte molecules and the nanoporous matrix surface, and (iv) the medium inside pores (e.g., air, water, ethanol, etc.). According to these factors, bigger molecules with higher refractive index, chemical interaction with the NAA surface, and aqueous medium will provide sharper changes in the effective optical thickness. Furthermore, in the case of PLS, photoluminescent analytes within the excitation range of the NAA sensor will produce more significant changes in the effective optical thickness as a result of their photoactivity (i.e., contribution to the total signal collected from the sensing platform). To throw light on this issue, we measured the PLS and UV−visible spectra of two solutions of D-glucose and L-cysteine with the same analyte concentration (i.e., 50 mM) (Figure S6, Supporting Information). It was verified that, for a given concentration, D-glucose is much more photoluminescent than L-cysteine. This would explain why the sensitivity of PLS-NAA platforms is much higher than that of RIfS-NAA ones for detecting glucose under the same adsorption conditions.

Table 2. Sensing Parameters of Optimized PLS-NAA and RIfS-NAA Platforms Obtained from D-Glucose and L-Cysteine Tests

	sensing tests					
	D-glucose			L-cysteine		
sensing platform	LoD (mM)	S^a (% mM^{-1})	R^2	LoD (mM)	S^a (% mM^{-1})	R^2
PLS-NAA	10	0.013 ± 0.001	0.99	5	0.029 ± 0.002	0.97
RIfS-NAA	100	0.007 ± 0.001	0.87	5	0.026 ± 0.002	0.96

[a] S = sensitivity expressed in percentage of effective optical thickness change (ΔOT_{eff}) per concentration of analyte in mM.

Nevertheless, this difference in sensitivity becomes less remarkable when L-cysteine is detected because of its low photoluminescence and the specific adsorption conditions. Notice that these molecules, D-glucose and L-cysteine, are comparable in size and refractive index (i.e., similar UV−visible absorption spectra) albeit the former is much more photoluminescent than the latter. It was also verified that specific adsorption conditions established through silane adsorption make the sensing performance of both platforms comparable, when a nonphotoactive substance as L-cysteine is analyzed. In addition, specific adsorption increases the sensitivity of both sensing platforms (i.e., PLS-NAA and RIfS-NAA) as a result of an enhanced chemical interaction between the analyte molecules and the NAA surface (i.e., more analyte molecules are effectively immobilized through the nanoporous matrix). Nonetheless, it is worthwhile mentioning that, as other studies referenced in this work have demonstrated, lower limits of detection (i.e., nM) can be achieved by these sensing platforms through high affinity binding protocols of adsorption.[29,34]

■ CONCLUSIONS

To conclude, we have presented a comparative study about the sensing performance of optical biosensors based on PLS-NAA and RIfS-NAA platforms when detecting different analytes under distinct adsorption conditions. The optimization process of these optical biosensing platforms by structural engineering of the nanoporous structure revealed that thinner nanoporous films with wider pores provide more intense optical signals for sensing purposes. Furthermore, it was established that PLS-NAA platforms are more sensitive toward glucose molecules immobilized onto the NAA network under nonspecific conditions, with a lower limit of detection of 0.010 M and a sensitivity of 0.013 ± 0.001% mM^{-1}. In addition, the sensing performance of these biosensors for detecting L-cysteine under specific adsorption conditions was studied. In this case, both sensing platforms showed comparable sensing parameters (i.e., LoD and *S*), albeit PLS-NAA platforms demonstrated a slightly better performance. Therefore, it has been established that photoluminescent biosensors based on nanoporous anodic alumina are more sensitive toward such biological substances as glucose and cysteine. Nevertheless, as this study has also shown, the performance of these biosensors is not only dependent on the sensing platform but also upon the properties of analyte molecules and the adsorption conditions through the nanoporous matrix. This study contributes to the understanding and development of optimized optical biosensors based on nanoporous anodic alumina platforms combined with PLS and RIfS, which are envisaged for a broad range of biosensing applications in medicine and industry.

■ ASSOCIATED CONTENT

Supporting Information

Further content about the fabrication conditions and geometric characteristics of the NAA platforms used in this study as well as their relationship which was established by calibration curves obtained from SEM images; raw data of ΔOT_{eff} used in Figure 4a and a graphical example of these calculations; FITC and FT-IR analyses of functionalized and infiltrated samples; graphical definition of the optimized parameter OP; and photoluminescence and UV−visible spectra of 50 mM D-glucose and L-cysteine aqueous solutions, which were used to support some hypotheses made in this study. This material is available free of charge via the Internet at http://pubs.acs.org.

■ AUTHOR INFORMATION

Corresponding Author

*Phone: + 61 8 8313 4648. Fax: +61 8 8303 4373. E-mail: dusan.losic@adelaide.edu.au.

Author Contributions

The manuscript was written through contributions of all authors. All authors have given approval to the final version of the manuscript.

Notes

The authors declare no competing financial interest.

■ ACKNOWLEDGMENTS

Authors acknowledge the financial support provided by the Australian Research Council (ARC) through the Grants DP120101680 and FT110100711 and the School of Chemical Engineering—The University of Adelaide (UoA). Authors thank Mr. Jason Peak, Mr. Michael Jung, and Mr. Jeffrey Hiorns from the mechanical workshop of the School of Chemical Engineering (UoA) for their help and support with the fabrication of the experimental setups used in this study and the Adelaide Microscopy (AM) Centre for FEG-SEM characterization.

■ REFERENCES

(1) Wang, X. D.; Wolfbeis, O. S. *Anal. Chem.* 2013, *85*, 487−508.
(2) Borisov, S. M.; Wolfbeis, O. S. *Chem. Rev.* 2008, *108*, 423−461.
(3) McDonagh, C.; Burke, C. S.; MacCraith, B. D. *Chem. Rev.* 2008, *108*, 400−422.
(4) Santos, A.; Macías, G.; Ferré-Borrull, J.; Pallarès, J.; Marsal, L. F. *ACS Appl. Mater. Interfaces* 2012, *4*, 3584−3588.
(5) Jia, R. P.; Shen, Y.; Luo, H. Q.; Chen, X. G.; Hu, Z. D.; Xue, D. S. *Solid State Commun.* 2004, *130*, 367−372.
(6) Feng, C. L.; Zhong, X.; Steinhart, M.; Caminade, A. M.; Majoral, J. P.; Knoll, W. *Adv. Mater.* 2007, *19*, 1933−1936.
(7) Santos, A.; Balderrama, V. S.; Alba, M.; Formentín, P.; Ferré-Borrull, J.; Pallarès, J.; Marsal, L. F. *Adv. Mater.* 2012, *24*, 1050−1054.
(8) Green, R. J.; Frazier, R. A.; Shakeshe, K. M.; Davies, M. C.; Roberts, C. J.; Tendler, S. J. B. *Biomaterials* 2000, *21*, 1823−1835.
(9) Koutsioubas, A. G.; Spiliopoulos, N.; Anastassopoulos, D.; Vradis, A. A.; Priftis, G. D. *J. Appl. Phys.* 2008, *103*, 094521.
(10) Hiep, H. M.; Yoshikawa, H.; Tamiya, E. *Anal. Chem.* 2010, *82*, 1221−1227.
(11) Dhathathreyan, A. *J. Phys. Chem. B* 2011, *115*, 6678−6682.
(12) Fan, Y.; Hotta, K.; Yamaguchi, A.; Teramae1, N. *Opt. Express* 2012, *20*, 12850−12859.
(13) Hotta, K.; Yamaguchi, A.; Teramae, N. *ACS Nano* 2012, *6*, 1541−1547.
(14) Lau, K. H. A.; Tan, L. S.; Tamada, K.; Sander, M. S.; Knoll, W. *J. Phys. Chem. B* 2004, *108*, 10812−10818.
(15) Lau, K. H. A.; Duran, H.; Knoll, W. *J. Phys. Chem. B* 2009, *113*, 3179−3189.
(16) Anker, J. N.; Hall, W. P.; Lyandres, O.; Shah, N. C.; Zhao, J.; Van Duyne, R. P. *Nat. Mater.* 2008, *7*, 442−453.
(17) Yeom, S. H.; Kim, O. G.; Kang, B. H.; Kim, K. J.; Yuan, H.; Kwon, D. H.; Kim, H. R.; Kang, S. W. *Opt. Express* 2011, *19*, 22882−22891.
(18) Lang, X.; Qiu, T.; Zhang, W.; Yin, Y.; Chu, P. K. *J. Phys. Chem. C* 2011, *115*, 24328−24333.
(19) Ko, H.; Tsukruk, V. V. *Small* 2008, *4*, 1980−1984.
(20) Ji, N.; Ruan, W.; Wang, C.; Lu, Z.; Zhao, B. *Langmuir* 2009, *25*, 11869−11873.
(21) Velleman, L.; Bruneel, J. L.; Guillaume, F.; Losic, D.; Shapter, J. G. *Phys. Chem. Chem. Phys.* 2011, *13*, 19587−19593.
(22) Kondo, T.; Miyazaki, H.; Nishio, K.; Masuda, H. *J. Photochem. Photobiol. A* 2011, *221*, 199−203.

(23) Lin, V. S. Y.; Motesharei, K.; Dancil, K. P. S.; Sailor, M. J.; Ghadiri, M. R. *Science* **1997**, *278*, 840−843.
(24) Jane, A.; Dronov, R.; Hodges, A.; Voelcker, N. H. *Trends Biotechnol.* **2009**, *27*, 230−239.
(25) Alvarez, S. D.; Li, C. P.; Chiang, C. E.; Schuller, I. K.; Sailor, M. J. *ACS Nano* **2009**, *3*, 3301−3307.
(26) Kumeria, T.; Losic, D. *Nanoscale Res. Lett.* **2012**, *7*, 88−97.
(27) Casanova, F.; Chiang, C. E.; Li, C. P.; Roshchin, I. V.; Ruminski, A. M.; Sailor, M. J.; Schuller, I. K. *Nanotechnology* **2008**, *19*, 315709.
(28) Kumeria, T.; Kurkuri, M. D.; Diener, K. R.; Parkinson, L.; Losic, D. *Biosens. Bioelectron.* **2012**, *35*, 167−173.
(29) Kumeria, T.; Losic, D. *Phys. Status Solidi RRL* **2011**, *5*, 406−408.
(30) Ligler, F. S. *Anal. Chem.* **2009**, *81*, 519−526.
(31) Pacholsky, C.; Sartor, M.; Sailor, M. J.; Cunin, F.; Miskelly, G. M. *J. Am. Chem. Soc.* **2005**, *127*, 11636−11645.
(32) Pacholsky, C.; Yu, C.; Miskelly, G. M.; Godin, D.; Sailor, M. J. *J. Am. Chem. Soc.* **2006**, *128*, 4250−4252.
(33) Orosco, M. M.; Pacholsky, C.; Sailor, M. J. *Nat. Nanotechnol.* **2009**, *4*, 255−258.
(34) Harper, J.; Sailor, M. J. *Anal. Chem.* **1996**, *68*, 3713−3717.
(35) Andrew, J. S.; Anglin, E. J.; Wu, E. C.; Chen, M. Y.; Cheng, L.; Freeman, W. R.; Sailor, M. J. *Adv. Funct. Mater.* **2010**, *20*, 4168−4174.
(36) Ruminski, A. M.; King, B. H.; Salonen, J.; Snyder, J. L.; Sailor, M. J. *Adv. Funct. Mater.* **2010**, *20*, 2874−2883.
(37) Chen, M. Y.; Sailor, M. J. *Anal. Chem.* **2011**, *83*, 7186−7193.
(38) Chen, M. Y.; Klunk, M. D.; Diep, V. M.; Sailor, M. J. *Adv. Mater.* **2011**, *23*, 4537−4542.
(39) Santos, A.; Kumeria, T.; Losic, D. *TrAC, Trends Anal. Chem.* **2013**, *44*, 25−38.
(40) Masuda, H.; Fukuda, K. *Science* **1995**, *268*, 1466−1468.
(41) Masuda, H.; Hasegwa, F. *J. Electrochem. Soc.* **1997**, *144*, L127−L130.
(42) Masuda, H.; Yada, K.; Osaka, A. *Jpn. J. Appl. Phys.* **1998**, *37*, L 1340−L1342.
(43) Nielsch, K.; Choi, J.; Schwirn, K.; Wehspohn, R. B.; Gösele, U. *Nano Lett.* **2002**, *2*, 677−680.
(44) DeLouise, L. A.; Miller, B. L. *Anal. Chem.* **2005**, *77*, 1950−1956.
(45) DeLouise, L. A.; Kou, P. M.; Miller, B. L. *Anal. Chem.* **2005**, *77*, 3222−3230.
(46) Md Jani, A. M.; Kempson, I. M.; Losic, D.; Voelcker, N. H. *Angew. Chem., Int. Ed.* **2010**, *49*, 7933−7937.
(47) Abràmoff, M. D.; Magalhaes, P. J.; Ram, S. J. *Biophotonics Int.* **2004**, *11*, 36−42.

SCHOOL OF CHEMICAL ENGINEERING

THE UNIVERSITY of ADELAIDE

Supporting Information

Optically Optimized Photoluminescent and Interferometric Biosensors Based on Nanoporous Anodic Alumina: A Comparison

Abel Santos, Tushar Kumeria and Dusan Losic*

School of Chemical Engineering, The University of Adelaide, SA 5005, Australia

Losic Group

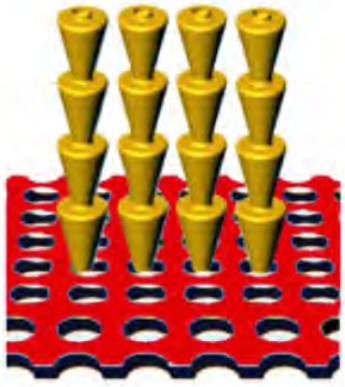

NanoTech Research

S1. Fabrication Conditions and Geometric Characteristics of NAA platforms

NAA platforms were fabricated by anodizing aluminum (Al) foils by the two-step process. After fabrication, the geometric characteristics of these NAA platforms (i.e. the pore length and its diameter) were established by SEM images acquired through a scanning electron microscope (FEG-SEM FEI Quanta 450), which were subsequently analyzed by the standard image processing package ImageJ (public domain program developed at the RSB of the NIH). The fabrication conditions and the geometric characteristics of the different NAA platforms are summarized in **Table S1** and **Figure S1**.

		t_{pw} (min)				
$(L_p; d_p)$ (μm ; nm)		0	4	8	12	16
t_{an} (h)	0.5	(1.8±0.2 ; 29±2)	(1.8±0.2 ; 40±2)	(1.8±0.2 ; 47±2)	(1.8±0.2 ; 55±2)	(1.8±0.2 ; 64±2)
	1.0	(3.6±0.2 ; 29±2)	(3.6±0.2 ; 40±2)	(3.6±0.2 ; 47±2)	(3.6±0.2 ; 55±2)	(3.6±0.2 ; 64±2)
	1.5	(5.3±0.3 ; 29±2)	(5.3±0.3 ; 40±2)	(5.3±0.3 ; 47±2)	(5.3±0.3 ; 55±2)	(5.3±0.3 ; 64±2)
	2.0	(6.4±0.4 ; 29±2)	(6.4±0.4 ; 40±2)	(6.4±0.4 ; 47±2)	(6.4±0.4 ; 55±2)	(6.4±0.4 ; 64±2)
	2.5	(8.4±0.2 ; 29±2)	(8.4±0.2 ; 40±2)	(8.4±0.2 ; 47±2)	(8.4±0.2 ; 55±2)	(8.4±0.2 ; 64±2)

Table S1. Anodization conditions and geometric characteristics of the different NAA platforms used in this study.

Notice that, all these measurements were repeated three times at different parts of the NAA sample (i.e. cross-section and top view) and three different NAA samples were analyzed per geometric parameter (i.e. 9 measurements per geometric parameter and anodization conditions). Finally, the obtained values were statistically treated by calculating averages and experimental errors.

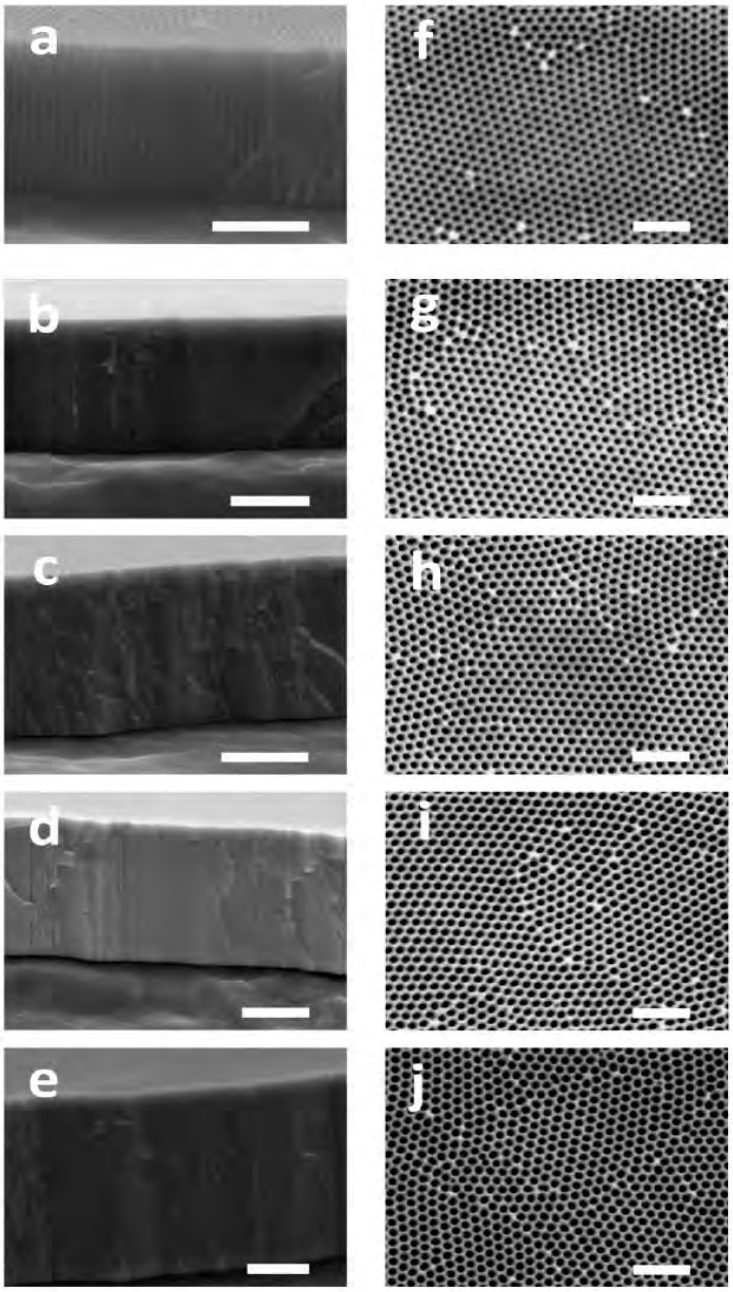

Figure S1. Set of SEM cross-section and top view images of NAA platforms featuring different pore lengths and diameters. a) t_{an} = 0.5 h (scale bar = 1 μm). b) t_{an} = 1.0 h (scale bar = 2 μm). c) t_{an} = 1.5 h (scale bar = 2.5 μm). d) t_{an} = 2.0 h (scale bar = 2.5 μm). e) t_{an} = 2.5 h (scale bar = 2.5 μm). f) t_{pw} = 0 min (scale bar = 500 nm). g) t_{pw} = 4 min (scale bar = 500 nm). h) t_{pw} = 8 min (scale bar = 500 nm). i) t_{pw} = 12 min (scale bar = 500 nm). j) t_{pw} = 16 min (scale bar = 500 nm).

S2. Fluorescein Isothiocyanate (FITC) Visual Test

The functionalization process through the APTES-GTA protocol was validated through a fluorescein isothiocyanate (FITC) visual test reported elsewhere.[1] This was carried out by dipping two NAA platforms, one functionalized and the other one non-functionalized, into an aqueous solution of FITC 200 μg mL^{-1} for 2 h at room temperature and subsequent washing with distilled water. **Figure S2** shows a digital photography of these NAA platforms. This reveals that the functionalized sample acquired a yellow tonality as a result of the FITC immobilization through the NAA pores with the activated APTES layer whereas the non-functionalized sample kept the characteristic transparent color of NAA fabricated in oxalic acid under mild anodization conditions.

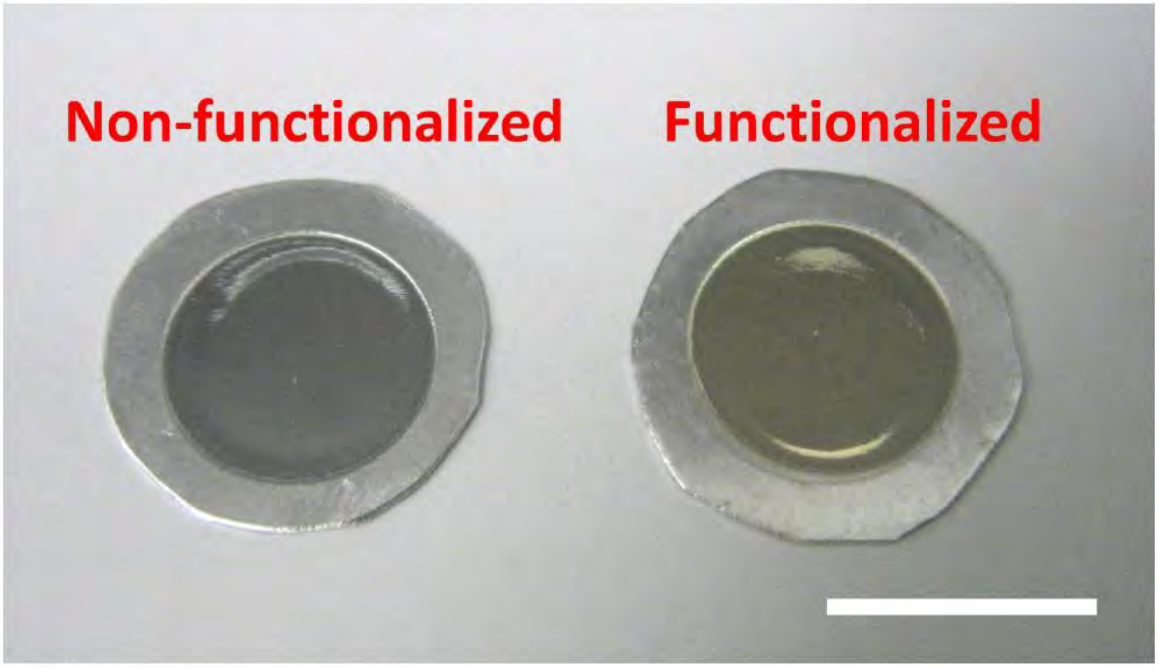

Figure S2. Digital photography of two NAA platforms functionalized and non-functionalized with APTES after the FITC visual test (scale bar = 1 cm).

S3. Raw Data OT_{eff} of and its Calculation

As an example, **Table S2** compiles the values of OT_{eff} measured before and after detection of D-glucose in NAA platforms combined with PLS.

D-Glucose in PLS-NAA under non-specific adsorption conditions

[Glucose] (M)	$OT_{eff\text{-}0}$ (nm)	$OT_{eff\text{-}f}$ (nm)	ΔOT_{eff} (nm) †	ΔOT_{eff} (%)
0.01	4060.4 ± 1.9	4067.9 ± 1.6	7.5 ± 1.6	0.20 ± 0.04
0.05	4060.1 ± 1.5	4076.9 ± 1.2	16.8 ± 1.2	0.40 ± 0.03
0.10	4062.3 ± 4.2	4117.7 ± 4.1	55.4 ± 4.1	1.40 ± 0.10
0.20	4066.6 ± 2.2	4230.3 ± 21.2	163.7 ± 20.3	4.18 ± 0.50
0.55	4064.8 ± 1.4	4397.4 ± 16.2	332.6 ± 16.2	8.29 ± 0.40
1.20	4069.1 ± 2.1	4688.3 ± 12.2	619.2 ± 12.2	15.46 ± 0.30

Table S2. Raw data corresponding to the calculation of ΔOT_{eff} for detection of D-glucose under non-specific adsorption conditions in PLS-NAA sensing platforms (these values correspond are represented in **Figure 4a** of this manuscript). $OT_{eff\text{-}0}$ and $OT_{eff\text{-}f}$ indicate the effective optical thickness of these NAA platforms before and after adsorption of D-glucose molecules, respectively. †Calculated as: $\Delta OT_{eff} = \Delta OT_{eff\text{-}f} - \Delta OT_{eff\text{-}0}$.

Notice that $OT_{eff\text{-}0}$ is the effective optical thickness of the NAA platform without considering the angle of incidence (in this case 40^{o}, as indicated in the manuscript for PLS). After applying **Equation 1**, we found that the obtained physical thickness of these samples (i.e. L_p – pore length) was in good agreement with the estimation obtained from the calibration curves shown in **Figure 2** of this manuscript.

As a graphical example of these calculations, **Figure S3** shows the PLS and FFT spectra of NAA platforms used to detect D-glucose 1.20 M.

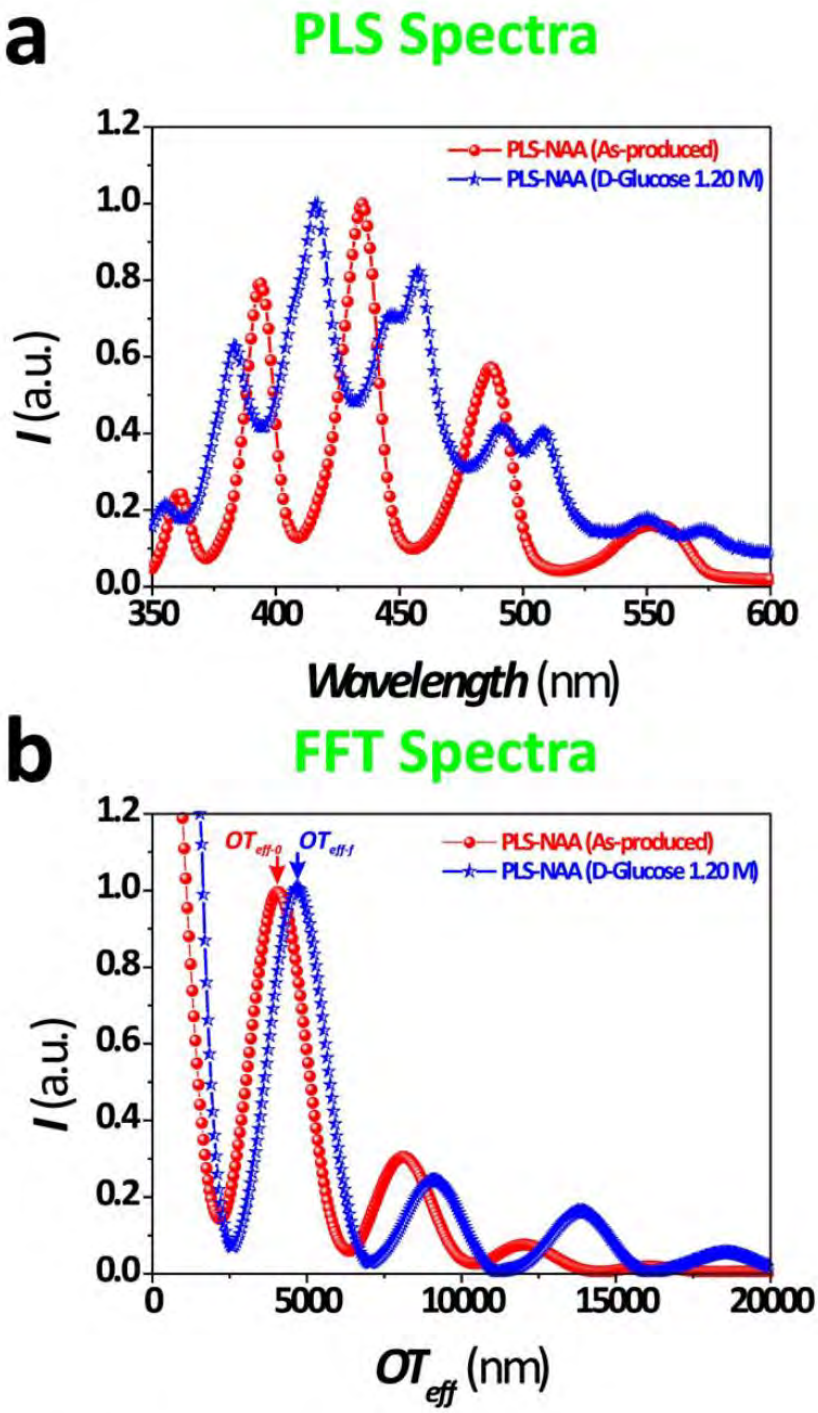

Figure S3. PLS and FFT spectra of NAA platforms used to detect D-glucose 1.20 M. a) PLS spectrum before and after adsorption of D-glucose. b) FFT spectrum before and after adsorption of D-glucose.

S4. Fourier Transform IR (FTIR) Spectroscopy Analysis

Two NAA platforms infiltrated with aqueous solutions of D-glucose and L-cysteine 50 mM were analyzed through Fourier transform IR (FTIR) spectroscopy (**Figure S4**). To this end, the remaining aluminum substrate was removed from the NAA backside by wet chemical etching in a saturated solution of hydrochloric acid and cupric chloride (HCl / $CuCl_2$). Notice that the FTIR spectrum of as-produced NAA samples was used as a background. FTIR spectra were collected in a FTIR spectrometer (Nexus 6700 Nicolet ThermoFisher). The number of scans was set to 32 with a resolution of 4 cm^{-1}. All spectra were collected in the range 4000-1500 cm^{-1} in transmission mode.

Figure S4a shows the FTIR spectrum of a NAA platform infiltrated with D-glucose under non-specific immobilization conditions. This shows a strong peak that corresponds to the bands from 2900 to 3450 cm^{-1} assigned to CH and OH vibrational groups of D-glucose molecules.[2] **Figure S4b** shows the FTIR spectrum of a NAA platform infiltrated with L-cysteine under specific immobilization conditions. A strong peak is observed at around 2540 cm^{-1} in the IR spectrum, which is associated with the SH stretching mode of L-cysteine molecules.[3]

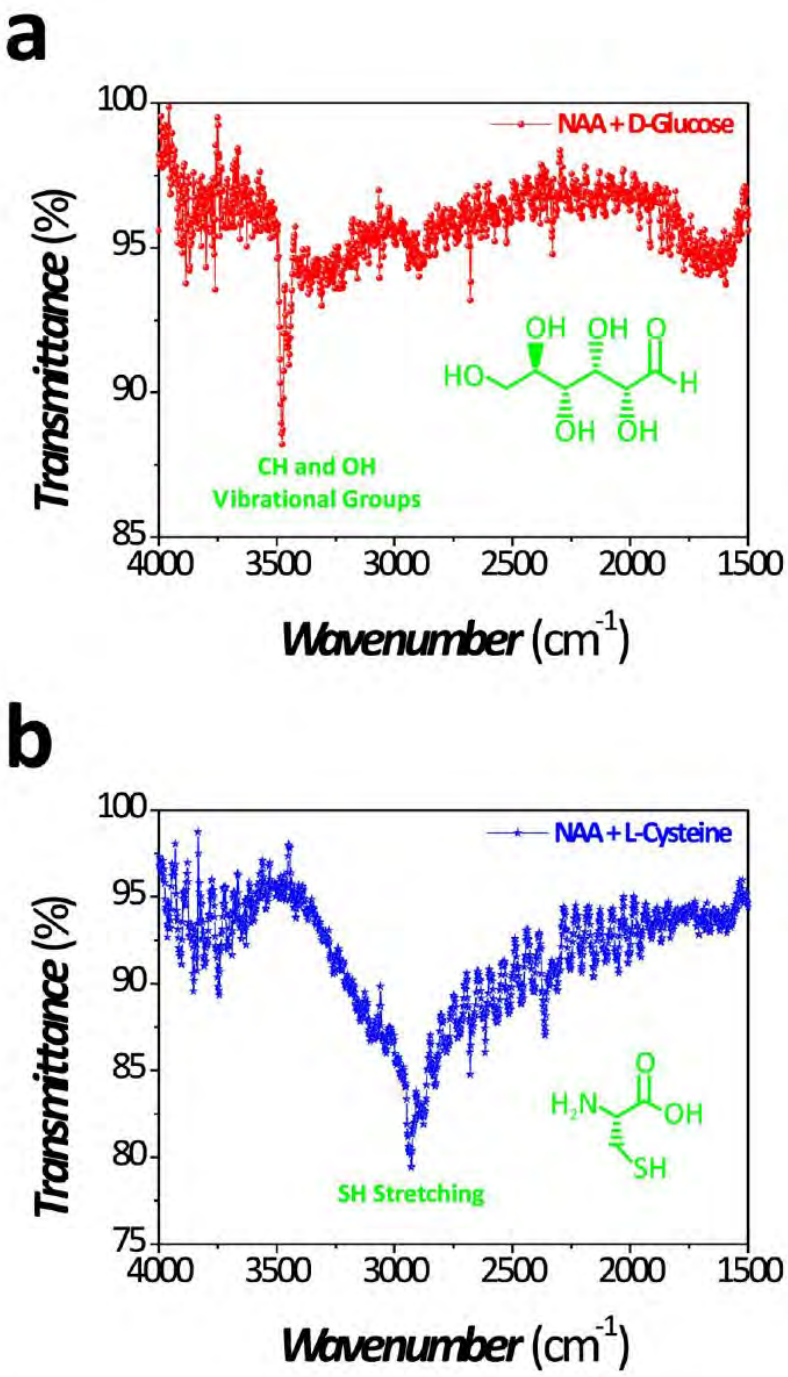

Figure S4. FTIR spectra of NAA platforms infiltrated with D-glucose 50 mM (a) and L-cysteine 50 mM (b) under specific and non-specific immobilization conditions.

S5. Definition of Optical Parameter *OP*

The sensing parameter used in PLS-NAA and RIfS-NAA platforms is the effective optical thickness (OT_{eff}). This optical parameter makes it possible to establish the amount of analyte in the range of linear performance of these biosensors (i.e. range within which the effective optical thickness change is proportional to the analyte concentration). Therefore, to establish the most optimal NAA platform, we used the parameter *OP*, which is defined as the ratio between the maximum peak intensity and its width at half of the intensity value calculated from the FFT spectra obtained from the PLS and RIfS spectra (i.e. effective optical thickness peak). **Figure S5** shows the definition of this parameter, which was used to optimize the different sensing platforms analyzed in this study (i.e. PLS-NAA and RIfS-NAA).

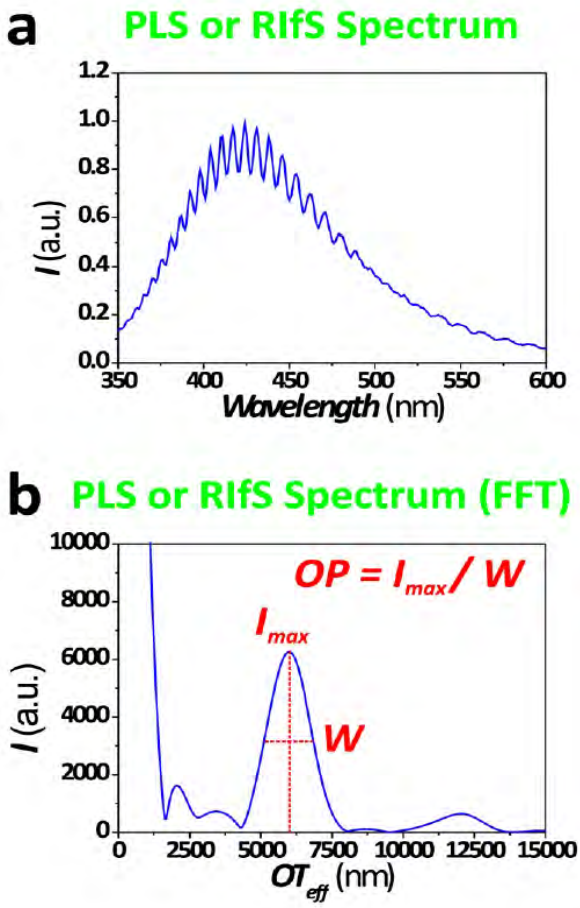

Figure S5. Definition of the parameter *OP* obtained from the PLS or RIfS spectrum (a) after applying the fast Fourier Transform (FFT) (b).

S6. PLS and UV-visible Spectra of D-Glucose and L-Cysteine Solutions

The PLS and UV-visible spectra of two solutions of D-glucose and L-cysteine with the same analyte concentration (i.e. 50 mM) were acquired in order to study the optical properties of these analytes. PLS spectra were acquired in a spectrofluorometer (Fluoromax-4 Horiba Jobin Yvon) equipped with a Xe lamp used as the excitation light source at room temperature. The excitation wavelength (λ_{ex}) was set to 320 nm with a slit size of 5 nm. UV-visible spectra were acquired in a UV-visible spectrometer (Carry 60 spectrophotometer Agilent technologies). As **Figure S6a** shows, it was verified that D-glucose is much more photoluminescent than L-cysteine. Nevertheless, both solutions showed a very low and comparable absorbance in the wavelength range analyzed in this study (**Figure S6b**).

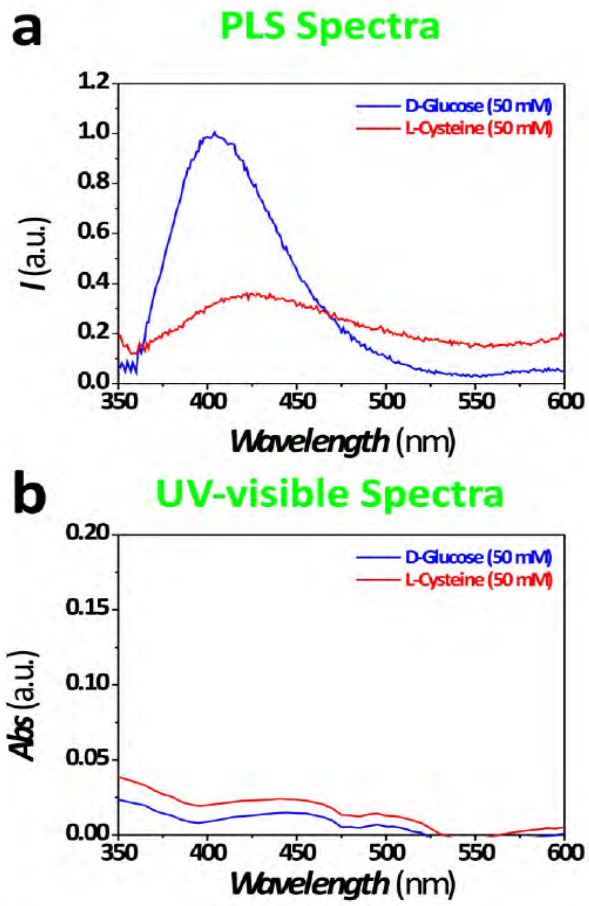

Figure S6. PLS (a) and UV-visible (b) spectra of aqueous solutions of D-Glucose and L-Cysteine 50 mM.

References

(1) Md Jani, A. M.; Kempson, I. M.; Losic, D.; Voelcker, N. H. *Angew. Chem., Int. Ed.* **2010**, *49*, 7933–7937.

(2) Ibrahim, M.; Alaam, M.; El-Haes, H.; Jalbout, A. F.; de Leon, A. *Ecletica Quim.* **2006**, *31*, 15–21.

(3) Pawlukojc, A.; Leciejewicz, J.; Ramirez-Cuesta, A. J.; Nowicka-Scheibe, J. *Spectrochim. Acta, Part A* **2005**, *61*, 2474–2481.

CHAPTER 8

REAL-TIME and IN-SITU DRUG RELEASE MONITORING from NANOPOROUS IMPLANTS UNDER DYNAMIC FLOW CONDITIONS by REFLECTOMETRIC INTERFERENCE SPECTROSCOPY

Tushar Kumeria

School of Chemical Engineering, The University of Adelaide South Australia 5005, Australia

This chapter is based on a peer-reviewed article:

T. Kumeria, K. Gulati, A. Santos, D. Losic "Real-time and in situ drug release monitoring from nanoporous implants under dynamic flow conditions by reflectometric interference spectroscopy" *ACS Applied materials & interfaces*, 2013, **5**, 5436.

Statement of Authorship

Real-time and in situ drug release monitoring from nanoporous implants under dynamic flow conditions by reflectometric interference spectroscopy. *ACS Applied materials & interfaces*, 2013, **5**, 5436.

Tushar Kumeria (Candidate)

Under supervision of D. Losic and A. Santos, I developed, designed, and performed the experiments, interpreted and processed the data and wrote the manuscript for submission.

Signed Date: 10/04/2015

Karan Gulati

I helped Tushar Kumeria (Candidate) with drug loading and measuring the release of drug with conventional method. I give consent for Tushar Kumeria to present this paper for examination towards the Doctorate of philosophy.

Signed Date: 10/04/2015

Abel Santos

I acted as secondary supervisor for the candidate and aided in development and design of the experiments and evaluation of manuscript for submission. I give consent for Tushar Kumeria to present this paper for examination towards the Doctorate of philosophy.

Signed Date: 10/04/2015

Dusan Losıc

I acted as primary supervisor of the candidate and aided in evaluation of experimental design and manuscript for submission. I give consent for Tushar Kumeria to present this paper for examina f philosophy

Signed Date: 10/04/2015

CHAPTER 8: T. Kumeria, K. Gulati, A. Santos, D. Losic "Real-time and in situ drug release monitoring from nanoporous implants under dynamic flow conditions by reflectometric interference spectroscopy" *ACS Applied materials & interfaces*, 2013, **5**, 5436.

ACS APPLIED MATERIALS & INTERFACES

Research Article

www.acsami.org

Real-time and in Situ Drug Release Monitoring from Nanoporous Implants under Dynamic Flow Conditions by Reflectometric Interference Spectroscopy

Tushar Kumeria, Karan Gulati, Abel Santos, and Dusan Losic*

School of Chemical Engineering, The University of Adelaide, Adelaide, SA 5005, Australia

Supporting Information

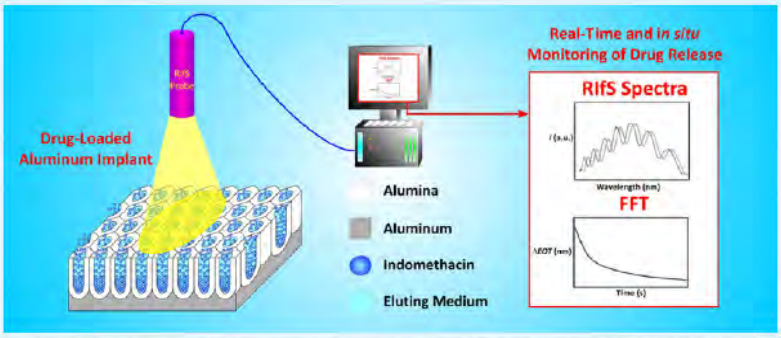

ABSTRACT: Herein, we present an innovative approach to monitoring in situ drug release under dynamic flow conditions from aluminum implants featuring nanoporous anodic alumina (NAA) covers used as a model of drug-releasing implants. In this method, reflectometric interference spectroscopy (RIfS) is used to monitor in real-time the diffusion of drug from these nanoporous implants. The release process is carried out in a microfluidic device, which makes it possible to analyze drug release under dynamic flow conditions with constant refreshing of eluting medium. This setup mimics the physiological conditions of biological milieu at the implant site inside the host body. The release of a model drug, indomethacin, is established by measuring the optical thickness change with time under four different flow rates (i.e. 0, 10, 30, and 50 μL min^{-1}). The obtained data are fitted by a modified Higuchi model, confirming the diffusion-controlled release mechanism. The obtained release rate constants demonstrate that the drug release depends on the flow rate and the faster the flow rate the higher the drug release from the nanoporous covers. In particular, the rate constants increase from 2.23 ± 0.02 to 12.47 ± 0.04 μg min$^{-1/2}$ when the flow rate is increased from 10 to 50 μL min^{-1}, respectively. Therefore, this method provides more reliable and relevant information than conventional in vitro drug release methods performed under static conditions.

KEYWORDS: *nanoporous anodic alumina, drug release control, dynamic flow conditions, nanoporous implants, optical thickness*

1. INTRODUCTION

Most current clinical therapies are based on intermittent oral or intravenous drug administration, which provide a high level of drug in blood right after the dose is administered. However, the drug level in the bloodstream immediately decreases. This is known as the peak-and-valley effect, which can generate many problems in clinical patients as the drug concentration in the bloodstream can reach toxic levels shortly after administration and subsequently fall below the therapeutic level, making the therapy inefficient. Furthermore, other inherent problems of these drug administration methods include low drug efficacy, poor bioavailability, and limited biodistribution. This has made these therapies unattractive for some clinical treatments like bone-related diseases (e.g., infection, cancer, osteoarthritis, etc.) as the blood supply is constrained by the poor perfusion in the bones, especially under traumatic conditions.[1−4] Another important issue to be accounted for increasing number of clinical patients with bone injuries/disorders like osteoporosis, severe fractures and cancers is our current lifestyle factors plus age-related conditions. In some cases, these patients require implants to support any bone structure for recovering partial or complete mobility. The benefits obtained from implants can be numerous although upon implantation these biomedical devices can lead to extensive inflammation, bacterial infection and poor implant-bone integration, which can ultimately lead to implant rejection/failure.[5−7] In this scenario, implantable local drug delivery systems are recognized to be the most attractive method to reduce implant-related problems and increase their integration in the host body. It is worth mentioning that local drug delivery systems also offer controlled and extended drug

Received: January 21, 2013
Accepted: June 3, 2013
Published: June 3, 2013

release, low dose requirement, and higher localized drug concentration, which reduce the disease treatment period.[8−10]

Recent advances in nanomedicine have enabled the use of several nanoporous materials including nanoporous anodic alumina (NAA), nanotubular anodic titania (NAT), and nanoporous silicon for local drug delivery administrations. These nanoporous materials are a promising alternative to other local drug delivery platforms (e.g. polymeric films and rubbers) as they neither erode nor degrade thus offer enhanced stability. Furthermore, these nanopores act as an efficient drug reservoir, which also allows a better control over the drug release kinetics.[11−15] Considerable research has been devoted in the past several years to study the applications of NAA and NAT as orthopedic, dental, coronary, and immunoisolation drug-releasing implants and chips, as a result of their chemical stability, controllable dimensions, tunable surface chemistry, high surface-to-volume ratio and biocompatibility.[12,13,16−19] Generally, the drug release performance of these structures is characterized through conventional in vitro batch monitoring process under static conditions (i.e., measuring the drug concentration from the UV−visible spectrum at fixed intervals of time).[20−22] Nonetheless, these systems cannot simulate dynamic in vivo conditions very closely as the eluting medium gets saturated of released drug after certain time. This reduces the concentration gradient between the bulk solution and the nanoporous implant (i.e. driving force) and significantly influences the release rate, making the results inaccurate. Therefore, there is an important lack of knowledge and understanding about the kinetics and mechanism governing drug release from nanoporous implants under dynamic flow conditions.[17,19,23] However, there is an increasing demand to develop localized drug delivery systems based on drug-releasing implants for its multiple advantages. To address this problem, new approaches have been recently reported to mimic the physiological conditions that prevail at the implant site in the host body. These systems used a continuous flow chamber in which the release kinetics of various antibiotics (i.e. amikacin, vancomycin gentamicin and tobramycin) from a poly-(methyl methacrylate) (PMMA) and calcium phosphate matrix were analyzed.[23−26] However, these techniques cannot be automated and multiple aliquots must be taken from the solution continuously throughout the whole release process, making the process labor intensive and less accurate for studying drug release mechanism within a short period of time (e.g. seconds or minutes).[17] To extensively monitor and understand the drug release kinetics, Gultepe et al. designed a fluorescence-based setup for monitoring in situ release of doxorubicin from nanoporous substrates in real-time. This setup acquired multiple readings over time without disturbing the release system, but was limited to fluorescent drugs or molecules under static conditions.[17]

To avoid the limitations of the systems described in the works just mentioned above, we designed a microfluidic device capable of accommodating a drug loaded nanoporous anodic alumina implant along with in situ drug release monitoring by a real-time technique as reflectometric interference spectroscopy (RIfS). This system combines both dynamic flow conditions and in situ drug release monitoring. RIfS is a versatile and highly sensitive detection technique based on the interference of white light reflected from a thin film. The detection principle is based on changes in the effective medium of the film, which can be easily monitored by measuring the effective optical thickness (EOT = $2n_{eff}L$), defined as the product between the effective refractive index of the film (n_{eff}) and its thickness (L).[27−30] Contrary to most of the current drug release monitoring systems, this system combines a microfluidic device, which makes it possible to maintain a high diffusion gradient between pores and eluting medium, with high resolution and real-time measurements of the released drug. This enables the study of drug release from nanoporous materials under physiological conditions. Indomethacin, an anti-inflammatory drug, is used as the model drug, whereas NAA is chosen as model of nanoporous substrate not only for its already proven capabilities (e.g., chemical and thermal stability, controllable dimensions and surface chemistry, biocompatibility, etc.), but also because it is highly optically active and generates well-resolved interference fringes.[31] To demonstrate the effectiveness of this system, we studied the effect of the flow rate of the eluting medium over the drug releasing performance of these NAA implants. This system simulates the drug diffusion from the nanoporous layer covering the implant to the surrounding tissues. Finally, the obtained results were validated and correlated both with experimental data obtained under conventional drug release conditions (i.e. static conditions) and theoretical values obtained from a modified Higuchi model in order to identify the mechanism of drug release.

2. EXPERIMENTAL SECTION

2.1. Materials. High-purity aluminum (Al) foils (99.997%) were supplied by Alfa Aesar (USA). Oxalic acid, ethanol (ChemSupply, Australia), chromic acid (Mallinckrodt, USA), phosphoric acid, and indomethacin (Sigma-Aldrich, Australia) were used as received. High-purity water was used for all solution preparation as produced by sequential treatments by Millipore system and a final filtering step through a 0.22 μm filter.

2.2. Preparation of NAA Implants. A two-step electrochemical anodization process was used to fabricate NAA with structurally engineered geometric characteristics as reported elsewhere.[32] Briefly, Al foils 1.5 × 1.5 mm^2 were sequentially sonicated in ethanol (EtOH) and distilled water for 15 min and dried under a nitrogen stream. First anodization was carried out in an aqueous solution of oxalic acid 0.3 M ($H_2C_2O_4$) at 6°C and 50 V for 10 h. Then, the resulting nanoporous anodic alumina layer was removed by wet chemical etching in an oxide removal solution (i.e., chromic acid 0.2 M (H_2CrO_4) and phosphoric acid 0.4 M (H_3PO_4)) for 3 h at 60 °C. Next, pre-textured Al substrates obtained by this process were subjected to final anodization, which was carried out for 40 min under the same conditions to obtain self-ordered nanopores, the pore diameter and length of which were approximately 30−35 nm and 4.5 μm, respectively.

2.3. Drug Loading and Release through Conventional Method. NAA substrates were loaded with an ethanolic solution of indomethacin 1% w/v by three different loading methods reported elsewhere:[21,22] (i) method 1, drug loaded inside the pores and on the NAA surface; (ii) method 2, drug loaded exclusively inside the NAA pores; and (iii) method 3, drug loaded only on the NAA surface. In method 1, 10 μL of drug solution were dropped onto the NAA substrates and allowed to dry by evaporation so that the drug solution wetted the pore walls as well as the top surface of the NAA substrate.

Method 2 was achieved by dropping the same amount of drug onto the NAA substrates but cleaning its surface by soft wiping and plasma cleaning treatment (plasma system ATTO, Deiner Scientific, Germany) to remove the excess of drug from the NAA surface. In method 3, 10 μL of drug solution was dropped onto the NAA substrates and evaporated in an oven at 80 °C under air atmosphere. In this way the solvent was evaporated before the drug solution wetted the pore walls. These loading processes were repeated 10 times to obtain an equivalent amount of drug loading in all the NAA implants.

To determine the amount of drug loaded into these NAA substrates, we performed a thermogravimetric analysis (Hi-Res

Modulated TGA 2950). First, the correct characteristic temperature peak for indomethacin decomposition was determined by heating 25 mg of pure drug in the platinum pan of the TGA balance from 20 to 800 °C. The drug peak was identified and used to calculate the total amount of drug present in the NAA substrates. The total drug loadings obtained by methods 1, 2, and 3 were established by averaging the resulting amount of drug in three different NAA implants, respectively.

Conventional in vitro drug release from NAA implants was investigated through changes in the UV-visible absorbance with time (Cary 60 spectrophotometer, Agilent Technologies, Australia). Briefly, NAA implants loaded with drug were immersed in 5 mL of PBS (pH 7.4) under static conditions. One milliliter of this solution was extracted for UV−visible characterization and replaced by 1 mL of fresh PBS after every measurement. First, measurements were taken at short intervals of 5 min during the first 100 min to monitor the initial drug release. After this, measurements were performed every 24 h until the total amount of drug was released into the eluting medium. These absorbance measurements were carried out at a wavelength of 320 nm, which is the characteristic absorbance wavelength for indomethacin. All the drug release measurements were repeated 3 times and statistical analysis was performed.

2.4. Flow Cell for in Situ Drug Release from NAA Implants. An unbounded microfluidic flow cell was fabricated in two reusable halves with a top glass cover and a microstructured base chip. The base chip was fabricated by hot embossing of the microstructure in solid PMMA. A brass stamp machined by a CNC micromachining (Supermill-2M, Kira, Japan) was replicated by embossing under pressure at 4.3 MPa and 130 °C in a hot embosser-substrate bonder (EVG, 520-HE, USA). The resulting microstructure consisted of two microchannels (i.e., single inlet-single outlet and triple inlet-single outlet), with the width and depth of 200 and 100 μm, respectively. These microchannels delivered the fluid into a 36 mm^2 cavity of 200 μm depth to accommodate 100 μm thick NAA implants. Hence, a further 100 μm space was left above the NAA substrate to allow the eluting medium to pass through the cavity without obstructions. Furthermore, an array of micropillars before the cavity chamber enabled an even distribution of the fluid over the NAA surface (see Figure S1 in the Supporting Information). These two halves of the microfluidic device (i.e. base chip and cover glass) were sealed together by a clamp, which allows the integration of the optical probe for RIfS measurements. Fresh PBS solution was flown through the system by a syringe pump (Fusion touch, Chemyx, USA). The flow rate was modified from 0 to 50 μL min^{-1} according to the reduced diffusion around bones in the physiological milieu (i.e. target soft tissues for these drug eluting implants). The blood flow rate calculated for cortical and cancellous bones in 20 weeks old pigs are up to 7.5 and 21.3 mL min^{-1} per 100 g of tissue, respectively.[23] The intension behind using these flow rates was not only to closely imitate the blood flow conditions observed per gram bone tissue of a 20 week old pig but also to maintain the constant concentration gradient between NAA implant and eluting medium.

2.5. RIfS Setup for in Vitro Release Monitoring. RIfS measurements were performed in a setup composed of a Y-junction optical fiber probe. One end of this optical probe was connected to a tungsten halogen light source (LS-1LL, Ocean Optics, USA) and the other end to a miniature spectrophotometer (USB 4000, Ocean Optics, USA). The common end of the probe was used to focus white light from the source and collect the reflected light from the drug-loaded NAA implants in the microfluidic cell. The obtained data were collected from an illuminated circular spot of 3 mm in diameter while the spectral range was 400-900 nm. For in situ monitoring of drug release, RIfS spectra were saved at an interval of 10 s with an integration time of 20 ms. The effective optical thickness (EOT) was obtained by applying Fast Fourier Transform to the RIfS spectra in Igor Pro library (Wavemetrics, USA). The release of indomethacin from these NAA implants was monitored through changes in effective optical thickness at different flow rates (i.e., 0 to 50 μL min^{-1}). All the in situ measurements were repeated 3 times and the obtained data were statistically analyzed.

2.6. Characterization of NAA Implants. The structural characteristics of NAA substrates such as pore diameter and thickness were established by image analysis from scanning electron microscopy (SEM) images (FEI Quanta 450, Japan). All samples for SEM characterization were coated by a 5 nm platinum layer before analysis.

3. RESULTS AND DISCUSSION

3.1. Structure and Morphology of NAA Implants. The geometric characteristics of the prepared NAA implants were established by scanning electron microscopy (SEM). Figure 1 shows a set of SEM images of the top surface and cross-sectional structure of resulting NAA implants after a two-step anodization process. These presented self-ordered and vertically aligned cylindrical pores with hexagonal arrangement, the pore diameters and lengths of which were 35-40 nm

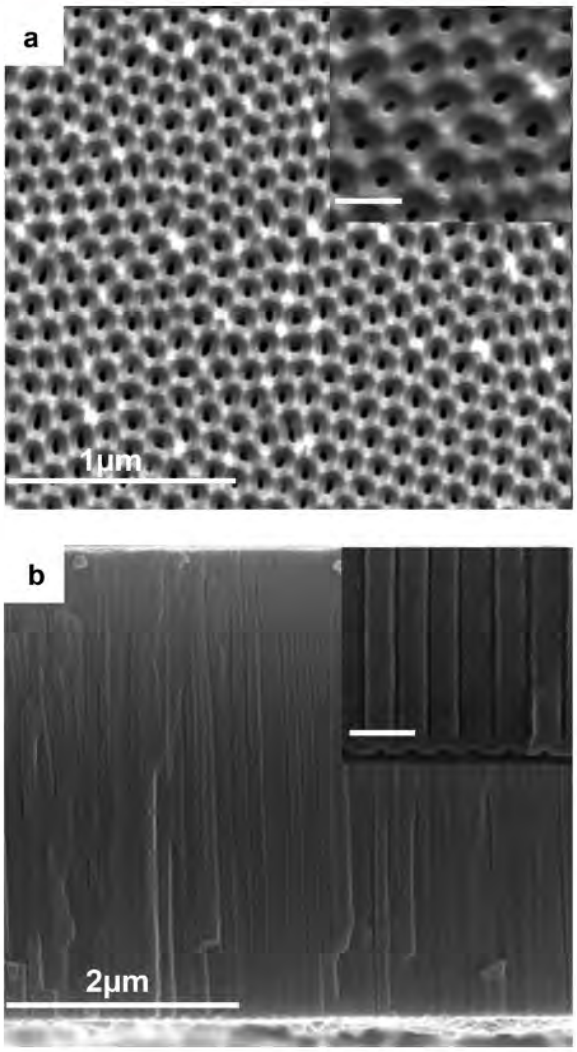

Figure 1. SEM images of prepared NAA substrates used as drug-releasing implants. (a) Top view showing hexagonally arranged pores with a high-magnification image in inset (scale bar = 100 nm). (b) Cross-section view with straight nonbranched pores with inset showing the oxide barrier layer at the bottom of the pores (scale bar = 100 nm).

(Figure 1a) and 4.5-5.0 μm (Figure 1b), respectively. The pores were closed at their bottom with an oxide barrier layer and thus capable of acting as a reservoir for drug molecules. The geometric characteristics of these NAA substrates were structurally engineered to hold a substantial amount of drug inside the pores with optimized optical response for RIfS measurements.[31]

3.2. Drug Loading and Release Monitored by Conventional Methodology. A set of thermogravimetric analyses (TGA) were performed on NAA implants loaded with indomethacin by methods 1, 2, and 3 to determine the total amount of drug loaded by different loading strategies. The weight change from 200 to 375°C was associated with the decomposition of pure indomethacin. According to the obtained weight reduction curve, we found that the total amount of drug loaded was 68 ± 11 μg, 53 ± 6 μg and 71 ± 9 μg for loading methods 1, 2 and 3, respectively (see Figure S2 in the Supporting Information). The amount of drug loaded in these NAA substrates by all the loading methods (i.e., method 1, method 2, and method 3) is summarized in Table S1 in the Supporting Information.

Figure 2 summarizes the results obtained for drug release experiments carried out by the conventional method under

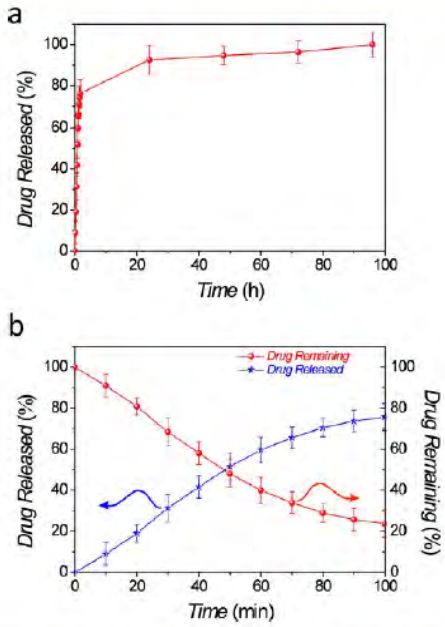

Figure 2. Drug release plots from NAA implants under static conditions (error bars correspond to standard deviations obtained after averaging 3 measurements). (a) Release pattern for the complete drug release during 4 days. (b) Amount of drug released (left scale) and amount of drug remaining in pores (right scale) during the first 100 min of release.

static conditions. The drug release pattern shown in Figure 2a can be described in two phases: namely, (i) an initial fast release of drug and (ii) a slow sustained release for 4 days in the course of which 100 % of the drug is eluted from the nanoporous implant. Initial release of indomethacin during the first 100 min is illustrated in Figure 2b. This verifies that around 75% of the total amount of drug was released from the NAA implant (i.e., 50 ± 4 μg) after 100 min. The initial release phase is related with a fast diffusion of the freely available loosely bound superficial drug molecules from the NAA implant surface because of the high concentration gradient of drug between the NAA implant and the eluting medium (i.e. phosphate buffer saline (PBS) solution). Nevertheless, a different pattern of drug release was observed after the 1st day of release, reaching a very slow release rate over the following 4 days. Approximately 1.6 μg of drug were released after 24 h from day 1 till day 4 of the release experiment. Hence, the drug release followed a linear trend in cumulative drug release amount. Notice that the release kinetics of this phase is controlled by the diffusion of drug molecules along the pores to the bulk eluting medium at the surface of the NAA implant.

3.3. Drug Release under Dynamic Flow Conditions Monitored by RIfS. Drug release from NAA implants under dynamic flow conditions was performed in a specially designed microfluidic cell, which made it possible to monitor the drug release in real-time and in situ conditions by RIfS. The optical thickness change was used as the sensing parameter to measure the concentration of released drug molecules from the NAA pores. Fresh PBS was flowed through the device at 30 μL min^{-1} not only to mimic biological fluid circulation inside the host body but also to maintain a high concentration gradient of drug between the NAA pores and the eluting medium. Figure 3

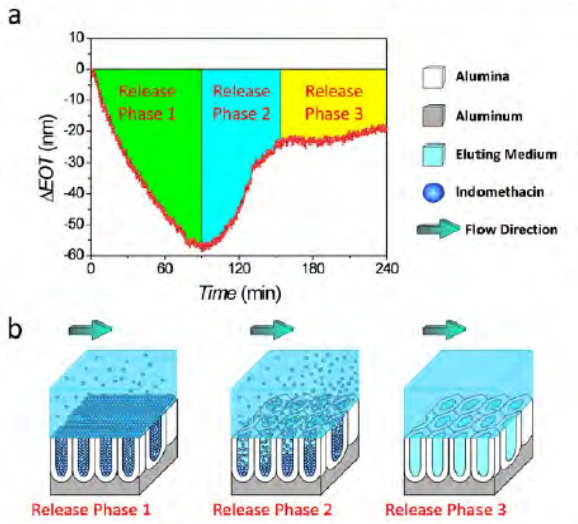

Figure 3. Relationship between ΔEOT with time and different drug release phases under dynamic conditions (flow rate = 30 μL min^{-1}). (a) ΔEOT change with time and different release phases. (b) Schematic diagram showing the evolution of drug release with time from the NAA implants under dynamic conditions.

shows the release pattern obtained through the effective optical thickness change (ΔEOT) generated by the release of drug from the NAA implants for 240 min. The release curve obtained by RIfS consists of three characteristic phases: namely, (i) an initial decrease in ΔEOT, (ii) an increase in ΔEOT, and (iii) final constant value of ΔEOT.

The initial release of drug and the decrease in ΔEOT are ascribed to the fast diffusion of drug molecules residing on the NAA surface. ΔEOT decreases for 100 min and starts to increase after this point. This increment is thought to be related with the drug release from the pore walls to the PBS solution inside the pores, which increases the refractive index of the

effective medium. This suggests that this second phase is limited by drug diffusion from pores as result of drug-surface interactions. Finally, ΔEOT reaches a stable value, which corresponds to the NAA implant in PBS. This denotes that the drug has been entirely released from the NAA implant.

A set of control tests was carried out in order to confirm our hypothesis about the relationship between the observed drug release pattern and ΔEOT (see Figure S3 in the Supporting Information). The first control test was performed with a NAA implant loaded by Method 2 (i.e. drug only inside the pores). It was observed an initial decrease in ΔEOT for the first 3 min of release followed by a noticeable increment until Δ*EOT* reached a stable value in approximately 15 min at a flow rate of 50 μL min^{-1} (see Figure S3a in the Supporting Information). The results clearly confirmed that this release pattern is related to diffusion of drug molecules from the pores. Although some amount of drug still remained on the NAA implant surface after surface cleaning by physical and plasma cleaning treatment, this can be considered almost negligible. A second control test was performed with a NAA implant loaded with drug by Method 3 (i.e., drug loaded exclusively on the NAA implant surface). These results show that ΔEOT decreases throughout until it reaches a constant value. No increment of Δ*EOT* was observed after that, demonstrating that the drug release takes place only from the NAA implant surface and not from its pores (see Figure S3b in the Supporting Information). The aforementioned control experiments justified the triphasic release pattern presented in Figure 3.

Optimal drug dosage and release rate under dynamic conditions (i.e. similar to physiological milleu at implant site) is an esential requirement for drug-relasing implants used in any specific therapy. These characteristics cannot be established by means of conventional drug-relase monitoring systems under static conditions. As a proof of the capability of this system, we studied the effect of four flow rates (i.e., 0, 10, 30, and 50 μL min^{-1}) over the drug release profile in NAA implants infiltrated by Method 1 (i.e. drug loaded on the NAA surface and inside its pores) (Figure 4). A control experiment was performed

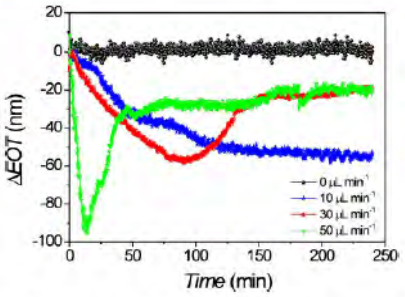

Figure 4. ΔEOT evolution with time for drug release from NAA implants loaded by Method 1 (i.e. drug inside the pores as well as on the surface of the implant) under dynamic conditions at different flow rates from (i.e., from 0 to 50 μL min^{-1}).

under non-flow condition (i.e., 0 μL min^{-1}) and no changes in ΔEOT were observed throughout. This is due to the very small volume of the chamber of our microfuidic device (i.e., 3.6 μL, approximately), which is not big enough to maintain a concentration gradient between the elluting buffer and the drug loaded NAA substrate. A slight decrease in ΔEOT was observed at 10 μL min^{-1}, demonstrating that under these conditions, drug was removed from the NAA surface but not from the pores as a result of the slow flow rate. Nevertheless, experiments performed at 30 and 50 μL min^{-1} presented a triphasic drug release pattern with an initial decrease in ΔEOT (i.e., release of drug molecules from the NAA implant surface) followed by an increase (i.e., release of drug molecules from pores) and a final stationary state (i.e., end of drug release). It was verified that the faster the flow rate, the faster the drug release from both the NAA implant surface and its pores. Furthermore, it was also observed that the ΔEOT peak, which is defined as the transition from the release phases 1 and 2, followed a proportionally reverse trend (i.e. the faster the flow rate the lower the ΔEOT peak), decreasing as: -44 ± 4 nm at 10 μL min^{-1}, -56 ± 3 nm at 30 μL min^{-1}, and -89 ± 7 nm at 50 μL min^{-1}. It is noteworthy that ΔEOT reached its stable value (i.e., release phase 3) faster at 50 μL min^{-1} (i.e., 35 min) than at 30 μL min^{-1} (i.e., 55 min). This result can be explained in terms of buffer exchange rate as the faster the flow rate the faster the buffer solution in the cell chamber was replaced by fresh one (i.e. every 23, 7, and 4 s at 10, 30, and 50 μL min^{-1}, respectively). In other words, the concentration gradient of drug was higher at faster flow rates, increasing the drug release rate as it acts as the driving force of the release process (i.e., diffusion control). These results are in good agreement with previous studies showing that the flow rate affects the drug release from drug loaded polymeric matrices.[23] To the best of our knowledge, this is the first study confirming a similar effect in nanoporous implants based on non-eroding inorganic matrices.

3.4. Release Kinetics: Synergy between Conventional and in Situ Release Monitoring. To establish the relationship between the amount of drug released and the optical thickness change measured at a constant flow rate, we performed a calibration experiment (Figure 5). In this experiment, we related Δ*EOT* with the amount of drug released at certain time, which was established by analyzing the UV-visible spectra of the eluted buffer at the output of the flow cell at 30 μL min^{-1} during the initial release phase (i.e. within the first 100 min of release). ΔEOT and the amount of drug were determined by RIfS and UV-visible spectroscopy, respectively. These were found to be in a good agreement (Figure 5a). Furthermore, as Figure 5b shows, there is a linear relationship between both parameters (i.e. ΔEOT and amount of drug released determined by RIfS and UV−visible spectroscopy, respectively). This result verifies the suitable performance of our optical sensing system to monitor drug release under the aforementioned conditions. Notice that this fast release has been observed in many studies albeit only a few detailed investigations have reported about the release phenomena at this regime, being ignored by most of the mathematical models. Therefore, real-time and in situ monitoring of drug release provides an outstanding advantage over conventional methods as this system makes it possible to collect multiple readings at milisecond time intervals under dynamic conditions. This is crucial to understand the initial fast release of drug from nanoporous implants and it plays an important role in the efficiency of the treatment dependening upon the therapy and drug. Initial fast release could be useful for therapies which require fast release of drug (i.e., wound treatment, inflammation and bacterial infection, etc.). On the other hand, it is not advisable for treatment of conditions that require long-term sustained drug release such as implants (i.e., bone implants, stents, etc.).[17,24,33]

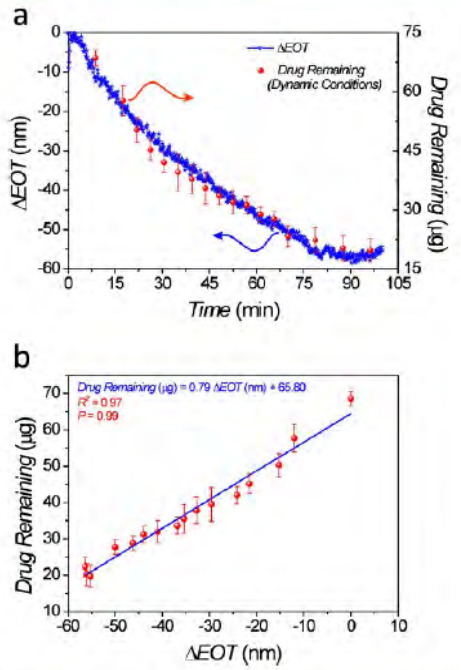

Figure 5. Establishment of relationship between optical thickness and amount of drug released (error bars correspond to standard deviations obtained after averaging 3 measurements). (a) Evolution of ΔEOT at 30 μL min^{-1} and remaining drug inside the NAA pores with time under dynamic conditions established by conventional method. (b) Calibration curve establishing a correlation between the amount of drug remaining and ΔEOT measured during in situ drug release monitoring.

The experimental data obtained from these experiments were fitted to a typical mathematical model for drug delivery kinetics (i.e. Higuchi model).[17,24,34,35] This model, which is based on the Fickian diffusion equation, describes the release of drugs from insoluble matrices. Under such assumptions as perfect sink conditions and significantly higher initial drug concentration in the release platform than in the eluting medium, this model can be used to describe the diffusion-controlled release of water-soluble and poorly water-soluble drugs from inert noneroding porous platforms.

A modified Higuchi equation can be written as eq 1

$$f = \frac{m(t)}{M} = at^{1/2} + b \quad (1)$$

where f is the fraction of drug released, m is the amount of drug released at time t, which can be calculated from ΔEOT, M is the initial amount of drug in the NAA implant determined by TGA, and a and b are fitting parameters.

Therefore, the rate of drug release for this system can be calculated by derivating eq 1. The obtained result shows that the drug release rate is inversly proportional to the square root of time (eq 2).

$$\frac{dM(t)}{dt} = kt^{1/2} \quad (2)$$

where k is the rate constant given by eq 3.

$$k = \frac{1}{2}Ma \quad (3)$$

Table 1 summarizes the rate constant values obtained after fitting the drug release data to the aforementioned Higuchi model from NAA implants obtained under static and dynamic conditions as well as their corresponding R^2 values. The corresponding fitting lines are presented in Figure S4 in the Supporting Information. At first glance, it is observed that the drug release under dynamic conditions at 50 μL min^{-1} is approximately four-fold higher than that obtained under static ones. However, the drug release under dynamic conditions at lower flow rates (i.e., 10 and 30 μL min^{-1}) is comparable to that obtained under static conditions. Notice that the increment of k with the flow rate confirms that the faster the flow rate the higher the amount of drug released from the NAA implants. Furthermore, the high R^2 values verify the $t^{1/2}$ dependence of the drug release, which is a characteristic factor of Fickian diffusion mechanism. These experimental fittings for both methods are in good agreement with the Higuchi model, which justifies our approach for monitoring drug release from nanoporous materials in real-time under dynamic flow conditions by means of reflectometric interference spectroscopy.

4. CONCLUSIONS

To conclude, in this study we have successfully demonstrated the ability of a noneroding and biocompatible platform, nanoporous anodic alumina, to be used as nanoengineered drug eluting implant for biomedical applications. NAA implants were loaded with anti-inflammatory drug indomethacin and their in vitro release profiles were established under static and dynamic conditions by comparative measurements between UV−visible spectroscopy and reflectometric interference spectroscopy. A pronounced difference in drug release time was observed with release extending up to 4 day under static conditions while it lasted only a few hours under dynamic ones. As for this, we studied the effect of the flow rate over the drug release pattern at four different flow rates similar to the physiological milieu at the implant site in the host body. These experimental data were fitted to a modified Higuchi model. Both, experimental data and model fittings verified that the faster the flow rate the higher the amount of released drug. Furthermore, the obtained results suggest that the release mechanism under dynamic conditions was diffusion-controlled.

Table 1. Fit Parameters of the Higuchi Model for the Release of Indomethacin from NAA Implants under Static and Dynamic Flow Conditions at Different Flow Rates

static conditions		dynamic conditions					
		flow rate 10 μL min^{-1}		flow rate 30 μL min^{-1}		flow rate 50 μL min^{-1}	
k (μg min$^{-1/2}$)	R^2	k (μg min$^{-1/2}$)	R^2	k (μg min$^{-1/2}$)	R^2	k (μg min$^{-1/2}$)	R^2
3.02 ± 0.02	0.95	2.23 ± 0.02	0.95	2.80 ± 0.06	0.99	12.47 ± 0.04	0.96

These results established that to combine dynamic flow conditions with real-time and in situ monitoring of drug release makes it possible to simulate the biological environment at the implant site. The obtained results by this method are more reliable and accurate than those obtained under conventional static conditions. Therefore, we consider this study as an important contribution towards a better understanding of drug release under dynamic conditions, which is crucial to develop more efficient and optimized local drug delivery systems featuring nanoporous layer as drug containers. This approach can be dearly useful to design drug-releasing implants with improved performance and prevent common problems such as infections, lack of integration with surrounding tissues, inflammations, and even total rejection by the host body.

■ ASSOCIATED CONTENT

Supporting Information

Further information about the design of the microfluidic device, determination of drug loading amount, control experiments for confirming the trend of ΔEOT with the different loading methods, and finally, the kinetic model fitting curves for static and dynamic drug release experiments at all the measured flow rates. This material is available free of charge via the internet at http://pubs.acs.org.

■ AUTHOR INFORMATION

Corresponding Author

*E-mail: dusan.losic@adelaide.edu.au.

Author Contributions

The manuscript was written through contributions of all authors. All authors have given approval to the final version of the manuscript.

Notes

The authors declare no competing financial interest.

■ ACKNOWLEDGMENTS

Authors acknowledge the financial support provided by the Australian Research Council (DP 120101680, FT 110100711) and the School of Chemical Engineering – University of Adelaide. We are also thankful to Prof M.J. Sailor (UCSD) for providing FFT analysis software. We thank the Australian National Fabrication Facility (South Australian Node) (ANFF-SA) for the design and fabrication of the microfluidic device.

■ REFERENCES

(1) Langer, R. *Nature* 1998, *392*, 5−10.
(2) Langer, R. *Science* 2001, *293*, 58−59.
(3) Jain, J. P.; Modi, S.; Domb, A. J.; Kumar, N. *J. Controlled Release* 2005, *103*, 541−563.
(4) Porter, J.; Ruckh, T.; Popat, K. *Biotechnol. Prog.* 2009, *25*, 1539−1560.
(5) Belt, H.; Neut, D.; Schenk, W.; Horn, J. R.; Mei, H. C.; Busscher, H. J. *Acta Orthop.* 2001, *72*, 557−571.
(6) Lucke, M.; Schmidmaier, G.; Sadoni, S.; Wildemann, B.; Schiller, R.; Haas, N.; Raschke, M. *Bone* 2003, *32*, 521−531.
(7) Ainslie, K.; Thakar, R.; Bernards, D.; Desai, T. Inflammatory Response to Implanted Nanostructured Materials. In *Biological Interactions on Materials Surfaces*; Puleo, D. A., Bizios, R., Eds.; Springer: New York, 2009; pp 355−371.
(8) Allen, T. M.; Cullis, P. R. *Science* 2004, *303*, 1818−1822.
(9) Gulati, K.; Aw, M. S.; Findlay, D.; Losic, D. *Ther. Delivery* 2012, *3*, 857−873.
(10) Liu, H.; Webster, T. *J. Biomater.* 2007, *28*, 354−369.
(11) Adiga, S. P.; Jin, C.; Curtiss, L. A.; Monteiro-Riviere, N. A.; Narayan, R. J. *WIREs: Nanomed. Nanobiotechnol.* 2009, *1*, 568−581.
(12) Gulati, K.; Aw, M. S.; Losic, D. *Nanoscale Res. Lett.* 2011, *6*, 1−6.
(13) Losic, D.; Simovic, S. *Expert Opin. Drug Delivery* 2009, *6*, 1363−1381.
(14) Maluenda, G.; Lemesle, G.; Waksman, R. *Clin. Pharmacol. Ther.* 2009, *85*, 474−480.
(15) Gultepe, E.; Nagesha, D.; Sridhar, S.; Amiji, M. *Adv. Drug Delivery Rev.* 2010, *62*, 305−315.
(16) Popat, K. C.; Eltgroth, M.; LaTempa, T. J.; Grimes, C. A.; Desai, T. A. *Small* 2007, *3*, 1878−1881.
(17) Gultepe, E.; Nagesha, D.; Casse, B. D. F.; Banyal, R.; Fitchorov, T.; Karma, A.; Amiji, M.; Sridhar, S. *Small* 2009, *6*, 213−216.
(18) La Flamme, K. E.; Popat, K. C.; Leoni, L.; Markiewicz, E.; La Tempa, T. J.; Roman, B. B.; Grimes, C. A.; Desai, T. A. *Biomaterials* 2007, *28*, 2638−2645.
(19) Simovic, S.; Losic, D.; Vasilev, K. *Chem. Commun.* 2010, *46*, 1317−1319.
(20) Aw, M. S.; Addai-Mensah, J.; Losic, D. *Chem. Commun.* 2012, *48*, 3348−3350.
(21) Aw, M. S.; Addai-Mensah, J.; Losic, D. *J. Mater. Chem.* 2012, *22*, 6561−6563.
(22) Gulati, K.; Aw, M. S.; Losic, D. *Int. J. Nanomed.* 2012, *7*, 2069−2076.
(23) Gbureck, U.; Vorndran, E.; Barralet, J. E. *Acta Biomater.* 2008, *4*, 1480−1486.
(24) Braun, W.; Frommelt, L.; Thull, R. *BIOmaterialien* 2011, *7*, 286−290.
(25) Hall, E. W.; Rouse, M. S.; Jacofsky, D. J.; Osmon, D. R.; Hanssen, A. D.; Steckelberg, J. M.; Patel, R. *Diagn. Microbiol. Infect. Dis.* 2004, *50*, 261−265.
(26) Perry, A. C.; Rouse, M. S.; Khaliq, Y.; Piper, K. E.; Hanssen, A. D.; Osmon, D. R.; Steckelberg, J. M.; Patel, R. *Clin. Orthop. Relat. Res.* 2002, *403*, 49−53.
(27) Kumeria, T.; Kurkuri, M. D.; Diener, K. R.; Parkinson, L.; Losic, D. *Biosens. Bioelectron.* 2012, *35*, 167−173.
(28) Kumeria, T.; Losic, D. *Physica Status Solidi (RRL)* 2011, *5*, 406−408.
(29) Kumeria, T.; Parkinson, L.; Losic, D. *Nanoscale Res. Lett.* 2011, *6*, 1−7.
(30) Alvarez, S. D.; Li, C. P.; Chiang, C. E.; Schuller, I. K.; Sailor, M. J. *ACS Nano* 2009, *3*, 3301−3307.
(31) Kumeria, T.; Losic, D. *Nanoscale Res. Lett.* 2012, *7*, 88−97.
(32) Masuda, H.; Fukuda, K. *Science* 1995, *268*, 1466−1468.
(33) Huang, X.; Brazel, C. S. *J. Controlled Release* 2001, *73*, 121−136.
(34) Siepmann, J.; Siepmann, F. *Int. J. Pharm.* 2008, *364*, 328−343.
(35) Arifin, D. Y.; Lee, L. Y.; Wang, C. H. *Adv. Drug Delivery Rev.* 2006, *58*, 1274−1325.

SCHOOL OF CHEMICAL ENGINEERING | THE UNIVERSITY of ADELAIDE

Supporting Information

Real-time and *in situ* drug release monitoring from nanoporous implants under dynamic flow conditions by reflectometric interference spectroscopy

Tushar Kumeria, Karan Gulati, Abel Santos, Dusan Losic*

School of Chemical Engineering, The University of Adelaide, Adelaide, SA 5005, Australia

Losic Group

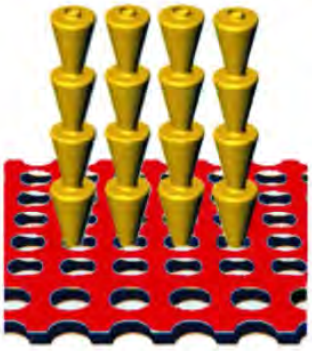

NanoTech Research

Real-time and *in situ* drug release monitoring from nanoporous implants under dynamic flow conditions by reflectometric interference spectroscopy

1) Flow cell for *in situ* drug release monitoring by RIfS measurements

Our microfluidic device is presented in **Figure S1a**, which consists of three main parts 1) base chip which is made by embossing the microchannel pattern into a solid PMMA block, 2) glass cover with holes aligned to the inlet and outlet on the base chip and 3) a metal clamp with optical windows for RIfS measurements and to bind the base chip and cover glass together physically. The base chip contains two different microfluidic structures to be used for various applications (**Figure S1b**). The width and depth of the microchannel are 200 and 100 µm, respectively. The microchannel delivers the fluid into a 6 mm x 6 mm, 200 µm deep square cavity that accommodates 100 µm thick NAA implants. So, there is further 100 µm space in the cavity, left above the NAA substrate allowing liquid to pass through the cavity without any obstruction. Micropillar mixers present prior to the sample cavity ensure the even distribution of fluid over NAA chip (**Figure S1c**). The microfluidic device is connected to a syringe pump via polyurethane micro tubing for supplying buffer to the cavity.

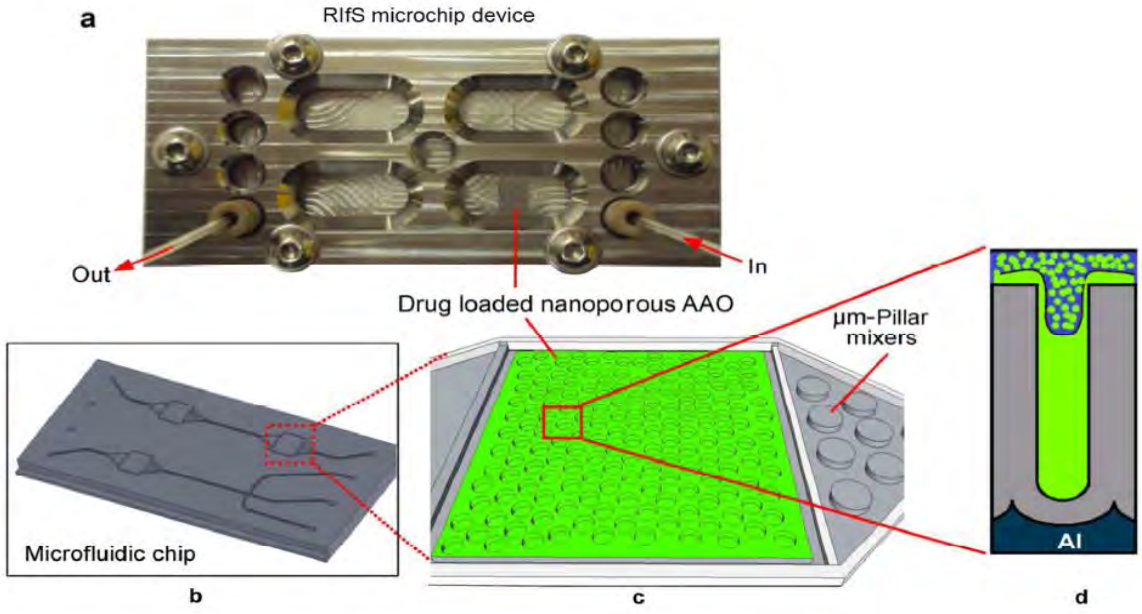

Figure S1. Flow cell device. a) Digital photograph of the microfluidic device (top) showing a drug loaded NAA implant where the RIfS probe can be focused from top through an optical window. b) Schematic of the complete design of the base chip. c) Magnified view of the cavity where the drug loaded NAA implant is integrated on the base chip. d) Scheme of NAA pores filled with drug.

2) Establishment of drug amount by TGA experiments

Thermogravimetric analysis was performed to determine the drug loading in each NAA implant by the three infiltration methods used in this study (**Figure S2**). Although the amount of drug solution dropped on each sample during loading was the same a slight variation in loading was observed. The amount loaded by each method is given in **Table S1**. Low loading amount obtained by loading method 2, is a result of soft wiping by tissue and plasma cleaning of sample to remove the drug present on the surface.

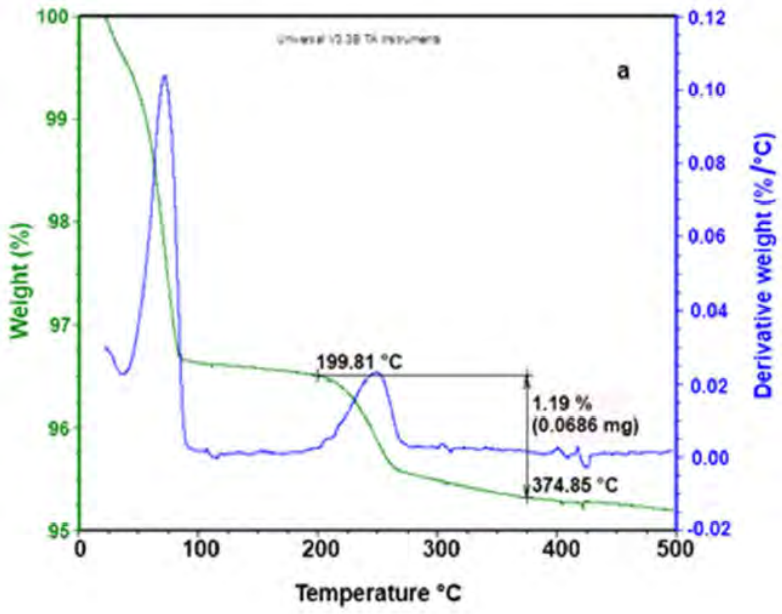

Figure S2. Thermogravimetric analysis (TGA) to calculate the drug loading in NAA implants infiltrated by different methodologies (e.g. TGA profile to establish the amount of loaded drug in a NAA substrate by Method 1).

Real-time and *in situ* drug release monitoring from nanoporous implants under dynamic flow conditions by reflectometric interference spectroscopy

3) Drug loading achieved for three loading methods

Table S1 presents the amount of drug loaded into NAA implants by means of the aforementioned three loading methods. This parameter was determined by TGA. Drug amount loaded by Method 1 and Method 3 was similar while loading was less by Method 2 due to wiping and plasma cleaning of the surface after infiltration.

Table S1. Amount of drug loading obtained by the three loading methods used in this study.

	Method 1	**Method 2**	**Method 3**
Description	Inside pores and on the surface	Only inside pores	Only on the surface
Amount of drug loaded (μg)	68 ± 11	53 ± 6	71 ± 9

Method 1 drug loaded inside the pores and on the NAA surface (10 μL of drug solution were dropped onto the NAA implants and allowed to dry by evaporation so that the drug solution wetted the pore walls as well as the top surface of the NAA implant).,

Method 2 drug loaded exclusively inside the NAA pores (10 μL of drug solution were dropped onto the NAA implants and its surface was subsequently cleaned by soft wiping and plasma cleaning treatment to remove the excess of drug from the NAA surface).

Method 3 drug loaded only on the NAA surface (10 μL of drug solution were dropped onto the NAA implants and quickly evaporated in an oven at 80°C under air atmosphere to evaporate the solvent before the drug solution wetted the pore walls).

These loading processes were repeated 10 times to obtain an equivalent amount of drug loading in all the NAA implants and the measured amount of drug obtained by each method was averaged from three different NAA implants.

4) RIfS drug release measurements for pore and surface-based releases (control experiment to validate hypotheses)

In order to prove the release pattern shown in **Figure S3**, we conducted two control experiments by monitoring *ΔEOT* for release from NAA implants loaded by Methods 2 and 3. We observed that *ΔEOT* only increased in case of samples loaded by Method 2 while it only decreased in case of samples loaded by Method 3. These control experiments were carried out at a flow rate of 50 µL min^{-1}.

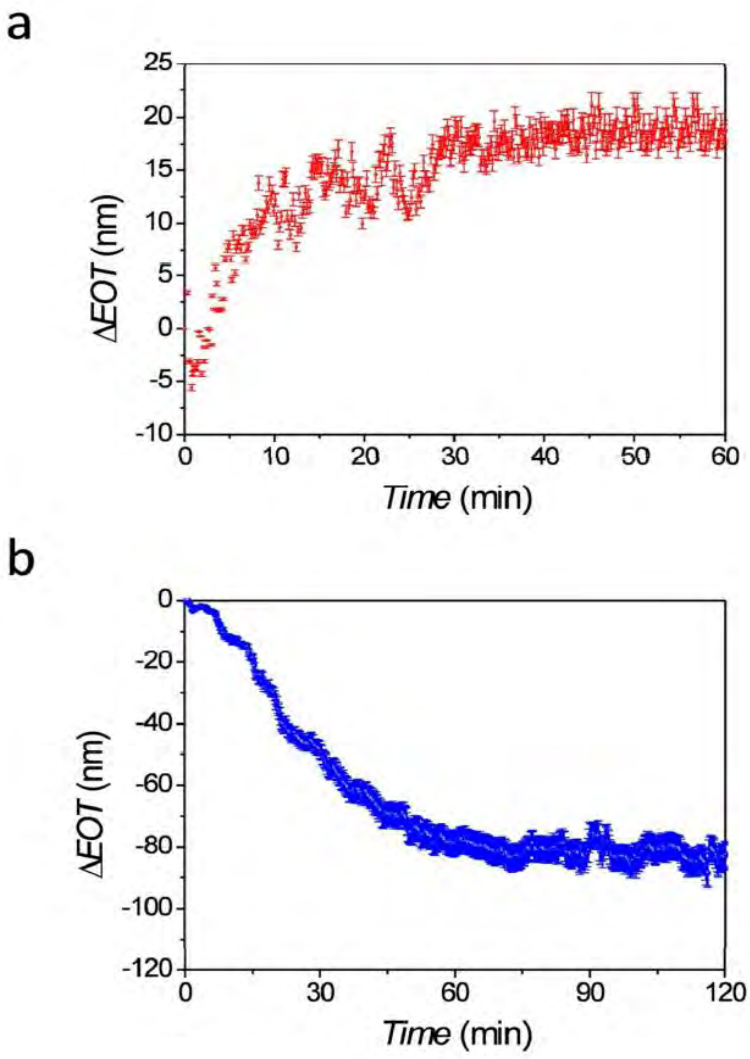

Figure S3. RIfS measurements for drug release experiments from NAA implants loaded by a) Method 2 (i.e. drug loading only inside the NAA pores) and b) Method 3 (i.e. drug loading only onto the NAA surface).

Real-time and *in situ* drug release monitoring from nanoporous implants under dynamic flow conditions by reflectometric interference spectroscopy

5) Drug release modeling from experimental results

Experimental data for initial release under static and dynamic conditions were fitted by a modified Higuchi model (**Equation 1 in the manuscript**) to measure the kinetics and establish the mechanism of indomethacin release. *ΔEOT* values for the first phase of release under dynamic conditions were converted into corresponding amount of drug remaining in the NAA implant by using linear fitting obtained from the calibration curve **(Figure 5b in the manuscript)**. The first phase lasted approximately 100 min for flow rates 10 and 30 µL min^{-1} while it only continues for 15 at 50 µL min^{-1} (**Figure 4 in the manuscript)**. Thus, the calculated drug amounts were subtracted from the initial concentration of drug available in each NAA implant (i.e. 68.6 µg). In this way, we calculated the cumulative drug released over time, which was fitted to the proposed Higuchi model for obtaining kinetics of the release under static and dynamic conditions at different flow rates (**Figure S4**).

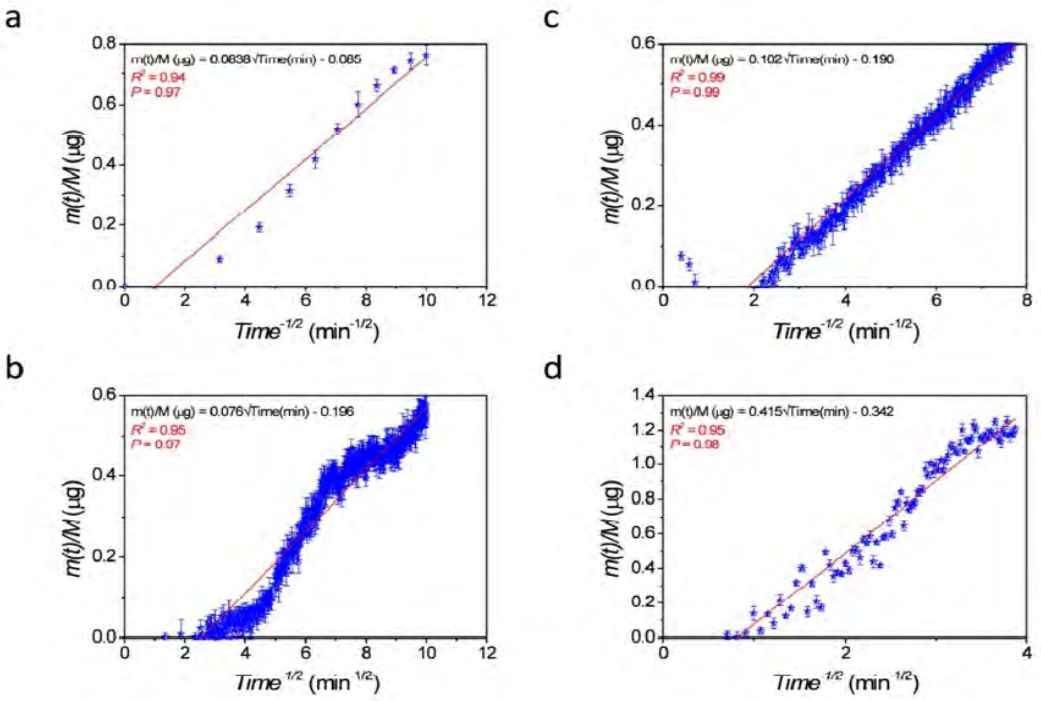

Figure S4. Drug release modeling of initial release phase fitted to the proposed Higuchi model for drug release under a) static conditions and dynamic conditions at b) 10 µL min^{-1}, c) 30 µL min^{-1} and d) 50 µL min^{-1} (*R* and *P* are the adjustment correlation and Pearson's coefficients, respectively).

CHAPTER 9

CONCLUSIONS and RECOMMENDATIONS for FUTURE WORKS

Tushar Kumeria

School of Chemical Engineering, The University of Adelaide, South Australia 5005, Australia

9.1 Conclusions

This thesis advances the knowledge about structural and optical engineering of NAA, surface functionalization, and application of NAA as a sensing substrate with reflectometric interference spectroscopy. The first major contribution of this thesis is understanding, designing, and optimizing the structural parameters of NAA for optical sensing applications. The second major contribution of this thesis is the understanding of surface chemistry of NAA in order to functionalize its surface with silanes for imparting selective surface groups for sensing applications. This was used to develop a portable, ultrasensitive, and label-free detection tool for determining gold (III) ions in environmental and biomedical scenarios. Understanding of controlling the pore geometries, in particular the ability to engineer the pore diameter of NAA substrates along the thickness of the film was used to generate 1D porous photonic structure as NAA based rugate filters. These complex porous photonic structures were selectively modified with silanes in order to detect ionic mercury for environmental and biomedical applications. The sensing performance of NAA as a substrate was compared using RIfS and photoluminescence, in which PLS proved to be more efficient. However, the results predict that method of analyte adsorption plays a crucial role in determining the sensing performance of a system. Final contribution of this thesis is to demonstrate that RIfS in combination with NAA can not only be used for sensing but to determine the release of target agent from inside its pores such as therapeutic agents. This combination also makes it possible to mimic the dynamic flow conditions that prevail inside the host body and provide a more accurate measure of kinetics of release of therapeutics. The following sections outline the specific conclusions drawn from all the studies included in this thesis.

9.1.1. Ultrasensitive Nanoporous Interferometric Sensors for Label-Free Detection of Gold (III) Ions

A highly sensitive and selective, portable, and label-free sensor for detection of gold (III) ions using NAA as the substrate and RIfS as the sensing technique was developed. The following conclusions were drawn from this study.

1. NAA substrate with hexagonally packed straight pores (i.e. no branching along the pore length) and controlled thickness could be obtained by carefully tuning the anodization parameters. The prepared NAA sensing substrate displays extraordinary optical properties, showing well resolved interference pattern in reflection spectrum.
2. The surface of NAA sensing substrate can be easily modified with organo-silane self-assembled monolayers (SAMs) via a simple chemical vapor deposition process. Interestingly, the CVD modification method provides organo-silane SAMs with terminal group still active for further binding to analyte of interest. In this chapter, the surface of NAA substrates was modified with silane having a thiol terminal to provide the sensing substrate with selectivity towards gold (III) ions.
3. The developed Au (III) ions sensor shows a broad analysis range from 0.1 to 750 µM Gold (III) ions with a linear detection range between 0.1 to 80 µM gold (III) ions solution. The lower limit of detection was 100 nM gold (III) ions solution.

   The sensor was highly selective towards detection of gold (III) ions even in presence of other interfering ions. This was confirmed by monitoring the RIfS response on exposure to aqueous solutions of Fe^{3+}, Mg^{2+}, Co^{2+}, Cu^{2+}, Ni^{2+}, Ag^{+}, and Pb^{2+} ions (at 40 µM concentration). Also, the developed NAA based RIfS sensing system was capable of selectively detecting gold (III) ions even in binary mixtures of different metal ions (i.e. 1:1, 40 µM: 40 µM, Pb^{2+} and Ag^{+}, Au^{3+} and Pb^{2+}, and Au^{3+} and Ag^{+}).

4. The real-life application of the NAA-RIfS gold (III) ions sensors was proven by successful detection of 40 μM Au^{3+} ions in tap-water and PBS.
5. Lastly, the binding kinetics of gold (III) ions with thiol groups on NAA surface were obtained by fitting the RIfS data to Langmuir and Freundlich isotherm models. The obtained fitting suggests that the binding of gold (III) ions to thiol groups on NAA surface follow a monolayer adsorption model as the data fits well to Langmuir isotherm.

9.1.2. Structural and Optical Nanoengineering of Nanoporous Anodic Alumina Rugate Filters for Real-Time and Label-Free Biosensing Applications

A novel method for anodization of Al to produce 1D porous photonic structure as rugate filters was established and the performance of the prepared NAA rugate filters was optimized under non-specific binding conditions by infiltrating the pores with glucose solutions of different concentrations. The following conclusions were drawn from this study.

1. A pseudosinusoidal potentiostatic anodization approach was adopted to prepare NAA-RFs. Four different types of NAA-RFs were fabricated by modifying the anodization conditions, which enabled the engineering of the effective medium of NAA in depth. These NAA-RFs display significant difference in their reflection stop band position in the optical spectrum.
2. The optical characteristics of these four NAA-RFs were assessed by reflection measurements by manipulating the effective medium (i.e. refractive index) of the pores of NAA-RFs by infiltration with glucose solutions. Peak position of the reflection stop band was taken as the critical parameter for this study.

3. The obtained optical reflection data revealed NAA-RFs could present a low limit of detection down to 0.01 M (i.e. refractive index of 1.333) with a sensitivity of 4.93 nm M^{-1} (i.e. 164 nm per refractive index units) and a linearity of 0.998.
4. Finally, the data was fitted to Looyenga–Landau–Lifshitz model to theoretically verify and validate the obtained experimental results.

Therefore, this chapter contributes to the understanding and development of optimized optical biosensors based on structurally engineered nanoporous anodic alumina platforms with enhanced optical signals.

9.1.3. Nanoporous Anodic Alumina Rugate Filters for Sensing of Ionic Mercury: Toward Environmental Point-of-Analysis Systems

A point of analysis type portable and lable-free detection system for analyzing ionic mercury in environmental and biomedical samples was developed using structurally and optically optimized NAA-RFs obtained from previous study. The following conclusions were drawn from this study.

1. The NAA-RFs were successfully fabricated using the pseudo-sinusoidal anodization process described in **Chapter 4** and functionalized with mercapto-silane to selectively bind and detect ionic mercury in environmental samples.
2. The linear working range of the developed ionic mercury detection system ranged between 1 to 100 µM, with a low limit of detection of 1 µM (i.e. 200 ppb) and a sensitivity of 0.072 nm μM^{-1}.
3. The selectivity of the system was analyzed by exposing the NAA-RFs modified with mercapot-silane to other interfering ionic species including 2 mM aqueous solutions of Co^{2+}, Mg^{2+}, Ni^{2+}, Cu^{2+}, Pb^{2+}, Fe^{3+}, Ca^{2+}, Cr^{6+} and Ag^{+} ions.
4. The sensor displayed capabilities to detect ionic mercury in complex solvents such as tap water (i.e. SA Water – Adelaide) and environmental water collected from a local river (i.e.

River Torrens – Adelaide) with concentrations of the model solutions being 5 and 40 µM. This proves the practical application of the developed system for environmental detection of toxic heavy metals.

9.1.4. Advanced Structural Design of Nanoporous Photonic Structures: Modulating Nanopore Architecture to Enhance Sensing Properties

The importance of an optimal design of the pore geometry and shape of NAA sensing platforms was established by comparing two different pore geometries on NAA (i.e. NAA with straight pores and NAA-DBRs, distributed Bragg reflectors with layered modulations). The sensing performance of the two structures was assessed under specific adsorption and non-specific adsorption conditions (i.e. binding of ionic mercury to mercapto-terminal on NAA surface and pore infiltration with glucose solutions, respectively). The following conclusions were drawn from this study.

1. Two types of NAA photonic structures featuring different pore geometries (i.e. pore lengths and diameters) and shapes (i.e. straight and modulated pores) are produced by tailoring the voltage profile during anodization process.
2. The optical characteristics of both the NAA photonic structures were assessed in detail by reflectometric interference spectroscopy (RIfS).
3. The RIfS data concludes that NAA-DBRs are more sensitive than the NAA with straight pores as the former responds much better to changes in refractive index than the later. The sensing performance under non-specific adsorption conditions (i.e. pore infiltration with glucose) was analyzed as a function of thickness for both the NAA photonic structures. The NAA-DBR was found to be twice as sensitive as its counterpart and could detect half analyte at half the concentration in comparison to NAA with straight proes.

4. The most sensitive structure of NAA-DBR was compared with NAA straight pores of similar pore length for detection of ionic mercury. Even in this case (i.e. specific adsorption) NAA-DBR proved to be a much better porous structure for sensing applications.

9.1.5. Optically Optimized Photoluminescent and Interferometric Biosensors Based on Nanoporous Anodic Alumina: A Comparison

This chapter compares the sensing performance of nanoporous anodic alumina based optical biosensors using photoluminescence spectroscopy (PLS) and reflectometric interference spectroscopy (RIfS). First, the pore structure of NAA (i.e. pore diameter and pore length) was optimized in terms of their optical signals obtained by PLS and RIfS. The most optimal NAA structure was compared for its sensing performance by detecting two different analytes: D-glucose and L-cysteine under non-specific and specific adsorption conditions, respectively with PLS and RIfS. The following conclusions were drawn from this study.

1. The optimization process of the optical signal from NAA with different structural parameters using PLS and RIfS, revealed that thinner nanoporous films with wider pores provide more intense optical signals for sensing purposes.
2. PLS-NAA sensing combination were more sensitive toward glucose molecules infiltration under non-specific conditions, with a lower limit of detection of 0.010 M and a sensitivity of 0.013 ± 0.001 % mM^{-1}.
3. The sensing performance of these biosensors for detecting L-cysteine under specific adsorption conditions revealed that both sensing platforms (I.e. RIfS-NAA and PLS-NAA) showed comparable sensing parameters (i.e. *LoD* and *S*), albeit PLS-NAA platforms demonstrated a slightly better performance.

9.1.6. Real-Time and In Situ Drug Release Monitoring From Nanoporous Implants under Dynamic Flow Conditions by Reflectometric Interference Spectroscopy

An innovative approach to monitor *in situ* drug release under dynamic flow conditions from nanoporous anodic alumina (NAA) based implants were established using RIfS. The release process is carried out under dynamic flow conditions in a microfluidic device, which makes it possible to analyze drug release under constant refreshing of eluting medium thus mimicking the physiological conditions of biological milieu at the implant site inside the host body.

1. NAA implants were successfully loaded with anti-inflammatory drug indomethacin and their *in vitro* release characteristics were established under static and dynamic conditions by comparative measurements between UV-visible spectroscopy and reflectometric interference spectroscopy, respectively.
2. A pronounced difference in drug release time was observed with release extending up to 4 day under static conditions while it lasted only a few hours under dynamic flow conditions in a microfluidic flow cell.
3. The experimental data fitted to Higuchi model verified that the faster the flow rate the higher the amount of released drug. The obtained release rate constants clearly suggest the release of drug from NAA pores is a function of flow rate (i.e. rate of refreshing the concentration gradient). In particular, the rate constants increased from 2.23 ± 0.02 to 12.47 ± 0.04 μg $min^{-1/2}$ when the flow rate is increased from 10 to 50 μL min^{-1}, respectively. This method provides more reliable and relevant information than conventional *in vitro* drug release methods performed under conventional static conditions as it closely mimics the physiological conditions that exist at the implant site in the host body.

9.2. Recommendations for Future work

The results of this thesis advance the knowledge on structural and optical engineering of NAA for sensing applications. However, further studies are required to increase our understanding of this important field of structural and optical engineering of NAA for environmental and biomedical sensing for a wide range of analytes. A number of tasks which still need to be studied are listed below:

1. Although a number of photonic structures have been produced in NAA but the studies related to optical properties of NAA still are at their nascent stage. So, a large amount of work and efforts need to be put in this are to develop even more complex and versatile photonic structures in NAA such as true rugate filters, microcavities, directional mirrors and so on. New porous photonic crystals fabricated by structural engineering of NAA can be prepared by new anodization profiles such as sinusoidal, superimposed sinusoidal, square wave, and so on. These new NAA based photonic structures could provide higher sensitivity for detection of a large variety of analytes in solution and vapor phase.
2. Second, major area that needs huge amount of attention in order to develop highly sensitive and selective sensors based on NAA is its surface chemistry. A vast number of techniques are available to modify the chemistry of NAA surface. However, stability, activity, and reproducibility of these surface chemistries is still questionable. In this direction, continues and large number of efforts and resources are needed to optimize the existing functionalization techniques. Furthermore, new methods and chemistries are needed to develop catering to specific target analytes.
3. The other important field of study for sensing is to characterize the binding mechanisms and kinetics of an analyte-reception reaction in order to optimize sensing performance. This is really necessary as the time of analysis is directly dependent on the binding kinetics of the analyte to receptor. Also, mass transport is another similar field that needs to be covered as

the kinetics of reactions in a nanoporous substrate differs from kinetics under bulk conditions.

4. Efforts also need to be put into development of simpler and cost-effective optical devices. For this, setups which do not need optical fiber and can be realized with low-cost spectrometer need to be developed. Also, so far only visible range of the spectrum is covered by NAA passed photonic crystals based sensing systems, therefore, detailed studies should be carried out for development of photonic crystals with optical signatures in near infra-red (NIR) or ultra-violet (UV) range of the spectrum. Could you include detection by mobile phones
5. The hexagonally organized pores of NAA is a boon and has opened doors for fabricating optical sensors in combination with techniques as localized surface plasmon resonance (LSPR), surface enhanced Raman spectroscopy (SERS) and others. NAA surface can be coated with noble metals layers and the hexagonal pore patter gives rise to regularly organized nanocaps like pattern, which act as hot-spot for excitation or SPR and SERS. Therefore, more efforts need to be put in to this research field to develop NAA based portable and point-of care sensors. Furthermore, the ability of SERS to provide qualitative information about the analyte should also be researched in details in order to develop NAA based SERS sensors with ability to fingerprint the chemicals. Such fingerprint and barcoding of chemical can prove to be useful for several industries, especially wine industry (in South Australia).

APPENDIX A

PHOTO-SWITCHABLE MEMBRANES based on PEPTIDE-MODIFIED NANOPOROUS ANODIC ALUMINA: TOWARD SMART MEMBRANES FOR ON-DEMAND MOLECULAR TRANSPORT

Tushar Kumeria

School of Chemical Engineering, The University of Adelaide South Australia 5005, Australia

T. Kumeria, J. Yu, M. Alsawat, M. D. Kurkuri, A. Santos, A. D. Abell, Dusan Losic "Photo-Switchable Membranes based on Peptide-Modified Nanoporous Anodic Alumina: Toward Smart Membranes for On-Demand Molecular Transport**"** *Advanced Materials*, 2015, **DOI:** 10.1002/adma.201500473.

Materials Views
www.MaterialsViews.com

ADVANCED MATERIALS
www.advmat.de

COMMUNICATION

Photoswitchable Membranes Based on Peptide-Modified Nanoporous Anodic Alumina: Toward Smart Membranes for On-Demand Molecular Transport

Tushar Kumeria, Jingxian Yu, Mohammed Alsawat, Mahaveer D. Kurkuri, Abel Santos, Andrew D. Abell,* and Dusan Losic**

The controlled transport of molecules across membranes is central to nature (e.g., in protein channels and ion pumps) but also to many highly valuable applications such as desalination, on-demand drug delivery, chromatography, and others. Artificial nanoporous membranes provide an important tool for studying the mechanisms and dynamics associated with molecular transporting across a membrane. In particular, artificial membranes allow the study of membrane surface interactions, size-exclusion effects, and other key determinants of transmembrane molecular transport; while also providing an opportunity to control or regulate the molecular transport on demand.[1–3] A number of strategies have been developed to fabricate artificial membranes with tunable and controlled molecular transport properties.[1,4] The incorporation of responsive polymeric brushes or hydrogels onto porous membranes (i.e., nanoporous anodic alumina, porous polymers, porous silicon, and carbon nanotube membranes) is the most common one, which allows the preparation of smart membranes with stimuli responsive molecular transport properties.[4] It is noteworthy that polymer brushes respond to a broad range of possible external stimuli (i.e., thermal, electrical, light, ionic strength, and pH) with fast stimuli response and do not completely block the pores (i.e., under optimized grafting conditions).[5] Previous studies on photoresponsive membranes utilized photosensitive systems including azobenzene, triphenyl-methane and spiropyran based photochromes, photoresponsive liquid crystals, and photoresponsive polypeptides in combination with polymer or zeolite based membranes.[5b] These systems have been employed in gas and salt separation, pervaporation, reverse osmosis, photocontrolled viscosity modulation, colloidal stability, surface wettability, and solvent permeability.[5b] However, these examples did not give rise to a fully reversible transport performance and presented long response time, limiting their practical applicability.

Stimuli responsive polymers have been grafted on to nanoporous anodic alumina membranes (NAAMs) to allow controlled and responsive molecular and ionic transport with a focus on on-demand and actuated release of model drugs to target chronic diseases that require daily dosing (i.e., angina pectoris, migraine, or other hormone-related diseases).[5c,6] However, grafting of stimuli responsive polymer brushes generally involves modifying the top surface or the pore mouth of the NAAMs, resulting in minimal chemical interactions between transporting molecules and the grafted polymer (as the polymer brushes are not present throughout the nanochannels). Furthermore, the polymerization process used in their preparation often results in nonuniform polymer chains, leading to nonuniform distribution of pore diameter across the membrane and bulk material with inefficient swelling and de-swelling properties. Also, this leads to randomly organized functional groups, giving rise to poor immobilization efficiency for biosensing, filtration, and chromatography applications.[5b,7] NAAMs have been prepared by electrochemical anodization of aluminum and offer straight cylindrical nanopores with minimal tortuosity, controllable geometry and tunable surface chemistry.[8] An alternative approach to overcome the inherent limitations of polymer-based stimuli responsive membranes, while providing the practical and functional requirements for selective on-demand molecular transport applications, is to synthetically modify nanoporous membranes with optically switchable molecules. This study presents for the first time, a photo stimuli responsive membrane system based on NAAMs functionalized with an azobenzene-containing photoswitchable peptide (PSP). PSP molecules were selectively immobilized along the internal surface of the NAAM pores, in order to manipulate the effective pore diameter of the NAAMs, depending on their isomeric form. This pore diameter modulation then regulates the transport of model dye molecule (Rose Bengal (RosB)) across the PSP modified NAA membranes. Exposure to specific wavelengths of light (364 nm in this case) switches the azobenzene component of PSP from a *trans* to a *cis* isomer, such that the associated change in PSP geometry controls the pore diameter of NAAMs and hence the

T. Kumeria, M. Alsawat, Dr. M. D. Kurkuri, Dr. A. Santos, Prof. D. Losic
School of Chemical Engineering
The University of Adelaide
Adelaide SA-5005, Australia
E-mail: dusan.losic@adelaide.edu.au

Dr. J. Yu, Prof. A. D. Abell
ARC Centre of Excellence for Nanoscale BioPhotonics (CNBP)
School of Chemistry and Physics
The University of Adelaide
Adelaide SA-5005, Australia
E-mail: jingxian.yu@adelaide.edu.au; andrew.abell@adelaide.edu.au

Dr. M. D. Kurkuri
Centre for Nano and Material Sciences
Jain University
Jain Global Campus
Bangalore-562112, India

DOI: 10.1002/adma.201500473

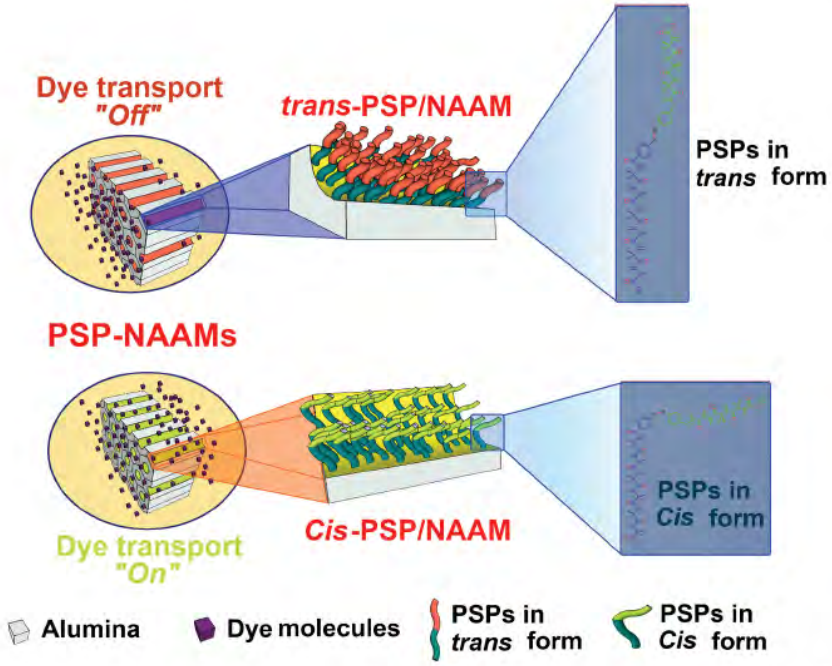

Figure 1. Schematic illustration of photoswitchable peptide-modified NAAMs (PSP-NAAMs), the transport properties of which were assessed by a U-tube permeation cell. PSP molecules in their *trans* or *cis* state effectively switch *Off* or *On*, respectively, which in turn regulates the molecular transport of a model dye molecule (RosB) through PSP-NAAMs.

selective transport of RosB, see **Figure 1**.[9,10] Photomediated switching of the PSP is experimentally confirmed by UV–Visible spectroscopy, contact angle measurements, atomic force microscopy (AFM), and molecular transport characterization including reversible *On*/*Off* switching of RosB transport across PSP/NAAMs as a function of PSP isomeric state (i.e., *cis* = *On* and *trans* = *Off*). A schematic illustration of the concept of photoregulated molecular transport through PSP-modified NAAMs is presented in Figure 1.

The photoswitchable peptide used in the study (**Figure 2**) consists of an azobenzene-derivative reversible light switch (4-aminomethyl phenylazobenzoic acid, Figure S1, Supporting Information), which is flanked by two Aib (α-aminoisobutyric acid) oligomers (Aib_3 and Aib_6) designed to help define the peptide geometry.[11] Aib oligomers were used specifically, since they are known to form predictable and stable helical structures, which are crucial for modulating the "effective pore diameter" in the NAAMs. The peptide was synthesized using the solid phase peptide synthesis (SPPS) procedure as detailed in the Supporting Information. This particular azobenzene derivative was chosen as the chromophore undergoes fast photocontrolled reversible isomerism, while remaining chemically stable.[10] An additional advantage of optically actuated switches is that they are nonresponsive to electromagnetic interference.[12] The resulting PSP compound was purified using reverse-phase high performance liquid chromatography (HPLC) and characterized using ^{1}H nuclear magnetic resonance spectroscopy (^{1}H NMR) (Figure S2, Supporting Information).

The photoisomerization of the PSP molecules was initially characterized by recording the UV–Vis spectrum after exposure to 440 and 364 nm wavelength lights. For this, first the PSP molecules were exposed to 440 nm wavelength of light for 10 min in order to give a photostationary state predominantly containing the *trans* PSP isomer. The absorption spectrum was then obtained which showed a strong band at 325 nm and a weak band at 430 nm (Figure 2a). The PSP solution was then illuminated at 364 nm to isomerize the *trans* isomer to the *cis*. A noticeable decrease in the peak at 325 nm was observed on exposing the PSP to 364 nm for 10 min (Figure 2a), which is consistent with formation of the *cis* isomer and the associated disappearance of the *trans* isomer. The switching between the isomers was found to be reversible, and it could be repeated for several cycles with complete recovery of the absorption signal. In order to define the backbone conformations of the peptide, the lowest energy conformers for both the *trans* and *cis* states of the photoswitchable compound **C1** were determined in Gaussian 09, with tight convergence criteria using a hybrid B3LYP method with 6–31G** basis set (Figure 2b,c). The molecular model predicts the length of the *trans* PSP structure to be ≈2.41 nm and 1.93 nm for the *cis* state.

Nanoporous anodic alumina membranes used in this work were fabricated through a two-step electrochemical anodization in 0.3 M sulfuric acid at 6 °C and 25 V, to obtain membranes with a nominal pore-channel diameter of 20 ± 3 nm (Supporting Information).[7] SEM images of NAAMs are depicted in **Figure 3**, where Figure 3a shows the top view of a

Materials Views
www.MaterialsViews.com

ADVANCED MATERIALS
www.advmat.de

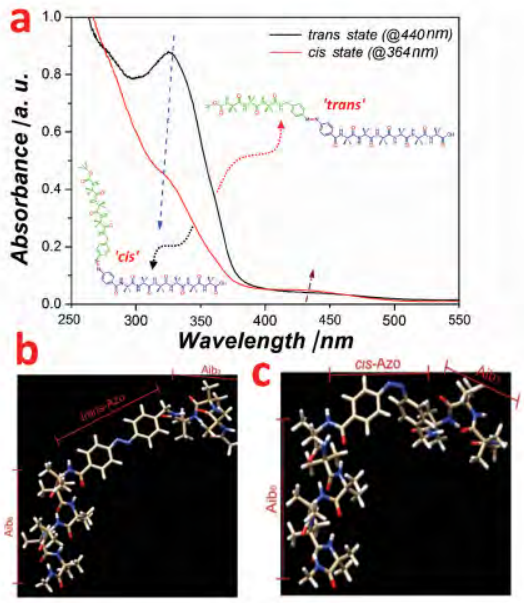

Figure 2. a) Absorbance spectrum of photoswitchable compound (i.e., PSP) under different isomeric states on exposure to specific wavelengths of light (with PSP isomeric structures inset). Computational models of photoswitchable peptide in its b) *trans* state and c) *cis* state.

NAAM and Figure 3b presents a cross-sectional view, with the inset showing perfectly straight and vertically aligned cylindrical nanopores. SEM images of the top and bottom surfaces of NAAMs, after pore opening using phosphoric acid (H_3PO_4 5 wt%) at 35 °C, are provided in Figure S3, Supporting Information, and show no damage to the top surface of NAAMs besides complete removal of barrier layer and in turn open pores at the bottom. Also, a digital photograph of the same NAAM sample (i.e., central transparent portion) is provided in Figure S3 inset, Supporting Information. Note that the thickness of NAAMs used for this study was fixed to 50 µm by adjusting the anodization time. Photoswitchable NAAMs were fabricated by covalent immobilization of PSP molecules onto 3-aminopropyl triethoxysilane (APTES) modified NAAMs.

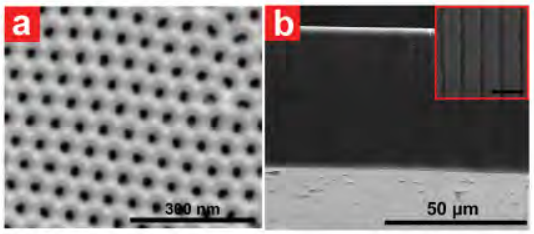

Figure 3. Typical SEM images of NAAM prepared in sulfuric acid electrolyte. a) Top view with self-organized pores. b) Cross-sectional view showing entire thickness of the NAAM with a magnified view inset (scale bar: 100 nm)

DIPEA/HATU (N,N-diisopropylethylamine/1-[bis(dimethylamino) methylene]-1H-1,2,3-triazolo[4,5-b]pyridinium3-oxid hexafluorophosphate) coupling reagents were used to form an amide linkage between carboxyl group on PSP molecules as well as acetic acid molecular spacer and amine group on APTES. This not only covalently couples PSP molecules to NAAMs inner surface, but also incorporates acetic acid spacers to ensure efficient and homogeneous switching PSP molecules between the two isomeric states (i.e., *trans* and *cis*) (Supporting Information).[13] Functionalization was confirmed by Fourier transform infrared (FTIR) and energy dispersive X-ray (EDX) spectroscopy as shown in Figure S4, Supporting Information. The FTIR spectrum for the APTES-NAAM and PSP/NAAM are shown in Figure S4a, Supporting Information, confirming successful functionalization of NAAMs with APTES and PSP molecules, respectively. The presence of a carbon peak for only the top surface of PSP/NAAMs in EDX spectra presented in Figure S4b, Supporting Information, confirms the selective attachment of PSP molecules on NAAMs.

Initially, the *cis*/*trans* switching capabilities of PSP molecules on a solid surface were examined by contact angle measurements after covalently attaching PSP molecules to silicon wafer surface using the aforementioned process. The PSP-modified Si wafers were first exposed to 364 nm light for 20 min to isomerize surface bound PSP to the *cis* isomer, and this was then subjected to water contact angle (WCA) measurements. Subsequent exposure to 440 nm light to enrich the *trans* PSP isomer on the Si surface was also followed by WCA measurements. The results shown in Figure S5a–c, Supporting Information, reveal an average WCA of 64° and 81° for PSP molecules in *trans* and *cis* states, respectively. The lower WCA for PSP molecules in the *trans* state is due to hydrophilic terminal group on the free end of PSP, whereas higher WCA for *cis* state is due to carbon backbone of the PSP molecules. This process was repeated three times to confirm the reversibility of the photoswitchable isomeric states of PSP molecules. The WCA measurements on NAAMs functionalized with PSP (Figure S5d, Supporting Information) displayed similar results to WCA measurements on Si wafer with an average WCA of 44° and 53° for *trans* and *cis* states of PSP molecules, respectively.

Next, we assessed the molecular transport performance of PSP modified NAAMs after exposure to 364 and 440 nm wavelength of light (i.e., PSP molecules under *cis* and *trans* isomeric states) using RosB as model molecule. This was examined by clamping PSP-modified membranes between two halves of a U-tube permeation unit composed of a feed and a permeate chamber (Figure S6, Supporting Information). The amount of RosB dye molecules transported was measured in real-time by following the changes in absorbance in the permeate chamber at 552 nm using a miniature fiber optical spectrometer (Supporting Information).[14] In this experiment, a PSP/NAAM was first exposed to 364 nm for 20 min in order to provide a photostationary state enriched in the *cis* azobenzene isomer (*cis*-PSP/NAAM). This *cis*-PSP/NAAM was then packed in the U-tube permeation cell and changes in absorbance of the RosB dye molecules in the permeate chamber were measured for 5 h. This was repeated with a PSP-modified NAAM, which had been exposed to 440 nm for 20 min in order to provide a photostationary state enriched in the *trans* azobenzene isomer

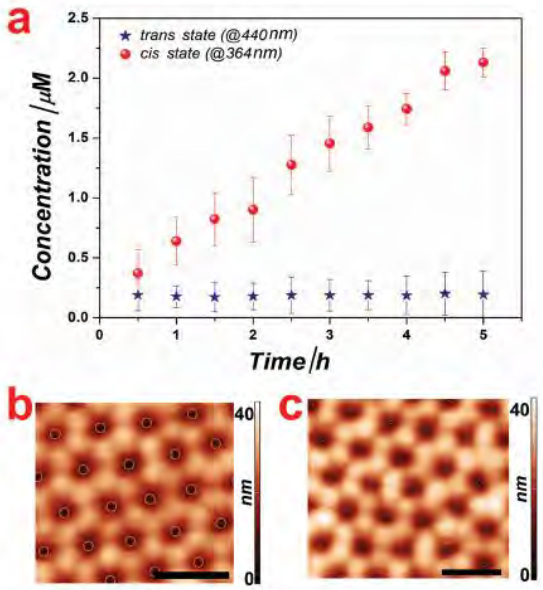

Figure 4. a) Molecular transport of dye (RosB) through PSP/NAAM under different isomeric states of PSP. AFM height images of PSP/NAAMs corresponding to its b) *cis* state and c) "*trans*" state of the PSP, respectively (scale bar: 100 nm).

(*trans*-PSP/NAAM) prior to transport analysis. **Figure 4**a shows changes in concentration of RosB in the permeate chamber for *cis*-PSP/NAAM and *trans*-PSP/NAAM systems. A linear increase in the concentration of RosB in the permeate chamber occurred for the *cis*-PSP/NAAM system. In contrast, the transport of RosB from the feed to the permeate chamber was greatly reduced for the *trans*-PSP/NAAM system. RosB concentrations of $0.194 \pm 0.0098 \times 10^{-6}$ M and $2.134 \pm 0.056 \times 10^{-6}$ M were obtained in the permeate chamber after 5 h, which corresponds to a permeation flux of 3.48×10^{-4} μmol h^{-1} cm^{-3} and 3.79×10^{-2} μmol h^{-1} cm^{-3} for *trans*-PSP/NAAM and *cis*-PSP/NAAM, respectively. Figure 4b,c shows AFM images of this system in the *cis*-PSP/NAAM and *trans*-PSP/NAAM configurations. The average pore diameter of *cis*-PSP/NAAM and *trans*-PSP/NAAM was 20 ± 3 nm and 13 ± 5 nm, respectively. These clearly show a significant change in the diameter of pores on exposure to 364 nm and 440 nm light, respectively, which are in good agreement with the obtained permeation flux data. Line section analysis of the AFM images is provided in Figure S7, Supporting Information, which shows that under *cis* photostationary state AFM can recognize the pore depth in more details as compared to the *trans* photostationary state of PSP/NAAM. The ability of this system to perform on-demand transport of dye molecules was then demonstrated by cyclic switching between the two photostationary states (i.e., *cis* and *trans*) of azobenzene group of PSP molecules grafted onto NAAMs surface. This was carried out by cyclic exposure of PSP/NAAM to 440 and 364 nm wavelengths of light and transport of RosB was monitored in real-time to measure the molecular transport rate. **Figure 5** shows transport of RosB across PSP/NAAM as

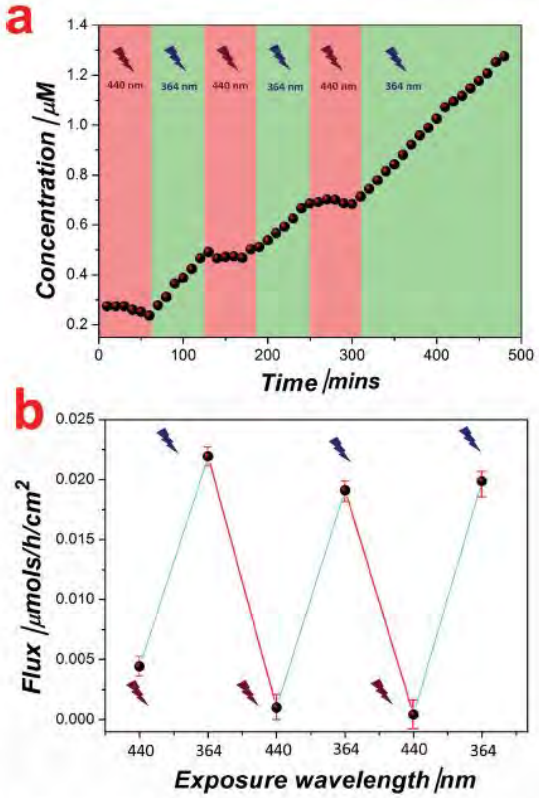

Figure 5. a) Molecular transport of dye (RosB) through PSP/NAAM after alternative exposure to 440 and 364 nm light. b) Flux of dye transport through PSP/NAAM as a function of different wavelengths of light.

a function of exposure to 364 and 440nm wavelength of light establishing the on-demand transport of dye molecules from the feed to the permeate chamber as a function of the exposure wavelength. The PSP/NAAM system was first exposed to 440 nm for 60 min, resulting in very low molecular transport. This was followed by exposure to 364 nm light, which resulted in a sharp increase in the concentration of dye in the permeate chamber (Figure 5a) presumably due to isomerism of *trans* to *cis* with an associated change in pore size. The RosB transport results (Figure 5) demonstrate that the proposed system is able to switch between *On* and *Off* states, thus allowing for on-demand transport of dye molecules. This system mimics a cell membrane's ability to control the transport the nutrients and molecules on demand. It clearly demonstrates its suitability for applications involving reversible transport. The trend for the flux data and is presented in Figure 5b showing the average flux for PSP/NAAM at 440 nm is 9.24×10^{-4} μmol h^{-1} cm^{-2} and 2.04×10^{-2} μmol h^{-1} cm^{-2} for 364 nm.

Note that, although the pores of PSP/NAAM were not completely closed on exposure to 440 nm, transport of dye molecules was effectively reduced, becoming almost negligible (Figure 4b). This suggests that the terminal groups (positively charged amine terminals) on PSP molecules immobilized onto

the inner surface of NAAMs, also played a role in controlling the transport of dye molecules (negatively charged RosB). To confirm the role of electrostatic interaction on transport properties of RosB, the transport properties of a PSP/NAAMs with PSP molecules attached only on the pore mouths were analyzed (Supporting Information). To this end, a NAAM was selectively functionalized with an APTES layer on its top surface (5 µm; 10% of its total thickness – 50 µm). This membrane was prepared using a previously described process.[7c] The top 5 µm layer was then covalently modified with PSP molecules using the aforementioned functionalization procedure and subjected to RosB transport after exposure to 364 and 440 nm wavelength of light (i.e., at enriched *cis* and *trans* azobenzene photostationary states, respectively, (Figure S6b, Supporting Information)). The dye flux for NAAM having only top 5 µm PSP layer on exposure to 440 nm was measured at 3.0×10^{-3} µmol h^{-1} cm^{-2}, which is one order of magnitude faster than that obtained with *trans*-PSP/NAAM (i.e., on exposure to 440 nm wavelength of light) when the inner surface of the pores are entirely modified with PSP molecules. These results confirm that electrostatic interactions between the dye molecules and PSP molecules attached onto the inner surface of NAAM pores play a significant role in controlling the RosB transport. Therefore, the switchability of PSP/NAAMs is associated with a twofold effect; namely: (i) physical constriction of the nanopores and (ii) enhanced electrostatic interaction between positively charged PSP and negatively charged RosB molecules in synergy with pore diameter enlargement or constriction (i.e., molecular transport across PSP/NAAMs is governed by a combined effect of size exclusion and chemical interaction) (Figure S6b, Supporting Information). Furthermore, we assessed the effect of molecular spacers on efficiency of enrichment of a single photostationary state and hence, the transport properties of the proposed system. A schematic illustration of PSP immobilized inside NAAM with acetic acid spacers is provided in the Supporting Information along with the molecular size of acetic acid, RosB dye, APTES monolayer, and *cis* and *trans* photostationary states of PSP (Figure S8a, Supporting Information). To this end, another set of NAAMs were functionalized with PSP lacking the acetic acid spacer molecules and the transport of RosB dye molecules through these membranes was evaluated (Figure S8b, Supporting Information).[15] The average dye flux through these PSP/NAAMs was 2.58×10^{-2} µmol h^{-1} cm^{-2} at 440 nm exposure, which is about two orders of magnitude higher than that obtained when spacers are intercalated between PSP molecules. The transport of the same molecules through these PSP/NAAMs on exposure to 364 nm was determined to be 4.26×10^{-2} µmol h^{-1} cm^{-2}, which is almost two fold higher than that obtained when spacer molecules are intercalated between PSP molecules. The inferior RosB transport performance of the PSP/NAAMs, without spacers, could be due to the co-existence of both *cis* and *trans* photostationary states of azobenzene group on PSP, resulting in nonuniform interaction of dye molecules with the PSP and irregular diameter of the NAAMs pores. These results confirm that spacer molecules are essential to effectively enrich a single (i.e., *cis* or *trans*) photostationary state of azobenzene group on PSP molecules, which is in good agreement with previous studies.[14] Additionally, we studied the effect of the pore size of NAAMs. The transport of dye molecules through PSP-modified NAAMs featuring an average pore diameter of 35 nm, was found to be much slower than that of NAAMs with smaller pore diameters. Moreover, the control over switching of the transport of dye molecules was poor as it is dependent on the synergistic effect of pore size constriction and chemical interactions between dye and PSP molecules, which is in good agreement with the aforementioned results (Figure S8c, Supporting Information).

We also correlated the change in flux (J) and the pore diameter (d) according to a modified Hagen–Poiseuille equation defining the flux through a membrane with cylindrical straight pores as Equation (1) (Supporting Information)[6a]

$$\frac{J_2}{J_1} = \frac{d_2^4}{d_1^4} \tag{1}$$

where, the subscripts 1 and 2 represent the *trans* and *cis* states of photostationary state of azobenzene moiety on PSP, respectively. It is assumed that the change in thickness of PSP/NAAM is almost negligible in comparison to the change in pore diameter during switching between the two photostationary states (i.e., *cis* and *trans*) (Figure S9, Supporting Information). By substituting the values of the geometric features established from AFM and SEM analysis, $d_2 = 20$ nm (i.e., *cis* state) and $h_1 = h_2 =$ 50 000 nm, (Figures 3 and 4b,c) and $J_2/J_1 = 2.03 \times 10^{-2}/9.24 \times 10^{-4}$, d_1 (i.e., *trans* state) is calculated as 10 nm, which is close to the value measured by AFM (13 nm) (Figure 4c). This slight variation in the calculated (i.e., 10 nm) and experimentally determined pore diameter (i.e., 13 nm) is likely due to the Hagen–Poiseuille equation used to calculate the pore diameter, which does not account for the electrostatic interactions between the dye molecules and PSP groups inside NAAM pores.

Kinoshita and co-workers developed a range of photoswitchable polypeptide based stimuli responsive membranes systems using polymer membranes (mostly poly(L-glutamic acid) membrane). These photoresponsive membranes were employed for controlled ionic transport targeting desalination and reverse osmosis application. However, the transport properties of these membranes were irreversible and dependent on external factors (i.e., pH, temperature and others).[5b-f] Notice that, the use of PSP, a photoswitchable peptide composed of 4-aminomethyl phenylazobenzoic acid molecules sandwiched between two Aib (α-aminoisobutyric acid) oligomers (Aib3 and Aib6), into a membrane system with fully controllable and reversible molecular transport properties is a unique and exclusive characteristic of the presented study. In this regard, Table S1, Supporting Information, summarizes and compares the performance of previously reported photoswitchable membranes to the PSP/NAAMs presented in this study.

In conclusion, novel functional membranes with capabilities of controlled and on-demand molecular transport were developed using photoswitchable peptides and nanoporous anodic alumina membranes. The photoregulated molecular transport properties of these structures were assessed using model molecule (Rose Bengal dye). The molecular transport across photoswitchable peptide-modified nanoporous anodic alumina membranes (PSP-NAAMs) system can be reversibly and cyclically actuated by switching the photostationary state of the azobenzene unit on PSP molecules. The controlled transport of

RosB molecules is based on synergy between the size-exclusion effects and affinity between dye molecules and surface chemistry on PSP/NAAMs. The on-demand photostationary state switching response time of PSP molecules was found to be less than 10 min, and thus on-demand regulation in this system is possible by optical stimulation. Given these promising results, we suggest that this system could be applied for water purification and various biotechnological applications.

Supporting Information

Supporting Information is available from the Wiley Online Library or from the author.

Acknowledgements

M.D.K. and A.S. contributed equally to this work. Authors acknowledge the financial support provided by the Australian Research Council (ARC) Centre of Excellence for Nanoscale BioPhotonics (CNBP), the Australian Research Council (DP 120101680, FT 110100711, and DE14010054), Centre for Advanced Nanomaterials (CAN) at The University of Adelaide, School of Chemical Engineering and Department of Chemistry at The University of Adelaide. The computational aspects of this work were supported by an award under the National Computational Merit Allocation Scheme for J.Y. on the National Computing Infrastructure (NCI) National Facility at the Australian National University and M.D.K. also acknowledge Department of Science and Technology (DST/TM/WTI/2K14/213), India for financial support.

Received: January 29, 2015
Revised: March 17, 2015
Published online:

[1] a) K. B. Jirage, J. C. Hulteen, C. R. Martin, *Science* **1997**, *278*, 655; b) B. B. Lakshmi, C. R. Martin, *Nature* **1997**, *388*, 758; c) J. Wu, K. Gerstandt, H. Zhang, J. Liu, B. J. Hinds, *Nat. Nanotechnol* **2012**, *7*, 133; d) M. Majumder, N. Chopra, B. J. Hinds, *J. Am. Chem. Soc.* **2005**, *127*, 9062; e) M. Majumder, N. Chopra, B. J. Hinds, *ACS Nano* **2011**, *5*, 3867; f) S. Szobota, E. Y. Isacoff, *Annual Rev. Biophys.* **2010**, *39*, 329; g) C. R. Martin, M. Nishizawa, K. Jirage, M. Kang, S. B. Lee, *Adv. Mater.* **2001**, *13*, 1351.

[2] a) K. H. Wee, R. Bai, E. M. V. Hoek, V. V. Tarabara, *Encyclopedia of Membrane Science and Technology*, John Wiley & Sons, Inc., Hoboken, NJ **2013**; b) D. Wandera, S. R. Wickramasinghe, S. M. Husson, *J. Membrane Sci.* **2010**, *357*, 6; c) S. M. Webster, D. del Camino, J. P. Dekker, G. Yellen, *Nature* **2004**, *428*, 864.

[3] a) S. B. Lee, C. R. Martin, *J. Am. Chem. Soc.* **2002**, *124*, 11850; b) R. Karnik, R. Fan, M. Yue, D. Li, P. Yang, A. Majumdar, *Nano Lett.* **2005**, *5*, 943.

[4] a) H. Alem, A. S. Duwez, P. Lussis, P. Lipnik, A. M. Jonas, S. Demoustier-Champagne, *J. Membrane Sci.* **2008**, *308*, 75; b) F. Liu, C. H. Du, B. K. Zhu, Y. Y. Xu, *Polymer* **2007**, *48*, 2910; c) S. J. Lue, J. J. Hsu, T. C. Wei, *J. Membrane Sci.* **2008**, *321*, 146.

[5] a) R. B. Vasani, S. J. McInnes, M. A. Cole, A. M. M. Jani, A. V. Ellis, N. H. Voelcker, *Langmuir* **2011**, *27*, 7843; b) F. P. Nicoletta, D. Cupelli, P. Formoso, G. De Filpo, V. Colella, A. Gugliuzza, *Membranes* **2012**, *2*, 134; c) T. Kinoshita, M. Sato, A. Takizawa, Y. Tsujita, *J. Chem. Soc. Chem. Commun.* **1984**, *14*, 929; d) T. Kinoshita, M. Sato, A. Takizawa, Y. Tsujita, *Macromolecules* **1986**, *19*, 51; e) T. Kinoshita, M. Sato, A. Takizawa, Y. Tsujita, *J. Chem. Soc. Chem. Comm.* **1986**, *108*, 6399; f) M. Sato, T. Kinoshita, A. Takizawa, Y. Tsujita, *Macromolecules* **1988**, *21*, 3419; g) S. K. Kumar, J. D. Hong, *Langmuir* **2008**, *24*, 4190.

[6] a) G. Jeon, S. Y. Yang, J. Byun, J. K. Kim, *Nano Lett.* **2011**, *11*, 1284; b) C. Song, W. Shi, H. Jiang, J. Tu, D. Ge, *J. Membrane Sci.* **2011**, *372*, 340; c) P. F. Li, R. Xie, J. C. Jiang, T. Meng, M. Yang, X. J. Ju, L. Yang, L. Y. Chu, *J. Membrane Sci.* **2009**, *337*, 310.

[7] a) T. Kumeria, M. Bariana, T. Altalhi, M. Kurkuri, C. T. Gibson, W. Yang, D. Losic, *J. Mater. Chem. B* **2013**, *1*, 6302; b) C. Tao, J. Wang, S. Qin, Y. Lv, Y. Long, H. Zhu, Z. Jiang, *J. Mater. Chem.* **2012**, *22*, 24856; c) T. R. Hoare, D. S. Kohane, *Polymer* **2008**, *49*, 1993.

[8] a) O. Jessensky, F. Müller, U. Gösele, *Appl. Phys. Lett.* **1998**, *72*, 1173; b) H. Masuda, K. Fukuda, *Science* **1995**, *268*, 1466; c) A. M. M. Jani, I. M. Kempson, D. Losic, N. H. Voelcker, *Angew. Chemie* **2010**, *122*, 8105.

[9] O. Babii, S. Afonin, M. Berditsch, S. Reißer, P. K. Mykhailiuk, V. S. Kubyshkin, T. Steinbrecher, A. S. Ulrich, I. V. Komarov, *Angew. Chemie Int. Ed.* **2014**, *53*, 3392.

[10] a) M. M. Russew, S. Hecht, *Adv. Mater.* **2010**, *22*, 3348; b) Y. J. Liu, G. Y. Si, E. S. Leong, N. Xiang, A. J. Danner, J. H. Teng, *Adv. Mater.* **2012**, *24*, 131; c) Y. B. Zheng, B. K. Pathem, J. N. Hohman, J. C. Thomas, M. Kim, P. S. Weiss, *Adv. Mater.* **2013**, *25*, 302; d) S. L. Chen, C. C. Chu, V. K. S. Hsiao, *J. Mater. Chem. C* **2013**, *1*, 3529.

[11] a) S. Zhu, M. Riou, C. A. Yao, S. Carvalho, P. C. Rodriguez, O. Bensaude, P. Paoletti, S. Ye, *Proc. Natl. Acad. Sci. USA* **2014**, *111*, 6081; b) A. A. Beharry, O. Sadovski, G. A. Woolley, *J. Am. Chem. Soc.* **2011**, *133*, 19684.

[12] A. L. Ricchiuti, D. Barrera, K. Nonaka, S. Sales, *Opt. Lett.* **2014**, *39*, 5729.

[13] a) A. Adochitei, G. Drochioiu, *Rev. Roum. Chim.* **2011**, *56*, 783; b) T. Kumeria, A. Santos, D. Losic, *ACS Appl. Mater. Interfaces* **2013**, *5*, 11783.

[14] a) T. Altalhi, M. Ginic-Markovic, N. Han, S. Clarke, D. Losic, *Membranes* **2010**, *1*, 37; b) T. Altalhi, T. Kumeria, A. Santos, D. Losic, *Carbon* **2013**, *63*, 423.

[15] D. T. Valley, M. Onstott, S. Malyk, A. V. Benderskii, *Langmuir* **2013**, *29*, 11623.

APPENDIX B

NANOPOROUS ANODIC ALUMINA PLATFORMS: ENGINEERED SURFACE CHEMISTRY and STRUCTURE for OPTICAL SENSING APPLICATIONS

Tushar Kumeria

School of Chemical Engineering, The University of Adelaide South Australia 5005, Australia

T. Kumeria, A. Santos, D. Losic "Nanoporous anodic alumina platforms: Engineered surface chemistry and structure for optical sensing applications" *Sensors*, 2014, **14**, 11878.

Sensors **2014**, *14*, 11878-11918; doi:10.3390/s140711878

OPEN ACCESS

sensors

ISSN 1424-8220

www.mdpi.com/journal/sensors

Review

Nanoporous Anodic Alumina Platforms: Engineered Surface Chemistry and Structure for Optical Sensing Applications

Tushar Kumeria, Abel Santos * and Dusan Losic

School of Chemical Engineering, Engineering North Building, The University of Adelaide, North Terrace Campus, Adelaide SA 5005, Australia;
E-Mails: tushar.kumeria@adelaide.edu.au (T.K.); dusan.losic@adelaide.edu.au (D.L.)

* Author to whom correspondence should be addressed; E-Mail: abel.santos@adelaide.edu.au; Tel.: +61-08-8313-1535; Fax: +61-08-8313-4373.

Received: 12 May 2014; in revised from: 23 June 2014 / Accepted: 25 June 2014 / Published: 7 July 2014

Abstract: Electrochemical anodization of pure aluminum enables the growth of highly ordered nanoporous anodic alumina (NAA) structures. This has made NAA one of the most popular nanomaterials with applications including molecular separation, catalysis, photonics, optoelectronics, sensing, drug delivery, and template synthesis. Over the past decades, the ability to engineer the structure and surface chemistry of NAA and its optical properties has led to the establishment of distinctive photonic structures that can be explored for developing low-cost, portable, rapid-response and highly sensitive sensing devices in combination with surface plasmon resonance (SPR) and reflective interference spectroscopy (RIfS) techniques. This review article highlights the recent advances on fabrication, surface modification and structural engineering of NAA and its application and performance as a platform for SPR- and RIfS-based sensing and biosensing devices.

Keywords: nanoporous anodic alumina; surface modification; optical biosensor; plasmon resonance; reflective interferometry

Acronyms: Nanoporous anodic alumina: NAA, Surface plasmon resonance: SPR, Reflectometric interference spectroscopy: RIfS, Porous silicon: pSi, Titania nanotubes: TiNTs, Pore diameter: D_p, Inter-pore distance: D_{int}, Pore length: L_p, Oxide barrier layer thickness: L_b, Mild anodization: MA, Hard anodization: HA, Photoluminescence: PL, Effective optical thickness: OT_{eff}, Chemical vapor deposition: CVD, Atomic layer

deposition: ALD, Surface enhanced Raman scattering: SERS, Water contact angle: WCA, Carbon nanotubes: CNTs, Self-assembled monolayers: SAMs, Layer-by-Layer: LbL, Polyelectrolyte: PE, Silica nanotubes: SNTs, Distributed Bragg reflector: DBR, Rugate filters: RF, Localized surface plasmon resonance: LSPR/LPR, Waveguide: WG, Limit of detection: LOD, Fabry–Pérot: FP, Fast Fourier transform: FFT, Volatile sulfur compounds: VSCs, Circulating tumor cells: CTCs, Phosphate buffer solution: PBS.

1. Introduction

In recent years, an increasing amount of research has been focused on exploring the production of novel nanoporous materials and their application for developing highly sensitive chemical and biosensing devices. These novel analytical devices based on nanoporous materials are cost-effective, highly sensitive due to the large surface-to-volume ratio, and additionally show excellent selectivity when coupled to biorecognition elements [1]. In particular, nanoporous materials synthesized by electrochemical techniques such as porous silicon (pSi), nanoporous anodic alumina (NAA), and titania nanotube arrays (TiNTs) are the top choice of researchers as chemical and biosensing substrates [2,3]. These nanoporous materials have been combined with various optical (e.g., surface plasmon resonance, reflective interference, optical waveguiding, Raman spectroscopy and others) and physical (e.g., electrochemical or impedance technique, piezoelectric, surface acoustic wave and so on) detection methods to develop highly innovative and capable analytical tools [3]. Amid these nanoporous materials, NAA prepared by anodization of aluminum foil, possesses outstanding chemical, optical, and mechanical properties such as chemical resistance, thermal stability, hardness, biocompatibility and large specific surface area. Particularly, its high specific surface area to volume ratio is dearly useful to enhance optical signals when target molecules (analytes) are attached inside the nanopores [3,4]. Therefore, NAA is an excellent platform to develop sophisticated and relevant applications as selective molecular separation, chemical/biological sensing, catalysis, cell adhesion and culture, data storage, energy generation and storage, drug delivery and template synthesis [3–6]. These properties make NAA substrates excellent platform for developing advanced, smart, simple and cost-effective analytical devices. In addition, the ability to engineer its pore size, geometry, and surface chemistry make NAA even a more versatile nanomaterial as these features can be tuned in order to integrate separation and sensing capabilities into all-in-one devices [3]. Recently, the use of NAA for chemical and biosensing applications has gained a very fast pace with potential for future commercialization. The perfectly organized nanoporous structure of NAA, its optical activity and the ability to modify its structure and chemistry have resulted in its vast application as a substrate for surface plasmon resonance and reflective interference-based detection systems [3]. However, no literature review has highlighted and summarized these developments.

Herein, for the first time, we review the major advances and developments of chemical and biosensing systems based on NAA in combination with surface plasmon resonance (SPR) and reflectometric interference spectroscopy (RIfS). First, we present the fundamental aspects of the fabrication and structure of NAA prepared by electrochemical anodization of aluminum. Next, recent advances on the modification of the surface chemistry of NAA using various techniques are reported. Then, we present the most outstanding works in structural engineering of NAA relating aimed at engineering its optical

properties. Finally, we present examples of recent advances on SPR and RIfS chemical and biosensing systems based on NAA, providing details of their principles, performance and practical applications.

2. Fabrication and Structure of NAA

Aluminium oxide has been used since the early 1900s due to its chemical and corrosion resistance properties. Keller *et al.* in 1953, for the first time, described the structure of anodically grown alumina as a close-packed hexagonally organized duplex structure with a porous and a barrier type oxide layer [7]. In general, the structure of self-organized NAA can be described as a matrix of alumina with close-packed arrays of hexagonally-arranged cells with a cylindrical pore at its center that grows perpendicularly to the surface of the aluminum substrate [8]. It is noteworthy that during anodization an electrochemical equilibrium between the rate of oxide growth and its dissolution through the barrier layer at pore bottom is achieved, which is essential for steady state growth and hexagonal packing of nanopores [9,10]. Free-standing NAA substrate can be obtained by selectively etching the underlying aluminum after anodization. Membrane type NAA can be produced by further etching the oxide barrier layer at the pore bottom. This results in membranes with vertically-straight nanochannels. The key structural parameters of NAA are pore diameter (D_p), inter-pore distance (D_{int}), pore length (L_p) and oxide barrier layer thickness (L_b). Figure 1 presents a schematic of a typical NAA structure along with scanning electron microscopy (SEM) images of its top and cross-sectional surface. The structural features of NAA (*i.e.*, D_p, D_{int}, L_p, and others) can be precisely controlled by the anodization conditions. In this regard, the geometric features of NAA can be varied in the range of 10–400 nm for pore diameter, 50–600 nm for inter-pore distance, from several nanometers to hundreds of micrometers for pore length, and 30–250 nm for the oxide barrier layer thickness. Other important characteristic parameters of NAA are its pore density (δ_p) and porosity (P), which can be obtained in a range between 109–1011/cm^2 and 5%–50%, respectively [9,11]. During the last decades, the effect of the anodization conditions on the structural features of NAA and self-organizing of pores has been extensively investigated. Anodization parameters such as the anodization voltage, electrolyte type, concentration and temperature have been recognized to be the most critical to control the self-ordering process and the geometry of the resulting NAA structures [11–13]. Aqueous solutions of sulphuric acid (H_2SO_4), oxalic acid ($H_2C_2O_4$) and phosphoric acid (H_3PO_4) are the most commonly used electrolytes for preparation of NAA by conventional anodization process at voltages of 25, 40, and 195 V, respectively [14–16]. This process is called ''mild'' anodization (MA) as moderate voltages and temperatures are used during the anodization. Other acids have also been reported to yield self-organization of NAA pores, which include aqueous solutions of citric, malic, malonic, tartaric and sulfamic acids [12,17–21]. However, the pore organization achieved with these acid electrolytes is poor in comparison to the conventionally used acids (*i.e.*, sulphuric acid, oxalic acid, and phosphoric acid). Each acid electrolyte has its respective optimum anodization voltage and temperature, which leads the pore growth under self-organizing conditions [22]. Self-organizing conditions for different electrolytes are provided in Table 1

Figure 1. (**a**) Schematic describing the structural characteristics of NAA (*i.e.*, pore diameter: D_p, pore length: L_p, barrier layer thickness: L_b, and interpore distance: D_{int}); (**b**) Top and (**c**) cross-sectional SEM images of NAA.

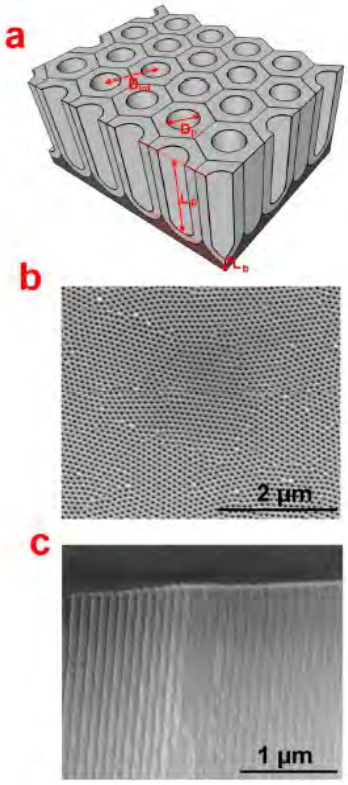

Table 1. Summary of the self-organizing conditions and pore diameters obtained during MA and HA regimes for the most commonly used electrolytes in NAA fabrication.

Acid Electrolyte	Mild Anodization				Hard Anodization			
	T (°C)	*V* (V)	D_p (nm)	Ref.	*T* (°C)	*V* (V)	D_p (nm)	Ref.
H_2SO_4 0.3 M	5	25	25	[15]	0	40	30	[23]
$H_2C_2O_4$ 0.3 M	5–8	40	30	[14]	0–1	140	50	[8]
H_3PO_4 0.1 M	0–1	195	160	[16]				
H_3PO_4:C_2H_5OH: H_2O (1:20:79 v/v)					−10 to 0	195	80–140	[9]

The major milestone in the history of NAA fabrication was reported in 1995, when Masuda and Fukuda successfully prepared highly self-organized NAA with very narrow size distribution and extremely high aspect ratios by using a two-step anodization process [14–16]. In this approach, the porous oxide layer obtained by first anodization is selectively removed to pre-structure the aluminum (Al) surface. This leads to perfect self-organization of pores from top to bottom during the second anodization step. Pre-structuring of Al surface improves the pore arrangement during two/multi-step anodization. However, the slow pore-growth rate in the range of 2–7 µm/h (depending on the electrolytic conditions) is an inherent disadvantage of mild anodization. This problem was solved by a new anodization approach called ''hard'' anodization (HA) introduced by Gösele and co-workers [8]. Under HA conditions (*i.e.*, high voltages and low temperatures) considerably higher pore-growth rates

in the range of 50–100 μm/h could be attained. These two anodization regimes (*i.e.*, MA and HA), under different electrolytic conditions combined with chemical etching, provided new approaches to engineer the structure of NAA with desired pore dimensions and shapes. Several strategies like periodic anodization profiles (voltage or current) with or without replacement of the acid electrolyte have been successfully explored to fabricate NAA with complex pore geometries. These electrochemical approaches have made it possible to fabricate NAA with different pore morphologies, including funnel-type, branched pores, periodically-shaped pore structures, and hierarchical and multi-structured pores. These nanostructures have been demonstrated using the aforementioned anodization and post-synthesis treatment processes [24–28]. This ability to structurally engineer the pores of NAA *ad lib* in combination with current surface modification methods provides new tools to modify and improve the properties of NAA for developing highly sensitive and selective chemical and biosensing systems. Notice that highly ordered NAA structures can be produced by other nanofabrication approaches, which have been established to precisely control the growth of NAA. Some of them are stamp imprinting and lithography techniques (*i.e.*, colloid sphere lithography, electron-beam lithography, focused-ion beam lithography, holographic lithography, direct laser writing lithography and Ar plasma etching). The choice of the fabrication technique depends on the scale of required pore arrangement, grade and arrangement of organization and pore size and shape. The structural (*i.e.*, pore diameter, pore length and inter-pore distance) and chemical (*i.e.*, distribution and content of impurities, crystallographic phase) properties of NAA are crucial in determining its optical properties. Thus, the fabrication and structural engineering become the key factors when designing optical sensing devices based on NAA.

3. Properties, Surface Chemistry and Surface Functionalization of NAA

3.1. Properties of NAA

NAA is a magnificent platform for developing chemical and biosensing devices due to its distinctive physical and chemical properties. Optical characteristics of NAA such as its photoluminescence (PL), transmittance, reflectivity, and absorbance can be used as principle of detection in highly sensitive and selective chemical and biosensing tools [3]. The pores of NAA can also act as container for holding chemical and biological payloads/molecules that take part in recognition reaction. Another advantage of NAA is that all the microfabrication and miniaturization techniques available for silicon technology can be readily employed for fabricating NAA structures. In this regard, the generation of micropatterns on NAA structures is very useful approach for the development of microfluidics and microarray-based sensing devices. It is worth stressing that the presence of impurities in the inner layer of pores (*i.e.*, close to the pore center) and high density of hydroxyl groups make functionalization of NAA very simple using various techniques (e.g., chemical vapour deposition, sol-gel, dip coating, self-assembly, atomic layer deposition and others). These processes can be used to endow NAA with chemical/physical selectivity toward target molecules (e.g., antigens, DNA, proteins, and enzymes) [29]. These modifications can specifically be aimed at enhancing a wide range of properties of NAA such as its reflectivity, hydrophobicity or hydrophilicity, anti-fouling, and chemical resistance, depending upon its intended application.

3.2. Surface Chemistry and Surface Functionalization of NAA

NAA possess a layered surface chemistry with electrolytic impurities distributed in an onion-like layered manner. It is intended that the chemical structure of NAA is composed of an outer layer close to the center of pore and an inner layer away from the central pore. The outer layer is composed of aluminium oxide (Al_2O_3) contaminated with acid electrolyte impurities and the inner layer is mainly composed of pure Al_2O_3 [22]. This has been proven previously by several investigations, however, the number of layers reported by each study is different. Thompson *et al.* argue that chemical structure of NAA has two layers of onion-like structure where the outer layer is contaminated with anionic species form electrolyte and the inner layer is dense pure alumina [30]. However, there are other studies that point out that the chemical structure of NAA actually consists of more than two layers. As for this, Yamamoto *et al.* revealed that the chemical structure of NAA is composed of three chemical layers as indicated by its photoluminescence spectrum after specified chemical etching steps [31]. A recent study by our group on the other hand suggests that the real chemical structure of NAA is composed of four onion-like layers with decreasing electrolytic impurities from the outer to the inner layer [32]. A schematic of the chemical structure of NAA is provided in Figure 2.

Figure 2. (**a**) Schematic of top and cross-sectional view showing the distribution of impurities in a NAA pore cell; (**b**) Four different stages of dissolution of NAA alumina layer under acidic conditions (5 *v* % H_3PO_4 at 35 °C) (adapted with permission from reference [32]).

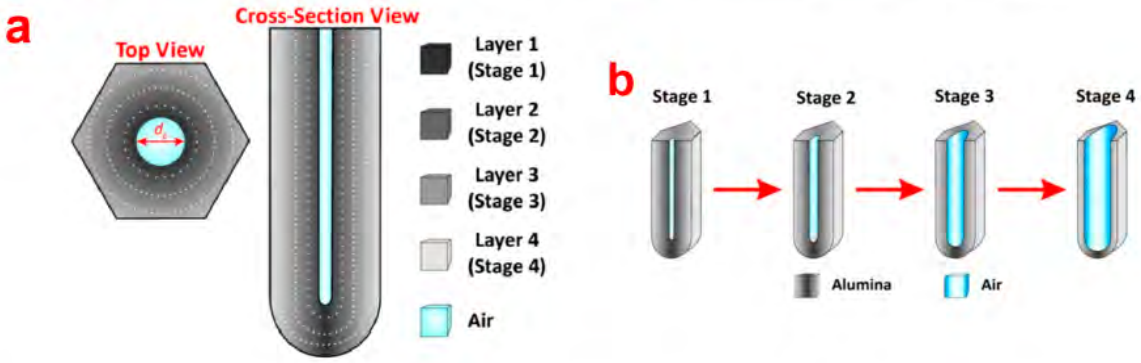

The chemical dissolution of NAA was monitored in real-time by reflectometric interference spectroscopy and changes in effective optical thickness (OT_{eff}) and intensity of the OT_{eff} peak lead to the aforementioned conclusion. A vast number of surface modification techniques have been developed to protect NAA from acidic environment and impart specific functionalities to its surface. These techniques can be divided into two main categories as physical/gas-phase deposition (*i.e.*, thermal vapor deposition, chemical vapor deposition (CVD), plasma polymerization and atomic layer deposition (ALD)) and chemical modifications (*i.e.*, self-assembly processes of silanes, organic and phosphonic acids, layer-by-layer deposition, polymer grafting, sol–gel processing, electrochemical and electroless deposition) [29]. Subsequent modifications of these surface functionalities of NAA can be used for either to prepare other functional nanomaterials (e.g., nanorods, nanoparticles, nanotubes) or attach biomolecules inside the pores of NAA. The most commonly used approaches for modifying the surface of NAA are described in Figure 3. Further control on the functionalities of NAA surface

can be obtained by using a combination of any of these modification techniques on NAA for specific applications.

Figure 3. A summary of typical wet chemical and gas phase techniques used to modify the surface of NAA (reprinted with permission from [29]).

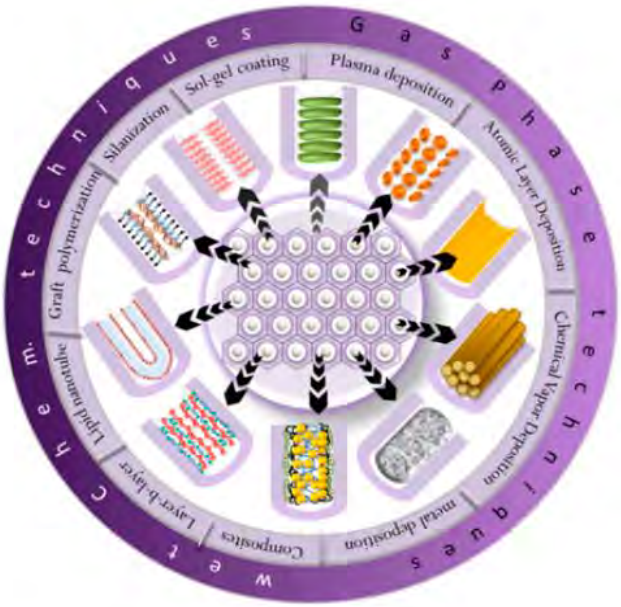

3.2.1. Gas-Phase Techniques

Gas-phase functionalization techniques including thermal vapor deposition, sputtering, pulsed laser deposition, chemical vapor deposition and plasma polymerization are employed to deposit a wide variety of materials as metals, metal oxides, nitrides, and carbon nanotubes inside NAA [33]. These methods can be used to tune the properties of NAA for specific applications, the most important examples of which are summarized in the following sections.

Metal Coating Using Thermal Vapor, Sputtering and Electron-beam Deposition

Metals films including gold, silver, platinum, palladium, titanium and nickel are generally deposited on NAA using thermal vapor deposition technique. These films are aimed at improving conductivity, reflectivity and chemical stability of NAA substrates [33]. Coatings of metals such as Au, Pd, Pt and Ti are reportedly used to improved catalytic properties of NAA, whereas Ni or Co coatings impart magnetic properties to NAA substrates. Metal coatings also serve as the basis for further chemical modification of NAA to help in binding various chemical and biological species with particular relevance for optical sensing and molecular separation applications [29]. The main disadvantage of these techniques is that the penetration depth is limited and only the top surface of NAA is modified.

Gold coatings on NAA substrates have been used as a base layer for layer-by-layer assembly of α,ω-diorganophosphonate/zirconium(IV), which plays a crucial role in confining LBL multilayers inside the pores and preventing them from being suspended over the top of the NAA substrate [34]. Platinum coatings were used by Toh *and coworkers* to apply electric field to the NAA membrane for

separation of charged proteins. Additionally, the same group achieved size-selective separation by increasing the thickness of the sputtered Pt layer [35,36]. Hexagonal arrangements of NAA pores has been exploited by several groups to prepare surface enhanced Raman scattering (SERS) substrates by depositing noble metals on it [37,38]. Qui *et al.* deposited an Ag layers on the top surface of NAA templates using a direct-current magnetron sputtering. The resulting metal caps on the surface act as Raman hot spots (Figure 4) [37]. This nanocap SERS-active hot-spot structure provides new opportunities for the fabrication of robust, exceptionally sensitive, cost-effective and large-area chemical and biological sensors. Béron *et al.* fabricated highly ordered patterned Permalloy nanometric structures by depositing Fe-Pd using ion beam sputtering on top of an anodic aluminium oxide nanoporous template. Their micro-magnetic simulations indicate the presence of Permalloy on one side of the pores, forming an anisotropic nanopillar array combined with an antidot array [39,40].

Figure 4. SEM images of DC-magnetron Ag sputter-coated NAA membranes fabricated at different voltages and sputtering time set to 10 min (scale bar = 100 nm): (**a**) 20 V; (**b**) 30 V; (**c**) 40 V; (**d**) 50 V; (**e**) 60 V. (Adapted with permission from [37]).

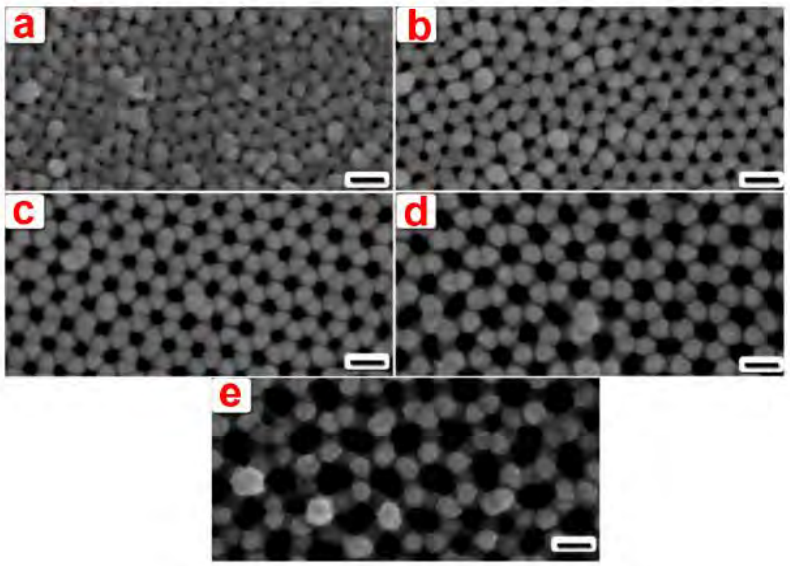

Plasma Polymer Deposition

Plasma polymerization can be used to deposit reactive and biocompatible polymer films with controlled thickness and chemical functionality with a wide range of functional groups, including amine, carboxyl, hydroxyl, epoxy and aldehyde groups. Brenov *et al.* for the first time, reported on the modification of NAA by plasma polymerization [41]. They prepared Janus-type NAA membranes by depositing hydrophobic fluorocarbon polymer from plasma polymerization of C_4F_8 on one side of the NAA membranes while the other side was left unmodified. Water contact angle (WCA) on the hydrophobic side of the NAA membranes was reported (WCA) 150°, while the other side had a WCA lower than 20°. Additionally, the pore diameter on the functionalized side of the NAA membranes was reduced from 160 to 80 nm. In order to improve both structural and surface properties of NAA membranes, Losic *et al.* functionalized their top surface by plasma polymerization of *n*-heptylamine.

They were able to precisely tune the pore diameter of NAA from 20 nm to <5 nm by adjusting the time duration of the plasma deposition [42]. The process yielded an amine terminal rich surface. However, it is worthwhile noting that this functionalization approach is limited to surface-based applications due to the poor depth penetration inside the nanopores of NAA (Figure 5).

Figure 5. (**a**) A schematic illustration of n-heptylamine coating on NAA; (**b**) Scheme showing the shadowing effect resulting in blocking of pores with long time deposition; (**c**) AFM images of plasma-coated NAA for different time periods. (Adapted with permission from [42]).

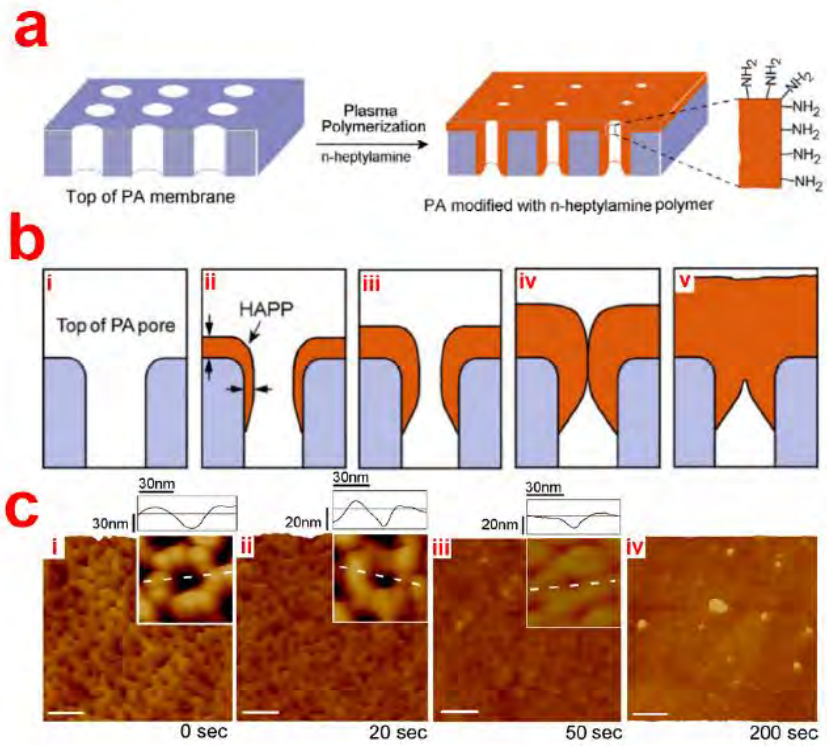

Atomic Layer Deposition (ALD)

ALD enables the precise deposition of a broad range of materials, including oxides, nitrides, sulfides and metals coatings. The resulting coatings present high mechanical, chemical and thermal stability, and optical activity. This technique has been extensively exploited for modifying the inner surface of NAA as a result of its penetration distance inside nanopores. Studies on ALD modification of NAA demonstrate that silica, titania and alumina can be controllably deposited inside NAA pores to reduce its pore dimensions, improving its catalytic, optical and transport properties and generate 1D nanostructures [43–46]. In this regard, Velleman *et al.* deposited silica (SiO_2) inside NAA by ALD method to reduce the pore diameter and subsequent modification with specific silane chemistry, which endowed NAA with chemical selectivity towards transporting dye molecules [5]. In addition, ALD has been used to prepare ultra-high aspect ratio nanotubes/wires of various materials, including pure metals (Cu, Ni, and Co) and their oxides (e.g., ZnO, TiO_2, and ZrO_2) [46–49]. For example, highly uniform, densely packed and vertically aligned TiO_2 nanotubes were fabricated by ALD inside NAA

templates using $TiCl_4$ as a precursor. The NAA template was then chemically removed to yield nanotubes with perfectly controllable tube diameter, spacing and wall thickness [50]. In a similar manner, ZnO-nanowires were produced by ALD deposition inside NAA templates [51]. Bachmann and co-workers fabricated magnetic nanotube arrays in NAA templates with modulated pores by means of depositing Fe_3O_4 via ALD using ferrocene and ozone as precursors (Figure 6) [52,53].

Figure 6. (**a**) A schematic illustration of fabrication of modulated pore NAA and subsequent deposition of magnetic nanotubes; (**b**) SEM and TEM images of the prepared magnetic nanotubes. (Adapted with permission from [53]).

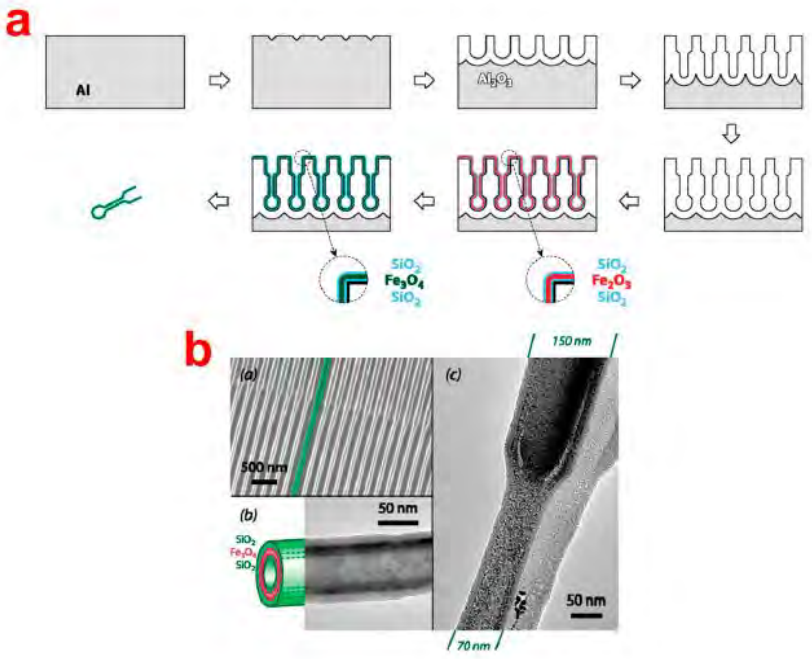

Chemical Vapor Deposition (CVD)

Chemical vapor deposition (CVD) involves dissociation of gaseous molecules by heat, light or plasma to form stable and conformal films on a substrate. CVD is mostly used to grow carbon nanotubes (CNTs) inside NAA pores [54–56]. This process provides vertically aligned arrays of CNTs with controlled dimensions. The carbon layer grows inside the NAA pores via pyrolysis of carbon source (mainly acetylene gas) at elevated high temperature (>600 °C) for varying time [57]. A wide range of carbon sources (either as liquid, gas or solid) have been used for growing CNTs. Recently, our group demonstrated the ability of this technique to recycle plastic waste and convert it into CNTs inside NAA templates (Figure 7) [58]. These CNTs-NAA membranes were demonstrated to be useful for tuning the transporting of dye molecules. In other recent studies by our group, CVD technique was used to deposit monolayers of organosilane (*i.e.*, APTES and MPTES) inside NAA pores [59,60]. To this end, NAA substrates were heated to temperatures in excess of 110 °C with these silanes under vacuum conditions. APTES modification of NAA substrate were used to selectively bind biomolecules, whereas MPTES (mercapto-silane) modified NAA were used to selectively detect gold and mercury ions in aqueous media.

Figure 7. (**a**) A scheme showing the setup used to grow CNTs inside NAA templates by CVD; (**b**) Schematic illustration of recycling process of plastic by CVD process to yield CNTs. (Adapted with permission from [58]).

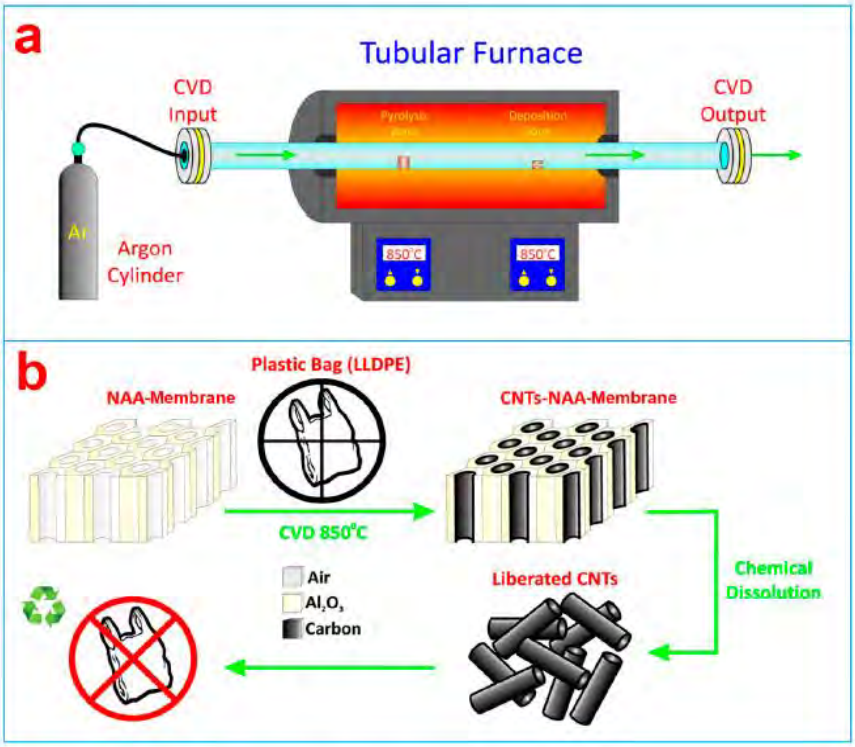

3.2.2. Wet Chemical Techniques of Surface Modification

Attaching other molecules to the surface of NAA is a productive manner to use its high surface area. The inherent presence of anionic impurities in its structure makes the pore surface of NAA prone to attack by oxides to generate surface hydroxyl groups, which act as nucleation centers for its further covalent functionalization. The advantage of wet chemical approaches is that they are usually based on self-assembly phenomenon, which results in full and uniform monolayer surface coating. Unlike physical surface modification, chemical surface modification result in no noticeable change in the structural properties of the NAA substrate [29]. Several groups of compounds such as carboxylic acids, organosilanes and phosphonic acids have been used to impart selective surface chemistry to NAA surface. These compounds are known to form highly uniform monolayers on NAA surfaces.

Self Assembled Monolayers

Self-assembled monolayers (SAMs) are assemblies of organic molecules formed by spontaneous attachment and arrangement of molecules from the liquid phase onto solid surfaces. SAMs of desired molecules can be prepared on NAA in several ways. Pioneering works were focused on self-assembly of alkanethiols on gold-coated NAA surfaces [61]. This process has been extended to SAMs based on organosilanes and phosphonates, which can present a broader range of functional terminals (e.g., amine, carboxyl, epoxy, *etc.*).

Organosilane Modification of AAO

Organosilanes can be readily formed onto the native or hydroxylated surface of NAA. Organosilanization of NAA has been effectively used to control its wettability and adsorption properties. Wide varieties of organosilanes are commercially available, which can be covalently bound onto the surface of NAA by simply incubating the hydroxylated NAA substrate in silane solution [62]. A schematic of silanization of hydroxylated NAA is provided in Figure 8.

Figure 8. Schematic of silanization process used for modifying NAA. (Adapted with permission from [62]).

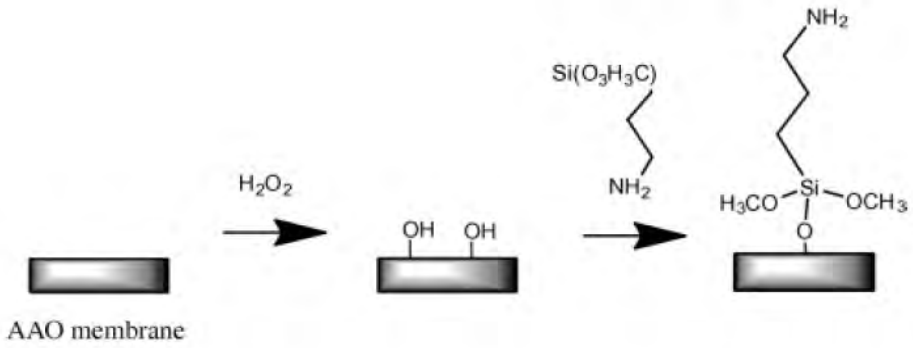

The variety of silanes used for modifying NAA and their applications are listed in Table 2. Tuning the wettability of NAA surface has been demonstrated by selectively forming SAMs of silanes with hydrophobic terminal groups such as alkyl-trichloro-silanes or perfluoroalkyl-silanes [5,63–65]. Ku *et al.* demonstrated that alkyl-trichlorosilanes with chain length C1–C8 can be used to effectively render the surface of NAA completely hydrophobic, such that even after fully immersing the NAA into an aqueous medium (buffer in this case), pores remain filled with air [65]. In contrast, silanes with active functional groups as PEG-silanes, amine-terminated silanes, epoxy-terminated silanes and others have been used to increase the wettability of NAA. Functionalization of NAA by PEG-silane has been proven to prevent NAA structures from biofouling for long-term use under *in vitro* or *in vivo* conditions, improve biocompatibility for immunoisolation, and to reduce the effective pore diameter of NAA for molecular separation applications [66–68].

Table 2. Summary of the variety of silanes used to functionalize NAA and their applications.

Types	Silane Name	Modification Method	Application(s)	Ref.
Amino-silane	Aminopropyl-triethoxy silane	Solution based	Immobilization	[29,58]
PEG-silane	mPEG-silane	Solution based	Hydrophylization	[65–67]
Fluorinated-silane	perfluoroalkyl-silanes	Solution based	Transporting and separation	[5]
Mercapto-silane	Mercaptopropyl-triethoxy silane	CVD based	Sensing	[59]

Furthermore, SAMs based on silanes have been extensively used as an initial active layer to immobilize other (bio)molecules, polymers, nanoparticles, DNA, cells, quantum dots, and lipid bilayers onto the surface of NAA structures [29,69–72]. Different silane chemistries can be used for immobilizing biomolecules such as growth proteins, peptides, lipid bilayers and antibodies. Amid them,

amino-propyltryethoxy silane (APTES) is the most commonly used silane for modification of NAA. APTES modification of NAA was shown to suspend lipid bilayers over the pores by first grafting N-hydroxy-succinimidyl carbonate-polyethylene–glycol (NHS-PEG) and subsequently fusing the vesicle onto the PEG layer [73]. Amine groups in APTES have also been revealed to act as surface-confined initiator for grafting of polymer brushes of poly(γ-benzyl-l-glutamate) (PBLG). PBLG polymer brushes can tailor the filtration and separation properties of NAA membranes [74]. Furthermore, APTES-modified NAA can be used to graft poly-N-isopropylacrylamide (PNIPAM) through atom-transfer radical polymerization (ATRP) [75]. Additionally, APTES-modified NAA supports have been used to assemble and fabricate metal nanoparticles or nanotubes by electroless deposition. Wang *et al.* synthesised Pd nanotubes using APTES-modified NAA templates, which were treated in an aqueous solution of $SnCl_2$ and HCl and subsequently immersed in a solution of $PdCl_2$ and HCl for specific time to generate Pd nanotubes by electroless deposition approach [76].

Figure 9. Schematic illustrating of silanization process for functionalizing the surface of NAA with multiple silanes (Adapted with permission from [77]).

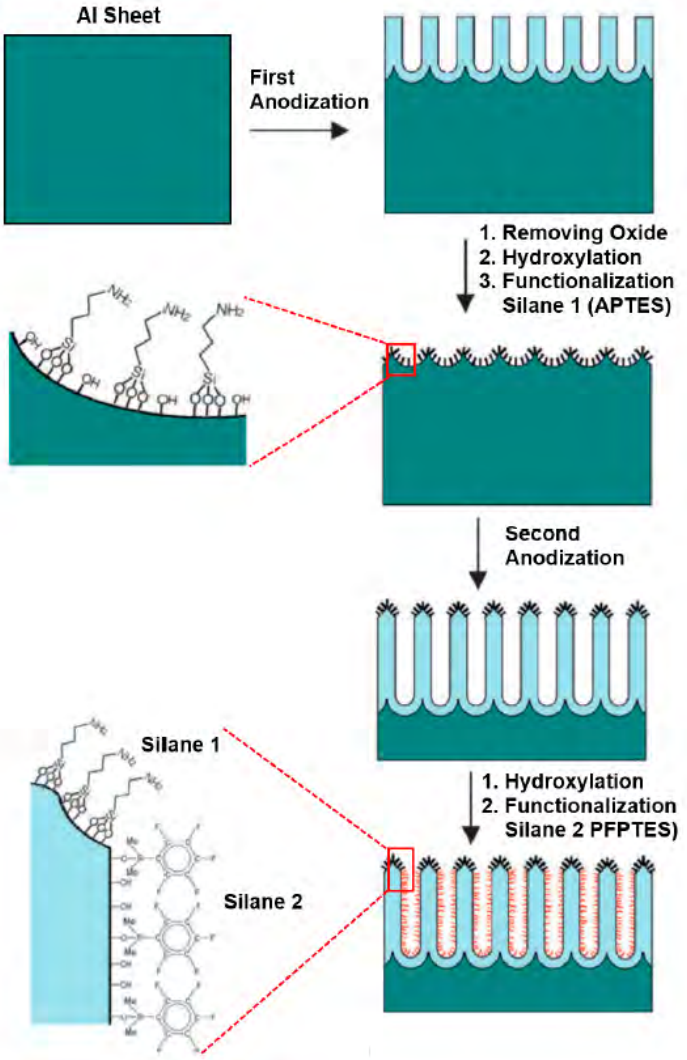

Sehayek *et al.* decorated NAA membranes with electrically conductive nanoparticles by passing them through APTES-functionalized NAA pores [78]. Lahav *et al.* also demonstrated the fabrication of bimetallic nanotubes of Au-Pd by immobilizing a mixture of Au and Pd nanoparticles inside APTES-modified NAA. This leaded to solidification of nanoparticles and formation of multiwall metallic nanotubes upon drying [79].

Our group demonstrated an innovative approach to attach multifunctional silane-based layers in a single NAA template. This multilayered surface modification approach was achieved by a series of anodization and silanization cycles repeated in a sequential fashion. This approach is useful for applications as membrane filtration and separation, as two different surface chemistries can be obtained with distinctly surface properties [77]. We successfully functionalized the surface of NAA with two or three layers of different silanes (pentafluorophenyl-dimethylpropylchloro-silane (PFPTES), APTES and N-triethoxysilylpropyl-(O-polyethyleneoxide)urethane (PEG-silane)), providing a range of surface functionalities and wettabilities as shown in Figure 9 [77,80]. This approach makes it possible to control the thickness of each functional silane layer by controlling the thickness of NAA grown during each anodization and silanization cycle. We further demonstrated the application of this method by selective transport of hydrophobic and hydrophilic dye molecules through membranes with hydrophobic and hydrophilic layers.

Functionalization with Organic and Phosphonic Acids

Allara and Nuzzo, initially reported on the qualitative and quantitative assessments of self-assembly of *n*-alkanoic acids of varying carbon chains (16–22 carbons) and terminal groups such as methyl, vinyl or propargyl groups [81,82]. Figure 10 defines the basic attachment process of *n*-alkanoic acids to NAA. Chang and Suen, displayed successful functionalization of NAA surface with n-alkannoic acids (*i.e.*, carboxylic acids) using a solvent-based functionalization method [83]. Cheow *et al.* used octanoic and octadecanoic acid as well as fluorinated organic acids such as trifluoroacetic acid, perfluoropentanoicacid and 2,3,4,5,6-pentafluorobenzoic acid, to impart hydrophobicity to NAA surfaces. The highest contact angle achieved by these functionalization approaches was 107° for perfluoropentanoic acid-modified NAA [84]. However, the functionalization process was reversible and the resulting functional monolayers were found to be unstable in aqueous environments. Similarly, Karaman *et al.* also modified the surface of NAA with a variety of short carbon chain (3–4 carbons) fluorinated and non-fluorinated carboxylic acids [85]. Eliasson's group have also shown that other organic molecules such as stearic acid and methyl stearate can form monolayers onto the surface of NAA [86].

Figure 10. Functionalization path of NAA surfaces with *n*-alkanoic acid. (Adapted with permission from [82]).

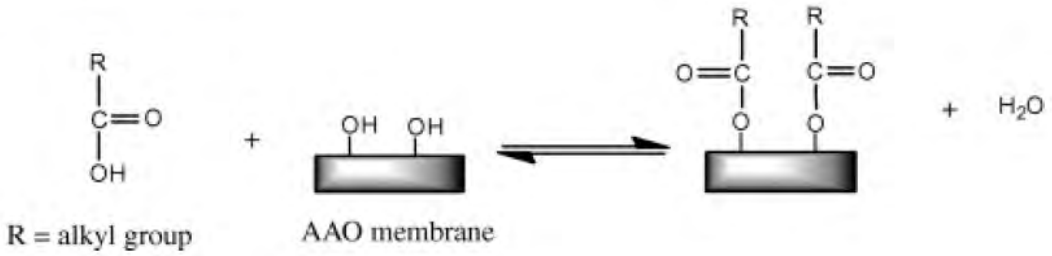

Phosphonic acids, on the other hand, do form stable monolayers on NAA surfaces , but there are only few examples of these compounds self-assembling onto NAA [29]. Recently, Debrassi *et al.* provided a comprehensive study on the stability of a range of monolayer forming compounds, including 1-hexadecylphosphonic acid (PA: phosphonic acid), 1-hexadecylcarboxylic acid (CA: carboxylic acid), 2-hydroxyhexadecylcarboxylic acid (2OHCA: α-hydroxycarboxylic acid), 1-hexadecyne (YNE: alkyne), 1-hexadecene (ENE: alkene), and 1-hexadecyltrimethoxysilane (SIL: silane) [87]. NAA modified with phosphonic acids was the most stable over a pH range 4–8 and temperatures up to 80 °C. They also found that the stability of NAA substrate modified with PA depends strongly on the terminal functional group of the monolayer. For instance, hydrophobic layers were less susceptible to pH and temperature changes than hydrophilic ones. In recent studies by our group, water soluble phosphonic acid (*i.e.*, 2-carboxyethyl phosphonic acid) was used to further attach streptavidin onto the surface of NAA [88,89]. These streptavidin-modified NAA substrates were then employed for impedance-based sensing of biotin (analyte) in aqueous buffer solution.

Lipid Bilayers

Lipid-bilayers are known to mimic cell membranes to a great extent, although their poor stability hinders their applications in several fields. NAA is accepted as a suitable substrate for supporting lipid-bilayers as different assemblies of lipid-bilayers can be obtained depending on the structural features of NAA and deposition methods with the ability to suspend lipid-bilayer on the NAA membrane top or confine them inside the nanopores [90,91]. Suspended lipid-bilayers on NAA substrates have shown long-term stability and act as channels for transporting ions. These suspended lipid-bilayers were fabricated by fusing lipid vesicles on gold-coated NAA substrates pre-treated to form SAMs of alkanethiols with negatively charged head group. Their fabrication approach consisted of gold coating of NAA surface followed by formation of a SAM of alkanethiols with a negatively charged head group [90,92,93]. Similarly, confined lipid-bilayers were fabricated using silanes-coated NAA membranes to achieve fusion of lipid vesicles inside the nanopores [94]. Smirnov and Poluektov, used this technique to deposit multiple lipid-bilayers and obtain lipid nanotubes [95]. They were also able to control the thickness of the lipid wall and confirmed the formation of lipid nanotubes through electron paramagnetic resonance, nuclear magnetic resonance spectroscopy and fluorescence microscopy.

Largueze *et al.* used a PEG-triggered fusion of lipid vesicles to deposit tethered lipid bilayers inside the pores of NAA [73]. To this end, NAA pores were functionalized with APTES and one side of the NAA membrane with a SAM of undecanethiol after gold coating. Then these multifunctional NAA membranes were incubated with lipid vesicles. After a fixed period of time these lipid vesicles were fused to NAA pore walls using PEG as a trigger (Figure 11). The potential of fabricating lipid-bilayers lies in designing sensitive biomimetic nano-channels that can be used for ion transporting and sensing applications.

Figure 11. Schematic presenting the step-wise process used to fabricate lipid-bilayers inside NAA pores using PEG triggering. (Adapted with permission from [73]).

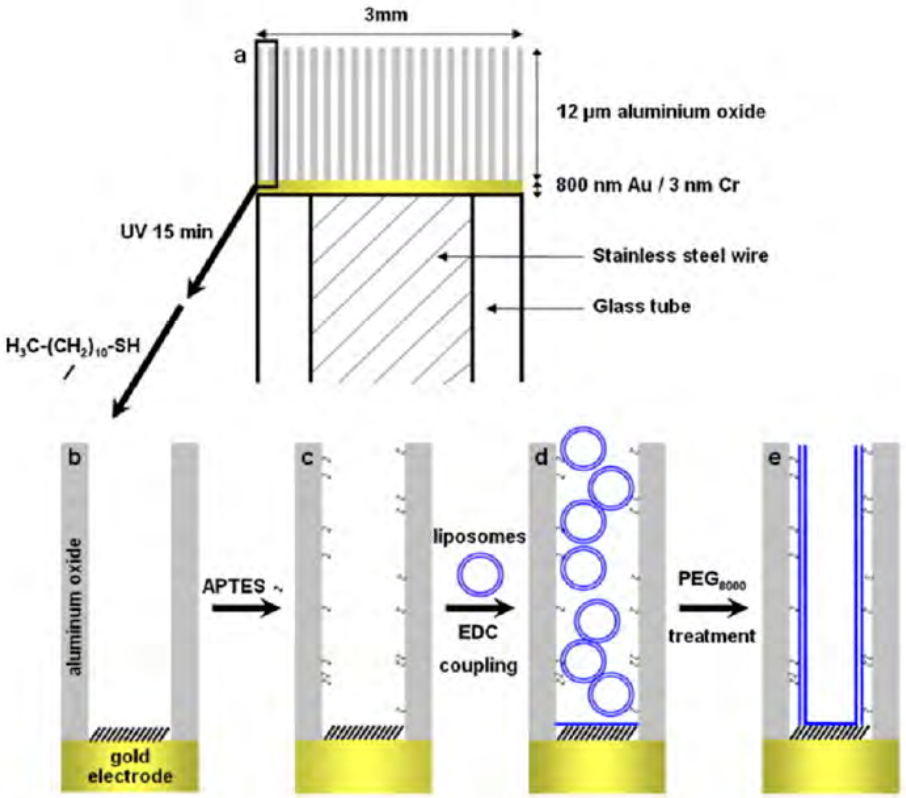

Layer-by-Layer Deposition

Layer-by-Layer (LbL) deposition is a very simple, inexpensive, and versatile technique used to obtain thin polyelectrolyte (PE) multilayers, the thickness of which can be controlled with nanometric resolutions, on different substrates. This is achieved by alternatively dipping the substrate into polyelectrolyte solutions of opposite charge (Figure 12a) [96]. This technique was demonstrated to be able to deposit PE layers inside NAA pores. So far, LbL technique has mainly been used to tune the transport properties of NAA membranes, attach nanoparticles or biomolecules inside NAA pores, and fabricate polyelectrolytic nanotubular structures using NAA as a template [29]. In this regard, Balachandra *et al.* used UV/ozone-treated NAA to adsorb Cu^{2+} ions, which were used to deposit multi-layers of PAA and PAH inside NAA membranes [97]. Notice that NAA pores remain open (or not blocked) after deposition of up to seven PE bilayers. So far, a vast number of PE combinations and compositions (e.g., PSS/PAH, PSS/PAH, $(PSS/PDADMAC)_4PSS$) have been used to efficiently control the flux, transport, rejection rate and selectivity of solutes through LbL-functionalized NAA membranes [98–100]. Furthermore, Dai *et al.* used LbL technique to immobilize antibodies inside the nanopores of NAA [101]. In this way, antibodies were immobilized onto the deposited layers of PE composed of $[PAA/PAH]_3PAH$ using carbodiimide coupling chemistry (Figure 12b). The same group showed that positively charged PE layers can be utilized to attach citrate-stabilized gold nanoparticles for catalytic applications [102]. LbL technique has employed NAA to synthesize nanotubes of soft

materials such as polyelectrolyte polymers, biomolecules, and metal organodiphosphonates. As an example, Li *and coworkers* introduced the concept of LbL assembly of polyelectrolyte multilayers inside nanoporous alumina template [103,104]. The assembly of polyelectrolyte milt-layers results in polymeric nanotubular structure that display complex but well-controlled wall morphologies and adjustable wall thickness.

Figure 12. (**a**) A general scheme showing steps for layer-by-layer deposition of polyelectrolytes; (**b**) LbL modification of NAA pores used to immobilize antibodies. (Adapted with permission from [96] and [101], respectively).

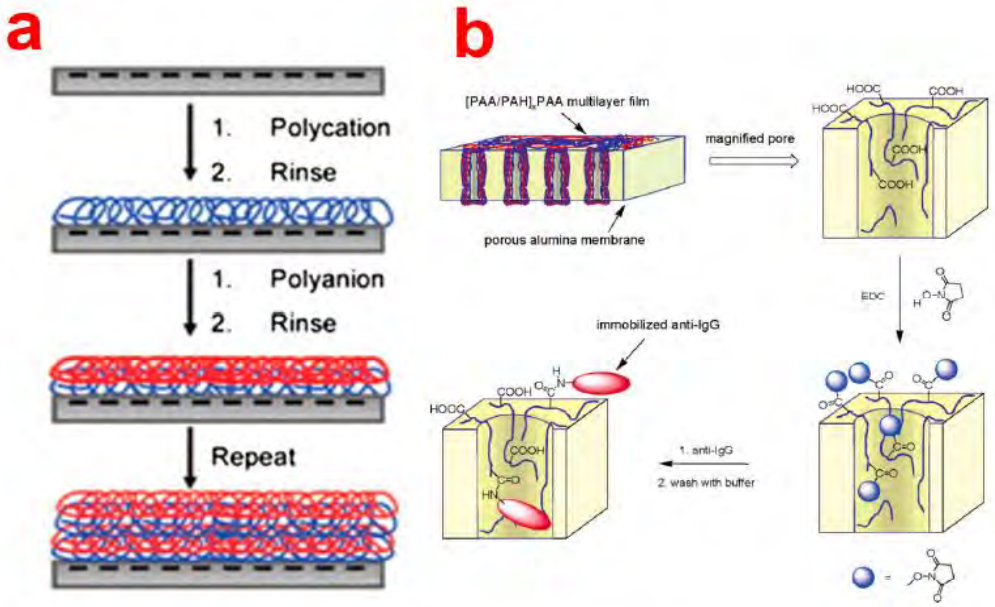

They deposited polyallylamine hydrochloride (PAH)/sodium poly(styrene sulfonate) (PSS) from aqueous solutions inside the pores of a NAA membrane assisted by pressure. The alumina walls were subsequently etched using aqueous NaOH solution to obtain liberated flexible $(PAH/PSS)_3$ nanotubes, which replicated the length and outer diameter of the NAA templates used in the synthesis process [103]. Similarly, Martin and co-workers reported the synthesis of DNA nanotubes supported by 1,10-decanediylbis(phosphonic acid) skin using sequential deposition of complementary nucleotides with specific sequences in a NAA membrane [105]. In this process, NAA was first immersed into a solution of (DOP) followed by a solution of $ZrOCl_2$ to form the (DOP)/Zr(IV) supporting skin. The inner surface of the nanotubes resulted from hybridization between multiple double-stranded DNA layers. The same group also demonstrated, for the first time, the synthesis of protein nanotubes by alternately exposing the NAA template to a solution of the glucose oxidase (GOx) or hemoglobin (Hb) [106]. Finally, glutaraldehyde was used as a cross-linker to hold these proteins together. This study also evidenced that GOx nanotubes catalyzed glucose oxidation, whereas heme-electroactivity of Hb nanotubes was retained. Apart from fabrication of novel nanomaterials, LbL has been used to attach functional molecules inside the pores of NAA. For example, Masumoto *et al.* adsorbed positively charged polyelectrolyte polymer poly-L-lysine inside the pores of NAA to obtain positively charged inner surfaces suitable to bind DNA molecules by electrostatic interactions [107]. A similar

strategy has been used to attach noble metal nanoparticles/cubes inside NAA pores (e.g., adsorption of poly(diallyldimethylammonium chloride) to attach gold nanoparticles or PAH/PSS polyelectrolyte multilayers for attachment silver nanocubes) [108].

Sol-Gel Chemistry

Sol-gel assembly process combined with NAA templates has been predominantly used to replicate and prepare novel nanostructures as nanotubes and nanorods or reducing the pore diameter and imparting different surface chemistries to NAA structures (Figure 13) [109]. The most widespread materials for sol-gel synthesis of nanostructures using NAA templates include silica, carbon, metal oxides (e.g., TiO_2, TiO_2–silica composite, SnO_2, NiO, *etc.*), and polymer-derived SiOC [29]. This technique is based on the hydrolysis of the sol-precursor on the NAA substrate by immersion, dipping or spin coating followed by solvent evaporation and formation of a glassy gel inside the pores [110]. The remaining solvent from the gel-NAA system is removed by subsequent thermal treatment. Sol–gel technique results in synthesis of high purity homogenous and multi-component structures with the ability to further control their properties such as structure, thermal stability and surface reactivity (using precursors with additional functional groups) [111,112]. Lee *et al.* prepared modified NAA membranes by depositing silica nanotubes using sol-gel template technique [113]. The prepared silica nanotubes were utilized for selective binding and delivery of enantiomeric therapeutic drug. He *et al.* have demonstrated the fabrication of silica nanotubes with different shapes using funnel-type NAA templates [114–116]. The obtained silica nanotubes with increasing diameter from one end to the other. These nanotubes are called as shape-coded silica nanotubes (SNTs) and were used for specific detection of rabbit anti-IgG from a mixture containing rabbit and human IgG antibodies. They also demonstrated that SNTs can be used for multiple analytes at the same time. As a proof of concept, SNTs featuring three different shape codes were functionalized with rabbit, mouse, and human IgG antibodies, which were subsequently used for simultaneous detection of anti-rabbit and anti-mouse IgG antibodies using a sandwich assay.

Wang *et al.* prepared carbon-based nanostructures such as carbon fibers and carbon ribbons with a circular mesoporous framework [117]. Phenol-formaldehyde presol was used as a precursor solution along with surfactants such as F127 ($EO_{106}PO_{70}EO_{106}$) and P123. First, the precursor solution was infiltrated inside the pores of NAA to form gel during the ageing time followed by calcination at 600 °C for 3 h to produce mesoporous carbon nanostructures. The same group prepared mesoporous titania nanotubes within NAA membranes by replacing the carbon source with a titania source (*i.e.*, titanium tetraisopropoxide, TTIP) and employed the mesoporous titania nanotubes as an electrode material in a high rate rechargeable lithium battery [118]. Platschek *et al.* extended this work by controlling the morphology of synthesized mesoporous carbons by manipulating the sol-to-surfactant ratio and the types of surfactants [119]. Confalonieri *et al.* displayed deliberate control over the spatial arrangement of nanoparticles using a novel method to assist the self-assembly of magnetic nanoparticles. For this, they spin coated iron oxide nanoparticle (20 nm) on the pretextured Al obtained after removal of first anodized NAA layer. The magnetic nanoparticles were found to form clusters of different arrangements within the valleys of pretextured Al, such as collars, chains and hexagonally closed islands. They used memory effect to probe the strength of magnetic interactions between particles [120].

Figure 13. (**a**) A schematic process for templating NAA structure to replicate silica nanotubes via sol-gel process; (**b**) TEM images of the resulting silica nanotubes templated from NAA. (Adapted with permission from [109]).

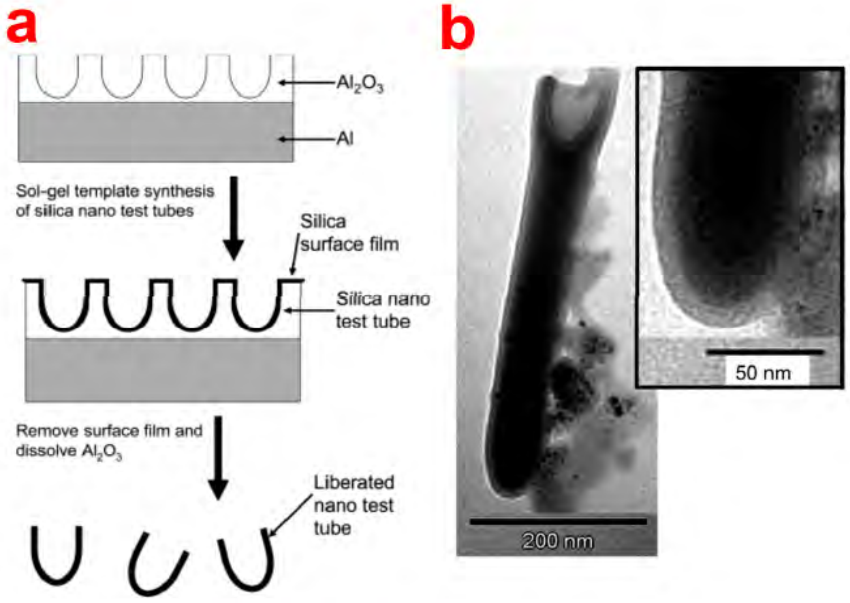

Electrochemical and Electroless Deposition of Metals

Electrochemical deposition is a simple, inexpensive method for modifying the pores of NAA with metal nanostructures. In comparison to other metal deposition techniques such as CVD, ALD or thermal metal deposition, the electrochemical method does not require expensive equipments and special conditions [121]. Different metal-based nanostructures (*i.e.*, nanowires, nanorods, nanotubes and nanoparticles) have been templated from NAA using this approach [29]. Recent developments in electrochemical deposition have made it possible to deposit multiple metals in the same NAA template for producing alloy nanostructures. Liu *et al.* prepared segmented Ag-Au alloy nanowires inside NAA templates using electrochemical deposition [122]. Burdick *et al.* demonstrated the fabrication of multisegmented nanowires of gold with short Ag spacers [123]. Generally, electrochemical deposition is carried out on NAA membranes, which makes it difficult to deposit metal inside thin NAA membranes. To overcome this, Lee *et al.* developed an alternating current (AC)-based electrochemical deposition technique to assembly gold nanoparticles within NAA membranes [124]. Recent advancement in electropolymerization have lead to fabrication of multisegmented composite nanorods and nanowires of conducting polymers with metals and semiconductors prepared by electrochemical deposition [121]. These metal decorated NAA substrates have been recently used as sensing platforms for such optical techniques as surface enhanced Raman spectroscopy. This was explored by Masuda's Group, who created a 3-D ordered mosaic of gold nanoparticles using the pores of NAA as a mask. The resulting nanostructures were used as sensing platforms in SERS-based detection of pyridine [125]. Electroless deposition, on the other hand, involves reduction of metal cations from an aqueous solution [126]. Martin and co-workers used this method to prepare gold/NAA composites, which were investigated for molecular separation processes [61]. Either metal nanotubes or nanorods/wires can be obtained from

electroless deposition depending on the deposition time. So, nanotubes are obtained with short times while solid nanorods/wires can be produced by longer deposition times [121]. Mu *et al.* fabricated SERS active arrays of Au nanoparticles with tunable particle gaps on NAA substrates. The pH and temperature conditions of the plating bath were reported as the main factor for controlling the size, shape and aggregation of Au nanoparticles during the electroless deposition process [127]. Wang *et al.* prepared a number of metal nanotubes (*i.e.*, Co, Ni and Cu) using NAA templates via electroless deposition on APTES-modified NAA membranes [76]. The inner diameter and length of the resulting nanotubes were adjusted by controlling the deposition times and the thickness of the NAA template, respectively. Other investigations synthesized Ag nanotubes with lengths over 10 μm inside NAA membranes. Furthermore, Ag nanoparticles of controlled size and smooth surface have been deposited inside NAA using this technique [29].

Lee *et al.* fabricated multisegmented metallic nanotubes by combining electroless and electrochemical deposition methods (Figure 14). In this approach, Sn (II) was first adsorbed onto the pore walls of NAA membranes from a solution of $SnCl_2$. Subsequently, exposure to Ag (I) led to spontaneous reduction and replacement of Sn (II) via a sensitization process, which was repeated several times. Ag nanoparticles decorated inside NAA membrane pores were isolated from each other, thus did not conduct current. Final electrochemical deposition of Au resulted in formation of Au nanotubes with a bimetallic stacked configuration [128]. Zhang *et al.* used AC electrodiposition to fabricate nanoporous anodic alumina films embedded with Fe. These films display vivid structural colors and magnetic properties. These properties were found to be dependent on oxidation time of aluminum [129].

Figure 14. SEM images of multisegmented metal nanotubes with a stacked configuration of metal inside NAA templates. (**a**) Cross-sectional SEM image of Au-Ni-Au-Ni-Au along the nanotube axis (Au: yellow and Ni: purple) (**b**) and (c) SEM images of multisegmented metal nanotubes after dissolution of the NAA in NaOH. (Adapted with permission from [128]).

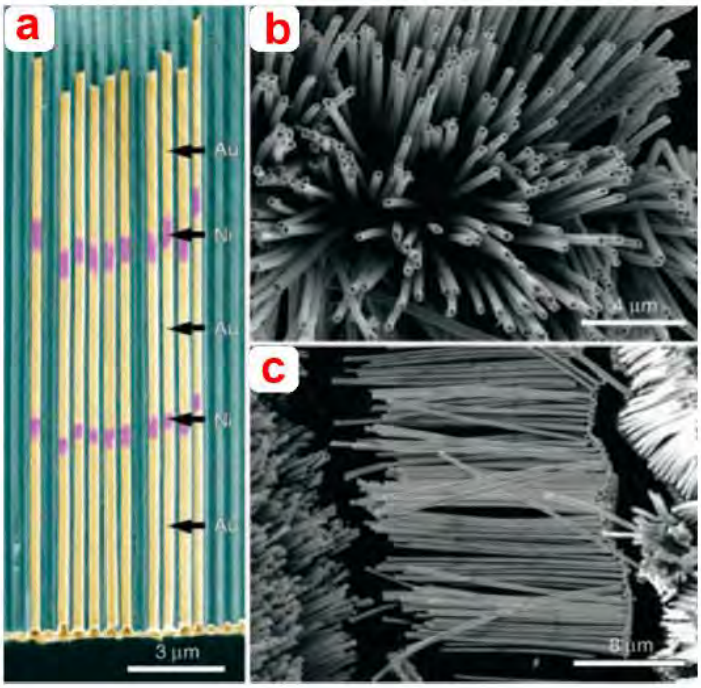

4. Structural Engineering and Optical Optimization of NAA

The porous architecture of NAA plays a key role in defining its optical properties. The nanoporous structure of NAA can be designed and engineered to produce a broad range of pore geometries with tailored optical properties. Engineered NAA structures can be designed to interact with light in different manners as to confine, guide, transmit, emit, and reflect it. Developments of different electrochemical anodization approaches have made it possible to design and engineer the structure of NAA to produce a new generation of optical nanostructures. So far, a large variety of NAA pore geometries (*i.e.*, modulated, hierarchical, serrated, three-dimensional, funnel-like, and multilayered) have been engineered by using innovative and unique anodization techniques [130–132]. Figure 15 shows SEM images and schematics of some of the most representative NAA structures generated by different electrochemical approaches. The precise engineering of the nanoporous structure of NAA can result in the generation of optically active structures such as distributed Bragg reflectors, microcavities, rugate filters, omnidirectional mirrors and waveguides [132]. These optical nanostructured devices are formed due to the ability of electrochemical anodization process to produce variations in porosity (*i.e.*, refractive index) of the NAA structure depending upon the type and regime of anodization. The most commonly used method to produce porosity variations is to switch between "Hard" and "Mild" anodization regimes repeatedly, which present different levels of porosity (*i.e.*, MA results in 10% porosity while HA only produces NAA with 3% porosity). Lee *et al.* used this approach to fabricate NAA with pore diameter modulations along the length of the pores (Figure 15a) [8]. In this method, perfectly ordered NAA was first prepared on an electropolished Al substrate in phosphoric acid electrolyte (H_3PO_4: 0.4 M, 110 V and 10 °C) after imprinting the pattern from a master stamp. After 15 min of anodization in H_3PO_4 the electrolyte was replaced with 0.015 M oxalic acid ($H_2C_2O_4$) and further anodized at 137 V at 0.5 °C for 2 min. NAA with highly uniform periodic modulations of the pore diameter and constant inter-pore distance were obtained by repeating the aforementioned two anodization processes. Notice that the anodization voltages were set such that they yield the same inter-pore distance in MA and HA conditions and prevented NAA pores from pore branching. The pore diameter of NAA during each anodization step was controlled by the anodization voltage and the acid electrolyte, whereas the length was controlled by the anodization time. This report inspired and let to overwhelming a number of studies on different electrochemical approaches to generate pore diameter modulations in NAA structures. As for this, Pitzschel *et al.* fabricated similar pore diameter modulations in NAA using the same electrolytes under different anodization conditions. In this case, the period of nanoimprint from a master stamp was 235 nm. They performed the first MA step under 72 V in 0.4 M aqueous H_3PO_4 at 10 °C and the hard step was performed under 93 V in 0.15 M $H_2C_2O_4$ at 5 °C in a 4:1 water/ethanol mixture. They further used this pore modulated structure to synthesize magnetic nanotubes by depositing Fe_3O_4 using ferrocene and ozone as precursors [53]. Losic *et al.* on the other hand, used a cyclic anodization approach, where pore modulations along the length are obtained by applying periodic oscillatory current signals with different profiles, amplitudes, and periods (Figure 15b) [24].

Figure 15. (**a**) Cross-sectional SEM images of pore diameter modulations in NAA produced by switching the anodization between MA and HA regimes; (**b**) Schematic illustration of cyclic anodization process introduced by Losic *et al.*; (**c**) Cross-sectional SEM images of high aspect ratio funnel-like NAA produced by Santos *et al.* (Adapted with permission from [8,24,25]).

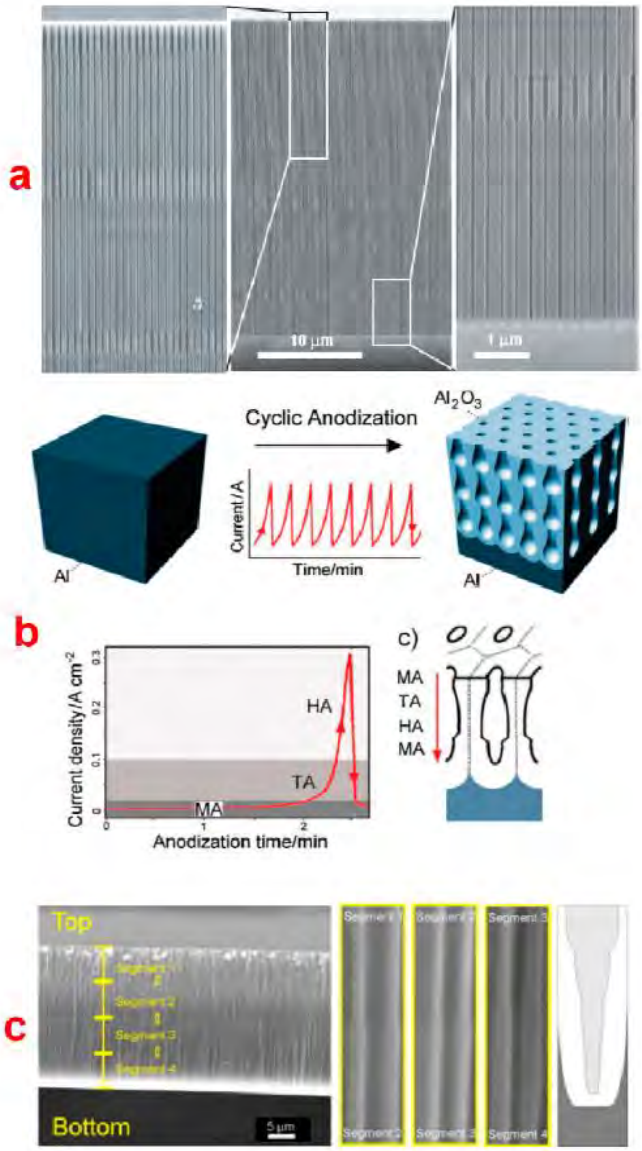

Santos *et al.* showed the fabrication of hierarchical type NAA where first anodization step is to obtain pre-patterned Al chip with concave cavities [133]. Subsequently, these pre-patterned Al chips are anodized under asymmetric anodization conditions (*i.e.*, changing one or more than one anodization conditions than the first anodization). The resulting NAA structure was observed to have multiple pores within single concave cavities, thus called a hierarchical NAA structure. Serrated-type NAA pores were first fabricated by Zhu *et al.* They also proposed a new growth model for NAA, which emphasizes on the close relationship between pore generation and oxygen evolution during the

formation of such NAA structures [134]. This study was further extended by Li *et al.* who also on the basis of the results obtained from their experiments and simulation attributed the initiation and formation of serrated-like NAA pores to the evolution of oxygen gas bubbles during the anodization [135]. 3-D type nanoporous structure in NAA was obtained by Losic *et al.* after combining cyclic anodization and wet chemical etching using phosphoric acid [28]. Likewise, Santos *et al.* combined discontinuous anodization and wet chemical etching steps with phosphoric acid to obtain a similar 3-D NAA pore structure [136].

Another interesting structure based on NAA is the funnel-like NAA, which can be produced by combining multiple anodization and pore widening steps [24,137,138]. This structure features a stack of NAA layers of decreasing pore diameter from top to bottom, therefore called funnel-like NAA structure (Figure 15c) [23]. The length of each stack is controlled by the time of anodization or the total charge (*i.e.*, integrated current passed through the system), whereas the pore diameter in that stack is established by the pore widening time. Nagaura *et al.* fabricated low aspect ratio funnel-like NAA and studied their structural changes by manipulating the number of anodization and pore widening cycles [137]. The same authors replicated this low aspect ratio funnel-like structure to create nickel films with nanoconical surface morphology [138]. Yanagishita *et al.* applied similar approach and replicated the funnel-like structure featuring different pore shapes to a polymer by photo-imprinting process [139]. The polymer replicates were studied for their antireflection behavior by measuring the amount of transmitted light. NAA nanostructures with more gradual changes in slope were found to be less reflective. Santos *et al.* fabricated high aspect ratio funnel-like NAA by controlling the length of each stack very precisely according to the total charge passed through the system. They demonstrated NAA funnel-like structure with two, three, and four stacks [24]. Li *et al.* reported tailoring of the shape of funnel-like NAA pore structures by new electrochemical approach [140]. They successfully demonstrated the fabrication of linear cones, whorl-embedded cones, funnels, pencils, parabolas and trumpets-like nanopore structures by controlling the fabrication parameters as anodization time, etching time and cycle times. Very recently, we reported on the fabrication of inverted funnel-like NAA, which has increasing pore diameter along the pore length from top to bottom [32]. This innovative structure was achieved by taking advantage of the fact that the chemical dissolution rate of NAA decreases after annealing at temperatures in excess of 100 °C. We made inverted funnel-like NAA with two and three stacks by combining annealing steps and anodization steps. In addition, formation of these inverted funnel-like structures was monitored in real-time using reflective interference spectroscopy method.Multilayered NAA structures can be used to fabricate a broad range of optical nanostructures such as DBRs, optical microcavities, rugate filters and other optical and photonic structures. They consist of multiple layers of NAA segments with different levels of porosity. Multilayered NAA structures have been fabricated by periodically alternating the voltage during the anodization process. Anodization profiles such as stepwise, sinusoidal, pseudo-sinusoidal, saw-like, *etc.* have been applied to engineer the porosity (*i.e.*, refractive index) of NAA in depth. This allows for specifically designing and engineering the light-matter interaction in NAA for subsequent applications in chemical and bio-sensing. Lee *et al.*, for the first time, displayed the ability to fabricate multilayered NAA via an electrochemical approach consisting of periodic pulses of low and high potential (*i.e.*, voltage in MA and HA regime) [26]. In this study, they performed anodization of pre-patterned Al chips through pulse anodization under potentiostatic conditions in sulphuric and oxalic acids. Nanotubular array structures with periodic neck-like constrictions along the length of the tubes were

observed for sulphuric acid electrolyte while NAA with periodically varying pore diameter were observed for oxalic acid electrolyte.

Sulka *et al.* applied a similar approach to fabricate layered NAA structures, which were subsequently used as templates for fabricating modulated metal nanowires. In another study, they demonstrated the application of this multilayered NAA structure as distributed Bragg reflector (DBR) [141]. The resulting NAA-based DBR structure had periodically modulated layers of NAA with low and high porosity (*i.e.*, refractive index). These DBR mirrors were observed to effectively reflect light in two different ranges of wavelength, which was in good agreement with the mathematical calculated reflection spectrum.

Zheng *et al.* prepared NAA based DBRs by anodizing Al chips under pseudo-sinusoidal voltage profile in oxalic acid electrolyte [142]. They studied the effect of the anodization temperature on the transmission peak of the prepared DBRs. The results predicted that almost the whole range of visible spectrum can be covered by adjusting the anodization temperature between 7 and 14 °C. Recently, Rahman *et al.* used an innovative cyclic anodization approach produce NAA-based DBRs [143]. They also studied the effect of pore widening time on the position of the photonic stop-band of the resulting DBRs. This study demonstrated the ability to control the photonic stop-band of these optical nanostructures by modulating the refractive index contrast between the layers through pore widening. More recently, Kumeria *et al.* fabricated nanoporous rugate filters by anodizing Al chips under pseudo-sinusoidal potentiostatic conditions in oxalic acid electrolyte [132]. They prepared four different types of rugate filters based on NAA and selected the most optimum structure based on their experimental and theoretical modeling (*i.e.*, the Looyenga–Landau–Lifshitz model) for sensing applications. This study demonstrated that optimize optical signals enable the precise control of the optical properties of nanoporous structures for chemical and bio-sensing applications.

5. Optical Sensing Applications

5.1. Plasmon Resonance Sensors Based on NAA

Since the first publication in the late 1970s, the potential of surface plasmon resonance (SPR) for characterization of thin films and monitoring analyte-receptor binding processes at metal interfaces has been greatly recognized [144]. Capabilities of SPR are real-time and in-situ measurements of a wide range of surface interactions, ligand-binding affinity, association/ dissociation kinetics, affinity constants, and highly sensitive surface-concentration measurements. During the last decades, SPR has been exploited such that more than 75% of research on optical biosensing was based on SPR [144]. This extensive exploitation of this sensing technique has resulted in the generation of new SPR configurations (*i.e.*, Grating, Otto, and Kretschmann configurations) and substrates (*i.e.*, nanostructured films, porous materials, nanoparticles, *etc.*). The use of nanomaterials has led to the discovery of a new type of SPR such as waveguiding and localized SPR (LSPR or LPR) that exclusively occurs in noble metal nanoparticles/structures. Notably, when the noble metal particles/structures (*i.e.*, gold, silver, *etc.*) are scaled down to nanometric level (*i.e.*, <100 nm), light interacts with particles much smaller than the incident wavelength [144]. This leads to the generation of plasmonic oscillations of a particular frequency that are localized around the nanoparticles. LPR oscillations are dependent on the size,

shape and surrounding environment of the nanoparticles/structures. The LPR is sensitive to changes in the local refractive index environment, which can be measured through shifts in the resonance wavelength or resolving the LPR. Recent studies have proven that close organization of metal nanoparticles/structures even leads to enhancement of LPR signals. In recent years, NAA has become a very attractive nanomaterial as a substrate for SPR-based sensing devices in SPR, waveguiding (WG), as well as LPR mode [145–147]. In this regard, typically a thin layer of NAA is either directly grown onto a prism or pre-formed NAA is glued to a metal coated prism using a refractive index matching glue. Surface plasmons are excited by an evanescent electromagnetic wave produced by the incidence of light on the surface under a Kretschmann configuration. In addition, NAA coated with noble metals presents highly organized metallic nano-caps, which have been utilized to excite plasmons under LPR mode and applied for chemical and bio-sensing applications. NAA-LPR-based SPR sensors are simple, inexpensive, compact and portable as it does not require a prism-based setup. Notice that the plasmonic characteristics of the SPR devices depend mainly on the surrounding refractive index within a range of few hundreds of nanometers beyond the metal film in Kretschmann configurations and LPR mode [144]. Thus, a thin layer of NAA within this thickness range can be applied onto the prism and used to develop nanoporous SPR sensors. Lau *et al.* combined NAA with waveguiding to develop a WG optical sensing platform, which was used to monitor reversible adsorption and desorption of bovine serum albumin (BSA) at different values of pH [146]. Their NAA-WG setup was based on a Kretschmann configuration with an intermediate Au layer between the prism and the NAA platform. A simpler and sensitive setup was developed by Yamaguchi *et al.* by directly depositing Al onto a prism and anodizing it to generate a nanoporous layer of 200 nm thick. The remaining unanodized Al (17 nm) acted as the metal layer to excite the plasmon for waveguide coupling [148]. Koutsioubas *et al.* on the other hand, fabricated NAA-based SPR sensors used to detect the formation of SAMs of octadecyl-phosphonic acid (ODP) [145]. Dhathathreyan demonstrated that the similar system can be used to quantify enzyme kinetics reaction [149]. In this study, the enzyme invertase was immobilized in the pores of 3 μm thick NAA layer with a pore diameter of 60 nm. The enzyme-substrate was flowed through a custom made flow cell and the digested product was detected by SPR. This system made it possible to study the activity of the immobilized enzyme, which was determined for different concentrations of sucrose at pH ranging from 3 to 6.5. The SPR results revealed a biphasic kinetics for both the adsorption of the enzyme and its interaction with the substrate. Maximum enzyme activity was observed at pH 4.5. In another study, Lau *et al.* monitored the grafting of poly(g-benzyl-L-glutamate) (PBLG) within the nanopores of NAA in real-teal time and in-situ using a SPR-NAA system [74]. Their results reveal that the conformation of PBLG inside the nanopores of NAA is due to confinement of polymer chains inside the pores, which was confirmed by comparing the results obtained with NAA and planar silicon dioxide surface. More recently, Hotta *et al.* used NAA-WG configuration demonstrated by Yamaguchi *et al.* and studied the enhancement of sensitivity (Figure 16a) [150].

Figure 16. (**a**) Schematic illustration of the SPR-NAA waveguide sensor developed by Hotta *et al.* and its typical reflection spectrum; (**b**) Schematic of NAA-LPR setup developed by Kim *et al.* by coating the top surface of NAA with gold to form nano-caps. (Adapted with permission from [150,151], respectively).

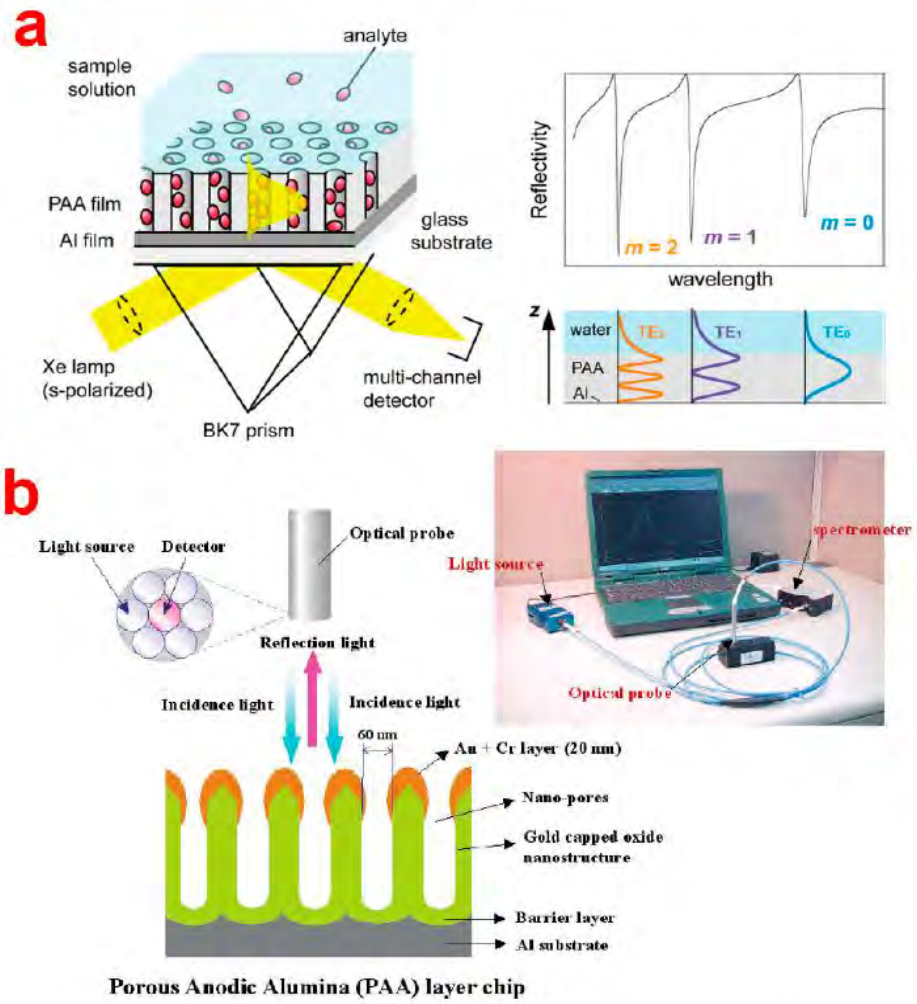

For this, the structure of NAA (*i.e.*, waveguiding layer) on Al (*i.e.*, cladding layer) was carefully engineered in terms of porosity, pore density, thickness, and refractive index to tune and optimize the optical WG and enhance the sensitivity of the system. The performance of the optimized NAA-WG was assessed by monitoring the adsorption of BSA molecules onto the nanopores of NAA. The most optimum NAA-WG sensor resulted in an extraordinarily large red shift (>300 nm) of a waveguide mode on adsorption of BSA. This extraordinary red shift was attributed to the large surface area of NAA, which results in a huge adsorption capacity. The theoretical calculations using Fresnel's equation suggested that the sensitivity of the NAA-WG sensor was much higher than that of conventional SPR sensors.

Another study by the same group, reports on enhancement of fluorescence signal on adsorption of fluorophore-labeled BSA (*i.e.*, BSA-AF) inside the nanopore surface of a NAA waveguiding film [152]. They monitored the adsorption of BSA-AF simultaneously using SPR and fluorescence spectroscopy. Enhancement of FL signal on NAA-WG is attributed to a combination of large surface area of NAA

and enhanced field due to waveguiding modes within the pores of NAA. As described above, LPR is another type of widely used SPR mode in combination with NAA substrate coated with noble metals (mostly gold or silver). This results in the formation of highly ordered arrays of metallic NPs of gold or silver (*i.e.*, nanocaps) on the top surface of the NAA. Figure 16b shows a typical LPR-NAA label-free biosensor fabricated on a gold-capped AAO substrate for detection of antigen-antibody binding. So far, NAA-based LPR sensors have been demonstrated for specific detection of proteins (e.g., BSA, avidin, DNA and thrombin) or binding events between biotin-avidin, complementary oligonucleotides, and 5-fluorouracil-anti-5- fluorouracil. In this regard, Kim *et al.* developed a new optical biosensor based on a gold-deposited NAA chip [151]. They observed that gold nanocaps resulted in an optical LPR pattern that was highly sensitive to the changes in the effective refractive index of the biomolecular layer attaching them. They demonstrated the detection of up to picomolar quantities of un-labeled oligonucleotides and the hybridization with synthetic DNA samples. Hiep *et al.* deposited gold on the top surface of NAA to form nanocaps and developed a NAA-LPR sensor to detect specific interactions between biomolecules such as biotin and avidin and 5-fluorouracil and anti-5-fluorouracil [147]. Another studies from the same group utilized NAA as a support for plasmonic gold nanoparticles (AuNPs). NAA fabricated by the two-step anodization process was exposed to cationic poly(allyl amine) to attach AuNPs on its surface. The pores of NAA trapped Au nanoparticles. Their experimental and simulation results show that the plasmonic spectra of this NAA-AuNPs composite were enhanced by the interference spectra of the NAA layer. This assembly of AuNPs on NAA substrate showed a high sensitivity towards solutions with different refractive indices [153]. In another study, Hiep *et al.* combined NAA-LPR with an electrochemical system for sensitive detection of toxic peptide (*i.e.*, melittin, the venom from the honey bees) with a lower limit of detection (LOD) at 10 ng/mL [154]. Yeom *et al.* used a similar strategy to form gold nanocaps on the top surface of NAA to develop an immunosensor featuring anti-CRP (C-reactive protein, a cardiac and inflammatory biomarker) antibody immobilised on the gold nanocaps [155]. Their system displayed an extraordinary lower limit of detection for CRP antigen at concentration 1 fg/mL due to LPR enhancement of the optical signals from NAA. Kim *et al.* used a similar system to detect picomolar quantities of untagged oligonucleotides on NAA-LPR platform.

5.2. Reflectometric Interference Spectroscopy (RIfS) Sensors Based on NAA

Reflectometric interference spectroscopy (RIfS) is another highly sensitive optical detection method that is based on the interaction of white light with films at micrometer scale. In this technique, white light is shined on a thin film and reflected at the two interfaces of the thin film resulting in amplification of the reflected light signal at wavelengths corresponding to the optical modes of the Fabry–Pérot (FP) cavity formed by the system thin film–surrounding medium (*i.e.*, the Fabry–Pérot effect) [156]. A model NAA-based reflective interference along with RIfS spectrum and real-time effective optical thickness change curve is presented in Figure 17a. The wavelength of each interference maximum in the RIfS spectrum is governed by the Fabry–Pérot relationship (Equation (1)) [157]:

$$OT_{eff} = 2n_{eff}LCos\theta = m\lambda \quad (1)$$

where OT_{eff} is the effective optical thickness of the thin film, n_{eff} is its effective refractive index, L is the actual thickness of the film, m is the order of the oscillation in the interference spectrum, the maximum of which is at wavelength λ, and θ is the angle of incidence. Therefore, any change in the effective refractive index of the thin film can be detected through shifts of the interference maximum. Shifts of the interference maximum can be further resolved by establishing the OT_{eff} of the thin film, which is calculated by applying fast Fourier transform (FFT) to the interference spectrum. The center of the resulting FFT Gaussian peak corresponds to OT_{eff} of the Fabry–Pérot cavity. Initially, polymer and metal oxide thin films were used to create FP cavities for RIfS application [157]. However, due to their limited surface area for analyte-receptor reaction, nanoporous thin films (*i.e.*, pSi, NAA, and TiNTs) have emerged as their potential alternative [3]. In the last two decades, Sailor and co-workers exploited porous silicon as a substrate combined with RIfS to develop highly sensitive optical chemical and bio-sensors [157–159]. Due to the chemical instability of porous silicon in biological medium, the same group developed a RIfS-based sensing system using NAA as an alternative to porous silicon. NAA offers several advantages over pSi such as better chemical and mechanical stability, ease of surface modification, and more controllable and defined nanoporous structure [159]. Furthermore, NAA also acts as Fabry–Pérot cavity and thus presents well-resolved interference peaks in the RIfS spectrum [160]. These interference peaks in the RIfS spectrum allow for real-time and in-situ monitoring of binding events of biomolecules and perform label-free optical sensing (Figure 17). NAA in combination with RIfS can be used to perform highly sensitive qualitative and quantitative detection of a broad range of analyte molecules. NAA-RIfS sensing platforms have been rapidly developed to detect gases, organic molecules and biomolecules [159,161,162]. For example, Pan *et al.* prepared a NAA-RIfS sensing platform for label-free detection of complementary DNAs [163]. Alvarez *et al.* developed a label-free NAA-RIfS immunosensor to selectively monitor the capturing of target antigens by their specific antibodies [160]. Their results revealed that significant effective optical thickness change occur only when there is an exclusive and selective antigen-antibody binding reaction occurring inside NAA pores. An *et al.* reported on the optimization of interference signals of NAA based on pore widening [164]. They measured the performance of RIfS with NAA pore widened for different time intervals by monitoring the changes in the effective optical thickness of NAA after adsorption of BSA and PSA (prostate specific antigen) antigen inside NAA pores. Their results reveal that NAA with widened pores offers better sensitivity. A more comprehensive study about optimization of RIfS signal from NAA was performed by Kumeria *et al.*, where they varied parameters such as pore diameter, pore length, and surface coatings to obtain the most optimum NAA structure for RIfS based sensing platforms [160]. In other studies, Kumeria *et al.* used the optimum NAA structure for RIfS to detect volatile sulphur compounds (*i.e.*, VSCs: hydrogen sulphide gas) and hydrogen gas [165,166]. For specific detection of hydrogen sulphide gas NAA substrate were coated with a thin film of gold, whereas hydrogen gas was detected on platinum coated NAA substrates. They also showed the capability of NAA-RIfS sensing platforms to detect VSCs in human malodour using the microfluidics-based Au coated NAA-RIfS sensing system [166]. Kumeria *et al.* further combined microfluidics and NAA-RIfS to develop a microchip biosensor for detecting and quantifying circulating tumour cells (CTCs) [167]. In this system, gold coated NAA were functionalized with anti-EpCAM antibodies that specifically capture the CTCs, and changes in OT_{eff} were used to monitor the capturing of CTCs [167]. This device was able to capture and detect CTCs in a single step without any pre-enhancement step. They also

demonstrated the ability of this system to detect CTCs in human blood as well. Dronov *et al.* reported the applicability of platinum-coated NAA to act as an interferometric transducer [168]. Their results reveal that metal coatings increase the signal to noise ratio and thus improve the capabilities of the system in terms of sensing. They compared the sensing performance of NAA with porous silicon substrate, which demonstrated that NAA provides more stable signals and a better sensing performance that those of porous silicon. In a recent study, Kumeria *et al.* demonstrated the ability of mercapto-silane modified NAA substrate for an ultrasensitive sensing platforms for detecting Au(III) ions in combination with RIfS (Figure 17a) [59]. Au(III) ions have become of great relevance to clinical applications due to their widespread use in gold-based drugs and bioimaging probes [59]. For this, NAA were modified with 3-mercaptopropyl-tirethoxysilane (MPTES), which imparted the NAA with selectively gold (III) ions. The sensing performance (*i.e.*, linear range, low limit of detection, saturation concentration, and selectivity) of the NAA-RIfS sensor was assessed through a series of experiments. They also demonstrated real-life application of this NAA-RIFS sensor by detecting gold (III) ions in tap water and phosphate buffer solution (PBS).

Interestingly, NAA-RIfS platforms not only can be used to monitor filling of NAA pores and the attachment of analyte molecules to the surface functional groups but also to study the release of molecules such as drugs from NAA substrates. Using this approach, Kumeria *et al.* monitored the release of a model drug, indomethacin, in real-time under dynamic flow conditions (Figure 17b) [169]. Their results revealed that the process is diffusion-controlled and the rate of drug release depends highly on the flow rate (*i.e.*, the faster the flow rate the higher the drug release from the nanoporous platform). This approach provides more accurate information than conventional *in vitro* drug release techniques performed under static conditions. A comparative study measuring the sensing performance of RIfS and photoluminescence spectroscopy (PLS) using NAA as substrate was recently reported by Santos *et al.* (Figure 17c) [60]. First, NAA with most optimum optical signal was obtained depending on the ratio of height to width of the effective optical thickness peak for both PLS and RIfS. This most optimal NAA structure was subjected to detection of glucose and L-cysteine under non-specific and specific binding conditions, respectively. Their results suggested that the type of the analyte molecules and their binding conditions play a crucial role in the determining the sensing performance of a device. Nevertheless, NAA-PLS platforms displayed better sensing performance (*i.e.*, linearity, higher sensitivity toward analytes and lower limit of detection) for both the analytes and binding conditions than NAA-RIfS platforms. Macias *et al.* fabricated a bilayered funnel-like NAA-RIfS sensing platform [170]. This structurally engineered NAA substrate generates a complex reflectivity spectrum. Their results show that a significant enhancement of the RIfS peak intensity on coating the top surface of the bilayer-NAA with gold layer. This biosensing platform was assessed by detecting BSA molecules and the results demonstrate the ability of bilayer-NAA-RIfS platform to detect BSA only in the effective optical thickness peak corresponding to the top layer and the total layer (*i.e.*, the whole bilayer) based on size exclusion.

Figure 17. (**a**) A schematic of NAA-RIfS sensor for detection of Au(III) ions developed by Kumeria *et al.* and plot showing its ability for real-time detection; (**b**) Real-time monitoring of drug release from NAA using RIfS; (**c**) The comparative study between RIfS-NAA and PLS-NAA sensors by Santos *et al.* showing ability of the two systems to generate barcodes. (Adapted with permission from [59,60,168]).

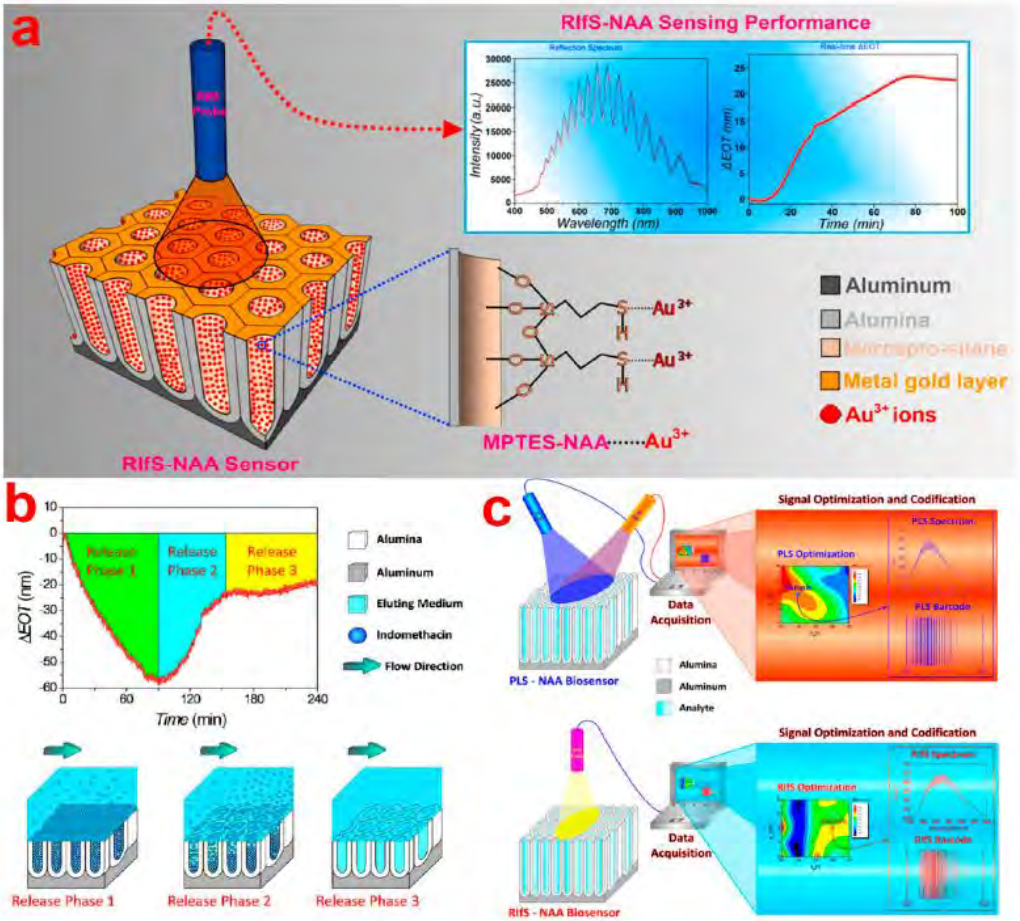

6. Future Perspective and Conclusions

We believe that there is still a huge potential for further improvement of basic properties of NAA, which can be utilized for broad and multidisciplinary research fields as materials science, nanotechnology, optics, electrochemistry, cell biology and medicine. Over the last few decades, the different approaches have made it possible to design the structure of NAA, resulting in better control over pore diameter, length, porosity and organization of pores. However, the real understanding of the self-organizing anodization process on aluminum is not complete. Thus, to generate and extend the range of NAA structures available, it is necessary to investigate this phenomenon intensely. For its wider commercial application, the cost is a critical factor for NAA to be used as a consumable, however, the cost of high purity aluminum may be bottom line in this scenario. In terms of surface chemistry, the surface properties of NAA can be finely tuned in limited ways due to inherent properties of the process used to functionalize NAA (*i.e.*, limited coverage, stability, and terminal groups). In the future we may expect

more versatile surface functionalization process to achieve chemistries unimaginable with present techniques and several research groups are already working towards it.

This review has summarized and presented the recent progresses in surface functionalization and modification of NAA and the developments for its use in localized plasmon and reflective interference based sensing systems. We have presented a detailed description about structure and surface modifications of NAA. We have also provided detail of the fundamental aspects of LPR and RIfS in combination with NAA platforms along with the most relevant concepts and examples of devices reported based on NAA and these optical techniques. Due to the advanced properties of NAA, it has emerged as a highly attractive alternative for development of broad range stable and functional sensing devices for clinical, industrial and environmental analyses. The ability to modify the surface of NAA with a wide range of functionalities to endow it with desired selectivity and specificity towards target analytes has pushed NAA for applications in several fields. We believe that future developments in structural engineering and chemical modifications of NAA will yield more innovative NAA-based sensing systems. Furthermore, a number of methods to structurally engineer the NAA make it further attractive nanostructures for development of future optical sensing devices. However, this review has demonstrated that there is still plenty of advances and developments to be made in the field of structural engineering, surface modification, and NAA-LPR and NAA-RIfS based sensing platforms.

Acknowledgments

This research was supported by the Australian Research Council (ARC) through the grant No. DE14010054 and the School of Chemical Engineering, The University of Adelaide.

Author Contributions

T.K., A.S. and D.L. contributed equally to this work.

Conflicts of Interest

The authors declare no conflict of interest.

References

1. Gyurcsányi, R.E. Chemically-modified nanopores for sensing. *TrAC Trends Anal. Chem.* **2008**, *27*, 627–639.
2. Ghicov, A.; Schmuki, P. Self-ordering electrochemistry: A review on growth and functionality of TiO_2 nanotubes and other self-aligned MOx structures. *Chem. Commun.* **2009**, 2791–2808, doi:10.1039/b822726h.
3. Santos, A.; Kumeria, T.; Losic, D. Nanoporous anodic aluminum oxide for chemical sensing and biosensors. *TrAC Trends Anal. Chem.* **2013**, *44*, 25–38.
4. Ingham, C.J.; ter Maat, J.; de Vos, W.M. Where bio meets nano: The many uses for nanoporous aluminum oxide in biotechnology. *Biotechnol. Adv.* **2012**, *30*, 1089–1099.
5. Velleman, L.; Triani, G.; Evans, P.J.; Shapter, J.G.; Losic, D. Structural and chemical modification of porous alumina membranes. *Microporous Mesoporous Mater.* **2009**, *126*, 87–94.

6. Losic, D.; Simovic, S. Self-ordered nanopore and nanotube platforms for drug delivery applications. *Exp. Opin. Drug Deliv.* **2009**, *6*, 1363–1381.
7. Keller, F.; Hunter, M.; Robinson, D. Structural features of oxide coatings on aluminum. *J. Electrochem. Soc.* **1953**, *100*, 411–419.
8. Lee, W.; Ji, R.; Gösele, U.; Nielsch, K. Fast fabrication of long-range ordered porous alumina membranes by hard anodization. *Nat. Mater.* **2006**, *5*, 741–747.
9. Alkire, R.C.; Gogotsi, Y.; Simon, P.; Eftekhari, A. *Nanostructured Materials in Electrochemistry*; John Wiley & Sons: Hoboken, NJ, USA, 2008.
10. Jessensky, O.; Müller, F.; Gösele, U. Self-organized formation of hexagonal pore arrays in anodic alumina. *Appl. Phys. Lett.* **1998**, *72*, 1173–1175.
11. Li, A.P.; Müller, F.; Bimer, A.; Nielsch, K.; Gösele, U. Hexagonal pore arrays with a 50–420 nm interpore distance formed by self-organization in anodic alumina. *J. Appl. Phys.* **1998**, *84*, 6023–6026.
12. Ono, S.; Saito, M.; Asoh, H. Self-ordering of anodic porous alumina formed in organic acid electrolytes. *Electrochim. Acta* **2005**, *51*, 827–833.
13. Losic, D.; Velleman, L.; Kant, K.; Kumeria, T.; Gulati, K.; Shapter, J.G.; Beattie, D.A.; Simovic, S. Self-ordering electrochemistry: A simple approach for engineering nanopore and nanotube arrays for emerging applications. *Aust. J. Chem.* **2011**, *64*, 294–301.
14. Masuda, H.; Fukuda, K. Ordered metal nanohole arrays made by a two-step replication of honeycomb structures of anodic alumina. *Science* **1995**, *268*, 1466–1468.
15. Masuda, H.; Hasegwa, F.; Ono, S. Self-ordering of cell arrangement of anodic porous alumina formed in sulfuric acid solution. *J. Electrochem. Soc.* **1997**, *144*, L127–L130.
16. Masuda, H.; Yada, K.; Osaka, A. Self-ordering of cell configuration of anodic porous alumina with large-size pores in phosphoric acid solution. *Jpn. J. Appl. Phys.* **1998**, *37*, L1340.
17. Surganov, V.; Morgen, P.; Nielsen, J.; Gorokh, G.; Mozalev, A. Study of the initial stage of aluminium anodization in malonic acid solution. *Electrochim. Acta* **1987**, *32*, 1125–1127.
18. Surganov, V.; Gorokh, G. Anodic oxide cellular structure formation on aluminum films in tartaric acid electrolyte. *Mater. Lett.* **1993**, *17*, 121–124.
19. Chu, S.; Wada, K.; Inoue, S.; Isogai, M.; Katsuta, Y.; Yasumori, A. Large-scale fabrication of ordered nanoporous alumina films with arbitrary pore intervals by critical-potential anodization. *J. Electrochem. Soc.* **2006**, *153*, B384–B391.
20. Ono, S.; Saito, M.; Ishiguro, M.; Asoh, H. Controlling factor of self-ordering of anodic porous alumina. *J. Electrochem. Soc.* **2004**, *151*, B473–B478.
21. Mozalev, A.; Mozaleva, I.; Sakairi, M.; Takahashi, H. Anodic film growth on al layers and ta–al metal bilayers in citric acid electrolytes. *Electrochim. Acta* **2005**, *50*, 5065–5075.
22. Nielsch, K.; Choi, J.; Schwirn, K.; Wehrspohn, R.B.; Gösele, U. Self-ordering regimes of porous alumina: The 10% porosity rule. *Nano Lett.* **2002**, *2*, 677–680.
23. Schwirn, K.; Lee, W.; Hillebrand, R.; Steinhart, M.; Nielsch, K.; Gösele, U. Self-ordered anodic aluminum oxide formed by H_2SO_4 hard anodization. *ACS Nano* **2008**, *2*, 302–310.
24. Santos, A.; Formentín, P.; Pallarès, J.; Ferré-Borrull, J.; Marsal, L.F. Structural engineering of nanoporous anodic alumina funnels with high aspect ratio. *J. Electroanal. Chem.* **2011**, *655*, 73–78.

25. Losic, D.; Lillo, M. Porous alumina with shaped pore geometries and complex pore architectures fabricated by cyclic anodization. *Small* **2009**, *5*, 1392–1397.
26. Lee, W.; Schwirn, K.; Steinhart, M.; Pippel, E.; Scholz, R.; Gösele, U. Structural engineering of nanoporous anodic aluminium oxide by pulse anodization of aluminium. *Nat. Nanotechnol.* **2008**, *3*, 234–239.
27. Meng, G.; Jung, Y.J.; Cao, A.; Vajtai, R.; Ajayan, P.M. Controlled fabrication of hierarchically branched nanopores, nanotubes, and nanowires. *Proc. Natl. Acad. Sci. USA* **2005**, *102*, 7074–7078.
28. Losic, D. Preparation of porous anodic alumina with periodically perforated pores. *Langmuir* **2009**, *25*, 5426–5431.
29. Md Jani, A.M.; Losic, D.; Voelcker, N.H. Nanoporous anodic aluminium oxide: Advances in surface engineering and emerging applications. *Prog. Mater. Sci.* **2013**, *58*, 636–704.
30. Thompson, G.E.; Wood, G.C. Anodic films on aluminium. In *Treatise on Materials Science and Technology*; Scully, J.C., Ed.; Academic Press. Inc.: New York, NY, USA, 1983; Volume 23, pp. 205–329.
31. Yamamoto, Y.; Baba, N.; Tajima, S. Coloured materials and photoluminescence centres in anodic film on aluminium. *Nat. Lett.* **1981**, *289*, 572–574.
32. Santos, A.; Kumeria, T.; Wang, Y.; Losic, D. *In situ* monitored engineering of inverted nanoporous anodic alumina funnels: On the precise generation of 3d optical nanostructures. *Nanoscale* **2014**, doi: 10.1039/C4NR01422G.
33. Lei, Y.; Cai, W.; Wilde, G. Highly ordered nanostructures with tunable size, shape and properties: A new way to surface nano-patterning using ultra-thin alumina masks. *Prog. Mater. Sci.* **2007**, *52*, 465–539.
34. Hou, S.; Harrell, C.C.; Trofin, L.; Kohli, P.; Martin, C.R. Layer-by-layer nanotube template synthesis. *J. Am. Chem. Soc.* **2004**, *126*, 5674–5675.
35. Cheow, P.S.; Ting, E.Z.C.; Tan, M.Q.; Toh, C.S. Transport and separation of proteins across platinum-coated nanoporous alumina membranes. *Electrochim. Acta* **2008**, *53*, 4669–4673.
36. Nguyen, B.T.; Ting, E.Z.C.; Toh, C.-S. Development of a biomimetic nanoporous membrane for the selective transport of charged proteins. *Bioinspir. Biomim.* **2008**, *3*, 035008.
37. Qiu, T.; Zhang, W.; Lang, X.; Zhou, Y.; Cui, T.; Chu, P.K. Controlled assembly of highly raman-enhancing silver nanocap arrays templated by porous anodic alumina membranes. *Small* **2009**, *5*, 2333–2337.
38. Zhang, L.; Fang, Y.; Zhang, P. Laser-mbe of nickel nanowires using aao template: A new active substrate of surface enhanced raman scattering. *Spectrochim. Acta A Mol. Biomol. Spectrosc.* **2008**, *69*, 91–95.
39. Béron, F.; Knobel, M.; Pirota, K.R. Magnetostatic behaviour of antidot arrays under the local influence of nanopillars. *J. Phys. D Appl. Phys.* **2012**, *45*, 505002
40. Béron, F.; Pirota, K.R.; Vega, V.; Prida, V.M.; Fernández, A.; Hernando, B.; Knobel, M. An effective method to probe local magnetostatic properties in a nanometric FePd antidot array. *New J. Phys.* **2011**, *13*, 013035.
41. Brevnov, D.A.; Barela, M.J.; Brooks, M.J.; López, G.P.; Atanassov, P.B. Fabrication of anisotropic super hydrophobic/hydrophilic nanoporous membranes by plasma polymerization of c4f8 on anodic aluminum oxide. *J. Electrochem. Soc.* **2004**, *151*, B484–B489.

42. Losic, D.; Cole, M.A.; Dollmann, B.; Vasilev, K.; Griesser, H.J. Surface modification of nanoporous alumina membranes by plasma polymerization. *Nanotechnology* **2008**, *19*, 245704.
43. Ott, A.W.; McCarley, K.C.; Klaus, J.W.; Way, J.D.; George, S.M. Atomic layer controlled deposition of Al_2O_3 films using binary reaction sequence chemistry. *Appl. Surf. Sci.* **1996**, *107*, 128–136.
44. Berland, B.S.; Gartland, I.P.; Ott, A.W.; George, S.M. *In situ* monitoring of atomic layer controlled pore reduction in alumina tubular membranes using sequential surface reactions. *Chem. Mater.* **1998**, *10*, 3941–3950.
45. Xiong, G.; Elam, J.W.; Feng, H.; Han, C.Y.; Wang, H.H.; Iton, L.E.; Curtiss, L.A.; Pellin, M.J.; Kung, M.; Kung, H.; *et al.* Effect of atomic layer deposition coatings on the surface structure of anodic aluminum oxide membranes. *J. Phys. Chem. B* **2005**, *109*, 14059–14063.
46. Knez, M.; Nielsch, K.; Niinistö, L. Synthesis and surface engineering of complex nanostructures by atomic layer deposition. *Adv. Mater.* **2007**, *19*, 3425–3438.
47. Elam, J.; Routkevitch, D.; Mardilovich, P.; George, S. Conformal coating on ultrahigh-aspect-ratio nanopores of anodic alumina by atomic layer deposition. *Chem. Mater.* **2003**, *15*, 3507–3517.
48. Lee, B.H.; Hwang, J.K.; Nam, J.W.; Lee, S.U.; Kim, J.T.; Koo, S.M.; Baunemann, A.; Fischer, R.A.; Sung, M.M. Low-temperature atomic layer deposition of copper metal thin films: Self-limiting surface reaction of copper dimethylamino-2-propoxide with diethylzinc. *Angew. Chem. Int. Ed. Engl.* **2009**, *48*, 4536–4539.
49. Lim, B.S.; Rahtu, A.; Gordon, R.G. Atomic layer deposition of transition metals. *Nat. Mater.* **2003**, *2*, 749–754.
50. Sander, M.S.; Côté, M.J.; Gu, W.; Kile, B.M.; Tripp, C.P. Template-assisted fabrication of dense, aligned arrays of titania nanotubes with well-controlled dimensions on substrates. *Adv. Mater.* **2004**, *16*, 2052–2057.
51. Norek, M.; Łuka, G.; Godlewski, M.; Płociński, T.; Michalska-Domańska, M.; Stępniowski, W.J. Plasmonic enhancement of blue emission from ZnOnanorods grown on the anodic aluminum oxide (AAO) template. *Appl. Phys. A* **2013**, *111*, 265–271.
52. Bachmann, J.; Jing, J.; Knez, M.; Barth, S.; Shen, H.; Mathur, S.; Gösele, U.; Nielsch, K. Ordered iron oxide nanotube arrays of controlled geometry and tunable magnetism by atomic layer deposition. *J. Am. Chem. Soc.* **2007**, *129*, 9554–9555.
53. Pitzschel, K.; Moreno, J.M.M.; Escrig, J.; Albrecht, O.; Nielsch, K.; Bachmann, J. Controlled introduction of diameter modulations in arrayed magnetic iron oxide nanotubes. *ACS Nano* **2009**, *3*, 3463–3468.
54. Miranda, L.D.; Short, R.T.; van Amerom, F.H.W.; Bell, R.J.; Byrne, R.H. Direct coupling of a carbon nanotube membrane to a mass spectrometer: Contrasting nanotube and capillary tube introduction systems. *J. Membr. Sci.* **2009**, *344*, 26–31.
55. Popp, A.; Engstler, J.; Schneider, J.J. Porous carbon nanotube-reinforced metals and ceramics via a double templating approach. *Carbon* **2009**, *47*, 3208–3214.
56. Park, S.; Kim, Y.S.; Kim, W.B.; Jon, S. Carbon nanosyringe array as a platform for intracellular delivery. *Nano Lett.* **2009**, *9*, 1325–1329.

57. Che, G.; Lakshmi, B.B.; Martin, C.R.; Fisher, E.R.; Ruoff, R.S. Chemical vapor deposition based synthesis of carbon nanotubes and nanofibers using a template method. *Chem. Mater.* **1998**, *10*, 260–267.
58. Altalhi, T.; Kumeria, T.; Santos, A.; Losic, D. Synthesis of well-organised carbon nanotube membranes from non-degradable plastic bags with tuneable molecular transport: Towards nanotechnological recycling. *Carbon* **2013**, *63*, 423–433.
59. Kumeria, T.; Santos, A.; Losic, D. Ultrasensitive nanoporous interferometric sensor for label-free detection of gold (III) ions. *ACS Appl. Mater. Interfaces* **2013**, *5*, 11783–11790.
60. Santos, A.; Kumeria, T.; Losic, D. Optically optimized photoluminescent and interferometric biosensors based on nanoporous anodic alumina: A comparison. *Anal. Chem.* **2013**, *85*, 7904–7911.
61. Martin, C.R. Nanomaterials: A membrane-based synthetic approach. *Science* **1994**, *266*, 1961–1966.
62. Szczepanski, V.; Vlassiouk, I.; Smirnov, S. Stability of silane modifiers on alumina nanoporous membranes. *J. Membr. Sci.* **2006**, *281*, 587–591.
63. Hendren, Z.D.; Brant, J.; Wiesner, M.R. Surface modification of nanostructured ceramic membranes for direct contact membrane distillation. *J. Membr. Sci.* **2009**, *331*, 1–10.
64. Odom, D.J.; Baker, L.A.; Martin, C.R. Solvent-extraction and langmuir-adsorption-based transport in chemically functionalized nanopore membranes. *J. Phys. Chem. B* **2005**, *109*, 20887–20894.
65. Ku, A.Y.; Ruud, J.A.; Early, T.A.; Corderman, R.R. Evidence of ion transport through surface conduction in alkylsilane-functionalized nanoporous ceramic membranes. *Langmuir* **2006**, *22*, 8277–8280.
66. Popat, K.C.; Mor, G.; Grimes, C.A.; Desai, T.A. Surface modification of nanoporous alumina surfaces with poly(ethylene glycol). *Langmuir* **2004**, *20*, 8035–8041.
67. La Flamme, K.E.; Popat, K.C.; Leoni, L.; Markiewicz, E.; La Tempa, T.J.; Roman, B.B.; Grimes, C.A.; Desai, T.A. Biocompatibility of nanoporous alumina membranes for immunoisolation. *Biomaterials* **2007**, *28*, 2638–2645.
68. Lee, S.W.; Shang, H.; Haasch, R.T.; Petrova, V.; Lee, G.U. Transport and functional behaviour of poly(ethylene glycol)-modified nanoporous alumina membranes. *Nanotechnology* **2005**, *16*, 1335–1340.
69. Vlassiouk, I.; Takmakov, P.; Smirnov, S. Sensing DNA hybridization via ionic conductance through a nanoporous electrode. *Langmuir* **2005**, *21*, 4776–4778.
70. Takmakov, P.; Vlassiouk, I.; Smirnov, S. Application of anodized aluminum in fluorescence detection of biological species. *Anal. Bioanal. Chem.* **2006**, *385*, 954–958.
71. Yang, Z.; Si, S.; Dai, H.; Zhang, C. Piezoelectric urea biosensor based on immobilization of urease onto nanoporous alumina membranes. *Biosens. Bioelectron.* **2007**, *22*, 3283–3287.
72. Hobler, C.; Bakowsky, U.; Keusgen, M. A functional immobilization of semiconductor nanoparticles (quantum dots) on nanoporous aluminium oxide. *Phys. Status Solidi A* **2010**, *207*, 872–877.
73. Largueze, J.B.; Kirat, K.E.; Morandat, S. Preparation of an electrochemical biosensor based on lipid membranes in nanoporous alumina. *Colloids Surf. B Biointerfaces* **2010**, *79*, 33–40.
74. Lau, K.A.; Duran, H.; Knoll, W. *In situ* characterization of n-carboxy anhydride polymerization in nanoporous anodic alumina. *J. Phys. Chem. B* **2009**, *113*, 3179–3189.

75. Li, P.F.; Xie, R.; Jiang, J.C.; Meng, T.; Yang, M.; Ju, X.J.; Yang, L.; Chu, L.Y. Thermo-responsive gating membranes with controllable length and density of poly(n-isopropylacrylamide) chains grafted by atrp method. *J. Membr. Sci.* **2009**, *337*, 310–317.
76. Wang, W.; Li, N.; Li, X.; Geng, W.; Qiu, S. Synthesis of metallic nanotube arrays in porous anodic aluminum oxide template through electroless deposition. *Mater. Res. Bullet.* **2006**, *41*, 1417–1423.
77. Jani, A.M.M.; Anglin, E.J.; McInnes, S.J.; Losic, D.; Shapter, J.G.; Voelcker, N.H. Nanoporous anodic aluminium oxide membranes with layered surface chemistry. *Chem. Commun.* **2009**, 3062–3064, doi:10.1039/b901745c.
78. Sehayek, T.; Lahav, M.; Popovitz-Biro, R.; Vaskevich, A.; Rubinstein, I. Template synthesis of nanotubes by room-temperature coalescence of metal nanoparticles. *Chem. Mater.* **2005**, *17*, 3743–3748.
79. Lahav, M.; Sehayek, T.; Vaskevich, A.; Rubinstein, I. Nanoparticle nanotubes. *Angew. Chem.* **2003**, *115*, 5734–5737.
80. Jani, A.M.M.; Kempson, I.M.; Losic, D.; Voelcker, N.H. Dressing in layers: Layering surface functionalities in nanoporous aluminum oxide membranes. *Angew. Chem. Int. Ed.* **2010**, *49*, 7933–7937.
81. Allara, D.L.; Nuzzo, R.G. Spontaneously organized molecular assemblies. 1. Formation, dynamics, and physical properties of n-alkanoic acids adsorbed from solution on an oxidized aluminum surface. *Langmuir* **1985**, *1*, 45–52.
82. Allara, D.L.; Nuzzo, R.G. Spontaneously organized molecular assemblies. 2. Quantitative infrared spectroscopic determination of equilibrium structures of solution-adsorbed n-alkanoic acids on an oxidized aluminum surface. *Langmuir* **1985**, *1*, 52–66.
83. Chang, C.S.; Suen, S.Y. Modification of porous alumina membranes with n-alkanoic acids and their application in protein adsorption. *J. Membr. Sci.* **2006**, *275*, 70–81.
84. Cheow, P.S.; Liu, L.; Toh, C.S. Grafting of nanoporous alumina membranes and films with organic acids. *Surf. Interface Anal.* **2007**, *39*, 601–610.
85. Karaman, M.E.; Antelmi, D.A.; Pashley, R.M. The production of stable hydrophobic surfaces by the adsorption of hydrocarbon and fluorocarbon carboxylic acids onto alumina substrates. *Colloids Surf. A Physicochem. Eng. Asp.* **2001**, *182*, 285–298.
86. Öberg, K.; Persson, P.; Shchukarev, A.; Eliasson, B. Comparison of monolayer films of stearic acid and methyl stearate on an al2o3 surface. *Thin Solid Films* **2001**, *397*, 102–108.
87. Debrassi, A.; Ribbera, A.; de Vos, W.M.; Wennekes, T.; Zuilhof, H. Stability of (bio)functionalized porous aluminum oxide. *Langmuir* **2014**, *30*, 1311–1320.
88. Kant, K.; Yu, J.; Priest, C.; Shapter, J.G.; Losic, D. Impedance nanopore biosensor: Influence of pore dimensions on biosensing performance. *Analyst* **2014**, *139*, 1134–1140.
89. Kant, K.; Kurkuri, M.D.; Yu, J.; Shapter, J.G.; Priest, C.; Losic, D. Impedance spectroscopy study of nanopore arrays for biosensing applications. *Sci. Adv. Mater.* **2014**, *6*, 1–7.
90. Schmitt, E.K.; Nurnabi, M.; Bushby, R.J.; Steinem, C. Electrically insulating pore-suspending membranes on highly ordered porous alumina obtained from vesicle spreading. *Soft Matter* **2008**, *4*, 250.

91. Proux-Delrouyre, V.; Elie, C.; Laval, J.M.; Moiroux, J.; Bourdillon, C. Formation of tethered and streptavidin-supported lipid bilayers on a microporous electrode for the reconstitution of membranes of large surface area. *Langmuir* **2002**, *18*, 3263–3272.
92. Schmitt, E.K.; Weichbrodt, C.; Steinem, C. Impedance analysis of gramicidin d in pore-suspending membranes. *Soft Matter* **2009**, *5*, 3347–3353.
93. Drexler, J.; Steinem, C. Pore-suspending lipid bilayers on porous alumina investigated by electrical impedance spectroscopy. *J. Phys. Chem. B* **2003**, *107*, 11245–11254.
94. Demé, B.; Marchal, D. Polymer-cushioned lipid bilayers in porous alumina. *Eur. Biophys. J.* **2005**, *34*, 170–179.
95. Smirnov, A.I.; Poluektov, O.G. Substrate-supported lipid nanotube arrays. *J. Am. Chem. Soc.* **2003**, *125*, 8434–8435.
96. Bruening, M.L.; Dotzauer, D.M.; Jain, P.; Ouyang, L.; Baker, G.L. Creation of functional membranes using polyelectrolyte multilayers and polymer brushes. *Langmuir* **2008**, *24*, 7663–7673.
97. Balachandra, A.M.; Dai, J.; Bruening, M.L. Enhancing the anion-transport selectivity of multilayer polyelectrolyte membranes by templating with Cu^{2+}. *Macromolecules* **2002**, *35*, 3171–3178.
98. Hong, S.U.; Bruening, M.L. Separation of amino acid mixtures using multilayer polyelectrolyte nanofiltration membranes. *J. Membr. Sci.* **2006**, *280*, 1–5.
99. Hong, S.U.; Malaisamy, R.; Bruening, M.L. Separation of fluoride from other monovalent anions using multilayer polyelectrolyte nanofiltration membranes. *Langmuir* **2007**, *23*, 1716–1722.
100. Hong, S.U.; Ouyang, L.; Bruening, M.L. Recovery of phosphate using multilayer polyelectrolyte nanofiltration membranes. *J. Membr. Sci.* **2009**, *327*, 2–5.
101. Dai, J.; Baker, G.L.; Bruening, M.L. Use of porous membranes modified with polyelectrolyte multilayers as substrates for protein arrays with low nonspecific adsorption. *Anal. Chem.* **2006**, *78*, 135–140.
102. Dotzauer, D.M.; Dai, J.; Sun, L.; Bruening, M.L. Catalytic membranes prepared using layer-by-layer adsorption of polyelectrolyte/metal nanoparticle films in porous supports. *Nano Lett.* **2006**, *6*, 2268–2272.
103. Yang, Y.; He, Q.; Duan, L.; Cui, Y.; Li, J. Assembled alginate/chitosan nanotubes for biological application. *Biomaterials* **2007**, *28*, 3083–3090.
104. Ai, S.; Lu, G.; He, Q.; Li, J. Highly flexible polyelectrolyte nanotubes. *J. Am. Chem. Soc.* **2003**, *125*, 11140–11141.
105. Hou, S.; Wang, J.; Martin, C.R. Template-synthesized DNA nanotubes. *J. Am. Chem. Soc.* **2005**, *127*, 8586–8587.
106. Hou, S.; Wang, J.; Martin, C.R. Template-synthesized protein nanotubes. *Nano Lett.* **2005**, *5*, 231–234.
107. Matsumoto, F.; Nishio, K.; Masuda, H. Flow-through-type DNA array based on ideally ordered anodic porous alumina substrate. *Adv. Mater.* **2004**, *16*, 2105–2108.
108. Kodiyath, R.; Malak, S.T.; Combs, Z.A.; Koenig, T.; Mahmoud, M.A.; El-Sayed, M.A.; Tsukruk, V.V. Assemblies of silver nanocubes for highly sensitive sers chemical vapor detection. *J. Mater. Chem. A* **2013**, *1*, 2777–2788.
109. Gasparac, R.; Kohli, P.; Mota, M.O.; Trofin, L.; Martin, C.R. Template synthesis of nano test tubes. *Nano Lett.* **2004**, *4*, 513–516.

110. Hench, L.L.; West, J.K. The sol-gel process. *Chem. Rev.* **1990**, *90*, 33–72.
111. Lakshmi, B.B.; Patrissi, C.J.; Martin, C.R. Sol-gel template synthesis of semiconductor oxide micro- and nanostructures. *Chem. Mater.* **1997**, *9*, 2544–2550.
112. Hunks, W.J.; Ozin, G.A. Challenges and advances in the chemistry of periodic mesoporous organosilicas (pmos). *J. Mater. Chem.* **2005**, *15*, 3716–3724.
113. Lee, S.B.; Mitchell, D.T.; Trofin, L.; Nevanen, T.K.; Söderlund, H.; Martin, C.R. Antibody-based bio-nanotube membranes for enantiomeric drug separations. *Science* **2002**, *296*, 2198–2200.
114. He, B.; Son, S.J.; Lee, S.B. Suspension array with shape-coded silica nanotubes for multiplexed immunoassays. *Anal. Chem.* **2007**, *79*, 5257–5263.
115. He, B.; Kim, S.K.; Son, S.J.; Lee, S.B. Shape-coded silica nanotubes for multiplexed bioassay: Rapid and reliable magnetic decoding protocols. *Nanomedicine* **2010**, *5*, 77–88.
116. He, B.; Son, S.J.; Lee, S.B. Shape-coded silica nanotubes for biosensing. *Langmuir* **2006**, *22*, 8263–8265.
117. Wang, K.; Birjukovs, P.; Erts, D.; Phelan, R.; Morris, M.A.; Zhou, H.; Holmes, J.D. Synthesis and characterisation of ordered arrays of mesoporous carbon nanofibres. *J. Mater. Chem.* **2009**, *19*, 1331–1338.
118. Wang, K.; Wei, M.; Morris, M.A.; Zhou, H.; Holmes, J.D. Mesoporous titania nanotubes: Their preparation and application as electrode materials for rechargeable lithium batteries. *Adv. Mater.* **2007**, *19*, 3016–3020.
119. Platschek, B.; Petkov, N.; Himsl, D.; Zimdars, S.; Li, Z.; Köhn, R.; Bein, T. Vertical columnar block-copolymer-templated mesoporous silica via confined phase transformation. *J. Am. Chem. Soc.* **2008**, *130*, 17362–17371.
120. Confalonieri, G.B.; Vega, V.; Ebbing, A.; Mishra, D.; Szary, P.; Prida, V.M.; Petracic, O.; Zabel, H. Template-assisted self-assembly of individual and clusters of magnetic nanoparticles. *Nanotechnology* **2011**, *22*, 285608.
121. Hurst, S.J.; Payne, E.K.; Qin, L.; Mirkin, C.A. Multisegmented one-dimensional nanorods prepared by hard-template synthetic methods. *Angew. Chem. Int. Ed. Engl.* **2006**, *45*, 2672–2692.
122. Liu, L.; Lee, W.; Huang, Z.; Scholz, R.; Gösele, U. Fabrication and characterization of a flow-through nanoporous gold nanowire/AAO composite membrane. *Nanotechnology* **2008**, *19*, 335604.
123. Burdick, J.; Alonas, E.; Huang, H.-C.; Rege, K.; Wang, J. High-throughput templated multisegment synthesis of gold nanowires and nanorods. *Nanotechnology* **2009**, *20*, 065306.
124. Lee, H.J.; Yasukawa, T.; Suzuki, M.; Lee, S.H.; Yao, T.; Taki, Y.; Tanaka, A.; Kameyama, M.; Shiku, H.; Matsue, T. Simple and rapid preparation of vertically aligned gold nanoparticle arrays and fused nanorods in pores of alumina membrane based on positive dielectrophoresis. *Sens. Actuators B* **2009**, *136*, 320–325.
125. Kondo, T.; Nishio, K.; Masuda, H. Surface-enhanced raman scattering in multilayered au nanoparticles in anodic porous alumina matrix. *Appl. Phys. Express* **2009**, *2*, 032001.
126. Ali, H.O.; Christie, I.R. A review of electroless gold deposition processes. *Gold Bull.* **1984**, *17*, 118–127.

127. Mu, C.; Zhang, J.-P.; Xu, D. Au nanoparticle arrays with tunable particle gaps by template-assisted electroless deposition for high performance surface-enhanced raman scattering. *Nanotechnology* **2010**, *21*, 015604.
128. Lee, W.; Scholz, R.; Nielsch, K.; Gösele, U. A template-based electrochemical method for the synthesis of multisegmented metallic nanotubes. *Angew. Chem.* **2005**, *117*, 6204–6208.
129. Zhang, J.J.; Hou, X.; Liu, L.H.; Sun, H.Y. Optical and magnetic properties of PAA@ Fe nanocomposite films. *AIP Adv.* **2013**, *3*, 072116.
130. Wang, K.; Liu, G.; Hoivik, N.; Johannessen, E.; Jakobsen, H. Electrochemical engineering of hollow nanoarchitectures: Pulse/step anodization (Si, Al, Ti) and their applications. *Chem. Soc. Rev.* **2014**, *43*, 1476–1500.
131. Montero-Moreno, J.; Sarret, M.; Müller, C. Some considerations on the influence of voltage in potentiostatic two-step anodizing of aa1050. *J. Electrochem. Soc.* **2007**, *154*, C169–C174.
132. Kumeria, T.; Rahman, M.M.; Santos, A.; Ferré-Borrull, J.; Marsal, L.F.; Losic, D. Structural and optical nanoengineering of nanoporous anodic alumina rugate filters for real-time and label-free biosensing applications. *Anal. Chem.* **2014**, *86*, 1837–1844.
133. Santos, A.; Ferré-Borrull, J.; Pallares, J.; Marsal, L. Hierarchical nanoporous anodic alumina templates by asymmetric two-step anodization. *Phys. Status Solidi A* **2011**, *208*, 668–674.
134. Zhu, X.; Liu, L.; Song, Y.; Jia, H.; Yu, H.; Xiao, X.; Yang, X. Oxygen bubble mould effect: Serrated nanopore formation and porous alumina growth. *Monatshefte Chem. Chem. Mon.* **2008**, *139*, 999–1003.
135. Li, D.; Zhao, L.; Jiang, C.; Lu, J.G. Formation of anodic aluminum oxide with serrated nanochannels. *Nano Lett.* **2010**, *10*, 2766–2771.
136. Santos, A.; Vojkuvka, L.; Alba, M.; Balderrama, V.S.; Ferré-Borrull, J.; Pallarès, J.; Marsal, L.F. Understanding and morphology control of pore modulations in nanoporous anodic alumina by discontinuous anodization. *Phys. Status Solidi A* **2012**, *209*, 2045–2048.
137. Nagaura, T.; Takeuchi, F.; Inoue, S. Fabrication and structural control of anodic alumina films with inverted cone porous structure using multi-step anodizing. *Electrochim. Acta* **2008**, *53*, 2109–2114.
138. Nagaura, T.; Takeuchi, F.; Yamauchi, Y.; Wada, K.; Inoue, S. Fabrication of ordered ni nanocones using a porous anodic alumina template. *Electrochem. Commun.* **2008**, *10*, 681–685.
139. Yanagishita, T.; Kondo, T.; Nishio, K.; Masuda, H. Optimization of antireflection structures of polymer based on nanoimprinting using anodic porous alumina. *J. Vac. Sci. Technol. B* **2008**, *26*, 1856–1859.
140. Li, J.; Li, C.; Chen, C.; Hao, Q.; Wang, Z.; Zhu, J.; Gao, X. Facile method for modulating the profiles and periods of self-ordered three-dimensional alumina taper-nanopores. *ACS Appl. Mater. Interfaces* **2012**, *4*, 5678–5683.
141. Sulka, G.D.; Hnida, K. Distributed bragg reflector based on porous anodic alumina fabricated by pulse anodization. *Nanotechnology* **2012**, *23*, 075303.
142. Zheng, W.J.; Fei, G.T.; Wang, B.; De Zhang, L. Modulation of transmission spectra of anodized alumina membrane distributed bragg reflector by controlling anodization temperature. *Nanoscale Res. Lett.* **2009**, *4*, 665–667.

143. Rahman, M.M.; Marsal, L.F.; Pallarès, J.; Ferré-Borrull, J. Tuning the photonic stop bands of nanoporous anodic alumina-based distributed bragg reflectors by pore widening. *ACS Appl. Mater. Interfaces* **2013**, *5*, 13375–13381.
144. Willets, K.A.; van Duyne, R.P. Localized surface plasmon resonance spectroscopy and sensing. *Annu. Rev. Phys. Chem.* **2007**, *58*, 267–297.
145. Koutsioubas, A.G.; Spiliopoulos, N.; Anastassopoulos, D.; Vradis, A.A.; Priftis, G.D. Nanoporous alumina enhanced surface plasmon resonance sensors. *J. Appl. Phys.* **2008**, *103*, 094521.
146. Lau, K.H.A.; Tan, L.-S.; Tamada, K.; Sander, M.S.; Knoll, W. Highly sensitive detection of processes occurring inside nanoporous anodic alumina templates: A waveguide optical study. *J. Phys. Chem. B* **2004**, *108*, 10812–10818.
147. Hiep, H.M.; Yoshikawa, H.; Tamiya, E. Interference localized surface plasmon resonance nanosensor tailored for the detection of specific biomolecular interactions. *Anal. Chem.* **2010**, *82*, 1221–1227.
148. Yamaguchi, A.; Hotta, K.; Teramae, N. Optical waveguide sensor based on a porous anodic alumina/aluminum multilayer film. *Anal. Chem.* **2008**, *81*, 105–111.
149. Dhathathreyan, A. Real-time monitoring of invertase activity immobilized in nanoporous aluminum oxide. *J. Phys. Chem. B* **2011**, *115*, 6678–6682.
150. Hotta, K.; Yamaguchi, A.; Teramae, N. Nanoporous waveguide sensor with optimized nanoarchitectures for highly sensitive label-free biosensing. *ACS Nano* **2012**, *6*, 1541–1547.
151. Kim, D.-K.; Kerman, K.; Saito, M.; Sathuluri, R.R.; Endo, T.; Yamamura, S.; Kwon, Y.-S.; Tamiya, E. Label-free DNA biosensor based on localized surface plasmon resonance coupled with interferometry. *Anal. Chem.* **2007**, *79*, 1855–1864.
152. Fan, Y.; Hotta, K.; Yamaguchi, A.; Teramae, N. Enhanced fluorescence in a nanoporous waveguide and its quantitative analysis. *Opt. Express* **2012**, *20*, 12850–12859.
153. Hiep, H.M.; Yoshikawa, H.; Taniyama, S.; Kondoh, K.; Saito, M.; Tamiya, E. Immobilization of gold nanoparticles on aluminum oxide nanoporous structure for highly sensitive plasmonic sensing. *Jpn. J. Appl. Phys.* **2010**, *49*, 06GM02.
154. Hiep, H.M.; Endo, T.; Saito, M.; Chikae, M.; Kim, D.K.; Yamamura, S.; Takamura, Y.; Tamiya, E. Label-free detection of melittin binding to a membrane using electrochemical-localized surface plasmon resonance. *Anal. Chem.* **2008**, *80*, 1859–1864.
155. Yeom, S.H.; Kim, O.G.; Kang, B.H.; Kim, K.J.; Yuan, H.; Kwon, D.H.; Kim, H.R.; Kang, S.W. Highly sensitive nano-porous lattice biosensor based on localized surface plasmon resonance and interference. *Opt. Express* **2011**, *19*, 22882–22891.
156. Gauglitz, G.; Ingenhoff, J. Design of new integrated optical substrates for immuno-analytical applications. *Fresenius J. Anal. Chem.* **1994**, *349*, 355–359.
157. Lin, V.S.Y.; Motesharei, K.; Dancil, K.P.S.; Sailor, M.J.; Ghadiri, M.R. A porous silicon-based optical interferometric biosensor. *Science* **1997**, *278*, 840–843.
158. Dancil, K.-P.S.; Greiner, D.P.; Sailor, M.J. A porous silicon optical biosensor: Detection of reversible binding of IgG to a protein a-modified surface. *J. Am. Chem. Soc.* **1999**, *121*, 7925–7930.
159. Alvarez, S.D.; Li, C.-P.; Chiang, C.E.; Schuller, I.K.; Sailor, M.J. A label-free porous alumina interferometric immunosensor. *ACS Nano* **2009**, *3*, 3301–3307.

160. Kumeria, T.; Losic, D. Controlling interferometric properties of nanoporous anodic aluminium oxide. *Nanoscale Res. Lett.* **2012**, *7*, 1–10.
161. Casanova, F.; Chiang, C.E.; Li, C.-P.; Roshchin, I.V.; Ruminski, A.M.; Sailor, M.J.; Schuller, I.K. Gas adsorption and capillary condensation in nanoporous alumina films. *Nanotechnology* **2008**, *19*, 315709.
162. Casanova, F.l.; Chiang, C.E.; Ruminski, A.M.; Sailor, M.J.; Schuller, I.K. Controlling the role of nanopore morphology in capillary condensation. *Langmuir* **2012**, *28*, 6832–6838.
163. Pan, S.; Rothberg, L.J. Interferometric sensing of biomolecular binding using nanoporous aluminum oxide templates. *Nano Lett.* **2003**, *3*, 811–814.
164. An, H.C.; An, J.Y.; Kim, B.-W. Improvement of sensitivity in an interferometry by controlling pore size on the anodic aluminum oxide chip pore-widening technique. *Korean J. Chem. Eng.* **2009**, *26*, 160–164.
165. Kumeria, T.; Losic, D. Reflective interferometric gas sensing using nanoporous anodic aluminium oxide (AAO). *Phys. Status Solidi (RRL) Rapid Res. Lett.* **2011**, *5*, 406–408.
166. Kumeria, T.; Parkinson, L.; Losic, D. A nanoporous interferometric micro-sensor for biomedical detection of volatile sulphur compounds. *Nanoscale Res. Lett.* **2011**, *6*, 1–7.
167. Kumeria, T.; Kurkuri, M.D.; Diener, K.R.; Parkinson, L.; Losic, D. Label-free reflectometric interference microchip biosensor based on nanoporous alumina for detection of circulating tumour cells. *Biosens. Bioelectron.* **2012**, *35*, 167–173.
168. Dronov, R.; Jane, A.; Shapter, J.G.; Hodges, A.; Voelcker, N.H. Nanoporous alumina-based interferometric transducers ennobled. *Nanoscale* **2011**, *3*, 3109–3114.
169. Kumeria, T.; Gulati, K.; Santos, A.; Losic, D. Real-time and *in situ* drug release monitoring from nanoporous implants under dynamic flow conditions by reflectometric interference spectroscopy. *ACS Appl. Mater. Interfaces* **2013**, *5*, 5436–5442.
170. Macias, G.; Hernández-Eguía, L.P.; Ferré-Borrull, J.; Pallares, J.; Marsal, L.F. Gold-coated ordered nanoporous anodic alumina bilayers for future label-free interferometric biosensors. *ACS Appl. Mater. Interfaces* **2013**, *5*, 8093–8098.